QUANTUM LIQUIDS AND QUANTUM CRYSTALS

Influence of electron–electron interaction on the mobility of electrons on the surface of liquid helium

I. N. Adamenko,* A. V. Zhukov, and K. É. Nemchenko

V. N. Karazin Kharkov National University, pl. Svobody 4, 61077 Kharkov, Ukraine
(Submitted February 29, 2000)
Fiz. Nizk. Temp. **26**, 631–637 (July 2000)

The mobility of a two-dimensional electron gas localized on the surface of liquid helium at low temperatures is found by solving the kinetic equation for the electron distribution function. The result for the mobility contains both the electron–ripplon interaction time and the electron–electron scattering time. The theory is valid for an arbitrary relationship between the electron–ripplon and electron–electron interaction times and gives the previously known expressions in the limiting cases. The results are compared with experimental data, and new experiments are proposed which can yield information about the electron–electron interaction. © *2000 American Institute of Physics.* [S1063-777X(00)00107-9]

INTRODUCTION

One of the most interesting experimentally realizable two-dimensional charged systems is a 2D electron gas localized on the surface of liquid helium.[1–6] It is of interest to study the dynamical properties of such systems because, in particular, the mobility and other kinetic characteristics of the electrons at low temperatures ($T \leqslant 0.6$ K) are determined not only by the electron–ripplon scattering but also by the electron–electron interaction.[6]

In previous theoretical papers[1,5,7,8] the emphasis was mainly on obtaining the momentum dependence of the electron–ripplon scattering frequency. This frequency was calculated in the now generally accepted form in Refs. 6 and 8 in the framework of the Born–Oppenheimer adiabatic approach.[9,10] Experiments[11–13] in which the mobility of the surface electrons in helium were measured by various methods and the corresponding theoretical calculations[14,15] attest, on the whole, to the validity of the electron–ripplon scattering theory.[5,8]

In Refs. 5 and 8 the mobility was calculated on the assumption of noninteracting electrons (the one-electron regime). Here it was understood that complete equilibrium had been established in the gas of ripplons, so that the mobility was determined solely by the electron–ripplon scattering. The one-electron theory gives a good description of the experimental data[16] at sufficiently small confining fields $E_\perp$, which correspond to a relatively small number n_e of electrons per unit surface area of the helium.

As the confining field is increased, the one-electron approximation is inadequate for describing the experimental data. The opposite limiting case, in which the electron subsystem is in equilibrium (the complete control regime) was considered theoretically and experimentally in Refs. 17 and 18. The complete control theory gives much better agreement with experiment[17] at high confining fields.

The problem addressed in the present paper is to calculate consistently the mobility of a 2D electron gas localized on the surface of liquid helium at low temperatures with both the electron–ripplon and electron–electron interactions taken into account.

SOLUTION OF THE KINETIC EQUATION

According to the results of Refs. 19–22, the ripplon–ripplon interaction time is much shorter than the electron–electron and electron–ripplon interaction times. This allows one to assume that the gas of ripplons is in equilibrium and can be described by an equilibrium Bose distribution function f_r. Then for the electron distribution function f_e it is sufficient to consider a single kinetic equation, which in the steady-state case is written as

$$eE_\parallel \frac{\partial f_e}{\partial p_z} = J(f_e, f_e) + J(f_e, f_r), \tag{1}$$

where e is the electron charge, $E_\parallel$ is the external driving electric field, which is directed along the z axis, and $J(f_e, f_e)$ and $J(f_e, f_r)$ are the binary collision integrals of electrons with electrons and electrons with ripplons, respectively. We shall henceforth ignore effects due to transitions of electrons to higher levels, assuming to the system is ideally 2D with a density n_e that is low enough so that the gas approximation holds. For a small deviation from the equilibrium state the solution of Equation (1) is conveniently sought in the form

$$f_e = f_e^{(0)} + \delta f_e, \tag{2}$$

where $f_e^{(0)} = [1 + \exp(\varepsilon - \mu_e)/T]^{-1}$ is the local equilibrium distribution function, $\varepsilon = p^2/2m$ is the electron energy, m is the electron mass, δf_e is the small deviation of the distribution function from local equilibrium, which is conveniently chosen in the form

$$\delta f_e = -g f_e', \quad \text{where} \quad f_e' = \frac{\partial f_e^{(0)}}{\partial \varepsilon}. \tag{3}$$

For finding g we introduce the Hilbert space of one-component vectors $|\psi\rangle$, with a scalar product defined by

$$\langle\psi|\chi\rangle = -\int \psi^* \chi f'_e d\Gamma. \tag{4}$$

Then, according to Refs. 23 and 24, the solution of the linearized Equation (1) can be written in vector form as

$$|g\rangle = -\hat{\mathcal{J}}^{-1}|\varphi\rangle, \tag{5}$$

where

$$|\varphi\rangle = \left|\frac{eE_\parallel}{m}\frac{1}{f'_e}\frac{\partial f_e^{(0)}}{\partial v_z}\right\rangle = \frac{eE_\parallel}{m}|p_z\rangle, \tag{6}$$

m, $\mathbf{p}$, and $\mathbf{v} = \partial\varepsilon/\partial\mathbf{p}$ are the mass, momentum, and velocity of the electron, respectively, and

$$\hat{\mathcal{J}} = \hat{\mathcal{J}}_{ee} + \hat{\mathcal{J}}_{er} \tag{7}$$

is the sum of linearized electron–electron and electron–ripplon collision operators. It should be noted that the inversion of the operator $\hat{\mathcal{J}}$ in (5) must in general be performed in a space of nonconserved quantities.[23,24] In that case the problem is simplified by making use of the fact that the total momentum of the electron system is not conserved, since the electrons interact with ripplons, so that

$$\hat{\mathcal{J}}|p_z\rangle = \hat{\mathcal{J}}_{er}|p_z\rangle \neq 0.$$

In accordance with the usual gasdynamic definition of the flux density of a gas,[25] the flow velocity of the electrons under the influence of the driving field is given by the expression

$$u_z = \frac{1}{mn_e}\int p_z f_e d\Gamma = -\frac{1}{mn_e}\int p_z f'_e g\, d\Gamma \equiv \frac{1}{mn_e}\langle p_z|g\rangle. \tag{8}$$

Starting from the definition of the mobility $\mu = u_z/E_\parallel$ and relations (5) and (8), we obtain

$$\mu = \frac{e}{m}\tau_\mu, \tag{9}$$

where

$$\tau_\mu = -\langle\varphi_1|(\hat{\mathcal{J}}_{ee} + \hat{\mathcal{J}}_{er})^{-1}|\varphi_1\rangle \tag{10}$$

is the characteristic time that determines the mobility,

$$|\varphi_1\rangle = \frac{1}{\sqrt{\rho}}|p_z\rangle, \tag{11}$$

and $\rho = \langle p_z|p_z\rangle$ is the mass density of the electron gas.

From here the problem is to find the explicit form of the characteristic time τ_μ (10). For this it is necessary to introduce complete set of orthonormalized vectors $|\varphi_\alpha\rangle$. As the first vector it is convenient to take the vector $|\varphi_1\rangle$ defined in (11). The choice of the remaining vectors is quite arbitrary and depends on what is convenient for calculations in a particular problem.[25,26] It is necessary only to satisfy the conditions of orthogonality and completeness:

$$\langle\varphi_\alpha|\varphi_{\alpha'}\rangle = \delta_{\alpha\alpha'}, \quad 1 \equiv \sum_{\alpha=1}^{\infty}|\varphi_\alpha\rangle\langle\varphi_\alpha|. \tag{12}$$

In the basis $|\varphi_\alpha\rangle$ expression (10) can be rewritten in the form[23,27]

$$\tau_\mu = -\left\{I_{er}^{(11)} - \sum_{\beta,\beta'\geqslant 2} I_{er}^{(1\beta)}[(I_{er}+I_{ee})^{-1}]_{\beta\beta'}I_{er}^{(\beta'1)}\right\}^{-1}. \tag{13}$$

Here

$$I_{er}^{(11)} = \langle\varphi_1|\hat{\mathcal{J}}_{er}|\varphi_1\rangle, \tag{14a}$$

$$I_{er}^{(1\beta)} = \langle\varphi_1|\hat{\mathcal{J}}_{er}|\varphi_\beta\rangle \quad (\beta\geqslant 2), \tag{14b}$$

$$I_{er}^{(\beta'1)} = \langle\varphi_{\beta'}|\hat{\mathcal{J}}_{er}|\varphi_1\rangle \quad (\beta'\geqslant 2), \tag{14c}$$

and the square matrices I_{er} and I_{ee} contain the matrix elements

$$I_{er}^{(\beta\beta')} = \langle\varphi_\beta|\hat{\mathcal{J}}_{er}|\varphi_{\beta'}\rangle, \quad I_{ee}^{(\beta\beta')} = \langle\varphi_\beta|\hat{\mathcal{J}}_{ee}|\varphi_{\beta'}\rangle \quad (\beta,\beta'\geqslant 2). \tag{15}$$

In obtaining expression (13) we have taken into account that electron–electron collisions conserve the total momentum of the system, i.e.,

$$\hat{\mathcal{J}}_{ee}|p_z\rangle = 0.$$

We note in particular that, unlike the classical approaches to solving the kinetic equations,[25,28,29] the result (13) contains in explicit form not only terms describing the interaction of electrons with ripplons but also terms due to electron–electron collisions.

In the next Section we show that for our problem the general solution can be written in closed analytical form in terms of the electron–ripplon and electron–electron collision frequencies.

CALCULATION OF THE TIME τ_μ

Although the matrices in Eq. (13) are infinite and nondiagonal, two important limiting cases follow directly from (13). First we set $I_{ee}\to\infty$. Physically this means instantaneous relaxation in the gas of electrons (complete control). In that case we have from (13)

$$\tau_\mu^{(\text{min})} = -\frac{1}{I_{er}^{(11)}} = \tau_{er}^{(cc)}, \tag{16}$$

where the time $\tau_{er}^{(cc)}$ (where cc stands for complete control) is given by the relation

$$\tau_{er}^{(cc)-1} = -\frac{\langle p_z|\hat{\mathcal{J}}_{er}|p_z\rangle}{\langle p_z|p_z\rangle}. \tag{17}$$

In the other limiting case $I_{ee}\to 0$, which corresponds to infinitely slow establishment of equilibrium in the electron subsystem (the one-electron regime). In this situation it follows from (13) that

$$\tau_\mu^{(\text{max})} = -\langle\varphi_1|\hat{\mathcal{J}}_{er}^{-1}|\varphi_1\rangle = \tau_{er}^{(1e)}. \tag{18}$$

With the use of the Cauchy–Bunyakovskiĭ inequality, it can be rigorously shown that

$$\tau_\mu^{(\text{max})} \geqslant \tau_\mu \geqslant \tau_\mu^{(\text{min})}. \tag{19}$$

To obtain an exact closed result for τ_μ we use the methods of matrix algebra. By virtue of the Hermitianity and positive definiteness of the matrix $-I_{ee}$, one can introduce a matrix $\mathcal{R}$ such that

$$-\mathcal{R}^+ I_{ee}\mathcal{R}=E, \tag{20}$$

where E is a unit matrix and $\mathcal{R}^+$ is the matrix that is the Hermitian conjugate of $\mathcal{R}$. Using (20), we obtain

$$(I_{er}+I_{ee})^{-1}=(I_{er}-\mathcal{R}^{+^{-1}}\mathcal{R}^+I_{ee}\mathcal{R}\mathcal{R}^{-1})^{-1}$$
$$=\mathcal{R}(\mathcal{R}^+I_{er}\mathcal{R}-E)^{-1}\mathcal{R}^+. \tag{21}$$

The matrix $-I_{er}$ (and, hence, $-\mathcal{R}^+I_{er}\mathcal{R}$) is also Hermitian and positive definite. Consequently, there exists a unitary matrix $\mathcal{U}$ such that

$$-\mathcal{U}^+\mathcal{R}^+I_{er}\mathcal{R}\mathcal{U}=\mathcal{Y}, \tag{22}$$

where $\mathcal{Y}$ is a diagonal matrix (i.e., $\mathcal{Y}_{\beta\beta'}=y_\beta\delta_{\beta\beta'}$) with non-negative elements ($y_\beta\geqslant 0$). Thus

$$(I_{er}+I_{ee})^{-1}=-\mathcal{R}\mathcal{U}(E+\mathcal{Y})^{-1}\mathcal{U}^+\mathcal{R}^+=-\mathcal{R}\mathcal{U}\mathcal{F}\mathcal{U}^+\mathcal{R}^+, \tag{23}$$

where $\mathcal{F}$ is a diagonal matrix with the coefficients

$$f_{\beta\beta'}=\frac{1}{1+y_\beta}\delta_{\beta\beta'}. \tag{24}$$

With allowance for (23) and (24), expression (13) can be written in the form

$$\tau_\mu^{-1}=\tau_{er}^{(cc)^{-1}}-\sum_{\beta\geqslant 2}\frac{|\alpha_\beta|^2}{1+y_\beta}=\tau_{er}^{(cc)^{-1}}-\sum_{\beta\geqslant 2}\frac{1}{1+y_\beta^{-1}}y_\beta^{-1}|\alpha_\beta|^2, \tag{25}$$

where

$$\alpha_\beta=\sum_{\alpha,\gamma\geqslant 2}I_{er}^{1\alpha}\mathcal{R}_{\alpha\gamma}\mathcal{U}_{\gamma\beta}. \tag{26}$$

From the positivity of $|\alpha_\beta|^2$ and y_β^{-1} it follows that there exists a quantity y such that

$$\tau_\mu^{-1}=\tau_{er}^{(cc)^{-1}}-\frac{1}{1+y^{-1}}\sum_{\beta\geqslant 2}y_\beta^{-1}|\alpha_\beta|^2. \tag{27}$$

We see from (23) that y_β is determined by the ratio of the characteristic time for interactions within the electron subsystem to the electron–ripplon relaxation time. Thus

$$y=\tau_{ee}/\tau_{er}^{(cc)}, \tag{28}$$

where the time τ_{ee} is determined by the electron–electron interaction.

Furthermore, for $\tau_{ee}\rightarrow\infty$ inequality (18) must be satisfied, so that

$$\sum_{\beta\geqslant 2}y_\beta^{-1}|\alpha_\beta|^2=\tau_{er}^{(cc)^{-1}}-\tau_{er}^{(1e)^{-1}}. \tag{29}$$

With (28) and (29) taken into account, the final expression for τ_μ^{-1} becomes

$$\tau_\mu^{-1}=\tau_{er}^{(cc)^{-1}}-\frac{1}{1+\tau_{er}^{(cc)}/\tau_{ee}}\{\tau_{er}^{(cc)^{-1}}-\tau_{er}^{(1e)^{-1}}\}. \tag{30}$$

Expression (30) can be rewritten in the more transparent form

$$\tau_\mu=\tau_{er}^{(cc)}\frac{1+\tau_{ee}\tau_{er}^{(cc)^{-1}}}{1+\tau_{ee}\tau_{er}^{(1e)^{-1}}}. \tag{31}$$

The final result (31) can be used to compare the theory with the available experimental data and to investigate the possible limiting cases.

COMPARISON OF THEORY AND EXPERIMENT

The first theoretical studies[5,8] of the mobility of an electron gas on the surface of liquid helium were done in the framework of the one-electron theory, i.e., it was assumed that there are no interactions between electrons and that the relaxation of the system is governed completely by the electron–ripplon interaction. Mathematically this means that the condition $\tau_{ee}\rightarrow\infty$ holds. In this limiting case it follows from Eq. (31) that

$$\tau_\mu=\tau_{er}^{(1e)}. \tag{32}$$

According to (18) and the definition of the scalar product (4), formula (32) gives

$$\tau_\mu^{(1e)}=\int_0^\infty\frac{xe^{-x}}{\nu(\tilde{x})}dx, \quad \tilde{x}=\frac{(2mTx)^{1/2}}{\hbar}, \tag{33}$$

which agrees with the known result.[5,6,8] In obtaining (33) we used as the electron–ripplon collision operator the calculated[5,8] electron–ripplon relaxation frequency $\nu(p)$, which depends on the momentum of the electron.

In the other limiting case, that of instantaneous establishment of equilibrium in the electron subsystem (the complete control regime), when $\tau_{ee}^{-1}\rightarrow\infty$, the general result (31) gives

$$\tau_\mu=\tau_{er}^{(cc)}=\left(\int_0^\infty x\nu(\tilde{x})e^{-x}dx\right)^{-1}, \tag{34}$$

which coincides with the result that was first obtained in Ref. 17.

With the general formula (31) obtained in this paper one can investigate all the intermediate cases with a finite electron–electron relaxation time τ_{ee}. In particular, it is of interest to determine the character of the dependence of τ_{ee} on the temperature and electron concentration n_e from a comparison with the experimental data.

The results that follow from formula (33) give a good description of the experimental data[16] on the mobility at low confining fields. Figure 1 shows the inverse electron mobility μ^{-1} as a function of temperature in the one-electron approximation, calculated according to (33) with $n_e=E_\perp/2\pi e=0.53\times 10^8$ cm^{-2}, and the experimental data.[16] Even with a small increase in the confining field, however, the agreement of the calculation according to (33) with the experiments[16] begins to degrade substantially. To improve the agreement of the theory with experiment at large confining fields, the theory of complete control, which had been developed in the theory of semiconductors,[30] was used in Ref. 17 to obtain the result (34). The results of a numerical calculation according to formulas (9) and (34) are presented in Fig. 2. Also shown there are the experimental data[16] for $n_e=3.2\times 10^8$ cm^{-2}. The agreement of theory and experiment in the two limiting cases supports the view that in the first case ($n_e=0.53\times 10^8$ cm^{-2}) the one-electron regime is realized in the ex-
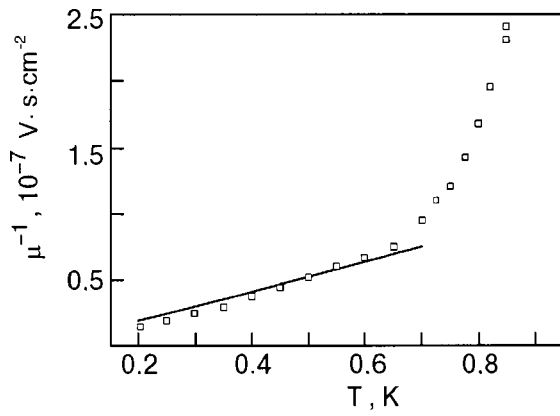
FIG. 1. Inverse electron mobility as a function of the helium temperature at $n_e = 0.53 \times 10^8$ cm^{-2}. Solid line—calculation according to formula (33), □—the experimental data of Ref. 16. At high temperatures ($T > 0.7$ K) the interaction with the gas phase of helium must be taken into account.

FIG. 3. Inverse electron mobility versus the electron concentration for $T = 0.5$ K. Solid curve—calculation according to formula (34), the dashed curve—according to formula (33), □—experimental data from Ref. 16.

periments, whereas for $n_e = 3.2 \times 10^8$ cm^{-2} the electron system has passed into the complete control regime. It remains unclear, however, how such a relatively small increase in the electron concentration could lead to such a large change in the characteristic electron–electron interaction time, which goes from $\tau_{ee} \gg \tau_{er}$ to $\tau_{ee} \ll \tau_{er}$.

Figure 3 shows how the calculated dependence of the mobility on the electron density compares with the experimental data[16] in the two limiting regimes. We see that the theory of complete control satisfactorily describes the experimental data in the entire range of electron concentrations used, whereas the one-electron regime gives agreement only at the lowest concentrations. The reason for the agreement of the theoretical results (33) and (34) at low confining fields is that the electron–ripplon scattering frequency in this limit is very weakly dependent on the electron momentum, so that the result for the mobility is practically independent of whether it is the frequency or time of the electron–ripplon interaction that is averaged. Here, as we see from the general formula (31), for $\tau_{er}^{(cc)} \approx \tau_{er}^{(1e)}$ the electron–electron interaction time does not contribute to the result for the mobility.
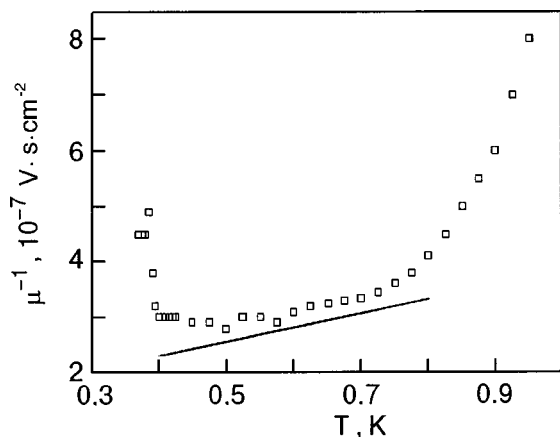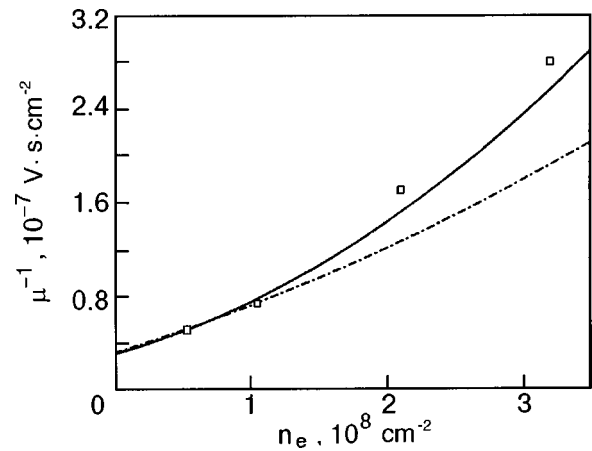

FIG. 2. Inverse electron mobility as a function of the helium temperature for $n_e = 3.2 \times 10^8$ cm^{-2}. Solid line—calculation according to formula (34), □—experimental data from Ref. 16. At low temperatures ($T < 0.4$ K) the crystallization of the electron system must be taken into account, and for $T > 0.7$, the interaction with the gas phase of helium.

Thus additional experimental studies are needed for unambiguous interpretation of the experimental data for low concentrations and $\tau_{ee} \approx \tau_{er}$ and also for observation of the intermediate regime. In particular, it is of interest to measure the mobility of the electrons upon independent variation of the confining field and the electron concentration ($n_e \neq E_\perp/2\pi e$). The electron–ripplon interaction frequency actually depends only on the confining field,[6] whereas the electron–electron interaction time depends on the concentration n_e. Thus as the confining field is increased at a constant low concentration $n_e \approx 0.53 \times 10^8$ cm^{-2}, the results of the calculation in the framework of the one-electron regime (33) and the complete control regime are no longer the same. Further change in n_e (at a constant high $E_\perp$) would make it possible to observe the intermediate regime and to determine the domain of applicability of the two regimes. We note that the mobility of 2D electrons on the surface of liquid helium upon independent variation of the electron concentration and confining field has already been measured.[11,31–33] However, the results of Refs. 11, 31, and 32 were mainly of a qualitative character: it was demonstrated that the mobility of the electrons is affected by electron–ripplon scattering, and the basic dependence of the mobility on the temperature and confining field was elucidated. No information about the electron–electron interaction can be obtained from the experiments of Refs. 11, 31, and 32 because they were done at very low electron concentrations ($10^5 - 10^6$ cm^{-2}) and at low confining fields, where the difference between $\tau_{er}^{(1e)}$ and $\tau_{er}^{(cc)}$ is small.

In Ref. 33 the properties of a 2D electron system with densities $n_e = 1.3 \times 10^8$ cm^{-2} and $n_e = 2.7 \times 10^8$ cm^{-2} were investigated experimentally over a wide range of confining fields (125–1570 V/cm). In those experiments, however, the driving fields were so high as to preclude obtaining data on the mobility as defined in the standard way.[25,28,29] For this reason in Ref. 33 the concept of a nonlinear mobility that depends on the external driving field was used.

At high values of the confining fields a weak nonlinearity was observed in the experiments of Ref. 33; this allows certain qualitative conclusions to be reached from a comparison with the theory developed here. For example, at n_e

$=1.3\times10^8$ cm^{-2} and $E_\perp=1570$ V/cm the value of the mobility from experiment is $\mu_{exp}\approx0.5\times10^6$ cm^2/(V·s), while calculations according to (33) and (34) give $\mu_{1e}=0.490\times10^6$ cm^2/(V·s) and $\mu_{cc}=0.325\times10^6$ cm^2/(V·s). This gives reason to assume that one-electron regime is actually realized at such concentrations and confining fields. A comparison of the experiment and theory for $n_e=2.7\times10^8$ cm^{-2} shows that the system is already in the intermediate regime. It should be emphasized, however, that these conclusions are only of a qualitative character, since a correct comparison can be done only with experimental data obtained at low driving fields in the absence of nonlinear mobility.

CONCLUSION

Starting from the kinetic Equation (1) for the electron distribution function, we have solved the problem of the mobility of a 2D electron gas localized on the surfaace of liquid helium at low temperatures. The final result (31) for the characteristic time, which determines the mobility, contains both the electron–ripplon interaction time and the electron–electron scattering time. The formula obtained (31) is valid for any relations between the electron–ripplon and electron–electron interaction times and gives the previously known expressions for the limiting cases of the one-electron regime (33) and the complete control regime (34). The results were compared with experimental data.

The use of a model in which the system undergoes a transition from the one-electron to the complete control regime requires an unusually strong dependence[16] of the electron–electron interaction time τ_{ee} on the electron concentration n_e. The analysis in this paper shows that the available experimental data admits the possibility of describing the electron system in the framework of the complete control theory over a wide range of concentrations. The features of the momentum dependence of the electron–ripplon frequency lead to the situation that the results of calculations using the one-electron and complete control theories are practically the same at low confining fields. For this reason it cannot be stated with certainty that the two limiting cases were realized in the experiments of Ref. 16.

We proposed exeeriments that will permit the observation of the transition from the one-electron to the complete control regime. The implementation of these experiments will yield information about how the time dependence of the electron–electron relaxation time depends on the various parameters of the system.

[*]E-mail: adamenko@pem.kharkov.ua

[1] M. W. Cole, Phys. Rev. B **2**, 4239 (1970).
[2] V. B. Shikin, Yu. Z. Kovdrya, and A. S. Rybalko, in *Physics of the Condensed State* [in Russian], Kharkov (1971), No. 15, p. 99.
[3] W. T. Sommer and D. J. Tanner, Phys. Rev. Lett. **27**, 1345 (1971).
[4] T. R. Brown and C. C. Grimes, Phys. Rev. Lett. **29**, 1233 (1972).
[5] V. B. Shikin and Yu. P. Monarkha, J. Low Temp. Phys. **16**, 193 (1974).
[6] V. B. Shikin and Yu. P. Monarkha, *Two-Dimensional Charged Systems in Helium* [in Russian], Nauka, Moscow (1989).
[7] G. D. Gaspari and F. Bridges, J. Low Temp. Phys. **21**, 535 (1975).
[8] Yu. P. Monarkha, Fiz. Nizk. Temp. **3**, 587 (1977) [Sov. J. Low Temp. Phys. **3**, 282 (1977)].
[9] M. Born and J. R. Oppenheimer, Ann. Phys. (Leipzig) **84**, 457 (1927).
[10] J. A. Reissland, *The Physics of Phonons*, Wiley, London (1973).
[11] A. S. Rybalko, Yu. Z. Kovdrya, and B. N. Esel'son, JETP Lett. **22**, 280 (1975).
[12] V. S. Édel'man, JETP Lett. **24**, 468 (1976).
[13] C. C. Grimes and G. Adams, Phys. Rev. Lett. **36**, 145 (1976).
[14] Yu. P. Monarkha, Fiz. Nizk. Temp. **2**, 1231 (1976) [Sov. J. Low Temp. Phys. **2**, 702 (1976)].
[15] P. M. Platzman and G. Beni, Phys. Rev. Lett. **36**, 626 (1976).
[16] R. Mehrotra, C. J. Guo, Y. Z. Ruan, D. B. Mast, and A. J. Dahm, Phys. Rev. B **29**, 5239 (1984).
[17] V. A. Buntar', Yu. Z. Kovdrya, V. N. Grigor'ev, Yu. P. Monarkha, and S. S. Sokolov, Fiz. Nizk. Temp. **13**, 789 (1987) [Sov. J. Low Temp. Phys. **13**, 451 (1987)].
[18] V. A. Buntar' and S. S. Sokolov, Fiz. Nizk. Temp. **16**, 845 (1990) [Sov. J. Low Temp. Phys. **16**, 497 (1990)].
[19] W. F. Saam, Phys. Rev. A **8**, 1918 (1973).
[20] H. Yould and V. K. Wong, Phys. Rev. B **18**, 2124 (1978).
[21] P. Roche, G. Deville, K. O. Keshishev, Phys. Rev. Lett. **75**, 3316 (1995).
[22] P. Roche, M. Roger, and F. I. B. William, Phys. Rev. B **53**, 2225 (1996).
[23] I. N. Adamenko, A. V. Zhukov, K. É. Nemchenko, and T. F. George, Fiz. Nizk. Temp. **23**, 574 (1997) [Low Temp. Phys. **23**, 428 (1997)].
[24] I. N. Adamenko, K. E. Nemchenko, A. V. Zhukov, C.-I. Um, T. F. George, and L. N. Pandey, J. Low Temp. Phys. **111**, 145 (1998).
[25] J. H. Ferziger and H. G. Kaper, *Mathematical Theory of Transport Processes in Gases*, North-Holland, Amsterdam (1972).
[26] A. I. Akhiezer, V. F. Aleksin, and V. D. Khodusov, Fiz. Nizk. Temp. **20**, 1199 (1994) [Low Temp. Phys. **20**, 939 (1994)].
[27] I. N. Adamenko, A. V. Zhukov, and K. É. Nemchenko, Fiz. Nizk. Temp. **22**, 1470 (1996) [Low Temp. Phys. **22**, 1117 (1996)].
[28] C. Cercignani, *Theory and Application of the Boltzmann Equation*, Scottish Academic Press, Edinburg and London (1975).
[29] L. D. Landau and E. M. Lifshitz, *Fluid Mechanics*, Pergamon Press, Oxford (1986); Nauka, Moscow (1988).
[30] F. G. Bass and Yu. G. Gurevich, *Hot Electrons and Strong Electromagnetic Waves in Semiconductor and Gas-Discharge Plasmas* [in Russian], Nauka, Moscow (1975).
[31] B. N. Esel'son, A. S. Rybalko, Yu. Z. Kovdrya, A. A. Golub, and S. S. Sokolov, J. Phys. **39**, C6 (1978).
[32] B. N. Esel'son, A. S. Rybalko, and S. S. Sokolov, Fiz. Nizk. Temp. **6**, 1120 (1980) [Sov. J. Low Temp. Phys. **6**, 544 (1980)].
[33] V. E. Sivokon', V. V. Dotsenko, S. S. Sokolov, Yu. Z. Kovdrya, and V. N. Grigor'ev, Fiz. Nizk. Temp. **22**, 715 (1996) [Low Temp. Phys. **22**, 549 (1996)].

SUPERCONDUCTIVITY, INCLUDING HIGH-TEMPERATURE SUPERCONDUCTIVITY

Critical currents in $YBa_2Cu_3O_{7-x}$ high-temperature superconducting thin films irradiated by 4-MeV electrons

Yu. V. Fedotov,* S. M. Ryabchenko, and A. P. Shakhov

Institute of Physics, National Academy of Sciences of Ukraine, pr. Nauki 46, 3650 Kiev, Ukraine

A decrease in the critical current density J_c of a $YBa_2Cu_3O_{7-x}$ thin film is observed after its irradiation by 4-MeV electrons. It is shown that the temperature dependence of J_c agrees with the idea of a granular structure of the film, with intergranular contacts of the superconductor–metal–insulator–superconductor type. © *2000 American Institute of Physics.* [S1063-777X(00)00207-3]

Research on radiation-stimulated changes in the magnetic and transport properties of high-T_c superconductors (HTSCs) can yield information about the mechanism of high-temperature superconductivity and the possibility of increasing the current-carrying capacity of HTSCs. By now there are a large number of papers on the subject. For example, the influence of neutron irradiation on the critical temperature T_c and critical current density J_c of superconducting single crystals and ceramics was investigated in Refs. 1–3. The change in the parameters of a HTSC upon irradiation by heavy-metal ions and protons was studied in Refs. 4–6. The effect of electron irradiation on the value of T_c and the transport properties of HTSCs was considered in Refs. 7–10. Since the maximum electron energy in these experiments did not exceed 350 keV, the defects that arose were due solely to displacements of the oxygen atoms. In Ref. 10 it was shown that when $YBa_2Cu_3O_{7-x}$ (YBCO) films were irradiated by low-energy ($E < 40$ keV) electrons, the oxygen defects are formed predominantly in the region of the CuO chains.

In this paper we investigate the influence of irradiation by electrons having a substantially higher energy (4 MeV) on the properties of thin (500 Å) films of the HTSC YBCO with $T_c = 89.6$ K. Epitaxial films of YBCO with the c axis perpendicular to the plane of the film were deposited on a $LaAlO_3$ substrate by the joint electron-beam evaporation of Y, BaF_2, and Cu and then annealed. The electron irradiation was carried out on an ÉLU-4 linear accelerator at room temperature. The density of the electron beam was chosen so that the temperature of the sample did not rise above 70–80 °C during the irradiation.

The parameters of HTSC films were measured by the low-frequency magnetic susceptibility method at a frequency of 937 Hz in the temperature range 77–100 K in the magnetic field of the Earth. The amplitude of the alternating magnetic field, which was perpendicular to the film plane, was varied over the range 0.001–5 mT. The detection system included an SR-830 lock-in amplifier connected to the RS-232 interface of a computer, which stored and carried out an additional averaging of the data obtained.

The contactless technique used to measure the critical current density is based on analysis of the dependence of the imaginary part of the complex magnetic susceptibility χ'' of the thin film on the amplitude h of the alternating magnetic field. According to Ref. 11, for a thin film oriented perpendicular to the alternating magnetic field, χ'' is given by

$$\chi'' = \frac{4}{\pi}\left[S(x) - \int_0^\pi \sin\alpha \, \sin^2\frac{\alpha}{2} S\left(x\sin^2\frac{\alpha}{2}\right) d\alpha \right], \quad (1)$$

where

$$S(x) = \frac{1}{2x}\left[\arccos\left(\frac{1}{\cosh x}\right) + \frac{\sinh x}{\cosh^2 x} \right]. \quad (2)$$

The quantity x is related to the amplitude h of the alternating magnetic field and the critical current density J_c by the relation

$$x = 2h/dJ_c$$

(d is the film thickness), which leads to interdependence of the critical current density and the components of the complex magnetic susceptibility of the HTSC film. As the amplitude of the alternating field is varied, expression (1) reaches a maximum at $h = h_m$. Here for a disk-shaped film the relation between J_c and h_m is determined by the relation $J_c = 1.013 h_m/d$. It was shown in Ref. 12 that this expression is also valid for films of other isometric shapes, including squares, as in our case.

Studies which we did on HTSC films irradiated by a 4-MeV electron beam to a dose of 3×10^{16} electrons/cm^2 showed that this irradiation dose does not affect the superconducting transition temperature of the sample (Fig. 1). At the same time, as a result of the irradiation the critical current density decreased substantially over the entire temperature interval investigated (Fig. 2).

Let us compare the temperature dependence found for the critical current density with the results obtained in the model of collective pinning of noninteracting vortices. In that model the character of the $J_c(T)$ curve is essentially related to the type of disorder responsible for the pinning and is determined by the temperature dependence of the corre-
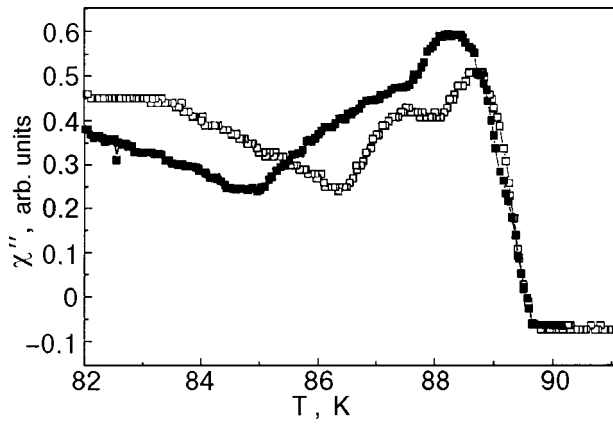
FIG. 1. Temperature dependence of the imaginary component of the complex susceptibility of a YBCO film before (□) and after (■) its irradiation by 4-MeV electrons (irradiation dose 3×10^{16} electrons/cm^2). The magnetic field amplitude $h = 0.003$ mT.

sponding parameter δ that characterizes the disorder. For pinning due to spatial variations of T_c (δT_c pinning), the temperature dependence of the corresponding disorder parameter δ_T has the form $\delta_T \sim (1 - T/T_c)^{-1/2}$, whereas the temperature dependence of the parameter δ_l characterizing the variation of the mean free paths (δl pinning) is given by $\delta_l \sim (1 - T/T_c)^{3/2}$ (Ref. 13). For both types of disorder the critical current density is given in the model of collective pinning of isolated vortices by the expression[13]

$$J_c = J_0 (\delta/\varepsilon)^{2/3}, \tag{3}$$

where $J_0 = c\Phi_0/(12\sqrt{3}\,\pi^2\lambda^2\xi)$ is the depairing current density, Φ_0 is the flux quantum, λ is the London depth, ξ is the coherence length, and ε^2 is the ratio of the longitudinal to transverse effective mass. It follows from Eq. (3) that the temperature dependence of the critical current density is determined by the temperature dependences of the depairing current J_0 and of the disorder parameter δ. At temperatures sufficiently close to T_c, as in our case, the temperature dependence of the depairing current J_0 can be obtained by using estimates for ξ and λ given by the BSC theory for $T \to T_c$, specifically $\xi \propto \lambda \propto (1 - T/T_c)^{-1/2}$, which gives
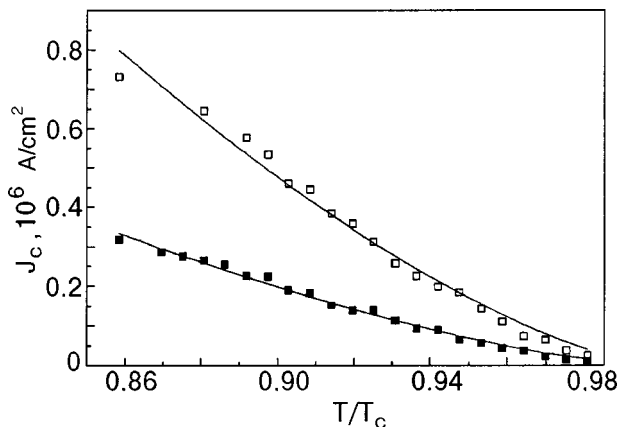

FIG. 2. Temperature dependence of the critical current density of a YBCO film before (□) and after (■) its irradiation by 4-MeV electrons (irradiation dose 3×10^{16} electrons/cm^2). The points are the values of J_c obtained by processing the experimental results; the solid curves are the approximations by a dependence of the form $J_c(T) = J_n(1 - T/T_c)^s$. The values of the parameters J_n and s are given in the text.

$J_0 \propto (1 - T/T_c)^{3/2}$. After substituting into (3) the expressions for the temperature dependence of J_0, δ_T, and δ_l, one can use the model of collective pinning of isolated vortices to obtain the temperature dependence of the critical current density for the different pinning mechanisms. For δ_T pinning this gives $J_c(T) \propto (1 - T/T_c)^{7/6}$, and for δ_l pinning $J_c(T) \propto (1 - T/T_c)^{5/2}$.

For comparison with the conclusions of the collective pinning theory, the experimental data (Fig. 1) were approximated by the expression $J_c(T) = J_n(1 - T/T_c)^s$, where J_n and s are adjustable parameters chosen to minimize the standard deviation. For the initial film this procedure gave $J_n = (1.44 \pm 0.19) \times 10^7$ A/cm^2, $s = 1.48 \pm 0.06$. For the irradiated film $J_n = (6.35 \pm 0.62) \times 10^6$ A/cm^2, $s = 1.51 \pm 0.04$. Thus the values of the exponent s that approximate the results of our experiments do not agree with any of the above versions of the model of collective pinning of isolated vortices.

An alternative description of the measured temperature dependence of the critical current density, in our view, can be obtained by taking into account the possible granular structure of the films used. That this is a real possibility is indicated by the comparatively small value of the critical current density of the films and the rather wide superconducting transition region, with a temperature dependence of $\chi''(T)$ that contains several components, as can be seen from Fig. 1. In such an analysis the temperature dependence of $J_c(T)$ should be governed by the temperature dependence of the critical current J_m of the intergranular contacts.

The temperature dependence of $J_m(T)$ has been considered in a number of papers for different models of the intergranular contacts. For example, the temperature dependence of the maximum current through contacts of the superconductor–normal metal–superconductor (SNS) and superconductor–insulator–superconductor (SIS) type was investigated in Refs. 14–16. For SNS and SIS contacts the temperature dependence was found to be $J_m \propto (T_c - T)^2$ and $J_m \propto (T_c - T)$, respectively, and for a contact of the SNIS type[16] $J_m \propto (T_c - T)^{3/2}$, which agrees with the temperature dependence $J_c \propto (T_c - T)^{3/2}$ obtained by us. However, this agreement does not mean that the intergranular contacts in our films can be unambiguously classified as being of the SNIS type, since an alternative explanation is the possible existence of parallel channels of the SNS and SIS type owing to nonuniformity of the film.

It should be noted that the values of the exponents s for the unirradiated and irradiated films are extremely close (their differences lie within the error limits). Thus in the framework of our analysis the differences between the critical currents of the irradiated and unirradiated samples must be due to a difference in the values of J_m. As we see from a comparison of the values of J_c for the irradiated and unirradiated films, and also in Fig. 2, in our case irradiation by fast electrons leads to a decrease in the critical current density. Such behavior may be a consequence of the rather high (exceeding the optimum with respect to J_c) concentration of pinning centers in the initial film. The high defect density in our films is also indicated by the substantial broadening and multicomponent form of the temperature dependence of χ'' (see Fig. 1).

A decrease in the critical current density in irradiated YBCO films with a high initial concentration of oxygen defects was observed in Ref. 6, whereas a similar irradiation of YBCO single crystals with a lower defect density had been found[17] to increase J_c.

The results suggest that the critical current density in our YBCO HTSC films (its temperature dependence, in particular) is largely determined by the granular structure of the films and the type of intergranular coupling. Since it has been established that irradiation by fast electrons does not affect the exponent of the temperature dependence of the critical current and, hence, must not affect the type of intergranular couplings, it can be assumed that the substantial decrease of the critical current density of our films as a result of electron irradiation is due to a high initial defect concentration, which exceeds the optimum value with respect to J_c.

*E-mail: fedotov@iop.kiev.ua

[1] K. E. Sikafus, J. O. Willis, P. J. Kung, W. B. Wilson, D. M. Parkin, M. P. Maley, F. W. Clinard, Jr., C. J. Salgado, R. P. Dye, and K. M. Hubbard, Phys. Rev. B **46**, 11862 (1992).

[2] R. Szymczak, A. E. Karkin, M. Baran, and H. Szymczak, Phys. Rev. B **50**, 9463 (1994).

[3] V. Sandu, S. Popa, J. Jaklovszky, and E. Cimpoiasu, J. Supercond. **11**, 245 (1998).

[4] T. K. Worthington, M. P. Fisher, and D. A. Huse, Phys. Rev. B **46**, 11854 (1992).

[5] L. Civale, L. Krusin-Elbaum, J. R. Thompson, R. Wheeler, A. D. Marwick, M. A. Kirk, Y. R. Sun, F. Holtzberg, and C. Feild, Phys. Rev. B **50**, 4102 (1994).

[6] M. E. Reeves, B. D. Weaver, and D. A. Krieger, Phys. Rev. B **45**, 2585 (1992).

[7] S. K. Tolpygo, J.-Y. Lin, M. Gurvich, S. Y. Hou, and J. M. Phillips, Phys. Rev. B **53**, 12454 (1996).

[8] S. K. Tolpygo, J.-Y. Lin, and M. Gurvich, Phys. Rev. B **53**, 12462 (1996).

[9] S. K. Tolpygo, J.-Y. Lin, M. Gurvich, S. Y. Hou, and J. M. Phillips, Physica C **269**, 207 (1996).

[10] E. M. Jackson, B. D. Weaver, G. P. Summers, P. Shapiro, and E. A. Burke, Phys. Rev. Lett. **74**, 3033 (1995).

[11] J. R. Clem and A. Sanchez, Phys. Rev. B **50**, 9355 (1994).

[12] M. Wurlitzer, M. Lorenz, K. Zimmer, and P. Esquinazi, Phys. Rev. B **55**, 11816 (1995).

[13] G. Blatter, M. V. Feigelman, V. G. Geshkenbein, A. I. Larkin, and V. M. Vinokur, Rev. Mod. Phys. **66**, 1125 (1994).

[14] P. de Gennes, *Superconductivity of Metals and Alloys*, Benjamin, New York (1966).

[15] P. de Gennes, Rev. Mod. Phys. **36**, 225 (1964).

[16] N. L. Rowell and H. J. Smith, Can. J. Phys. **54**, 223 (1976).

[17] R. B. van Dover, Nature (London) **342**, 85 (1989).

Translated by Steve Torstveit

Inelastic effects in Cr−Cr$_2$O$_3$−Pb−Sn$_x$O$_y$−Pb double tunnel structures

Yu. I. Stepurenko, V. E. Shaternik,* and É. M. Rudenko

Institute of Metal Physics, National Academy of Sciences of Ukraine, pr. Vernadskogo 36, 01680 Kiev GSP, Ukraine

Cr−Cr$_2$O$_3$−Pb−Sn$_x$O$_y$−Pb double tunnel junctions in which inelastic tunneling processes occur, are fabricated. The change in the superconducting order parameter in the middle Pb film upon variation of the temperature, film thickness, and resistivity of the Cr$_2$O$_3$ layer is investigated. The results are interpreted in the framework of theoretical models developed by Kirtley, Seidel, Grajcar, and others for inelastic tunneling processes. © *2000 American Institute of Physics.* [S1063-777X(00)00307-8]

INTRODUCTION

A study of the current–voltage characteristics of Cr−Cr$_2$O$_3$−Pb tunnel junctions has established[1] that their behavior is substantially influenced by inelastic tunneling with the participation of elementary excitations in the Cr$_2$O$_3$ barrier. When junctions between a high-T_c superconductor (HTSC) and a normal metal were made, it was discovered that they are quite different from the classical superconductor–insulator–normal metal (SIN) or superconductor–normal metal (SN) junctions. The main differences of the characteristics of HTSC–normal metal junctions are as follows: a) a strong smearing of the ''gap'' features; b) an increase or decrease in the differential conductance of the junctions with increasing bias voltage; c) a change in the value of the differential conductance of the junctions when the polarity of the bias voltage supply is reversed during the measurements. There have been different explanations offered for this behavior. For example, Cucolo *et al.*[2] proposed a model in which the density of states of the superconductor depends linearly on energy. Srikanth *et al.*[3] showed that the tunneling conductivity in the normal state of perovskite oxides also varies linearly with bias voltage. Moreover, nonstationary theories (resonating valence bonds[4] and marginal Fermi liquid[5]) have been proposed in order to explain the interesting experimental features of the behavior of the HTSCs, such as a linear temperature dependence of the resistance and a linear background in the tunneling conductance of HTSC–normal metal junctions.

However, Kirtley *et al.*[6] showed that the linear tunneling background is observed not only in HTSC–normal metal junctions but also in other systems (Al−Al$_2$O$_3$−Pb, Cr−Cr$_2$O$_3$−Pb, La$_{2−x}$Sr$_x$CuO$_4$), in which this background is explained in terms of inelastic tunneling. Here the nature of the inelastic interaction can be different, depending on the situation. Then, using the Blonder−Tinkham−Klapwijk (BTK) approach,[7] Kirtley[8] developed a model of inelastic tunneling for systems with conductivity. It was shown in Ref. 9 that inelastic processes near an HTSC–normal metal interface play a decisive role in the flow of current through the interface. In Ref. 10 the change in the differential conductance of HTSC–normal metal junctions upon the application of bias voltages of different polarities was described

in terms of inelastic processes related to the strong spin interaction that arises in the barrier on account of the displacement of the oxygen atoms in the YBa$_2$Cu$_3$O$_{7−x}$ unit cell under the influence of the applied voltage.

As we have said, a linear tunneling background was also observed in a study[1] of the differential conductance of Cr−Cr$_2$O$_3$−Pb tunnel junctions. That paper[1] discusses the possibility of explaining the existence of the linear background by the circumstance that the processes occurring in the flow of current through the barrier include inelastic processes together with the elastic tunneling. Increasing the applied bias voltage across the junction opens up more and more inelastic channels in parallel with the ordinary (elastic) channels, leading to growth of the differential conductance. It was proposed to represent the inelastic contribution to the conductance of a Cr−Cr$_2$O$_3$−Pb structure at zero temperature as

$$G_e^{\text{inel}}(V,0) = \text{const} \int_0^{|eV|} N_b(E)|g(E)|^2 dE, \tag{1}$$

where $N_b(E)$ is the density of states of the excitations in the barrier, and $g(E)$ is the electron–excitation interaction constant in the barrier. It is assumed that the excitations contributing to $G_e^{\text{inel}}(V,0)$ near $V(0)$ must be antiferromagnons, acoustic phonons of the antiferromagnetic insulator Cr$_2$O$_3$, or hybrid phonon–magnon modes.

A Cr−Cr$_2$O$_3$−Pb tunnel junction and a HTSC–normal metal junction (e.g., YBCO−Au) exhibit analogous behavior. It is well known that the majority of high-temperature superconductors are doped antiferromagnetic insulators.[11] Even if the oxygen doping in the insulator YBa$_2$Cu$_3$O$_6$ destroys the long-range antiferromagnetic order, the antiferromagnetic correlations within the CuO$_2$ planes is preserved all the way to complete saturation of YBa$_2$Cu$_3$O$_7$ with oxygen. Thus the inelastic antiferromagnetic spin–fluctuation scattering should play an important role in the tunneling of quasiparticles out of and into YBa$_2$Cu$_3$O$_{7−x}$ (Ref. 10), and at the same time, as was mentioned in the review,[12] it should influence the pairing in the superconductor.

This raises the question of whether inelastic processes, e.g., in a Cr−Cr$_2$O$_3$−Pb structure, can influence the measured
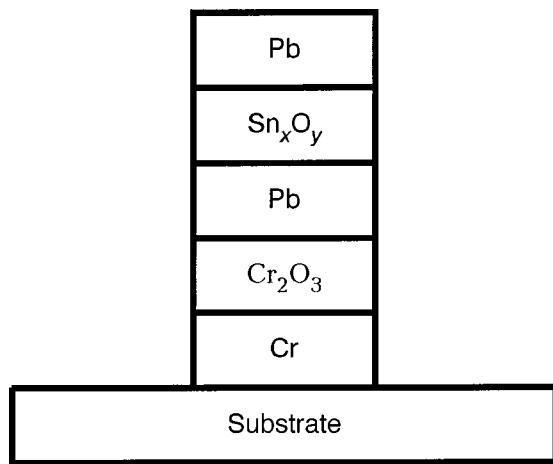
FIG. 1. Schematic illustration of the investigated tunnel junctions.

FIG. 2. Current–voltage characteristic of a Cr–Cr$_2$O$_3$–Pb junction and the voltage dependence of the differential conductance of such a junction.

value of the order parameter of the superconductor (Pb in the given structure) in tunneling experiments. A study of that question is the subject of this paper.

EXPERIMENT

Cr–Cr$_2$O$_3$–Pb–Sn$_x$O$_y$–Pb double tunnel structures were prepared. For comparison, Pb–Sn$_x$O$_y$–Pb ''reference'' junctions were made simultaneously with them in the same technological cycle. The chromium, tin, and lead films were deposited by thermal evaporation of the metals in vacuum on the chosen substrates—insulating slabs of single-crystal or polycrystalline sapphire. The chromium was deposited through a metal mask at a temperature of the substrate and mask of the order of 830 K; the thickness of the chromium film was of the order of 100 nm. Then the surface of the chromium film was oxidized in an atmosphere of air at normal pressure at a film temperature of 473–500 K in order to form a Cr$_2$O$_3$ oxide layer ≈ 5–10 nm thick. Next the first lead film, ≈ 20–30 nm thick, was deposited, followed by a ≈ 5 nm layer of tin, which was then oxidized to form a Sn$_x$O$_y$ tunnel barrier. Finally, an upper lead film 100 nm thick was deposited. The tunnel junctions are shown schematically in Fig. 1.

The current–voltage characteristics and their derivatives were measured for the constituent Cr–Cr$_2$O$_3$–Pb junctions of the double tunnel junctions. The voltage dependence of the differential resistance $(dV/dI)(V)$ was measured by the standard low-frequency technique of harmonic detection. The characteristics $(dI/dV)(I)$ were obtained by numerical transformation of the measured characteristics $(dV/dI)(V)$. A typical current–voltage characteristic of our Cr–Cr$_2$O$_3$–Pb junctions and the dependence of the differential conductance on the bias voltage are shown in Fig. 2.

The objects investigated were Pb–Sn$_x$O$_y$–Pb tunnel junctions situated on a Cr$_2$O$_3$ film and ''reference'' junctions situated directly on the sapphire substrate. Figures 3 and 4 show the current–voltage characteristics of the Cr–Cr$_2$O$_3$–Pb–Sn$_x$O$_y$–Pb junctions (curves B) and of the Pb–Sn$_x$O$_y$–Pb ''reference'' junctions (curves A), measured at several temperatures. The A curves have been slightly drawn out or compressed, as necessary, in order to bring the linear parts of the A and B curves into coincidence in the
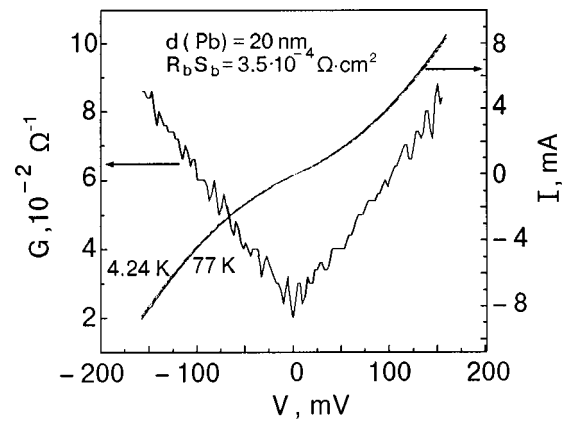
region beyond the gap. It is seen that the current step on the current–voltage characteristic at bias voltages equal to the half sum of the energy gaps of the superconductors is slightly shifted to higher bias voltages on the B curves relative to the A curves. Thus one observes a stimulation of the superconductivity of lead in case B in comparison with case A. The half sum of the energy gaps of the superconductors is determined from the position on the voltage axis of the maximum of the derivative $(dI/dV)(V)$ of the measured current–voltage characteristic.
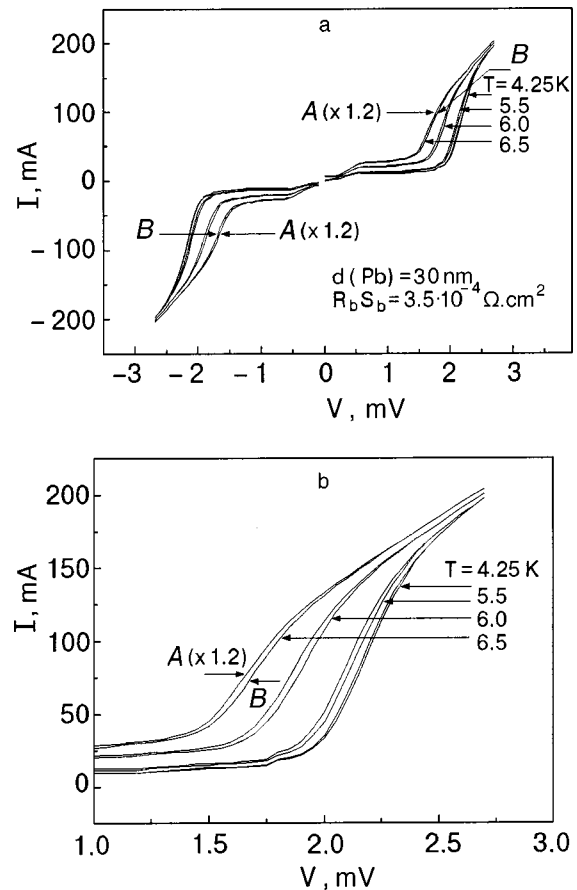
FIG. 3. a: Current–voltage characteristics of tunnel junctions Pb–Sn$_x$O$_y$–Pb (A) and Cr–Cr$_2$O$_3$–Pb–Sn$_x$O$_y$–Pb (B). b: Enlargement of the positive-bias part of the current–voltage characteristics of these junctions.
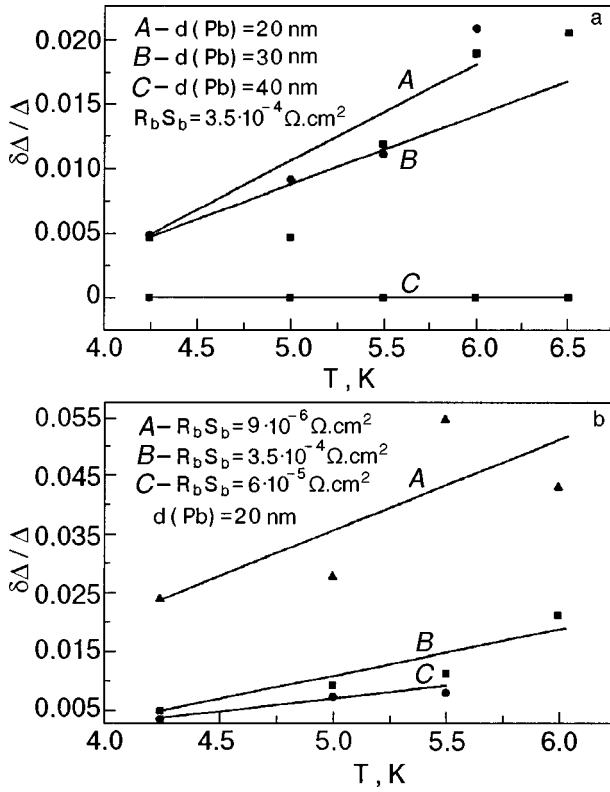
FIG. 4. Temperature dependence of the relative change in the order parameter of Pb for different thicknesses of the middle lead film (a) and of the Cr_2O_3 oxide layer (b).

We also studied the influence of the thickness of the superconductor film on the stimulation of superconductivity in $Cr–Cr_2O_3–Pb–Sn_xO_y–Pb$ tunnel structures. The results of the measurements are shown in Fig. 4a. It is seen that the stimulation vanishes when the middle superconductor film reaches a certain thickness. The effect of changing the thickness of the Cr_2O_3 oxide layer on the stimulation of superconductivity in $Cr–Cr_2O_3–Pb–Sn_xO_y–Pb$ double tunnel junctions was investigated experimentally. The results of the measurements are shown in Fig. 4b. We see that stimulation is observed over a rather wide interval of thicknesses and, hence, of specific resistances R_bS_b of the Cr_2O_3 insulator film.

DISCUSSION

In Ref. 9 a theoretical model for inelastic processes in tunnel junctions was developed on the basis of the Kirtley model and the Blonder–Tinkham–Klapwijk approach. It was shown that the inclusion of inelastic processes in the BTK theory causes the lifetime of the quasiparticles to become finite. To take into account the decrease in the lifetime of the quasiparticles in the presence of inelastic processes an inelastic scattering term is introduced in the Bogoliubov–de Gennes equation,[13] and, following the BTK approach,[7] the Bogoliubov coherence factors

$$\tilde{U}_0^2 = \frac{1}{2}\left[1 + \frac{\sqrt{(E+i\Gamma)^2 - \Delta^2}}{E+i\Gamma} \right] \tag{2}$$

and

$$\tilde{V}_0^2 = \frac{1}{2}\left[1 - \frac{\sqrt{(E+i\Gamma)^2 - \Delta^2}}{E+i\Gamma} \right], \tag{3}$$

are found, where Γ is the broadening parameter.

We see that $\tilde{U}_0$ and $\tilde{V}_0$ become complex in the whole energy range, unlike the functions U_0 and V_0, which are real for $E > \Delta$. The density of states is then expressed as follows:

$$\tilde{N}_{NS}(E,\Gamma) = Re(\tilde{U}_0^2 - \tilde{V}_0^2)^{-1} = Re\left[\frac{E+i\Gamma}{\sqrt{(E+i\Gamma)^2 - \Delta^2}} \right]. \tag{4}$$

This formula is similar to the expression given by Dynes.[14] We substitute the coefficients $\tilde{U}_0$ and $\tilde{V}_0$ into the expressions for the probability of both Andreev reflection, $A(E)$, and ordinary reflection, $B(E)$ (Ref. 7); see Table I.

The elastic current can be expressed as

$$I_d = C\int_{-\infty}^{+\infty} [f(E-eV-f(E)][1+A(E)-B(E)]dE, \tag{5}$$

where $f(E)$ is the Fermi distribution function and C is a constant that depends on the area of the junction. In Ref. 9 the theoretical dependence of the differential conductance of a junction with inelastic processes, $G_{NS}/G_{NN} \sim dI_{el}/dV$, was determined for different values of the barrier height Z and broadening parameter Γ. It is shown that the shortening of the lifetime leads to smearing of the gap feature on the $G_{NS}(V)/G_{NN}(V)$ curves. However, this still does not explain the fact that the differential conductance of a junction with inelastic processes can increase or decrease with increasing bias voltage, as is shown, e.g., in Fig. 2. Therefore, it was noted in Ref. 9 that an inelastic component of the current must be added to the elastic component described above. The theory of inelastic transport in metal–superconductor junctions with arbitrary transparency was developed by Kirtley.[8] As a first perturbation-theory approximation (neglecting the influence of inelastic processes on the quasiparticle distribution function) he proposed the following relation for the inelastic component of the current:

$$I_{inel}(V,\hbar\omega) = I_A(V,\hbar\omega) + I_B(V,\hbar\omega)$$
$$+ I_C(V,\hbar\omega) + I_D(V,\hbar\omega), \tag{6}$$

where I_A, I_B, I_C, and I_D are the inelastic currents of Andreev scattering, ordinary reflection, direct transmission, and branch crossing, respectively.[8] These current components depend on the values of $U_0(E)$ and $V_0(E)$, on the barrier height Z, and on $A(E)$ and $B(E)$, which are functions of $U_0(E)$, $V_0(E)$, and Z (see Table I), and on the value of the energy loss in inelastic process, $\hbar\omega$. For a wide inelastic energy loss distribution (IELD) the total inelastic conductance can be written in the form

TABLE I. Probabilities of Andreev and ordinary reflection.

$\gamma = U_0^2(U_0^2 - V_0^2)Z^2$	
$A(E)$	$B(E)$
$A(E) = aa*$	$B(E) = bb*$
$a = U_0V_0/\gamma$	$b = -(U_0^2 - V_0^2)(Z^2 + iZ)/\gamma$

$$G_{\text{intel}} \sim \sum_{j=1}^{N} \frac{\partial I_{\text{inel}}(V, \hbar \omega_j)}{\partial V}. \tag{7}$$

For simplification an equidistant IELD is assumed from zero to the boundary energy $\hbar \omega_c$; then

$$\hbar \omega_j = \frac{j}{N} \hbar \omega_c. \tag{8}$$

Here N is the number of energy levels responsible for the inelastic losses. It has been shown[9] that under the assumption of continuity of the IELD one can describe both a linear decrease and a linear increase in the differential conductance as the bias voltage is increased.

If the density of states for a junction with inelastic processes [see Eq. (4)] is measured with the use of the second tunnel junction, as in the case of $Cr-Cr_2O_3-Pb-Sn_xO_y-Pb$, then the current–voltage characteristic of the junction is described by the well-known formula in the tunneling Hamiltonian approximation:

$$I_V = C_2 \int_{-\infty}^{\infty} \tilde{N}_{\text{NS}}(E, \Gamma) N_S(E+eV)[f(E) - f(E+eV)] dE, \tag{9}$$

where N_S is the density of states of the superconductor in the BCS model,

$$N_S(E+eV) = \text{Re} \left[\frac{|E+eV|}{\sqrt{(E+eV)^2 - \Delta^2}} \right]. \tag{10}$$

It follows from Eq. (4) that the density of states of an NS junction with inelastic processes can be written in the form

$$N_{\text{NS}}(E, \Gamma) = \text{Re} \left[\frac{E + i\Gamma}{\sqrt{E^2 + 2i\Gamma E - \Gamma^2 - \Delta^2}} \right]. \tag{11}$$

Because of this, the order parameter Δ observed in a tunneling experiment comes out too high. This can explain why a stimulation of superconductivity in the superconductor film of a tunnel junction by the inelastic scattering of quasiparticles of the superconductor at the Cr_2O_3 tunneling barrier was observed in the present experiments.

To describe the formation of the linear background (the linear growth of the differential conductance) for $Cr-Cr_2O_3-Pb$ junctions, one can assume the existence of a smeared IELD. If the decrease in the lifetime of the quasiparticles due to inelastic scattering is taken into account, the discrete spectrum is smeared, and the appearance of a linear background can be explained even in the case of a discrete spectrum of excitations in the Cr_2O_3 barrier. In Ref. 9 it was proposed to replace $U_0(E)$, $V_0(E)$, and $N_S(E)$ by expressions (2), (3), and (4), respectively in order to introduce a shortening of the quasiparticle lifetime in this model. The slope of the linear background depends on both the barrier height Z and on the density of inelastic energy loss. By varying the parameter Z, one can describe both an increase and a decrease in the linear differential conductance in tunnel junctions with inelastic processes, such as the Cr_2O_3 in our case.

CONCLUSION

1. We have investigated experimentally the behavior of a tunnel junction with inelastic processes, $Cr-Cr_2O_3-Pb$.

2. The tunnel junction with inelastic processes was used to make $Cr-Cr_2O_3-Pb-Sn_xO_y-Pb$ double tunnel junctions, and their characteristics were investigated.

3. The stimulation of superconductivity in $Cr-Cr_2O_3-Pb-Sn_xO_y-Pb$ double tunnel junctions was investigated as a function of temperature, the thickness of the Pb superconductor layer, and the specific resistance of the Cr_2O_3 tunnel barrier.

[*]E-mail: shat@d24.imp.kiev.ua

[1] G. J. Rochlin and P. K. Hansma, Phys. Rev. B **2**, 1460 (1970).

[2] A. M. Cucolo, C. Noce, and A. Romano, Physica C **185–189**, 1899 (1991).

[3] H. Srikanth, K. Rajeev, G. V. Shivashankar, and A. K. Raychandhuri, Physica C **195**, 87 (1992).

[4] R. W. Anderson and Z. Zou, Phys. Rev. Lett. **60**, 132 (1988).

[5] P. B. Littlewood and C. M. Varma, Phys. Rev. B **45**, 12636 (1992).

[6] J. R. Kirtley, S. Washburn, and D. J. Scalapino, Phys. Rev. B **45**, 336 (1992).

[7] G. E. Blonder, M. Tinkham, and T. M. Klapwijk, Phys. Rev. B **25**, 4515 (1982).

[8] J. R. Kirtley, Phys. Rev. B **47**, 11379 (1993).

[9] M. Grajcar, A. Plecenik, P. Seidel, and A. Pfuch, Phys. Rev. B **51**, 16185 (1995).

[10] A. Plecenik, M. Grajcar, P. Seidel, S. Takacs, A. Matthes, M. Zuzcak, and S. Benacka, Physica C **301**, 234 (1998).

[11] S. Uchida, Jpn. J. Appl. Phys. **32**, 3784 (1993).

[12] V. M. Loktev, Fiz. Nizk. Temp. **22**, 3 (1996) [Low Temp. Phys. **22**, 1 (1996)].

[13] A. Plecenik, M. Grajcar, S. Benacka, P. Seidel, and A. Pfuch, Phys. Rev. B **49**, 10016 (1994).

[14] R. C. Dynes, J. P. Garno, G. B. Hertel, and T. P. Orlando, Phys. Rev. Lett. **53**, 2437 (1984).

Translated by Steve Torstveit

Quantum oscillations in a stack of superconducting cylinders in a magnetic field: crossover from the Aharonov–Bohm to the Little–Parks regime

V. M. Gvozdikov*

Department of Physics, Kharkov State University, 61077, Svobody Sq. 4, Kharkov, Ukraine
(Received February 1, 2000; resubmitted March 15, 2000)
Fiz. Nizk. Temp. **26**, 648–657 (July 2000)

The Aharonov–Bohm (AB) oscillations of the free energy, critical temperature T_c, magnetization M, and magnetic susceptibility χ as functions of the magnetic flux Φ through the hollow in a stack of mesoscopic superconducting cylinders are studied both analytically and numerically. The shape of these oscillations at low temperature T and small level broadening ν is generally nonsinusoidal and has singularities that depend on the superconducting order parameter Δ and stacking sequence. The period of the oscillations is equal to the normal flux quantum Φ_0. The harmonic amplitudes of the AB oscillations decrease exponentially if the diameter $2R$ of the cylinders becomes greater than the coherence length. Further increase of R results in a complete suppression of the AB oscillations and the development of parabolic Little–Parks (LP) oscillations of $T_c(\Phi)$ with half the period, $\Phi_s = \Phi_0/2$. Therefore a crossover from the AB to LP oscillations takes place as the diameter $2R$ is increased. It is shown that the temperature behavior of the magnetic susceptibility below the superconducting transition is $\chi \propto \exp(-T/T^*)$, where $T^* = \hbar v_0/2\pi^2 R$ (v_0 is the Fermi velocity, and $\hbar$ is Planck's constant). Such dependence of $\chi(T)$ has been observed recently in Ag wires coated with thin Nb layers in a weak external field [R. Frassanito *et al.*, Czech. J. Phys. **46**, 2317 (1996)].
© *2000 American Institute of Physics.* [S1063-777X(00)00407-2]

1. INTRODUCTION

Recently considerable attention has been devoted to studies of quantum oscillations in various artificially fabricated nanostructures subject to small external magnetic fields. In particular, different types of superconducting devices have been explored which exhibit oscillations of the critical temperature T_c upon monotonic variation of the external magnetic field H. Such oscillations have been observed in a fractal networks,[1,2] in Josephson junction arrays,[3] and various mesoscopic loops.[4–6] All these experiments show diverse and basically nonsinusoidal oscillation patterns for the transition temperature $T_c(H)$ with the superconducting flux quantum $\Phi_s = \hbar c/2e$ as a fundamental period. It was established that such oscillations could be sufficiently well understood and described within the Ginzburg–Landau (GL) approach. The GL equation, when linearized in the order parameter Ψ, is formally identical to the Schrödinger equation for a doubly charged (in units of the electron charge e) particle in a magnetic field. Thus, the double charge of the Cooper pairs, $2e$, is the physical reason standing behind the fact that quantity Φ_s determines the period of oscillations in the flux Φ for different nonsimply connected systems in the GL regime. The GL approach also proved to be successful in explanation of different known types of flux quantization in superconductors: the Little–Parks oscillations,[7,8] oscillations in superconducting fractal networks,[9–11] and in Josephson junction arrays.[12,13]

The Little–Parks (LP) oscillations of the critical temperature $T_c(H)$ have a parabolic shape and take place for samples whose sizes are of the order of the GL coherence length or greater. Oscillations as a function of flux in the GL regime are insensitive to the quantum phase interference phenomena due to the Aharonov–Bohm (AB) effect,[14] which is normally present in the quasiparticle energy spectrum of nonsimply connected mesoscopic superconductors. The AB effect has numerous applications in different mesoscopic structures: conducting, insulating, magnetic, and strongly correlated, a review of which can be found in Refs. 15 and 16. A general theoretical consideration of the AB effect in superconductors was given in the Ref. 17, where a number of theorems were formulated concerning hollow superconductors in a magnetic field.

The effect of flux quantization on the energy spectrum of excitations in a thin hollow superconducting cylinder and on the critical temperature $T_c(\Phi)$ was studied in Ref. 18. It was shown[18] that $T_c(\Phi)$ is an oscillatory function of the flux through the hollow $\Phi = H\pi R^2$ with a period $\Phi_0 = 2\Phi_s$ (R is the inner radius of the cylinder). The authors proved the periodicity of the critical temperature, $T_c(\Phi) = T_c(\Phi + \Phi_0)$, and estimated the amplitude of oscillations as

$$\frac{T_{c0} - T_c}{T_c} \approx \left(\frac{\lambda_B}{R}\right)^{1/2} \exp(-2\gamma R/\xi_0). \tag{1}$$

The explicit shape of oscillations was not found in Ref. 18. The notation adopted in Eq. (1) is as follows: $\xi_0 = \hbar v_0/\pi\Delta(0)$ is the coherence length, λ_B is the Bohr radius, and $\ln \gamma$ is the Euler constant.

The purpose of present paper is to study (both analytically and numerically) the Aharonov–Bohm oscillations of the critical temperature $T_c(\Phi)$, magnetization $M(\Phi)$, and susceptibility χ in superconductors in more detail and to show their formal relation to the de Haas–van Alphen oscillations in superconductors—a very active area of research at

the moment (see, for example, Refs. 25, 28, 29 and numerous references therein). To do this, we consider in what follows the AB oscillations of the free energy in a stack of weakly connected uniaxial hollow superconducting cylinders, which can be considered, for instance, as a model system for superconducting nanotubes.[30] We will show that the T_c and the magnetic susceptibility χ in the AB regime are oscillating functions of the flux due to the quantities $\cos(2\pi p\Phi/\Phi_0)$. For each integer p the amplitudes of these oscillations depend on the electron level broadening $\nu = \hbar/\tau$, the order parameter Δ, and the so-called stacking factor I_p, which depends on p in the very same fashion as for the de Haas–van Alphen (dHvA) oscillations in layered superconductors.[25] We will show, in particular, that $\chi \propto \exp(-T/T^*)$, where $T^* = \hbar v_0/2\pi^2 R$. This result exactly coincides with the experimental observation of the temperature behavior of the susceptibility in the Ag/Nb wire bundle reported in Ref. 19. The stacking factor I_p is a quantity which depends on the distribution of cylinders heights along the stack as well as the types of electrical contacts between them. It nontrivially modifies the amplitude of the pth oscillation harmonic and can be determined by the relation[25]

$$I_p = \int_{-\infty}^{\infty} g(\varepsilon)\exp(-i2\pi p\varepsilon/\varepsilon_0)d\varepsilon, \tag{2}$$

where $g(\varepsilon)$ is a one-dimensional density of states related to the electron motion along the field (along the stack, in our case) and ε_0 is the typical energy separation between the energy levels in the problem. We will show in what follows that in the AB regime of a stack of mesoscopic cylinders $\varepsilon_0 = \hbar^2 k_0/MR$, where k_0 stands for the Fermi momentum and M is the electron mass. In case of the de Haas–van Alphen oscillations in layered conductors[20,21] and superconductors,[25] one has $\varepsilon_0 = \hbar\Omega$, where Ω is the cyclotron frequency.

2. THE ENERGY SPECTRUM AND THE FREE ENERGY

Consider a stack of uniaxial thin hollow cylinders (or a tube) of inner radius R and thickness $d \ll R$, which is subject to an external magnetic field H along the axis of the stack. The cylinders may be uniform in size, or their heights may vary periodically along the tube or be randomly distributed quantities. We assume also that the tunneling barriers for electron hopping between neighboring cylinders are weak enough that one can neglect the spatial variations of the superconducting order parameter along the stack (see Ref. 31 and the discussion in Sec. 4 in this connection).

Before considering the superconducting properties of the system in question, let us first determine its energy spectrum and the wave functions in the normal state. Taking then the z axis of the cylindrical coordinates (ρ,φ,z) to be parallel to the stack, and separating variables in the Schrödinger equation $\hat{H}\Psi_\varepsilon = \varepsilon\Psi_\varepsilon$, we have

$$\Psi_\varepsilon(\mathbf{r}) = \frac{1}{(2\pi)^{1/2}}e^{in\varphi}f_l(\rho)\Psi_{\zeta m}(z), \tag{3}$$

$$\frac{1}{\rho}\frac{d}{d\rho}\left(\rho\frac{df_l}{d\rho}\right) + \frac{\hbar^2}{2M\rho^2}\left(n - \frac{\Phi(\rho)}{\Phi_0}\right)^2 f_l(\rho) = \varepsilon_{nl}f_l(\rho), \tag{4}$$

$$\hat{H}_z\Psi_{\zeta m}(z) = \zeta_m\Psi_{\zeta m}(z). \tag{5}$$

Here $\rho = R + r$ is the radial coordinate ($0 \leq r \leq d \ll R$), and $\Phi(\rho) = H\pi\rho^2$ is the flux through a circle of radius ρ. The Schrödinger Equation (5) describes the motion of an electron with energy $\zeta_m \equiv \varepsilon - \varepsilon_{nl}$ along the magnetic field (i.e., along the z axis). Taking into account that in a thin cylinder $r/R \ll 1$, we find from Eq. (4) the approximate energy spectrum for electrons in the cylinder:

$$\varepsilon_{nl} = \frac{\hbar^2}{2M}\left[\frac{\pi^2 l^2}{d^2} + \frac{1}{R^2}\left(n - \frac{\Phi}{\Phi_0}\right)^2\right]. \tag{6}$$

The appropriate radial wave function which satisfies the zero boundary conditions at the inner and outer surfaces of the cylinder, $f_l(R) = f_l(R+d) = 0$, is given by

$$f_l(\rho) = \sqrt{2/d}\,\sin\left[\frac{\pi(\rho-R)l}{d}\right]. \tag{7}$$

The quantum numbers in Eqs. (6) and (7) take the following values: $n = 0, \pm 1, \pm 2,..., l = 0,1,2,....$ To calculate the quasiparticle energy of the system under study in the superconducting state, one has to address the Bogoliubov-de Gennes (BdG) equations:

$$(\hat{H} - E_F)u(\mathbf{r}) + \Delta(\mathbf{r})v(\mathbf{r}) = Eu(\mathbf{r}),$$
$$-(\hat{H}^* - E_F)v(\mathbf{r}) + \Delta^*(\mathbf{r})u(\mathbf{r}) = Ev(\mathbf{r}), \tag{8}$$

where E_F is the Fermi energy.

Since the thickness of cylinders is much less than the BCS coherence length ξ, the order parameter Δ does not depend on the coordinate $\mathbf{r}$. Taking this into consideration and expanding the $u - v$ functions in the basis of Eq. (3),

$$u(\mathbf{r}) = \sum_\varepsilon u_\varepsilon\Psi_\varepsilon(\mathbf{r}), \quad v(\mathbf{r}) = \sum_\varepsilon v_\varepsilon\Psi_\varepsilon(\mathbf{r}), \tag{9}$$

we find the quasiparticle energy from the BdG Equations (8):

$$E_{nl} = \sqrt{(\varepsilon_{nl} - E_F)^2 + \Delta^2}. \tag{10}$$

Proceeding then in a standard fashion, we arrive at the spectral density for quasiparticles with a small damping, $\nu = \hbar/\tau$, as a sum of two Lorentzians,[22]

$$\rho_n(\xi_m,\omega) = \frac{1}{\pi}u_n^2\frac{\nu}{\nu^2 + (\omega + E_n(\xi_m))^2}$$
$$+ v_n^2\frac{\nu}{\nu^2 + (\omega + E_n(\xi_m))^2}. \tag{11}$$

The quantities u_n^2 and v_n^2 here stand for the coherence factors:

$$u_n^2(\xi_m) = \frac{1}{2}\left(1 + \frac{\varepsilon_n(\xi_m)}{E_n(\xi_m)}\right), \quad v_n^2(\xi_m) = \frac{1}{2}\left(1 - \frac{\varepsilon_n(\xi_m)}{E_n(\xi_m)}\right). \tag{12}$$

We put for simplicity $l = 1$, so that the quasiparticle energies in the normal and superconducting states become, respectively,

$$\varepsilon_n(\xi_m) = \varepsilon(R)\left(n - \frac{\Phi}{\Phi_0}\right)^2 + \xi_m - \mu, \tag{13}$$

and

$$E_n(\xi_m) = \sqrt{\varepsilon_n(\xi_m)^2 + \Delta^2},\tag{14}$$

where μ and $\varepsilon(R)$ are determined by the relations

$$\mu = E_F - \frac{\hbar^2 \pi^2}{2M d^2}, \quad \varepsilon(R) = \frac{\hbar^2}{2M R^2}.\tag{15}$$

Once the spectral density is found, the free energy of a superconductor can then be calculated with the help of the formula[23]

$$F = \int d\mathbf{r} \frac{|\Delta(\mathbf{r})|^2}{\lambda} - 2T \sum_{n,m}$$
$$\times \int_{-\infty}^{\infty} d\omega \rho_n(\xi_m, \omega) \ln\left[2 \cosh\left(\frac{\omega}{2T}\right)\right],\tag{16}$$

where λ is the BCS coupling constant. Using the integral representation[24] for the logarithm in Eq. (16)

$$\ln\left[\cosh\left(\frac{\omega}{2T}\right)\right] = \int_{-\infty}^{\infty} dz \frac{1 - \cos \omega z}{z \sinh \pi T z}\tag{17}$$

and the Poisson summation rule

$$\sum_{n_0}^{\infty} \chi(n) = \int_{-\infty}^{\infty} \chi(n) dn + 2 \operatorname{Re} \sum_{p=1}^{\infty} \int_a^{\infty} \chi(n) e^{i 2 \pi n p} dn,\tag{18}$$

where $n_0 - 1 < a < n_0$, we find the oscillatory part of the free energy in the form

$$F_{\text{osc}} = \frac{4 \pi T}{\varepsilon_0} \sum_{p=1}^{\infty} Q_p \Psi_p(T, \Delta, \nu) \cos\left(2 \pi p \frac{\Phi}{\Phi_0}\right).\tag{19}$$

It is important to note that nonoscillatory part of the free energy, determined by the first integral term in Eq. (18), does not depend on the flux, because $\varepsilon_n(\xi_m)$ in Eq. (13) depends on n through the combination $n - \Phi/\Phi_0$. Two factors $\Psi_p(T, \Delta, \nu)$ and Q_p have been introduced in Eq. (19):

$$\Psi_p(T, \Delta, \nu) = \int_{-\infty}^{\infty} dz G_p(z) \frac{e^{-\nu|z|}}{z \sinh(\pi T z)},\tag{20}$$

and

$$Q_p = \operatorname{Re}[I_p \exp(i 2 \pi p R k_0)].\tag{21}$$

The function $G_p(z)$ is determined by the integral

$$G_p(z) = \int_{-\infty}^{\infty} dn \cos(z \sqrt{(\varepsilon_0 n)^2 + \Delta^2}) \cos(2 \pi n p).\tag{22}$$

Thus the factor $\Psi_p(T, \Delta, \nu)$, given by Eq. (20), describes the damping of the AB oscillations of the free energy due to the BCS gap Δ and energy level broadening ν. The factor Q_p in Eq. (20) modulates the pth harmonic through the stacking factor I_p, which has already been determined by Eq. (2). It depends on the one-dimensional density of states associated with the electron motion along the stack

$$g(\varepsilon) = \sum_m \delta(\varepsilon - \xi_m).\tag{23}$$

The factor analogous to the I_p was introduced earlier in the theory of de Haas–van Alphen oscillations in layered conductors[20,21] and superconductors.[25]

The integral in Eq. (22) can be calculated exactly to yield[24]

$$G_p(z) = \frac{\pi}{\varepsilon_0}\left[\delta(z - z_p) + \theta(z - z_p) \frac{\partial}{\partial z} J_0(\Delta \sqrt{z^2 - z_p^2})\right],\tag{24}$$

where $\theta(z)$ is the Heaviside step function; $J_0(z)$ stands for the Bessel function; and $z_p = 2 \pi p / \varepsilon_0$. Now substituting Eq. (24) into Eq. (20), we have

$$\Psi_p(T, \Delta, \nu) = \Psi(z_p, \nu) + \int_{z_p}^{\infty} dz \Psi(z, \nu) \frac{\partial}{\partial z} J_0(\Delta \sqrt{z^2 - z_p^2}),\tag{25}$$

where

$$\Psi(z, \nu) = \frac{e^{-\nu|z|}}{z \sinh(\pi T z)}.\tag{26}$$

The second term in (25) vanishes when $\Delta = 0$, so that $\Psi(z_p, \nu)$ is the factor which determines the amplitudes of the AB oscillations in the stack in the normal state. The dependence of F_{osc} on the oscillating factors $\cos(2 \pi p \Phi/\Phi_0)$ is a manifestation of the AB effect[16,27] in mesoscopic systems. Amplitudes Q_p and Ψ_p formally are much the same as those appearing in the de Haas–van Alphen effect in layered superconductors in the vortex state below the upper critical magnetic field.[25] The latter is because in both cases oscillation effects arise due to the quantization of the energy spectrum in superconductors. The principal difference in the field dependence of $F_{\text{osc}}(H)$ in the de Haas–van Alphen and Aharonov–Bohm cases appears because of the different nature of the quantization. In case of the de Haas–van Alphen effect the strong external magnetic field itself is a quantizing factor, which yields a discrete Landau spectrum responsible for the periodicity of the free energy $F_{\text{osc}}(H)$ in the inverse magnetic field $1/H$. In case of the AB problem under study, the energy levels $\varepsilon_n(\xi_m)$ of Eq. (13) appear due to the size quantization in the mesoscopic sample, and the flux $\Phi \propto H$ enters the discrete spectrum $\varepsilon_n(\xi_m)$ as a parameter thereby making the free energy $F_{\text{osc}}(\Phi)$ in Eq. (24) a periodic function of the field itself. Physically, the dependence on Φ in the AB systems should vanish together with the size quantization in the bulk limit. In the next Sections we will see in detail how the AB oscillations manifest themselves in the mesoscopic tube under consideration, both in the normal and superconducting states.

3. THE CRITICAL TEMPERATURE OSCILLATIONS AND DIMENSIONAL CROSSOVER

Near the critical temperature one can expand the free energy in powers of Δ^2. Using Eqs. (16), (18), and (19), we have

$$F_S - F_N \approx \Delta^2\left[\alpha(T) - \frac{2}{\varepsilon_0} \sum_{p=1}^{\infty} Q_p N_p(T, \nu) \cos\left(2 \pi p \frac{\Phi}{\Phi_0}\right)\right] + \ldots,\tag{27}$$

where $\alpha(T)$ is the first coefficient of the standard Ginzburg–Landau expansion. In the case of a superconductor of small dimensions it can be found directly from the free energy determined by Eq. (16) (see Ref. 26 for details):

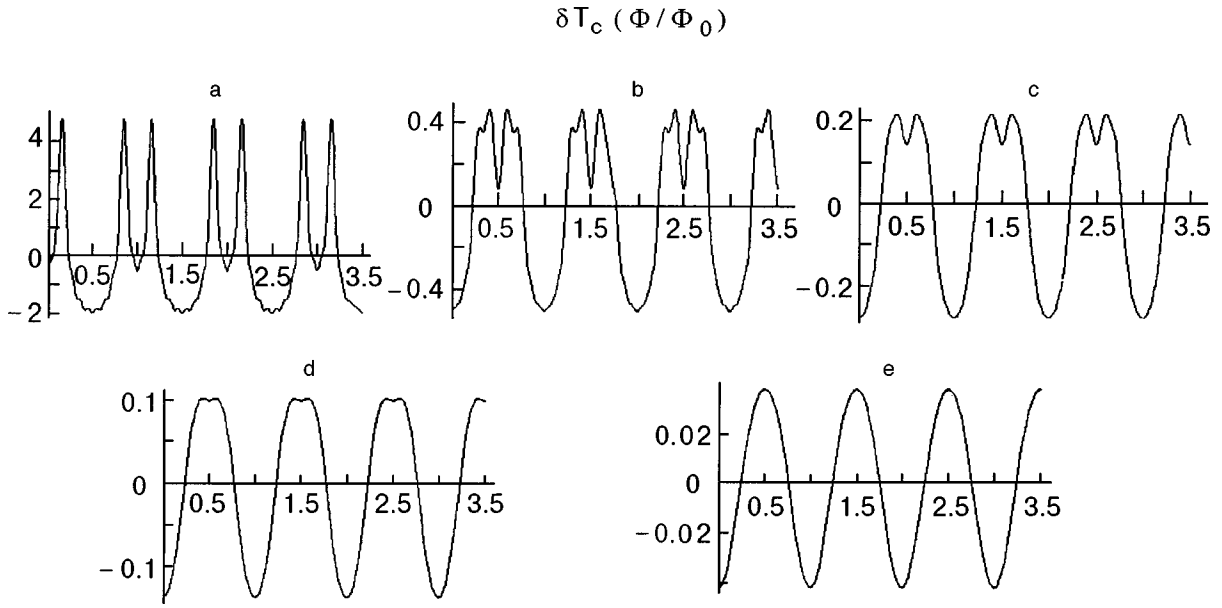$$\delta T_c \,(\Phi/\Phi_0)$$

FIG. 1. The Aharonov–Bohm oscillations of the critical temperature of a stack of hollow superconducting cylinders $\delta T_c(\Phi/\Phi_0) \equiv (T_c(\Phi) - T_c^*(R))/T_c^0(R)$ [see Eq. (30)] in units of the quantity $N(0)\varepsilon_0$ (Φ is the flux through a hollow, and Φ_0 denotes the flux quantum). The numerical calculations of $\delta T_c(\Phi)$ in Figs. 1a–1e are done for different values of the parameters $a = 2\pi^2 T_c^0(R)/\varepsilon_0$, $b = \nu/\pi T_c^0(R)$, $c = 4\pi\sigma/\varepsilon_0$, and $Rk_0 = 1000$: $a = 0.1$, $b = 1$, $c = 0.1$ (Fig. 1a); $a = 0.1$, $b = 1$, $c = 10$ (Fig. 1b); $a = 0.25$, $b = 1$, $c = 10$ (Fig. 1c); $a = 0.5$, $b = 1$, $c = 10$ (Fig. 1d); $a = 1$, $b = 1$, $c = 10$ (Fig. 1e).

$$\alpha(T) = N(0)\left[\ln\left(\frac{T}{T_c^0}\right) + \Psi\left(\frac{1}{2} + \frac{\nu}{2\pi T}\right) - \Psi\left(\frac{1}{2}\right)\right]. \qquad (28)$$

Here $T_c^0 = T_c^0(R)$ is the critical temperature of a small cylinder of radius R; Ψ stands for the digamma function; $N(0)$ is the density of states. The factor $N_p(T,\nu)$ entering the free energy expansion in Eq. (27) is determined by the integral

$$N_p(T,\nu) = \int_{a_p}^{\infty} dz \, \frac{\exp(-bz)}{\sinh z}, \qquad (29)$$

where $b = \nu/\pi T$ and $a_p = 2\pi R p/\xi(T)$. The coherence length depends on the Fermi velocity v_0 and the temperature according to the relation $\xi(T) = \hbar v_0/\pi T$.

The critical temperature of the stack can be determined from the Ginzburg–Landau expansion by equating to zero the term in the square brackets in Eq. (28). Taking into account a smallness of the oscillatory correction to the critical temperature $T_c^*(R)$ of a cylinder due to the Aharonov–Bohm effect, we have

$$T_c(\Phi) = T_c^*(R) - \frac{2T_c^0(R)}{N(0)\varepsilon_0}$$
$$\times \sum_{p=1}^{\infty} Q_p N_p[T_c^0(R), \nu]\cos\left(2\pi p \frac{\Phi}{\Phi_0}\right). \qquad (30)$$

Here $T_c^*(R) = T_c^0(R) - \pi\nu/8$ is the transition temperature of the cylinder, taking into account a small depression due to the size-quantization level broadening. Thus the critical temperature $T_c(\Phi)$ oscillates in the direct field with a period equal to the normal flux quantum Φ_0. The amplitudes of harmonics in Eq. (30) depend on two factors, Q_p and N_p, of which Q_p is proportional to the stacking factor I_p. This factor depends on the way which cylinders are stacked into a tube and on the type of electrical contact between them. Consider, as a specific example, a model in which identical cyl-

inders are stacked periodically into a tube and the tunnel junctions between them are described by a hopping integral σ. Such a model has recently found support in experiments on carbon nanotubes.[31] The corresponding density of states associated with the electron transport along the tube in this model is given by the relation $g(\varepsilon) = 1/\pi(4\sigma^2 - \varepsilon^2)^{1/2}$. Integration of Eq. (2) with this $g(\varepsilon)$ yields $I_p = J_0(4\pi\sigma p/\varepsilon_0)$, so that the factor Q_p becomes

$$Q_p = 2J_0\left(\frac{4\pi\sigma p}{\varepsilon_0}\right)\cos(2\pi p R k_0) \qquad (31)$$

($J_0(x)$ is the Bessel function). The case of a single cylinder corresponds to the prohibition of electron tunneling between the adjacent cylinders, i.e., $\sigma = 0$. The density of states in this limit is given by $g(\varepsilon) = \delta(\varepsilon)$, which implies that I_p equals unity and $Q_p = 2\cos(2\pi p R k_0)$. Having at hand Eqs. (29) and (31), one can calculate the sum in Eq. (30), which determines the shape of the oscillations of the critical temperature $\delta T_c(\Phi) \equiv (T_c(\Phi) - T_c^*(R))/T_c^0(R)$ in units of the quantity $N(0)\varepsilon_0$. The results of the numerical calculations of $\delta T_c(\Phi)$ for different values of the parameters $a = 2\pi^2 T_c^0(R)/\varepsilon_0$ and $b = \nu/\pi T_c^0(R)$ are shown in Fig. 1. We see that in general the shape of the Aharonov–Bohm oscillations of the transition temperature in the superconducting tube is not of the simple cosine form $\cos(2\pi\Phi/\Phi_0)$ because of the contributions from the higher harmonics ($p = 2,3,...$). It takes the harmonic sinelike form only for sufficiently large a and b as one can see in Fig. 1e. These quantities depend on $T_c^0(R)$ and the energy level broadening ν, which therefore act as factors damping the amplitudes and smearing the fine structure of these oscillations. The value of the hopping integral also strongly affects the shape and amplitudes of the oscillations, as one can tell by comparing Fig. 1a and Fig. 1b. The enhancement of σ changes the oscillation pattern and strongly depresses the amplitudes.

The temperature and broadening ν influence the amplitude of the pth harmonic through the factor $N_p(T,\nu)$, which decreases rapidly as the parameters b and a_p increase. In the case when $2\pi R \gg \xi(T)$, this factor becomes an exponential function

$$N_p(T,\nu) \approx \frac{2}{1+b}\exp\left[-\left(\frac{T}{T^*}\right)p\right]\exp\left(-\frac{\nu}{\pi T^*}\right) \qquad (32)$$

depending on some characteristic temperature $T^* = \hbar v_0/2\pi^2 R$, which is a decreasing function of the radius R. It follows then from Eqs. (30) and (32) that the quantum AB oscillations of the critical temperature decrease exponentially with R if $2\pi R \gg \xi(T_c^0)$. On the other hand, when R exceeds the Ginzburg–Landau coherence length $\xi_{GL}(T_c^0)$ (i.e., in the GL regime), the gradient term in the free energy expansion should be added to the right-hand side of Eq. (27).

$$\frac{1}{2m}\left|\left(\frac{\hbar}{i}\nabla - \frac{2eA}{c}\right)\Psi\right|^2. \qquad (33)$$

The Ginzburg–Landau order parameter Ψ in Eq. (33) is proportional to Δ [32]: $\Psi = \gamma^{1/2}\Delta$, where $\gamma^2 = 7\zeta(3)mv_0^2 N(0)/2\pi^2 T_c^0$ for clean superconductors and $\gamma^2 = \pi m v_0 N(0)l/12\hbar T_c^0$ for dirty superconductors. Here v_0 is the Fermi velocity, $\zeta(3)$ is the zeta function, and $l = \hbar v_0/\nu$. The fluxoid quantization in a thin superconducting cylinder makes the super-current velocity $v_s = (\hbar/mR)\min|(n - \Phi/\Phi_s)^2|$ an oscillatory function of the ratio Φ/Φ_s, which is a manifestation of the Little–Parks effect[7,8] (n is an integer). Thus the free energy expansion of Eq. (27) in the GL regime takes the form

$$F_S - F_N \approx \Psi^2\left[\gamma\left\{\alpha(T) - \frac{2}{\varepsilon_0}\sum_{p=1}^{\infty}Q_p N_p(T,\nu)\right.\right.$$
$$\left.\left.\times\cos\left(2\pi p\frac{\Phi}{\Phi_0}\right)\right\} + \frac{mv_s^2}{2}\right] + \dots. \qquad (34)$$

We see that two physically different regimes should be distinguished. In the mesoscopic regime, $2\pi R \leq \xi(T)$, the free energy given by Eq. (27) oscillates with period Φ_0 on account of the AB effect. In the Ginzburg–Landau regime, $2\pi R \gg \xi(T_c^0)$, the harmonic oscillations given by the sum over p in Eq. (34) vanish, and the period of oscillations becomes equal to the superconducting flux quantum $\Phi_s = \Phi_0/2$. In this case the oscillations are completely determined by the supercurrent term $mv_s^2/2$, as in the case of the conventional Little–Parks effect. The critical temperature oscillates in this regime according to the standard Little–Parks equation

$$T_c^0(\Phi) = T_c^*(R) + 0.73\frac{\xi_0 l}{R^2}T_0(R)\min\left[\left(n - \frac{\Phi}{\Phi_s}\right)^2\right]. \qquad (35)$$

Thus an increase of R results in a crossover from harmonic oscillations of the critical temperature $T_c(\Phi)$ with period Φ_0 in the Aharonov–Bohm regime [see Eq. (30)] to the parabolic Little–Parks oscillations with period Φ_s in the Ginzburg–Landau regime described by Eq. (35).

4. MAGNETIZATION, PERSISTENT CURRENT, AND SUSCEPTIBILITY OSCILLATIONS

Having at hand equations for the free energy, one can calculate the magnetization M and the susceptibility χ by taking derivatives:

$$M = -\frac{\partial F}{\partial H}, \quad \chi = \frac{\partial M}{\partial H}. \qquad (36)$$

Consider first the magnetization. In the AB regime H enters the free energy, as one can see from Eqs. (24) and (28), through the strongly oscillatory function $\cos(2\pi p\Phi/\Phi_0)$, so that taking the derivative in Eq. (36) is trivial and yields

$$M_{osc} = -\frac{4\pi T}{\varepsilon_0}\left(\frac{2\pi S}{\Phi_0}\right)$$
$$\times \sum_{p=1}^{\infty}Q_p\Psi_p(T,\Delta,\nu)p\sin\left(2\pi p\frac{\Phi}{\Phi_0}\right). \qquad (37)$$

It is instructive to begin the analysis of the shape of the function $M_{osc}(\Phi)$ with consideration of the limiting case $\Delta = \sigma = v = T = 0$, since the sum in Eq. (37) in this case can be calculated analytically. Setting to zero these parameters in Eq. (37), we have

$$M_{osc}(\Phi) = M_{osc}^+ + M_{osc}^-, \qquad (38)$$

where

$$M_{osc}^{\pm} = \frac{2S\varepsilon_0}{\pi\Phi_0}\sum_{p=1}^{\infty}\frac{(-1)^p}{p}\sin\left[2\pi p\left(\frac{\Phi}{\Phi_0}\pm Rk_0 + \frac{1}{2}\right)\right]. \qquad (39)$$

The sum in Eq. (39) is exactly a saw-tooth function of its argument in the parenthesis. Therefore the magnetization $M_{osc}(\Phi)$ of a single cylinder ($\sigma = 0$) at zero temperature and level broadening ν is a sum of two saw-tooth profiles, as is shown in Fig. 2a. The persistent current and the corresponding magnetization function $M_{osc}(\Phi)$ of a thin normal ring (first obtained by Kulik[27]) were studied in Ref. 33 and later discussed in detail in a review article.[34] Nonetheless, as one can see from Eq. (37), the magnetization of the tube is strongly affected by the additional factor $Q_p(\sigma)$. The role of the stacking factor $Q_p(\sigma)$ in the shape of $M_{osc}(\Phi)$ is nontrivial and is illustrated by the relative transfigurations of the oscillation patterns shown in Figs. 2a and 2b. Increasing the temperature and level broadening damp the amplitudes of the harmonics, making the form of $M_{osc}(\Phi)$ close to sinelike, as one can see in Fig. 2c. The shape of the magnetization oscillations in the superconducting tube calculated on the basis of Eq. (37) for different values of the parameters Δ, σ, ν, and T is shown in Fig. 3. The magnetization of the stack of cylinders is inherently related to the so-called persistent current $I = cM/S(S = \pi R^2)$. This current flows around the hollow and thereby creates the magnetization. Therefore oscillations of the magnetization as a function of flux also imply oscillations of the persistent current, with the amplitude $I_{osc}(\Phi) = cM_{osc}(\Phi)/S$. The oscillations of the susceptibility can be calculated by taking the derivative $\chi_{osc}(\Phi) = \partial M_{osc}(\Phi)/\partial H$. In the normal state, under the conditions $\Delta = \sigma = v = T = 0$, the magnetization function $M_{osc}(\Phi)$ is given by the saw-tooth function of Eq. (38) and is shown in
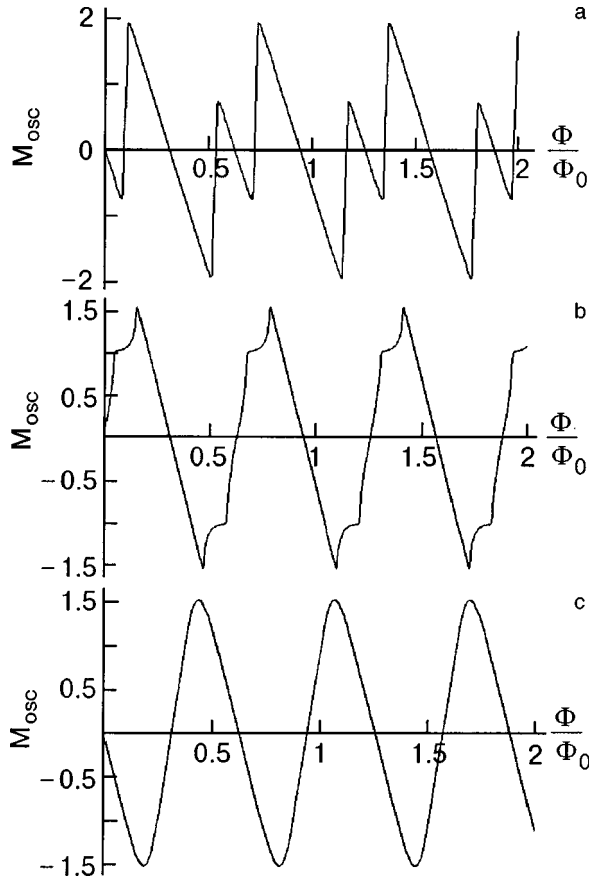
FIG. 2. The Aharonov–Bohm oscillations of the magnetization of a stack of hollow normal cylinders $M_{osc}(\Phi/\Phi_0)$ (given by Eq. (37) with $\Delta=0$) in units of the quantity $M(0)=2\varepsilon_0 S/\Phi_0$. The numerical calculations of $M_{osc}(\Phi/\Phi_0)$ in Figs. 1a–1c are done for different values of the parameters $a=2\pi^2 T_c^0(R)/\varepsilon_0$, $b=\nu/\pi T_c^0(R)$, $c=4\pi\sigma/\varepsilon_0$, and Rk_0:a=0.01, b =0.01, c=0.1, $Rk_0=1000$ (Fig. 1a); a=0.01, b=0.01, c=1, $Rk_0=100$ (Fig. 1b); a=0.01, b=0.01, c=0.1, $Rk_0=100$ (Fig. 1c).

Fig. 2a. Thus $\chi_{osc}(\Phi)$ in this case would have delta-function peaks at the jumps of the saw-tooth and a negative constant value between them. Temperature and ν, as well as Δ and σ, smear the singular features in $M_{osc}(\Phi)$, as one can see in Figs. 2a and 3c, making the $\chi_{osc}(\Phi)$ a harmoniclike function too. Near the transition temperature, provided that it is high enough that the higher harmonics can be neglected, we have from Eq. (27) a simple analytical expression for the susceptibility:

$$\chi \approx \frac{2}{\varepsilon_0}\left(\frac{2\pi S\Delta}{\Phi_0}\right)^2 Q_1 N_1(T,\nu)\cos\left(2\pi\frac{\Phi}{\Phi_0}\right). \qquad (40)$$

According to Eq. (32) the temperature behavior of the susceptibility near T_c is

$$\chi \propto \exp\left(-\frac{T}{T^*}\right). \qquad (41)$$

Such a temperature dependence of the magnetic susceptibility has been found recently in experiments on a bundle of electrically isolated Ag/Nb wires.[19] Every wire in the bundle was a very clean Ag cylinder coated with thin superconducting Nb layer. The authors of Ref. 19 also observed a crossover in the temperature behavior of the susceptibility which doubles the ratio $T/T^* \to 2T/T^*$ in the exponent of
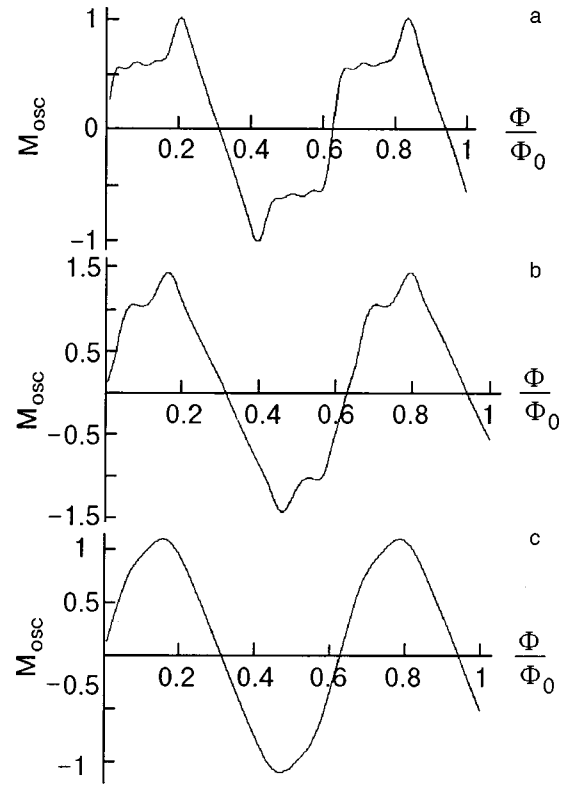

FIG. 3. The Aharonov–Bohm oscillations of the magnetization of a stack of hollow superconducting cylinders $M_{osc}(\Phi/\Phi_0)$ [see Eq. (37)] in units of the quantity $M(0)=2\varepsilon_0 S/\Phi_0$. The numerical calculations of $M_{osc}(\Phi/\Phi_0)$ in Figs. 1a–1c are done for different values of the parameters a $=2\pi^2 T_c^0(R)/\varepsilon_0$, b$=\nu/\pi T_c^0(R)$, c$=4\pi\sigma/\varepsilon_0$, d$=2\pi\Delta/\varepsilon_0$, and Rk_0:a $=0.01$, b=0.01, c=1, $d=0.05$, $Rk_0=1000$ (Fig. 1a); a=0.01, b=0.01, c =1, $Rk_0=100$, d=0.05 (Fig. 1b); a=0.01, b=0.5, c=1, d=0.5, Rk_0 $=1000$ (Fig. 1c).

$\chi(T)$ when $T<T^*$. We can relate this phenomenon to the fact that the quantity $\xi(T)=\hbar v_0/\pi T$ has a dual meaning in the problem in question. First, it is the coherence length that determines the amplitudes of the AB oscillations. Second, the length $\xi_N(T)=\hbar v_0/\pi T$ is known to be the length that determines the spatial scale of the proximity effect. In the context of our analysis this means that at the temperature $T=T^*$ the Ag cylinder became completely superconducting due to the proximity with the superconducting Nb coating, since at this temperature $\xi_N(T^*)=2\pi R$. As a result, the flux is expelled from the interior of the wire, and the cylinder can no longer trap the flux in the Ag core. Therefore the crossover observed in the Ag/Nb cylinders may be considered as a consequence of the crossover in the topology of the system as the temperature decreases: ''hollow'' cylinders with a flux trapped inside the normal Ag core (for temperatures $T>T^*$) became completely superconducting when T becomes less than T^* and expel the flux from the Ag core.

5. CONCLUSIONS

The original AB effect was formulated in Ref. 14 as a gedanken experiment in which the interference pattern of two electrons moving around a solenoid in the absence of a magnetic field depends on the flux through the solenoid. This theoretical prediction was soon confirmed in a real experiment done by Chambers.[35] Since then, different manifesta-

tions of the AB effect in solids have been studied, and many examples have been found in which various physical properties exhibit oscillations as functions of the flux with period Φ_0 (many references on the subject are found in the review articles).[15,16,34] A theory of the AB oscillations of the free energy in a metal ring and the related problem of the persistent currents in such systems was first considered in Ref. 27 (see also Ref. 36 in this connection) and was later generalized to the case of a superconducting ring in Ref. 18, where Aharonov–Bohm oscillations of the transition temperature $T_c(\Phi)$ were predicted. The theoretical analysis given in the present paper develops further the results of Refs. 18 and 27. For this purpose, we have studied the free energy of a stack of superconducting cylinders in an external magnetic field within the microscopic BCS model and have calculated analytically the oscillatory part of the free energy [see Eq. (19)]. We have also found explicit expressions for the AB oscillations of the critical temperature $T_c(\Phi)$ [Eq. (30)], the oscillatory part of the magnetization [Eqs. (37)–(39)], and the susceptibility $\chi(T)$ near the transition temperature [Eq. (40)]. The oscillatory dependence of all above quantities on the flux Φ with the fundamental period Φ_0 stems, in the final analysis, from the gauge invariance of the theory of nonsimply connected solids. In our particular case this flux dependence appears due to the quasiparticle energy given by Eq. (13). The results of a numerical analysis of these oscillations is shown in Figs. 1–3. These pictures demonstrate strongly nonsinusoidal oscillating patterns for the functions $T_c(\Phi)$ and $M_{\mathrm{osc}}(\Phi)$ in the case of low temperatures and small level broadening. Such nonsinusoidal behavior of the oscillations is caused by the small decrease of the amplitudes of the harmonics with their number p in this case. Increasing the temperature and ν as well as Δ damps the amplitudes of the harmonics and smears the singularities in the oscillation patterns, making them close to sinelike or cosinelike in shape. The way in which the cylinders are stacked into a tube also strongly affects the oscillation patterns through the factor Q_p of Eq. (21). This factor in turn depends on the stacking factor I_p given by Eq. (2) and determined by the density of states $g(\varepsilon)$ related to electron motion across the stack (along the tube). The dependence of the oscillation pattern on the hopping integral σ between cylinders in a stack in a model described by the factor of Eq. (31) is rather sophisticated and can be seen from a comparison of Figs. 2a and 2b. The Aharonov–Bohm effect has been observed recently in circular carbon nanotubes.[30] It was also shown that structural disorder effectively breaks carbon nanotubes into a series of cylinders (or dots) separated by tunneling barriers. The transmission probability between the cylinders was estimated[31] to vary within the limits 0.001–0.1. Thus nanotubes as well as coated wires are good candidates for physical realization of the model adopted in this paper.

Being quantum in nature, the AB oscillations of the critical temperature $T_c(\Phi)$ vanish exponentially when R is increased to values of the order of the GL coherence length. Further increase of R results in a dimensional crossover from the AB oscillations to the Little–Parks ones. The LP oscillations have half as large a period in the flux, $\Phi_s = \Phi_0/2$, and have the shape of periodic parabolas (see Eq. (35)). The LP oscillations take place in the GL regime $R \gtrsim \xi_{\mathrm{GL}}(T)$, in

which the quantum size effects are irrelevant and quantum AB oscillations are suppressed. The LP oscillations arise due to external-field-induced oscillations of the superconducting current of the Cooper pairs around a hollow in the cylinder. Since the Cooper pairs carry double electronic charge, the period of these oscillations in the flux becomes half as large as for the quantum AB oscillations. We also found that near the transition temperature the magnetic susceptibility $\chi(T)$ of the superconducting cylinder is given by Eq. (40), which, through the factor of Eq. (41), displays the nontrivial exponential temperature dependence observed in Ag/Nb wires.[19]

In conclusion, we would like to stress yet another important point of our analysis. The physics behind the quantum AB oscillations in superconductors, in essence, is very much similar to that which governs the dHvA oscillations in the vortex state. In spite of the fact that the AB oscillations are periodic in the direct field, the damping factors Ψ_p and Q_p entering Eq. (19) are akin to the corresponding factors in the dHvA oscillations in superconductors.[25] For example, the factor Ψ_p determined by Eq. (25), after the substitution $\varepsilon_0 = \hbar\Omega$, becomes identical to the corresponding factor in the dHvA oscillations describing the damping of the pth amplitude due to the superconducting gap $\Delta(T)$. It is impossible to single out experimentally the contribution of Δ to the damping of the dHvA oscillations in superconductors because of the spatial modulation of the order parameter $\Delta(\mathbf{r})$ caused by the vortices.[28] Since there are no vortices in the AB system under consideration, the comparative experimental studies of the damping of the AB and dHvA oscillations can provide the information necessary for separation of the ''vortex matter'' contribution to the damping of the dHvA oscillations in superconductors in the mixed state.

*E-mail: Vladimir.M.Gvozdikov@univer.kharkov.ua

[1] J. M. Gordon, A. M. Goldman, and J. Maps, Phys. Rev. Lett. **56**, 2280 (1986).
[2] A. Gerber and G. Deucher, Phys. Rev. Lett. **64**, 1585 (1990).
[3] H. R. Shea and M. Tinkham, Phys. Rev. Lett. **79**, 2324 (1997).
[4] V. V. Moshchalkov, L. Giedu, C. Strunk, R. Jonckheere, X. Qui, C. Van Haesendonck, and Y. Bruynseraede, Nature (London) **373**, 319 (1995).
[5] C. Strunk, V. Bruyndocx, V. V. Moshchalkov, C. Van Haesendonck, and Y. Bruynseraede, Czech. J. Phys. **46**, 2337 (1996); V. Bruyndocx, C. Strunk, V. V. Moshchalkov, C. Van Haesendonck, and Y. Bruynseraede, Czech. J. Phys. **46**, 2339 (1996).
[6] C. C. Abilio, P. Butand, T. Fournier, B. Pannetier, J. Vidal, S. Jedesko, and B. Dalzotto, Phys. Rev. Lett. **83**, 5102 (1999).
[7] W. A. Little and R. D. Parks, Phys. Rev. Lett. **9**, 9 (1962).
[8] R. P. Groff and R. D. Parks, Phys. Rev. **176**, 567 (1968).
[9] S. Alexander, Phys. Rev. B **27**, 1541 (1983).
[10] S. Alexander and E. Halevi, J. Phys. (France) **44**, 805 (1983).
[11] P. G. de Gennes, C. R. Acad Sci. **292**, 9 (1981).
[12] V. M. Vinokur, Zh. Éksp. Teor. Fiz. **93**, 113 (1987) [Sov. Phys. JETP **66**, 198 (1987)].
[13] L. L. Shohn and M. Tinkham, Phys. Rev. B **47**, 97 (); *ibid.* **B47**, 967 (1993).
[14] Y. Aharonov and D. Bohm, Phys. Rev. **115**, 485 (1959).

[15] A. G. Aronov and Y. S. Sharvin, Rev. Mod. Phys. **59**, 755 (1987).

[16] I. V. Krive and A. S. Rozhavsky, Int. J. Mod. Phys. **6**, 1255 (1992).

[17] C. N. Yang, Rev. Mod. Phys. **34**, 694 (1962).

[18] E. N. Bogachek, G. A. Gogadze, and I. O. Kulik, Phys. Status Solidi B **67**, 287 (1975).

[19] R. Frassanito, P. Visani, M. Niderost, A. C. Mota, P. Smeibidl, K. Swietca, W. Wendler, and F. Pobell, Czech. J. Phys. **46**, 2317 (1996).

[20] V. M. Gvozdikov, Sov. Phys. Solid State **26**, 1560 (1984); *ibid.* **28**, 179 (1986).

[21] V. M. Gvozdikov, Fiz. Nizk. Temp. **18**, 1128 (1992) [Sov. J. Low Temp. Phys. **18**, 790 (1992)].

[22] J. R. Schrieffer, *Theory of Superconductivity*, Benjamin, New York (1964); Nauka, Moscow (1970).

[23] J. Bardin, R. Kummel, A. E. Jacobs, and L. Tewordt, Phys. Rev. **187**, 556 (1969).

[24] I. S. Gradshtein and I. M. Ryzhik, *Tables of Integrals, Series, and Products*, Academic Press, New York (1980); Nauka, Moscow (1971).

[25] V. M. Gvozdikov and M. V. Gvozdikova, Phys. Rev. B **58**, 8716 (1998).

[26] V. M. Gvozdikov and E. Manninen, Fiz. Nizk. Temp. **6**, 1138 (1980) [Sov. J. Low Temp. Phys. **6**, 552 (1980)].

[27] I. O. Kulik, JETP Lett. **11**, 275 (1970).

[28] T. J. B. Janssen, N. Harrison, S. M. Hyden, P. Meeson, and M. Springford, Phys. Rev. B **57**, 11698 (1998).

[29] T. Maniv, V. N. Zhuravlev, I. D. Vagner, and P. Wyder, J. Chem. Solids **59**, (1998).

[30] J. Rollbuhler and A. A. Odintsov, *LT22 Proceedings, LT22 CDROM, paper N10 616. pdf* (1999).

[31] P. L. Mc Euen, M. Bockrath, D. H. Cobdeh, Y. G. Yoon, and S. G. Lois, Phys. Rev. Lett. **83**, 5098 (1999).

[32] L. P. Gor'kov, Zh. Éksp. Teor. Fiz. **36**, 1918 (1959) [Sov. Phys. JETP **9**, 1918 (1959)].

[33] H. F. Cheung, Y. Gefen, E. K. Reidel, and W. H. Shih, Phys. Rev. B **37**, 6050 (1988).

[34] A. A. Zvyagin and I. V. Krive, Fiz. Nizk. Temp. **21**, 687 (1995) [Low Temp. Phys. **21**, 533 (1995)].

[35] R. G. Chambers, Phys. Rev. Lett. **5**, 3 (1960).

[36] M. Buttiker, Y. Imry, and R. Landauer, Phys. Lett. A **96**, 365 (1983).

LOW-TEMPERATURE MAGNETISM

Phonon-assisted anti-Stokes excitation of the fluorescence of Mn²⁺ ions in the CsMnCl₃·2H₂O crystal

V. V. Eremenko,* V. I. Fomin, and V. S. Kumosov

B. Verkin Institute for Low Temperature Physics and Engineering, National Academy of Sciences of the Ukraine, 47 Lenin Ave., 61164, Kharkov, Ukraine

We demonstrate that anti-Stokes excitation of Mn^{2+} ions in the $CsMnCl_3 \cdot 2H_2O$ crystal can occur through multiphonon addition to the energy of the photons of exciting light. The deficit dE between the energy of the Mn^{2+} $^4T_1$ exciton and the photon energy of the He–Ne laser used as the source of illumination is compensated by simultaneous annihilation of several thermally activated lattice phonons. The absence of two-photon activation of the fluorescence was verified by measurement of the dependence of the fluorescence intensity on the intensity of the exciting light, which appears linear at a fixed energy mismatch dE. © *2000 American Institute of Physics.* [S1063-777X(00)00507-7]

1. INTRODUCTION

It is well known that fluorescence is usually optically excited using a frequency of the pumping source above the frequency of the fluorescent electronic transition. The positive difference between the energy of the exciting photon and the energy of the electronic level is expended on the creation of phonons (or another quasiparticles), so the process is called Stokes. The situation becomes quite different in the case when the difference has the negative sign. Then the only way to excite the electronic level is to add enough energy to the photon. Such a process is called anti-Stokes excitation of fluorescence, because it is accompanied by the simultaneous annihilation of some quasiparticles (usually thermally created). A number of experiments on anti-Stokes fluorescence excitation are known, but all of them deal with rare-earth compounds (see, for example, Refs. 1 and 2). In the present paper we investigate the anti-Stokes fluorescence excitation in a Mn-containing compound.

Recently we observed the presence of $^4T_1$ fluorescence of the Mn^{2+} ion at close to room temperatures under the condition of irradiation of a $CsMnCl_3 \cdot 2H_2O$ single-crystal sample with a He–Ne laser. This phenomenon is quite surprising at first glance because the energy of the lowest excitonic level $^4T_1$ in this compound is about $17\,064$ cm^{-1} (at 1.8 K),[3] whereas the energy of the exciting light is $15\,803$ cm^{-1}, so the energy difference $dE = 1\,261$ cm^{-1} is substantially higher than the sample temperature T.

$CsMnCl_3 \cdot 2H_2O$, or CMC, is strongly anisotropic due to its layered and chainlike crystal structure. The CMC structure is described by the orthorhombic space group $Pcca$ (D_{2h}^8).[4] The unit cell contains four formula units and has the dimensions $a = 9.060$ Å, $b = 7.285$ Å, and $c = 11.455$ Å. The Mn^{2+} ions are arranged in chains along the a axis. Each Mn^{2+} ion is surrounded by a coordination octahedron consisting of four Cl^- ions and two O^{2-} ions. Two of the Cl^- ions are shared by adjacent octahedra, while the other two belong to only one octahedron.

The strong anisotropy of various physical properties of CMC originates from its chainlike structure; for example, it is responsible for the quasi-one-dimensional character of the antiferromagnetic ordering of Mn^{2+} spins at low temperatures.[5] The vibrational spectra of CMC also reflect its layered and chainlike structure.[6–8] They contain extremely low-frequency optical excitations (30–50 cm^{-1}). The unit cell of CMC contains two chains which are symmetric to each other with respect to inversion. It was found earlier[6] that the Davidov splitting of the vibrational modes of the crystal, in consequence of the above fact, is small, so the interaction between chains is weak.

Detailed studies of the Stokes fluorescence show that the dynamic behavior of the Mn^{2+} $^4T_1$ exciton reflects the reduced dimensionality.[3,9–11] The optical excitations in CMC are localized, and the energy migration at low temperatures is very slow.[11] The strong coupling of the exciton with an OH stretching vibration causes its efficient nonradiative relaxation and quenching of the fluorescence. This is apparent from the increase of the fluorescence lifetime, by more than an order of magnitude, when the H_2O in CMC is replaced by heavy water D_2O (Ref. 10).

2. EXPERIMENTAL SETUP

CMC single crystals of good optical quality were grown from saturated solutions of $MnCl_2 \cdot 4H_2O$ and CsCl. The clearly distinguishable habit of the crystals used in our investigations allows one to easily cut oriented samples relative to the crystallographic directions for sample preparation. The samples have the form of a rectangular parallelepiped and were polished to optical quality.

The spectra were recorded using a JOBIN YVON U-1000 double monochromator with a cooled photomultiplier, photon-counting electronics, and digital data storage. In order to avoid the polarizing effect of the monochromator, a depolarization wedge was placed in front of the entrance slit. Polarized Raman scattering and fluorescence measure-
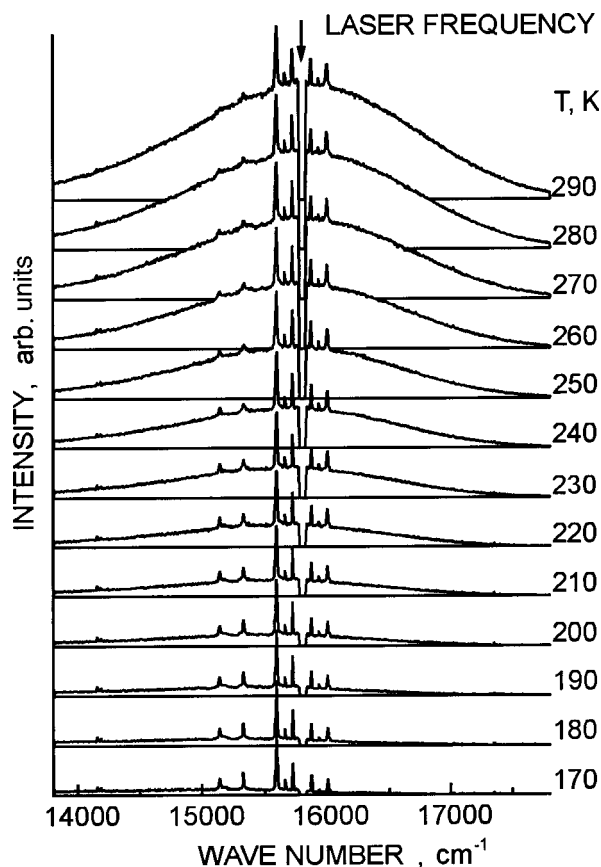
FIG. 1. Temperature dependence of the fluorescence overlapped with the Raman spectra excited by a He–Ne laser (15 803 cm^{-1}) in a CsMnCl$_3$·2H$_2$O single crystal. The fall in the spectra near the laser frequency is a result of shutting off the laser to prevent photomultiplier damage.

FIG. 2. Comparison of the fluorescence bands in a CsMnCl$_3$·2H$_2$O single crystal excited by He–Ne (solid lines) and He–Cd (dashed lines) lasers. The hatched areas represent the contribution of multi-phonon light scattering processes during excitation by a He–Ne laser.

ments were made using a right-angle scattering geometry. As sources of exciting light for the experiments we used a 0.5-mW He–Cd laser ($\lambda = 441.6$ nm) and a 40-mW He–Ne laser ($\lambda = 632.8$ nm). The sample was mounted in an optical cryostat for measurements over a wide temperature range. The temperature of a sample was measured to an accuracy of 1 K using a copper–Constantan thermocouple. The recorded spectra were corrected for instrument's spectral response to represent the results in the form of the quantum yield.

3. EXPERIMENTAL RESULTS AND DISCUSSION

The experimentally observed features are shown in Fig. 1, which exhibits the spectra for different temperatures, which look like narrow Stokes and anti-Stokes Raman lines on a broad background of a Gaussian-like shape. Evidence that the broad band is of a fluorescence nature was obtained by comparison with the spectra obtained in the irradiation of the sample at the shorter wavelength (441.6 nm) of the He–Cd laser at the same temperatures. The energy of the photons of this source is 22 645 cm^{-1}, which is about 5 580 cm^{-1} higher than the fluorescent electronic level of CMC, so we are then dealing with the usual process of fluorescence excitation. Figure 2 shows this comparison. A temperature-dependent scale factor is only used to fit these bands; these scale factors are subsequently used as the temperature dependence of the relative quantum yield of anti-Stokes excited fluorescence. To check the constancy of the experimental
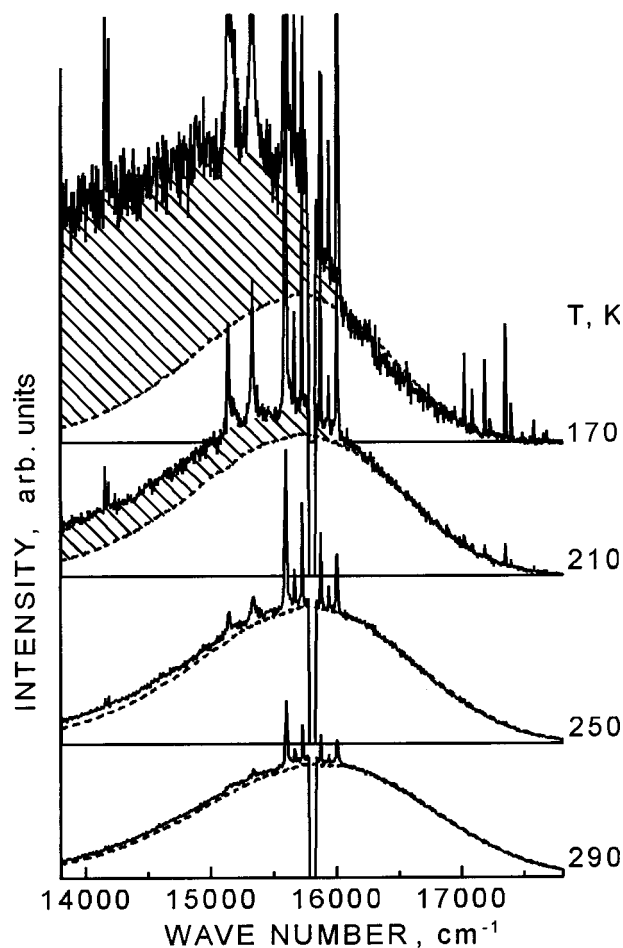
conditions during the experiments, we monitored whether the areas of some Raman lines conformed to the Bose law:

$$I_{\text{Stokes}} = I_0\{1 + [\exp(\hbar\omega/kT) - 1]^{-1}\},$$

where ω is the phonon frequency and T is the temperature. In the case of anti-Stokes excitation of the fluorescence with the He–Ne laser the most intense lattice phonons, with frequencies of about 75, 205, and 217 cm^{-1}, were used, whereas in the case of Stokes excitation (He–Cd laser) the very intense phonon line at about 3 380 cm^{-1}, corresponding to an OH stretching vibration, was used.

At low temperatures the relative contribution of Stokes multiphonon light scattering increases, with an increasing scale factor, as shown in Fig. 2, giving the illusion of a difference between shapes, whereas at the highest temperatures the shapes match rather well. So, to calculate the relative factor of the efficiency of anti-Stokes excitation in comparison to the Stokes, at every temperature the high-energy slope of the fluorescence band was fitted. This slope corresponds to the anti-Stokes part of the Raman spectrum where the contribution of multiphonon scattering decreases rapidly with increasing Raman shift.

In order to check the mechanism of anti-Stokes excitation of the fluorescence, we measured the dependence of the

emission intensity on the power of the He–Ne laser. It shows a linear dependence that excludes the possibility of multi-photon excitation.

Another exotic situation may give such a linear dependence, if one imagines that in the crystal there is some electronic level lower than $Mn^{2+}\ ^4T_1$ and lower than the energy of a He–Ne laser photon. Such a level (of defects, for example) is conjectured to have a very long lifetime, so it is fully excited even at an extremely low density of irradiation. Thus the level may play the role of the initial level for a second step excitation of the $Mn^{2+}\ ^4T_1$ electronic level. This scheme nevertheless does not stand up from the point of view of temperature dependence. Usually the lifetime of electronic excitations becomes longer with decreasing temperature, so the intensity of fluorescence must be at least nondecreasing, whereas the experiments display a contrasting behavior.

Polarization studies showed that the maximum intensity of the fluorescence band is observed with polarization along the direction of the chains, in the crystallographic direction *a*.

In order to check whether the experimentally observed temperature dependence of the quantum yield of the anti-Stokes excited fluorescence is consistent with the dependence of the absorption on the He–Ne laser wavelength, one needs to obtain the values of the absorption coefficient. The main problem of such measurements is the very small value of the absorption. Another way is to calculate the anti-Stokes part of the absorption band using Stepanov's equation,[12] which relates the shape of the fluorescence band with that of the absorption band, and vice versa. This expression has the form

$$\frac{I^{\text{YIELD}}(\omega)}{\kappa(\omega)} \propto \omega^2 \exp\left(\frac{\hbar(\omega_0 - \omega)}{kT}\right),$$

where $I^{\text{YIELD}}(\omega)$ is the quantum fluorescence yield at frequency ω; $\kappa(\omega)$ is the absorption coefficient at this frequency; and ω_0 is the frequency of the 0–0 electronic transition. Note that the expression has a universal character if the ground and excited states are in thermodynamic equilibrium and there are no alternative channels of absorption apart from the electronic transition. It is well known that phonons play an important role in processes of electronic absorption and radiation of light, so it is important to know the distribution functions of phonons in the electronic ground and excited states. We make the usual assumption that the initial phonon state is in thermal equilibrium with the medium and can be characterized by a Boltzmann distribution with an effective temperature T^*. In the case of optical absorption this is not an assumption but simply a definition of the ground state with $T^* = T$. For the case which involves excited electronic states this assumption is valid subject to some conditions. It is known that the $^4T_1$ exciton in CMC has a long lifetime (0.58 ms in CMC with ordinary water and 9.2 ms in CMC with heavy water at $T = 1.8$ K)[10] in comparison with the lifetime of an optical phonon (usually 10^{-9}–10^{-11} s), so the assumption that T^* is close to the lattice temperature T can be justified also.

The absorption spectra were measured at the same temperatures as the fluorescence spectra, using samples of different thicknesses mounted in the two channels of the setup. This allowed us to ignore the light reflectance from the sample surfaces in the absorption coefficient calculations.
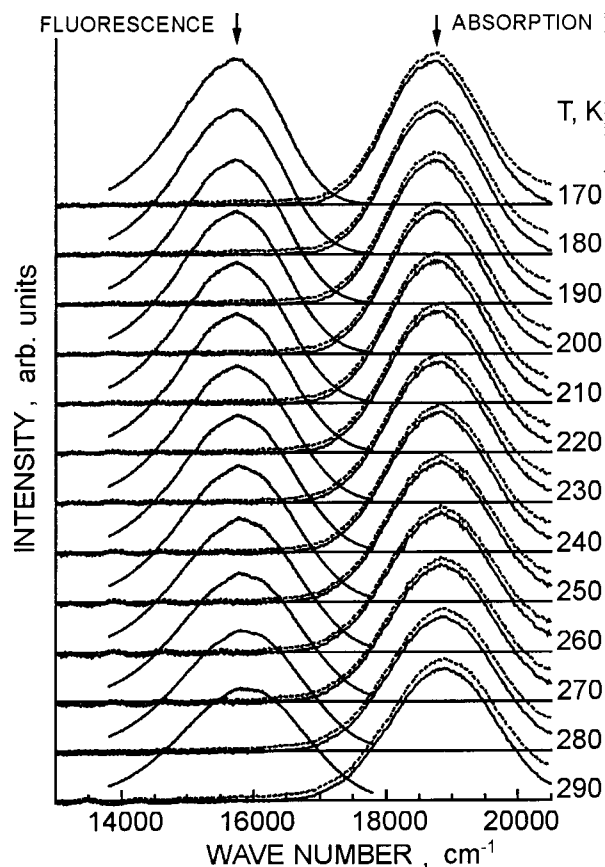

FIG. 3. Comparison of the fluorescence and absorption spectra of $CsMnCl_3 \cdot 2H_2O$ at different temperatures. The fluorescence was excited by a He–Cd laser (22 645 cm^{-1}). The solid absorption bands were obtained from the original ones (dashed bands) by subtracting the weak wing of the next absorption band with higher energy.

Thus, having experimental fluorescence and absorption spectra (see Fig. 3), it is possible to calculate the relative values of the absorption coefficient in the area of good transparency, if the frequency of the 0–0 electronic transition is known. The last problem may also be solved on the basis of the principle of so-called ''mirror'' symmetry of the fluorescence and absorption renormalized line shapes. The renormalization follows from the representation of the fluorescence yield and absorption coefficient in terms of the Einstein coefficients for spontaneous and stimulated electronic transitions. The renormalization has the form

$$\frac{I^{\text{YIELD}}(\omega_0 - \Delta\omega)}{(\omega_0 - \Delta\omega)^3} \propto \frac{\kappa(\omega_0 + \Delta\omega)}{(\omega_0 + \Delta\omega)},$$

where $\Delta\omega$ is the relative frequency counted from the electron transition frequency ω_0. An example of such a fitting is presented in Fig. 4. The slight difference between the fluorescence and absorption bands is a result of Franck–Condon interaction, which in the present case may only slightly violate the principle presented above. Figure 5 represents the temperature dependence of the 0–0 electronic transition frequency obtained in present experiments together with the result of a direct observation at 1.8 K.[3]
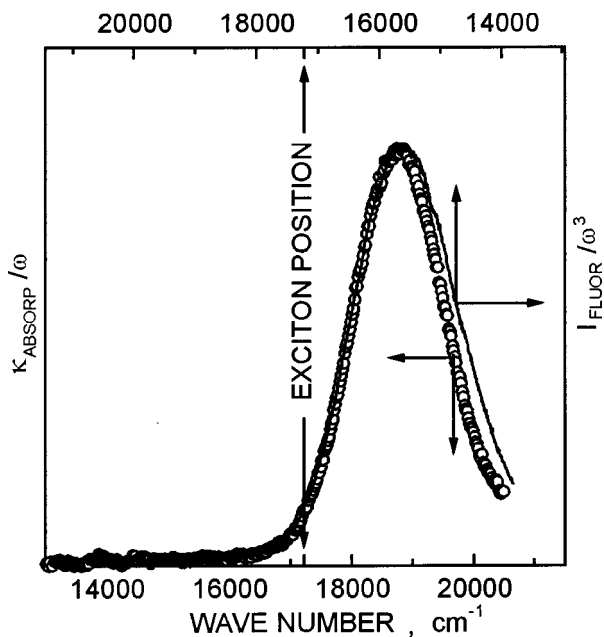
FIG. 4. Example of the fitting procedure for the determination of the pure exciton transition energy at a temperature of 230 K. The principle of ''mirror'' symmetry of the fluorescence and absorption renormalized line shapes is used. The slight difference between the bands is a result of the Franck–Condon interaction.

FIG. 6. Example of the fitting procedure for the determination of the weak absorption coefficient at the He–Ne laser frequency ($15\,803\ \text{cm}^{-1}$) by comparison of the real absorption spectrum (solid line) with the part of the absorption band (open circles) calculated from the corresponding fluorescence band using Stepanov's equation.

Using the results and methods presented above, the values of absorption coefficient at different temperatures were obtained. Examples of the use of Stepanov's law are shown in Fig. 6. A comparison of the directly observed areas of anti-Stokes excited fluorescence bands and the calculated absorption coefficients are in good agreement (Fig. 7).

It should be noted that the data obtained on the temperature dependence of the calculated absorption coefficient at the He–Ne laser wavelength and the corresponding experi-
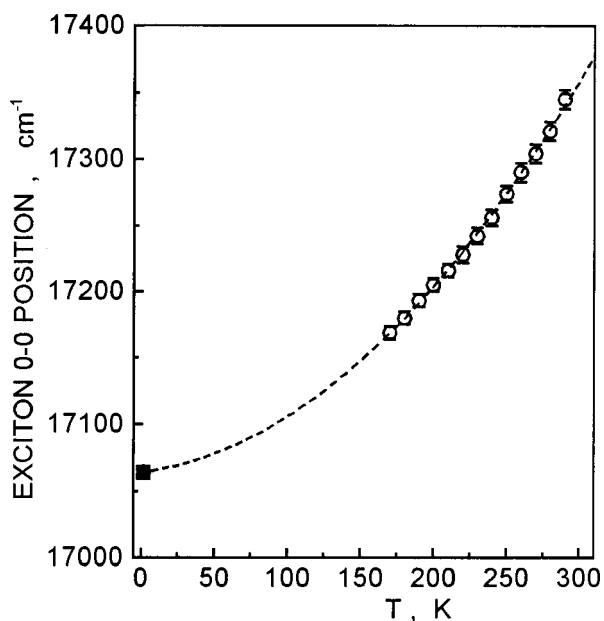
mental relative quantum yield of fluorescence conform well to the Arrhenius law (see Fig. 8). But the value obtained for the activation energy is not compatible with the real energy mismatches at all experimental temperatures. The cause of this illusion follows from a few accidental reasons. First of

FIG. 5. Temperature dependence of the frequency of a pure excitonic transition in a $CsMnCl_3 \cdot 2H_2O$ single crystal. The open circles represent the exciton positions calculated in the present paper, whereas the solid square is the result of direct observation at 1.8 K.[3] The interpolated dashed line $\omega = \omega_0 + AT + BT^2$ is plotted using the following parameters: $\omega_0 = 17\,064\ \text{cm}^{-1}$, $A = 0.139\ \text{cm}^{-1}/\text{K}$, $B = 0.0028\ \text{cm}^{-1}/\text{K}^2$.
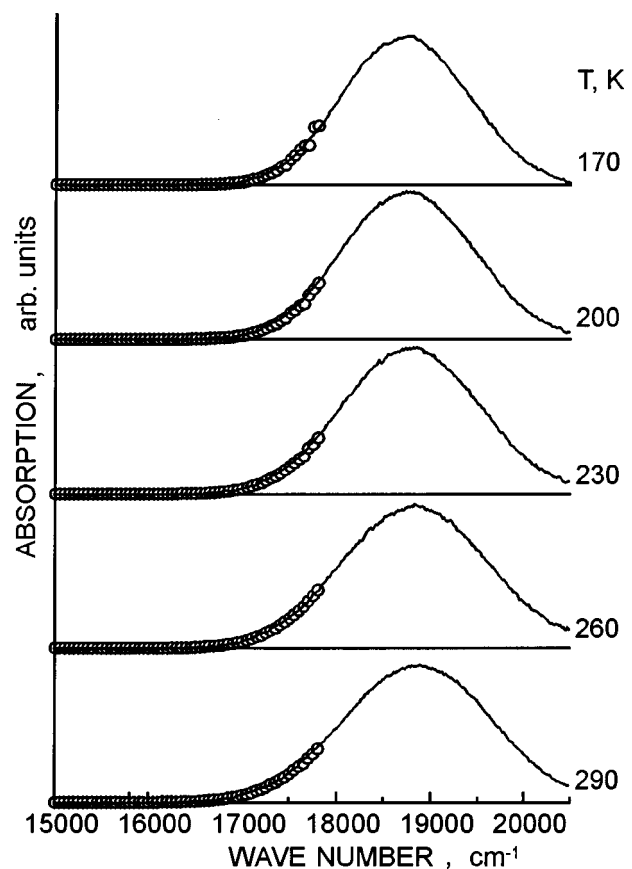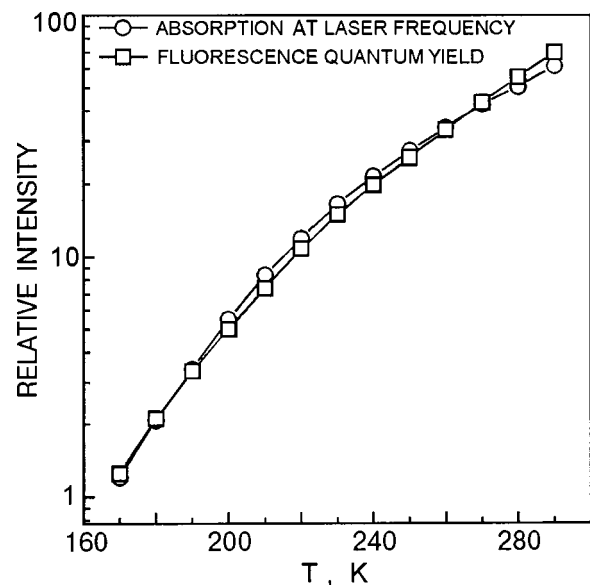

FIG. 7. Comparison of the data obtained for the absorption at the He-Ne laser frequency and the relative fluorescence quantum yield in a $CsMnCl_3 \times 2H_2O$ single crystal.
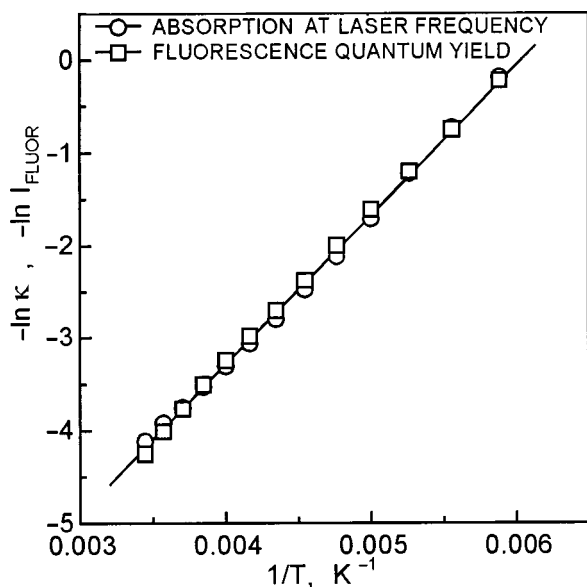
FIG. 8. Arrhenius temperature dependence of the relative absorption coefficient at the He-Ne laser frequency and the anti-Stokes excited fluorescence in a $CsMnCl_3 \cdot 2H_2O$ single crystal. The parameters of the interpolated line $y = y_0 + Bx$ are the following: $y_0 = -9.75$, $B = 1615$ K $= 1120$ cm^{-1}.

all, the position of the 0–0 excitonic level exhibits a temperature shift, as was shown above. In the temperature region of our experiments (170–290 K) the shift is close to linear (see Fig. 9). In addition, the position of the exciting wavelength at all temperatures remains near the maximum of the fluorescence band. Taking the above facts into account it is easier to understand the illusion. It follows from Stepanov's law that the absorption coefficient in the anti-Stokes region can be expressed in terms of the Stokes part of the fluorescence band as

$$\kappa(\omega) \propto \frac{I^{\text{YIELD}}(\omega)}{\omega^2} \exp\left(\frac{-\hbar(\omega_0 - \omega)}{kT} \right).$$
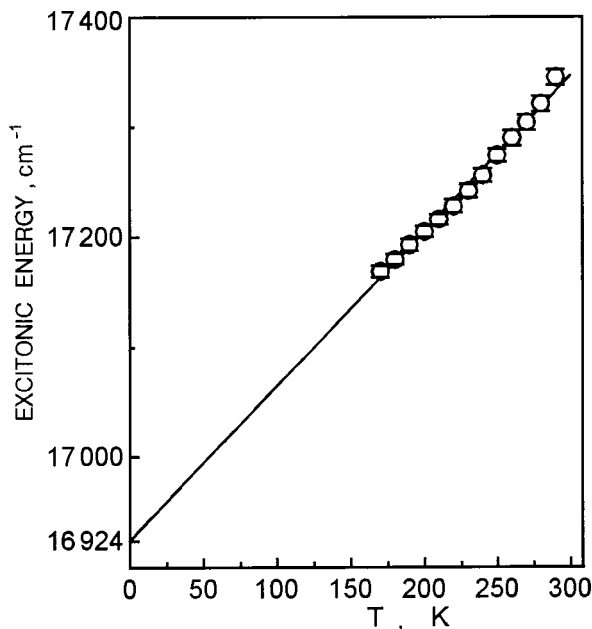

FIG. 9. Linear extrapolation of the experimentally determined temperature dependence of the 0-0 excitonic frequency in a $CsMnCl_3 \cdot 2H_2O$ single crystal.

Taking into account the approximately linear temperature dependence of $\omega_0 = \widetilde{\omega}_0 + \alpha T$, one can obtain the following:

$$\kappa(\omega) \propto \frac{I^{\text{YIELD}}(\omega)}{\omega^2} \exp\left(\frac{-\hbar(\widetilde{\omega}_0 - \omega)}{kT} \right) \exp\left(\frac{-\hbar \alpha}{k} \right).$$

Because the Stokes-excited $I^{\text{YIELD}}(\omega)$ hardly depends on the temperature at the frequency of the He–Ne laser (see Fig. 3), the Arrhenius law follows from the first exponent in the above expression, so the activation energy is simply the value $\hbar(\widetilde{\omega}_0 - \omega_{\text{laser}})$. If one uses the values given in the captions of Figs. 8 and 9 and a laser frequency 15 803 cm^{-1}, one more easily sees that the values obtained are in very good agreement $(\widetilde{\omega}_0 - \omega_{\text{laser}} = 16\,924 - 15\,803 = 1\,121$ cm$^{-1} \approx \Delta E = 1\,120$ cm$^{-1} = 1615$ K).

4. CONCLUSION

The experiments and calculations presented show that the anti-Stokes excitation of fluorescence in CMC has a phonon-assisted character. The possibility of fluorescence excitation with a great energy mismatch in comparison with the experimental temperatures seems likely to be a result of the chain like crystal structure of $CsMnCl_3 \cdot 2H_2O$, which produces many low-frequency vibrational modes. These modes give a high phonon density of states in the low-energy region and are a cause of the well-developed absorption and fluorescence intensity in the immediate vicinity of the 0-0 electronic transition in both the Stokes and anti-Stokes regions. As a result of this work, the temperature dependence of the energy of the lowest level of the $Mn^{2+4}T_1$ term in CMC was also obtained. It displays a very large temperature shift and reflects a large change in the crystal-field splitting of the level.

[*]E-mail: eremenko@ilt.kharkov.ua

[1] F. Ausel, Phys. Rev. B **13**, 2809 (1976).
[2] P. Raveendran, N. Sukar, and T. K. K. Srinivasan, Phys. Rev. B **55**, 4978 (1997).
[3] W. Jia, E. Strauss, and W. M. Yen, Phys. Rev. B **23**, 6075 (1981).
[4] S. J. Jensen, P. Anderson, and S. E. Rasmussen, Acta Chem. Scand. **16**, 1890 (1962).
[5] K. Nagata and Y. Jazuke, Phys. Lett. A **31**, 293 (1970).
[6] D. M. Adams and D. S. Newton, J. Chem. Soc. A **22**, 3499 (1971).
[7] W. Jia, E. Strauss, W. M. Yen, K. Xia, and M. Zhao, Phys. Rev. B **39**, 12853 (1989).
[8] V. P. Gnezdilov, V. V. Eremenko, V. S. Kurnosov, and V. I. Fomin, Fiz. Nizk. Temp. **17**, 630 (1991) [Sov. J. Low Temp. Phys. **17**, 331 (1991)].
[9] R. Ya. Bron, V. V. Eremenko, and E. V. Matyushkin, Fiz. Nizk. Temp. **5**, 344 (1979) [Sov. J. Low Temp. Phys. **5**, 163 (1979)].
[10] W. Jia, R. T. Brundate, and W. M. Yen, Phys. Rev. B **27**, 41 (1983).
[11] V. V. Eremenko, V. A. Karachevtsev, A. R. Kazachkov, V. V. Shapiro, and V. V. Slavin, Phys. Rev. B **49**, 11799 (1994).
[12] B. I. Stepanov, Dokl. Akad. Nauk SSSR **112**, 839 (1957).

This article was published in English in the original Russian journal. Reproduced here with stylistic changes by the Translation Consultant.

Anomalous behavior of longitudinally polarized sound waves in non-Heisenberg ferromagnets

Yu. A. Fridman* and D. V. Spirin

V. I. Vernadskiĭ Tavricheskiĭ National University, ul. Yaltinskaya 4, 95036 Simferopol, Ukraine
(Submitted February 7, 2000)
Fiz. Nizk. Temp. **26**, 664–670 (July 2000)

The spectra of coupled magnetoelastic waves in two-dimensional and three-dimensional non-Heisenberg magnets with biaxial anisotropy are investigated. It is shown that for a certain relationship of the material constants, three different phase states can be realized in the system. The phase transitions between these states occur by ''quantum spin reduction,'' and the unstable branch of elementary excitations at the phase transition point is a linearly polarized quasiphonon mode. © *2000 American Institute of Physics.* [S1063-777X(00)00607-1]

1. INTRODUCTION

It is well known that the magnetoelastic interaction in magnetically ordered systems leads to hybridization of the elastic and magnetic excitations, i.e., to magnetoelastic (ME) waves.[1] In this case the dynamic properties of the system are substantially altered. The changes are manifested with particular clarity in the neighborhood of orientational phase transitions (OPTs). For example, at the point of an OPT the soft mode is a transversely polarized quasiphonon branch of excitations (the dispersion relation of the quasiphonons changes from linear to quadratic), and a ME gap appears in the quasimagnon spectrum.[1,2] Then the longitudinally polarized sound waves are practically noninteracting with the magnetic subsystem.[1–3]

However, there are some experimental data[4–6] that indicate that under certain conditions the longitudinally polarized sound waves can interact with the magnetic subsystem. For example, a decrease of the longitudinal sound velocity in ErFeO₃ was observed in Ref. 5. In addition, it was noted in Ref. 7 that the softening of a longitudinally polarized quasiphonon mode in a biaxial ferromagnet is observed for a certain relationship between the single-ion anisotropy (SA) constants.

In this connection it is of interest to address the question of the interaction of longitudinally polarized acoustical modes with the magnetic subsystem.

Previous studies[8,9] have shown that no such effect is observed in Heisenberg magnets, and as the simplest model we therefore choose a biaxial non-Heisenberg ferromagnet. Furthermore, the compound ErFeO₃ contains rare-earth ions, whose magnetic properties are determined not only by the Heisenberg interaction but also by invariants of higher degrees. Therefore, we choose a model for this system in the form a biaxial ferromagnet with a biquadratic interaction, located in an external magnetic field parallel to the 0Z axis.

2. DISPERSION RELATION FOR COUPLED MAGNETOELASTIC WAVES IN A 2D FERROMAGNET

Let us examine the effects of interest to us for two-dimensional and three-dimensional ferromagnets. Let us first consider a 2D system, in which case the Hamiltonian is written

$$\mathcal{H} = -\frac{1}{2}\sum_{n,n'}[J_{n,n'}\mathbf{S}_n\cdot\mathbf{S}_{n'} + K_{nn'}(\mathbf{S}_n\cdot\mathbf{S}_{n'})^2]$$

$$+\frac{\beta_1}{2}\sum_n (S_n^x)^2 + \frac{\beta_2}{2}\sum_n (S_n^y)^2 + \frac{\beta_3}{2}\sum_n (S_n^z)^2$$

$$+\lambda\sum_n [u_{xx}(S_n^x)^2 + u_{yy}(S_n^y)^2 + u_{xy}(S_n^xS_n^y + S_n^yS_n^x)]$$

$$+\frac{E}{2(1-\sigma^2)}\int dr\left[\sum_i u_{ii}^2 + 2\sigma\sum_{ij} u_{ii}u_{jj} + 2(1\right.$$

$$\left.-\sigma)\sum_{ij} u_{ij}^2\right] - H\sum_n S_n^z, \tag{1}$$

where $J_{n,n'}$, $K_{n,n'}$ are the bilinear and biquadratic exchange constants, β_i are the single-ion anisotropy constants, λ is the magnetoelastic constant, u_{ij} is the symmetric part of the strain tensor components, E is Young's modulus, and σ is Poisson's ratio. In Hamiltonian (1) the two-dimensionality of the system is taken into account in the elastic and ME energies of the ferromagnet. To simplify the calculations we shall assume that the magnetic ion has spin $S=1$.

We introduce the notation $\tilde{\beta}_1 \equiv \beta_1 - \beta_3$, $\tilde{\beta}_2 \equiv \beta_2 - \beta_3$ and use the relation $(S^x)^2 + (S^y)^2 + (S^z)^2 = S(S+1)$; then the expression for the SA energy can be written

$$\mathcal{H}_{SA} = \frac{\tilde{\beta}_1}{2}\sum_n (S_n^x)^2 + \frac{\tilde{\beta}_2}{2}\sum_n (S_n^y)^2. \tag{2}$$

Let us consider the case $\tilde{\beta}_1 > 0$, $\tilde{\beta}_2 > 0$, $\tilde{\beta}_i \gg \lambda^2/E$. The Hamiltonian (1) then becomes

$$\mathcal{H} = -\frac{1}{2}\sum_{n,n'}[J_{n,n'}\mathbf{S}_n\cdot\mathbf{S}_{n'} + K_{nn'}(\mathbf{S}_n\cdot\mathbf{S}_{n'})^2]$$

$$+\frac{\tilde{\beta}_1}{2}\sum_n (S_n^x)^2 + \frac{\tilde{\beta}_2}{2}\sum_n (S_n^y)^2 + \lambda\sum_n [u_{xx}(S_n^x)^2$$

$$+u_{yy}(S_n^y)^2] + \lambda\sum_n [u_{xy}(S_n^xS_n^y + S_n^yS_n^x)]$$

$$+\frac{E}{2(1-\sigma^2)}\int dr[u_{xx}^2+u_{yy}^2+2\sigma u_{xx}u_{yy}$$

$$+2(1-\sigma)u_{xy}^2]-H\sum_n S_n^z. \tag{3}$$

Separating out in the exchange part of the Hamiltonian (3) the mean field $\langle S^z\rangle$ and the additional fields q_2^p ($p=0,2$) due to the quadrupole moment, we obtain the one-site Hamiltonian $\mathcal{H}_0(n)$:

$$\mathcal{H}_0(n)=-\bar{H}S_n^z-B_2^0Q_{2n}^0-B_2^2Q_{2n}^2+\frac{\tilde{\beta}_1}{2}(S_n^x)^2+\frac{\tilde{\beta}_2}{2}(S_n^y)^2$$

$$+\lambda[u_{xx}(S_n^x)^2+u_{yy}(S_n^y)^2+u_{xy}(S_n^xS_n^y+S_n^yS_n^x)], \tag{4}$$

where

$$\bar{H}=H+\langle S^z\rangle\left(J_0-\frac{K_0}{2}\right); \quad B_2^0=\frac{1}{6}K_0q_2^0;$$

$$B_2^2=\frac{1}{2}K_0q_2^2; \quad q_2^p=\langle Q_2^p\rangle; \quad Q_{2n}^0=3(S_n^z)^2-2;$$

$$Q_{2n}^2=\frac{1}{2}[(S_n^+)^2+(S_n^-)^2]; \quad S_n^{\pm}=S_n^x\pm iS_n^y.$$

To simplify the subsequent calculations we assume that $\tilde{\beta}_1=\tilde{\beta}_2=\beta$. Such a relationship of the SA constants corresponds to a ferromagnet with ''easy axis'' anisotropy, with its axis of easy magnetization parallel to the $0Z$ axis.

Solving the one-ion problem with the aid of Hamiltonian (4), we obtain the energy levels of the magnetic ion:

$$E_1=\frac{\beta}{2}+\frac{\lambda}{2}(u_{xx}^{(0)}+u_{yy}^{(0)})-B_2^0-\chi,$$

$$E_0=\beta+\lambda(u_{xx}^{(0)}+u_{yy}^{(0)})+2B_2^0, \tag{5}$$

$$E_{-1}=\frac{\beta}{2}+\frac{\lambda}{2}(u_{xx}^{(0)}+u_{yy}^{(0)})-B_2^0+\chi, \chi^2=\bar{H}^2+(B_2^2)^2$$

and the eigenfunctions of the one-site Hamiltonian (4)

$$\Psi_n(1)=\cos\delta|1\rangle+\sin\delta|-1\rangle, \Psi_n(0)=|0\rangle,$$

$$\Psi_n(-1)=-\sin\delta|1\rangle+\cos\delta|-1\rangle,$$

where $|i\rangle$ are the eigenvectors of the operator S^z, $\cos\delta=B_2^2/[\sqrt{(\chi-\bar{H})^2+(B_2^2)^2}]$, and $u_{ij}^{(0)}$ are the spontaneous strains, which are determined from the condition of minimum free energy density; they have the values

$$u_{xx}^{(0)}=u_{yy}^{(0)}=-\frac{\lambda}{E}\frac{1-\sigma}{2}, \quad u_{xy}^0=0.$$

The eigenfunctions of the Hamiltonian $\mathcal{H}_0(n)$ are used to construct the Hubbard operators $X^{M'M}\equiv|\Psi(M')\rangle\langle\Psi(M)|$ describing the transition of the magnetic ion from the state M' to the state M. In terms of the Hubbard operators the Hamiltonian (4) is diagonal, and the spin operators are related to the Hubbard operators as

$$S_n^+=\sqrt{2}\cos\delta(X_n^{10}+X_n^{0-1})+\sqrt{2}\sin\delta(X_n^{01}-X_n^{-10}),$$

$$S_n^-=(S_n^+)^+, \tag{6}$$

$$S_n^z=\cos 2\delta(H_n^1-H_n^{-1})-\sin 2\delta(X_n^{1-1}+X_n^{-11}).$$

Using the Green function method described in detail in Ref. 10, we can obtain the dispersion relation of coupled ME waves:

$$\det\|\delta_{ij}+G_0^ab(\alpha)a_{ir}(\alpha)A_{rj}$$

$$+B^0(k;\mu,\mu')T^{-\alpha}(k,\mu)G_0^ab(\alpha)T^{\beta}$$

$$\times(-k,\mu')G_0^{\beta}b(\beta)a_{ir}(\alpha,\beta)A_{rj}\|=0. \tag{7}$$

Here $T_n^{M(\alpha)}(q,\mu)$ are the amplitudes of the transformations:

$$T_n^{1-1}(q,\mu)=iT_n^{(0)}(q,\mu)\frac{\lambda\cos(2\delta)}{2}(e_\mu^xq_x-e_\mu^yq_y)$$

$$+T_n^0(q,\mu)\frac{\lambda}{2}(e_\mu^xq_y+e_\mu^yq_x),$$

$$T_n^{-11}(q,\mu)=iT_n^0(q,\mu)\frac{\lambda\cos(2\delta)}{2}(e_\mu^xq_x-e_\mu^yq_y)$$

$$-T_n^0(q,\mu)\frac{\lambda}{2}(e_\mu^xq_y+e_\mu^yq_x), \tag{8}$$

$$T_n^0(q,\mu)=\frac{\exp(iqn)}{\sqrt{2m\omega_\mu(q)}},$$

where m is the mass of the magnetic ion, $\omega_\mu(q)$ is the dispersion relation for μ-polarized sound, $\omega_\mu(q)=c_\mu q$, and c_μ is the sound velocity. The remaining quantities appearing in Eq. (7) are defined in Ref. 10.

The solutions of equations (7) determine the spectra of hybridized elementary excitations for arbitrary values of the single-ion anisotropy and biquadratic exchange constants and arbitrary temperatures.

3. PHASE STATE AND SPECTRA OF COUPLED MAGNETOELASTIC WAVES OF A 2D FERROMAGNET

Let us investigate the spectra of coupled ME waves governed by dispersion relation (7) at low temperatures ($T\ll T_C$, where T_C is the Curie temperature). Then the lowest energy level will be E_1, and only this level needs to be taken into account. This approximation simplifies the mathematical manipulations substantially.

Before determining the spectra of elementary excitations, let us consider the possible phase states of the system. For this we investigate the behavior of the order parameters of the system:

$$\langle S^z\rangle\approx\cos 2\delta, \quad q_2^0\approx 1, \quad q_2^2\approx\sin 2\delta. \tag{9}$$

From the last expression in (9) we can obtain an equation for $x\equiv q_2^2$:

$$x^4(-J_0^2+K_0J_0)+x^2\left[H^2+J_0^2+K_0J_0\right.$$

$$\left.+2H\left(J_0-\frac{K_0}{2}\right)\sqrt{1-x^2}\right]=0. \tag{10}$$

It is easy to see that one of the solutions for arbitrary values of the parameters of the system is $q_2^2 = 0$, which corresponds to realization of the ferromagnetic phase. There is one more solution:

$$q_2^2 = 1 - \frac{H^2}{(K_0 - J_0)^2},$$

which corresponds to a quadrupolar–ferromagnetic phase.

For $H = 0$ there obviously exists a quadrupolar phase with order parameters $\langle S^z \rangle = 0$, $q_2^0 = 1$, $q_2^2 = 1$. In a nonzero field there can exist both a ferromagnetic and a quadrupolar–ferromagnetic phase.

Thus three phases can be realized in the system under study: a ferromagnetic (FM) phase with $\langle S^z \rangle \approx 1$, $q_2^0 = 1$, and $q_2^2 = 0$; a quadrupolar–ferromagnetic (QFM) phase, and a quadrupolar (QP_1) phase, which is realized for $H = 0$. It should be noted that the QP_1 phase arises through the quantum spin reduction, and the FM–QFM phase transition also occurs through a decrease in the modulus of the magnetization vector.

We thus examine Eq. (7) in the following geometries: wave vector $\mathbf{k} \| 0X$, in which the polarization unit vector has the nonzero components e_l^x and e_τ^y. Since we are considering a 2D system, the third polarization e_t^z does not exist for acoustical excitations.

Taking Eq. (8) and our chosen geometry into account, we can write the dispersion relation (7) in the form of a product of two determinants, $\det_\|$ and $\det_\perp$:

$$\det{}_\| = \begin{vmatrix} 1 + x_{11} & x_{15} & x_{16} \\ x_{51} & 1 + x_{55} & x_{56} \\ x_{61} & x_{65} & 1 + x_{66} \end{vmatrix} = 0, \qquad (11)$$

$$\det{}_\perp = \begin{vmatrix} 1 + x_{22} & x_{23} & x_{27} & x_{28} \\ x_{32} & 1 + x_{33} & x_{37} & x_{38} \\ x_{72} & x_{73} & 1 + x_{77} & x_{78} \\ x_{82} & x_{83} & x_{87} & 1 + x_{88} \end{vmatrix} = 0, \qquad (12)$$

where

$$x_{ij} = G_0^\alpha b(\alpha) a_{ir}(\alpha) A_{rj} + B^0(k; \mu, \mu')$$
$$\times T^{-\alpha}(k, \mu) G_0^\alpha b(\alpha) T^\beta(-k, \mu') G_0^\beta b(\beta) a_{ir}(\alpha, \beta) A_{rj}.$$

Equations (11) and (12) determine the spectra of ''longitudinal'' (high-frequency) and ''transverse'' (low-frequency) quasimagnons, respectively:

$$\varepsilon_\|(k) = \gamma k^2 + 2(H + J_0 - K_0), \qquad (13)$$

$$\varepsilon_\perp(k) = \alpha k^2 + H + \frac{\beta}{2} - a_0. \qquad (14)$$

Here $\alpha = R_0^2 J_0$, where R_0 is the Heisenberg exchange radius, $\gamma = \tilde{R}_0^2 K_0$, where $\tilde{R}_0$ is the biquadratic exchange radius, and $a_0 = \lambda^2/(2E)$ is the ME coupling parameter.

Since all of the off-diagonal amplitudes of the transformations (except for T^{1-1} and T^{-11}) are zero, it follows from Eq. (12) that none of the quasiphonon modes interacts with the ''transverse'' quasimagnons.

As we have said, the magnetic momentum of the system is perpendicular to the $X0Y$ plane. For this reason, the non-zero spontaneous strains are equal to each other ($u_{xx}^{(0)} = u_{yy}^{(0)}$). This leads to the situation that the system under discussion is invariant with respect to rotations around the quantization axis, and this, in turn, as can be seen from Eq. (11), leads to degeneracy of the elastic excitations with respect to polarization, i.e., the spectrum of longitudinally (l) polarized quasiphonons is the same as the spectrum of of transversely (τ) polarized quasiphonons. Furthermore, it follows from Eq. (11) that the ''longitudinal'' quasimagnons interact with longitudinally polarized quasiphonons, which have a spectrum of the form

$$\omega_1^2(k) = \omega_1^2(k) \left[\frac{\gamma k^2 + 2(H + J_0 - K_0 - a_0)}{\gamma k^2 + 2(H + J_0 - K_0)} \right]. \qquad (15)$$

We see from (15) that in a magnet with a large biquadratic interaction ($K_0 > J_0$), a softening of the spectrum of longitudinally polarized quasiphonons occurs in the long-wavelength limit (for $\gamma k^2 \ll a_0$) when

$$H_c = K_0 + a_0 - J_0, \qquad (16)$$

and in this case the quasiphonon spectrum has the form

$$\omega_1^2(k) = \omega_l^2(k) \frac{\gamma k^2}{2 a_0}. \qquad (17)$$

Longitudinally polarized quasiphonons interact with a high-frequency (relaxational) magnetic mode $\varepsilon_\|(k)$, which for $H = H_c$ exhibits a ME gap:

$$\varepsilon_\|(0) = \varepsilon_{ME} = 2 a_0. \qquad (18)$$

Expressions (16)–(18) will also have meaning for another relationship among the material constants: $J_0 \geq K_0$, but $K_0 = J_0 < -a_0$. However, it seems to us that this relationship among the material constants is less realistic than $K_0 > J_0$.

As we have said, the low-frequency quasimagnon branch $\varepsilon_\perp(k)$ does not interact with the elastic subsystem. For $H = H_c$ it has a gap equal to

$$\varepsilon_\perp(0) = K_0 - J_0 + \frac{\beta}{2}.$$

For $H < H_0$ a QFM phase is realized in the ferromagnet ($0 < q_2^2 < 1$). For $H = 0$ it is the QP_1 phase with the ground state $\Psi(1) = (|1\rangle + |-1\rangle)/\sqrt{2}$ that is realized. In that phase the spectrum of ''transverse'' (low-frequency) quasimagnons has the form

$$\varepsilon_\perp^2(k) = \left(\gamma k^2 + \frac{\beta}{2} - a_0 \right) \left[\frac{\beta}{2} - a_0 + 2(K_0 - J_0) \right], \qquad (19)$$

and the spectrum of ''longitudinal'' (high-frequency) quasimagnons can be written as

$$\varepsilon_\|^2(k) = 2 \gamma k^2 (K_0 - J_0). \qquad (20)$$

From expression (19) one can determine the existence region of the QP_1 phase:

$$\frac{\beta}{2} > a_0. \qquad (21)$$

4. PHASE STATES AND SPECTRA OF COUPLED MAGNETOELASTIC WAVES OF A 3D FERROMAGNET

Let us consider a 3D ferromagnet at low temperatures. The Hamiltonian of the system will differ from (1) by the presence of additional terms in the magnetoelastic and elastic energies:

$$\mathcal{H} = -\frac{1}{2}\sum_{n,n'}[J_{nn'}\mathbf{S}_n\cdot\mathbf{S}_{n'}+K_{nn'}(\mathbf{S}_n\cdot\mathbf{S}_{n'})^2]+\frac{\beta}{2}\sum_n (S_n^x)^2$$

$$+\frac{\beta}{2}\sum_n (S_n^y)^2+\lambda\sum_n [u_{xx}(S_n^x)^2+u_{yy}(S_n^y)^2+u_{zz}(S_n^z)^2$$

$$+u_{xy}(S_n^xS_n^y+S_n^yS_n^x)]+\lambda\sum_n [u_{xz}(S_n^xS_n^z+S_n^zS_n^x)$$

$$+u_{yz}(S_n^yS_n^z+S_n^zS_n^y)]+\frac{E}{2(1-\sigma^2)}$$

$$\times\int dr\left[\sum_i u_{ii}^2+2\sigma\sum_{ij} u_{ii}u_{jj}+2(1-\sigma)\right.$$

$$\left.\times\sum_{ij} u_{ij}^2\right]-H\sum_n S_n^z. \tag{22}$$

Here all of the notation is analogous to (1). As before, we assume that the magnetic ion has spin $S=1$. The solution of the Schrödinger equation determines the energy levels of the magnetic ion:

$$E_1=\frac{\beta}{2}+\frac{\lambda}{2}(u_{xx}^{(0)}+u_{yy}^{(0)}+2u_{zz}^{(0)})-B_2^0-\chi,$$

$$E_0=\beta+\lambda(u_{xx}^{(0)}+u_{yy}^{(0)})+2B_2^0,$$

$$E_{-1}=\frac{\beta}{2}+\frac{\lambda}{2}(u_{xx}^{(0)}+u_{yy}^{(0)}+2u_{zz}^{(0)})-B_2^0+\chi, \tag{23}$$

$$\chi^2=\bar{H}^2+(B_2^2)^2.$$

The spontaneous strains, as before, are determined from the condition of minimum free energy density and have the form

$$u_{xx}^{(0)}=u_{yy}^{(0)}=-\frac{\lambda}{E}\frac{1-3\sigma}{2}, \quad u_{zz}^{(0)}=\frac{\lambda}{E}(1-\sigma),$$

$$u_{xy}^{(0)}=u_{zy}^{(0)}=u_{xz}^{(0)}=0.$$

The relation between the spin operators and Hubbard operators is the same as (6) at the same value of cos δ.

The subsequent calculations for the 3D system are analogous to those done before for the 2D ferromagnet. We note only that the amplitudes of the transformations in this case are different from those obtained before and have the form

$$T_n^{10}(q,\mu)=T_n^0(q,\mu)\frac{\lambda}{2\sqrt{2}}[i(\cos\delta-\sin\delta)\times(e_\mu^xq_z+e_\mu^zq_x)$$

$$+(\cos\delta+\sin\delta)(e_\mu^yq_z+e_\mu^zq_y)],$$

$$T_n^{01}(q,\mu)=T_n^0(q,\mu)\frac{\lambda}{2\sqrt{2}}[i(\cos\delta-\sin\delta)\times(e_\mu^xq_z+e_\mu^zq_x)$$

$$-(\cos\delta+\sin\delta)(e_\mu^yq_z+e_\mu^zq_y)],$$

$$T_n^{1-1}(q,\mu)=iT_n^0(q,\mu)\frac{\lambda\cos(2\delta)}{2}(e_\mu^xq_x-e_\mu^yq_y)$$

$$+T_n^0(q,\mu)\frac{\lambda}{2}(e_\mu^xq_y+e_\mu^yq_x),$$

$$T_n^{-11}(q,\mu)=iT_n^0(q,\mu)\frac{\lambda\cos(2\delta)}{2}(e_\mu^xq_x-e_\mu^yq_y)$$

$$-T_n^0(q,\mu)\frac{\lambda}{2}(e_\mu^xq_y+e_\mu^yq_x),$$

$$T_n^0(q,\mu)=\frac{\exp(i\mathbf{q}\cdot\mathbf{n})}{\sqrt{2m\omega_\mu(q)}}.$$

Let us investigate the spectra of coupled ME waves in a 3D ferromagnet. For this we use Eq. (7). The geometry of the problem remains as before: the wave vector $\mathbf{k}\|0X$, and the nonzero components of the polarization vector are e_l^x, e_τ^y, and e_t^z. It must be noted that when the three-dimensionality is taken into account there is one more transversely (t) polarized quasielastic mode.

As before, the equations for the order parameter (9) and (10) determine the existence region of the ferromagnetic, quadrupolar–ferromagnetic, and quadrupolar phases.

In the ferromagnetic phase the quasimagnon spectra have the same form as in the 2D case:

$$\varepsilon_\|(k)=2(H+J_0-K_0)+\gamma k^2,$$

$$\varepsilon_\perp(k)=H+\frac{\beta}{2}+a_0+\alpha k^2, \tag{24}$$

while the quasiphonon spectra are

$$\omega_1^2(k)=\omega_l^2\left[\frac{\gamma k^2+2(H+J_0-K_0-a_0)}{\gamma k^2+2(H+J_0-K_0)}\right],$$

$$\omega_2^2(k)=\omega_t^2\left[\frac{\alpha k^2+H+\beta/2}{\alpha k^2+H+\beta/2+a_0}\right]. \tag{25}$$

In this case, as in the 2D system, a degeneracy of the quasielastic excitations with respect to polarization occurs in the $X0Y$ plane, but now t-polarized phonons (ω_2) also arise.

It follows from (24) and (25) that at the point of the FM–QFM phase transition, the high-frequency quasimagnon mode $\varepsilon_\|(k)$ actively interacts with a longitudinally polarized quasiphonon. At the phase transition point ($H=H_c=K_0-J_0+a_0$) in the long-wavelength limit ($\gamma k^2\ll a_0$) the spectrum of the l-polarized quasiphonon softens:

$$\omega_1^2(k)=\omega_l^2(k)\frac{\gamma k^2}{2a_0},$$

and a ME gap appears in the spectrum of the high-frequency quasimagnons:

$$\varepsilon_\|(0)=\varepsilon_{ME}=2a_0.$$

The spectrum of the t-polarized quasiphonons does not undergo any substantial changes at the point of the FM–QFM phase transition; there is only a slight renormalization of the corresponding sound velocity:

$$\omega_2^2(k) = \omega_t^2(k)\left(1 - \frac{a_0}{K_0 - J_0 + \beta/2}\right).$$

In the quadrupolar phase, which, as before, is realized at $H = 0$, the spectra of elementary excitations are given by the expressions

$$\varepsilon_\perp^2(k) = \left(\gamma k^2 + \frac{\beta}{2} + a_0\right)\left(\frac{\beta}{2} - a_0 + 2(K_0 - J_0)\right),$$

$$\varepsilon_\parallel^2(k) = 2\gamma k^2(K_0 - J_0), \tag{26}$$

from which we obtain the existence condition for the QP_1 phase: $\beta/2 > a_0$. Thus, under our initial assumption $\beta \gg \lambda^2/E$, in a 3D ferromagnet with $J_0 < K_0$ the phase transition from the ferromagnetic to the QFM phase occurs via a phonon mode corresponding to longitudinal quasielastic oscillations. This transition is not an orientational transition but comes about through the quantum reduction of the average spin value.

CONCLUSION

The results of a study of the spectra of coupled ME waves in 3D and 3D biaxial ferromagnets with biquadratic and ME interactions show that for a large biquadratic exchange constant ($J_0 < K_0$) there can exist in the system a ferromagnetic phase (in fields $H > K_0 + a_0 - J_0$), a QFM phase ($K_0 + a_0 - J_0 > H > 0$), and a QP_1 phase (for $H = 0$).

The FM–QFM and QFM–QP_1 phase transitions are not orientational transitions but occur through a decrease in the average spin value. An unusual feature is the fact that the

mode that softens at the FM–QFM phase transition is a longitudinally polarized acoustical mode that interacts with the high-frequency (relaxational) quasimagnon branch. This result is a consequence of the purely quantum-mechanical effect of spin reduction. We note that an analogous system was investigated by a phenomenological method in Ref. 7. However, in view of the quantum nature of this effect, it was not observed, and the interpretation of the results of Ref. 7 is inaccurate.

It should be noted that if the Heisenberg exchange is predominant in the system ($J_0 > K_0$) or if the biquadratic exchange is absent ($K_0 = 0$), then, as can easily be seen from our results, only the ferromagnetic phase is realized in the system, and so there are no phase transitions.

*E-mail: man@expl.cris.crimea.ua

[1] E. A. Turov and V. G. Shavrov, Usp. Fiz. Nauk **140**, 429 (1983) [Sov. Phys. Usp. **26**, 593 (1983)].
[2] V. I. Ozhogin and V. L. Preobrazhenskiĭ, Usp. Fiz. Nauk **133**, 593 (1977).
[3] A. I. Akhiezer, V. G. Bar'yakhtar, and S. V. Peletminskiĭ, *Spin Waves* [in Russian], Nauka, Moscow (1967).
[4] G. Gorodetsky and B. Luthy, Phys. Rev. B **2**, 3688 (1970).
[5] N. K. Dan'shin, S. V. Zherlitsin, S. S. Zvada, G. G. Kramarchuk, M. A. Sdvizhkov, and V. D. Fil', Zh. Éksp. Teor. Fiz. **93**, 2151 (1987) [Sov. Phys. JETP **66**, 1227 (1987)].
[6] L. T. Tsimbal and M. K. Dan'shin, Zhurnal Fizichnikh Doslidzhen' **2**, 545 (1998).
[7] V. D. Buchel'nikov and V. G. Shavrov, Fiz. Tverd. Tela (St. Petersburg) **37**, 1402 (1995) [Phys. Solid State **37**, 760 (1995)].
[8] Yu. N. Mitsaĭ and Yu. A. Fridman, Ukr. Fiz. Zh. **35**, 459 (1990).
[9] Yu. N. Mitsaĭ, A. N. Maĭorova, and Yu. A. Fridman, Fiz. Tverd. Tela (St. Petersburg) **34**, 66 (1992) [Sov. Phys. Solid State **34**, 34 (1992)].
[10] Yu. A. Fridman and D. V. Spirin, Fiz. Nizk. Temp. **26**, 374 (2000) [Low Temp. Phys. **26**, 273 (2000)].

Translated by Steve Torstveit

Analysis of the temperature–field dependence of the magnetostriction in the antiferromagnetic phase of the easy-plane antiferromagnet CoCl$_2$

V. M. Kalita, A. F. Lozenko,* and S. M. Ryabchenko

Institute of Physics of the National Academy of Sciences of Ukraine, pr. Nauki 46, 03650 Kiev, Ukraine
(Submitted February 17, 2000)
Fiz. Nizk. Temp. **26**, 671–677 (July 2000)

An analysis is made of the experimental magnetic-field curves of the anisotropic (in the easy-plane) magnetostriction of the antiferromagnet CoCl$_2$ at different temperatures in the ordered phase. It is shown that the field dependence of the magnetostriction in a single-domain antiferromagnetic state remains proportional to the square of the applied field over the entire temperature range; this behavior corresponds well to the classic (Néel) scheme of collapse of the sublattice spins (spin flip). The temperature dependences of the intrasublattice and intersublattice contributions to the magnetoelasticity are proportional to each other. The temperature dependence of the spin-flip field obtained from the magnetostriction data agrees with that obtained previously from observations of the antiferromagnetic resonance (AFMR). The temperature dependence of the spontaneous anisotropy of the magnetostriction, obtained by extrapolating the magnetostriction in the single-domain state to zero field, is close to $\mathbf{M} \sim T^4$. © *2000 American Institute of Physics.* [S1063-777X(00)00707-6]

CoCl$_2$ crystals are layered dihalides with symmetry D_{3d}^5 and consist of Cl–Co–Cl sandwiches with ionic–covalent bonding within a sandwich and van der Waals bonds between sandwiches.[1] The layers of Co^{2+} ions form a hexagonal network in which the neighboring Co^{2+} ions are coupled by a relatively strong ferromagnetic exchange. The exchange interaction of the Co^{2+} ions of neighboring sandwiches is antiferromagnetic and extremely weak. At a temperature $T_N = 24.7$ K (Ref. 1) a three-dimensional antiferromagnetic order with a two-sublattice collinear magnetic structure is established in the CoCl$_2$ crystal, the magnetic moments being parallel within each sandwich layer and antiparallel to those in the adjacent layers.

The uniaxial anisotropy of the spin interactions in CoCl$_2$ in the direction perpendicular to the plane of the layer is extremely large, while the intralayer anisotropy is negligible. The sign of the uniaxial anisotropy is such that the magnetic moments of the two sublattices $\mathbf{M}_1$ and $\mathbf{M}_2$ are oriented in the plane of the layer. The smallness of the intralayer anisotropy leads to degeneracy of the directions of the antiferromagnetism vector $\mathbf{L} = \mathbf{M}_1 - \mathbf{M}_2$ in the plane. By applying a magnetic field $\mathbf{H}_\parallel$ along the axis of the crystal, one can achieve an orientation of $\mathbf{M}_1$ and $\mathbf{M}_2$ parallel to the axis. For this it is necessary to overcome the uniaxial anisotropy field, the value of which at $T = 4.2$ K, according to the data of Ref. 2, is ~ 150 kOe. For reorientation of the direction of $\mathbf{L}$ in the layer by a field $\mathbf{H}_\perp$ applied along the sandwich layer it is the small intralayer anisotropy that must be overcome. Then the vectors $\mathbf{L}$ and $\mathbf{H}_\perp$ are mutually perpendicular, although a canting of the moments $\mathbf{M}_1$ and $\mathbf{M}_2$ to the field direction (while remaining in the plane) will occur. As the field is increased, the canting of the sublattice magnetizations in the direction of $\mathbf{H}_\perp$ increases, and they become parallel to each other in the spin-flip field $H_{ff} \cong 2H_E$, where H_E is the effective exchange field of the interlayer antiferromagnetic interaction. At $T = 4.2$ K the spin-flip field is $2H_E \approx 32$ kOe.[3]

The octahedral crystalline field in which each of the Co^{2+} ions, which have a true spin of 3/2, is located interacts with them in such a way that the ground state of the ion becomes an orbital triplet. Because of the spin–orbit interaction and the trigonal crystalline field, it splits,[4] and the lower state becomes a Kramers doublet described by an effective spin $S_{\text{eff}} = 1/2$ and with a highly anisotropic g factor ($g_\perp = 6.0$, $g_\parallel = 3.1$; Ref. 3). Of the higher-lying Kramers doublets, the two closest to the ground state have energies of 699 and 1653 GHz.[5] Their occupation in the ordered state is negligible.[5,6] According to Refs. 6 and 7, the strong uniaxial magnetic anisotropy of CoCl$_2$ is due to the anisotropy of the intralayer exchange interactions.

The magnetic properties of CoCl$_2$ were studied intensively in the 1960s and 70s. Studies of the high-frequency and low-frequency antiferromagnetic resonances (AFMRs) were reported in Refs. 2, 3, 8, and 9, the temperature dependence of the spin-flip field H_{ff} (at which the frequency of the high-frequency AFMR goes to zero) in Ref. 9, the nuclear magnetic resonance of the Cl nuclei in the internal field of the magnetically ordered state in Ref. 10, and neutron scattering in Ref. 11.

In studies[9,12] of the low-frequency AFMR it was found that in CoCl$_2$, as in other layered dihalides of the iron group with easy-plane antiferromagnetic ordering, a spontaneous lowering of the symmetry in the easy plane occurs. The crystal spontaneously deforms in the direction of the vector $\mathbf{L}$. The spectrum of the low-frequency AFMR displays a characteristic gap[9] that reflects the spontaneous magnetostriction effect.[12]

Measurements of the induced magnetostriction in CoCl$_2$ were made in Refs. 12 and 13. The most remarkable result[12,13] was the practically total absence of spontaneous magnetostriction of the sample as a whole in the absence of an applied external field, despite the spontaneous magnetostrictive strain in the plane for each individual domain,

which is attested to by the onset of a gap in the spectrum of the low-frequency AFMR. The magnetostriction of the sample appears only upon its transition to a single-domain state under the influence of an external magnetic field $\mathbf{H}_\perp$. In Refs. 12 and 13 this was explained by the circumstance that in the multidomain state the direction of $\mathbf{L}$ and, hence, the strains in the different domains do not coincide, and the strains compensate each other for the sample as a whole. It has been established that the formation of these domains (which are called ''magnetoelastic'' in Ref. 13) is basically reversible as the magnetic field field $\mathbf{H}_\perp$ is turned on and off, although there is also a certain irreversible part, corresponding to a predominant preservation of domains with $\mathbf{L}\perp\mathbf{H}_\perp$, that remains present when the field is turned off. This irreversible part has also been detected in a neutron-diffraction study[11] of the antiferromagnetic domains in $CoCl_2$. In Ref. 14 a model was proposed in which the reversible magneto-elastic domain structure is assumed to arise as a consequence of the finite size of the crystal specimen.

A second feature of the magnetostriction of layered dihalides of the iron group (measurements have been made only at helium temperatures[12,13]) is that the relative changes in the dimensions of the crystals in the plane on account of the spontaneous and induced magnetostriction are unusually large ($\Delta l/l \sim 10^{-4}$).

A study of the temperature dependence of the parameters characterizing the spontaneous and induced magnetostriction and of the characteristic ''poling'' fields needed to eliminate the magnetoelastic domains is of interest both from the standpoint of obtaining concrete information about a given crystal and for the development of general concepts about easy-plane antiferromagnetic systems in which spontaneous symmetry breaking occurs as a result of a magnetoelastic interaction. In general the temperature dependence of the mechanisms of induced and spontaneous magnetostriction in antiferromagnetic crystals remain insufficiently studied. For this reason we have carried out a study of the temperature dependence of the magnetostriction in $CoCl_2$ at temperatures ranging from liquid-helium temperature to the antiferromagnetic ordering temperature T_N of the crystal.

EXPERIMENT

Measurements of the magnetostriction of $CoCl_2$ single crystals were made by a dilatometric method in Ref. 15. As was shown in Refs. 12 and 13, the induced magnetostriction of $CoCl_2$ has a hysteretic character, which is due to the presence of a partial irreversibility of the domain structure. Therefore, the values of the magnetostriction are somewhat different when the field is increased or decreased. In the single-domain state obtained when the multidomain structure is destroyed by a magnetic field, the values of the magnetostriction do not depend on whether the field is being increased or decreased,[13] and the data obtained as the magnetic field is increased (for example) can be used for analysis.

Figure 1 shows the $\mathbf{H}_\perp$ dependence of the strain ($\varepsilon = \Delta l/l$) of a $CoCl_2$ crystal in the direction along $\mathbf{H}_\perp$ in the temperature interval from 4.2 to 24 K. The character of the $\varepsilon(H_\perp)$ curve is qualitatively similar at all these temperatures. As $\mathbf{H}_\perp$ is increased from $\mathbf{H}_\perp = 0$ there is initially a rapid rise in the strain as the sample is ''poled'' into a single domain,
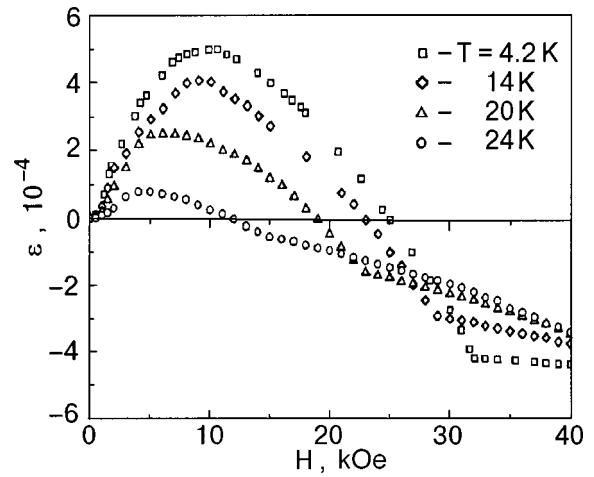

FIG. 1. Field dependence of the relative elongations of the $CoCl_2$ crystal, measured along a field lying in the easy plane for different temperatures (below $T_N = 24.7$ K).

and then, after the transition to a single-domain state, one observes the induced magnetostriction due to the canting of the sublattice magnetizations toward the field. In the course of this process the magnetostriction changes sign. In the spin-flip field H_{ff} a kink appears on the field dependence of the induced magnetostriction. As we see, the temperature dependence of the curves is manifested both in the values of the strains (they become smaller as the temperature is raised) and in the values of the fields for transition to the single-domain state (the region of the maxima on the curves) and, clearly, of the spin-flip fields of the sublattices.

The values of $\tilde{H}_{ff}(T) = H_{ff}(T)/H_{ff}(T=4.2$ K$)$ at various temperatures are shown in Fig. 2. For comparison the
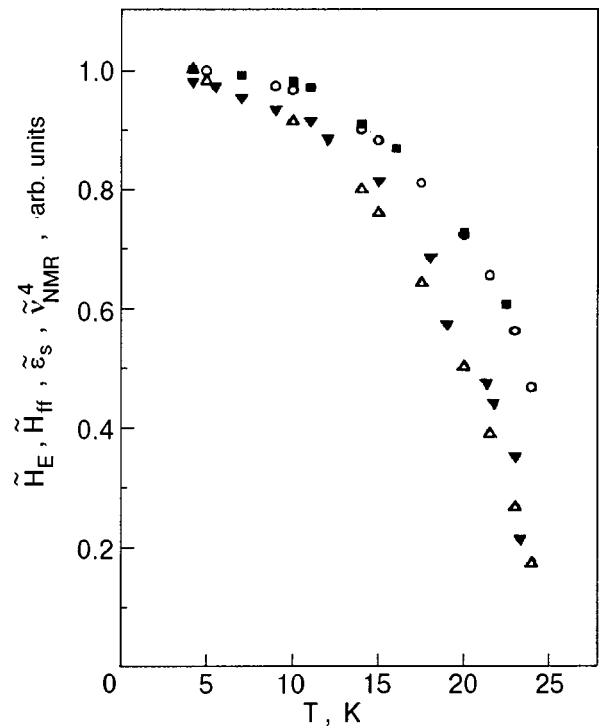
FIG. 2. Temperature dependence of the relative values of the spin-flip field $\tilde{H}_{ff}$ ($\bigcirc$) and $\tilde{H}_E$ ($\blacksquare$), the spontaneous anisotropic magnetostriction $\tilde{\varepsilon}_s$ ($\triangle$), and the fourth power of the NMR frequency, $\tilde{\nu}_{NMR}^4$ ($\blacktriangledown$).
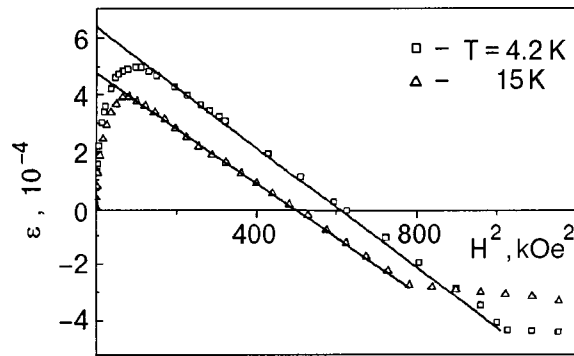
FIG. 3. The relative values of the magnetostriction of a crystal as a function of the square of the applied field at different temperatures.
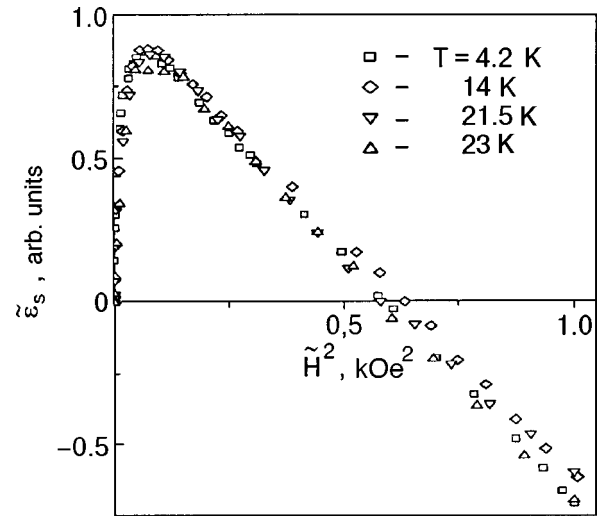

FIG. 4. Relative values of the magnetostriction, normalized to the value of the spontaneous anisotropic magnetostriction at each temperature ($\tilde{\varepsilon}(T,H) = \varepsilon(T,H)/\varepsilon_s(T)$), versus the square of the field, normalized to the square of the spin-flip field for each temperature ($\tilde{H}^2 = H^2/H_{ff}^2(T)$).

analogous values of the effective exchange fields $\tilde{H}_E(T) = H_E(T)/H_E(T=4.2\,\text{K})$ determined by AFMR from the value of $\mathbf{H}_\perp$ at which the high-frequency AFMR goes to zero.[9] The data from different methods of determining the temperature dependence of the spin-flip field are in good agreement.

Figure 3 shows the dependence of the strain of the crystal on the square of the field, $\varepsilon(H_\perp^2)$, at different temperatures. For fields at which the magnetostriction is determined by the canting of the sublattice spins in the single-domain state, i.e., fields up to H_{ff}, the strains remain proportional to the square of the field at all temperatures. This process corresponds to the parts of the curves approximated by straight lines in Fig. 3. Extrapolating them to $H_\perp = 0$, we obtain the hypothetical values of the spontaneous magnetostriction ε_s of the single-domain state. These are the values that would be observed if magnetoelastic domains did not arise in low fields and if the total spontaneous magnetostriction that is anisotropic in the easy-plane of the crystal were not compensated on the whole by the summation of strains in different directions in each of the domains.

It is of interest to elucidate how the coefficient of proportionality of the magnetostriction to $H_\perp^2$ in the single-domain state varies with temperature. In Fig. 4 the magnetostriction data obtained at various temperatures are plotted as a function of the square of the field, with the magnetostriction normalized to the spontaneous anisotropic magnetostriction at the same temperature, $\tilde{\varepsilon}(T,H) = \varepsilon(T,H)/\varepsilon_s(T)$, and with the square of the field normalized to the square of the spin-flip field at the same temperature, $\tilde{H}_\perp = H_\perp^2/H_{ff}^2(T)$. It is seen that with such a normalization the magnetostriction curves obtained for different temperatures coincide, within the experimental error, both in the single-domain state and in the region of the transition from the single-domain to the multidomain state.

The agreement of these curves in the single-domain region allows one to describe the magnetic field dependence of the induced single-domain magnetostriction throughout the temperature region $T < T_N$ by the relation

$$\varepsilon(T,H) = \varepsilon_s(T)\{1 - \xi[H_\perp/\tilde{H}_{ff}(T)]^2\}, \tag{1}$$

where ξ is a constant that is independent of the temperature (the value determined experimentally is $\xi = 1.6 \pm 0.05$).

At the same time, the agreement of the curves in Fig. 4 in the region of the transition from the single-domain to the

multidomain state means that the value of the spin-flip field of the sublattice magnetizations and the parameters of the field-induced rearrangement of the domain structure, e.g., the characteristic ''poling'' field, depend on temperature in a similar way.

Figure 2 shows the temperature dependence of the relative values of the anisotropic spontaneous magnetostriction $\tilde{\varepsilon}_s(T) = \varepsilon_s(T)/\varepsilon_s(T=4.2\,\text{K})$. It is useful to compare it with $H_{ff}(T)$ and with the temperature dependence of the sublattice magnetization, which is known from the NMR data for the Cl nucleus in zero field at different temperatures.[10] The NMR frequencies $\nu_{\text{NMR}}(T)$ are proportional to the sublattice magnetizations $M_{1,2}(T)$. Therefore, the normalized NMR frequencies $\tilde{\nu}(T) = \nu_{\text{NMR}}(T)/\nu_{\text{NMR}}(T=4.2\,\text{K})$ should be equal to the values of the normalized sublattice magnetization $\tilde{m}(T) = M_{1,2}(T)/M_{1,2}(T=4.2\,\text{K})$.[10]

Comparison of $\tilde{\varepsilon}_s(T)$ and $\tilde{\nu}_{\text{NMR}} = \tilde{m}(T)$ shows that $\tilde{\varepsilon}_s(T)$ can be represented as a quantity proportional to $\tilde{m}^n(T)$. Although the best fit is achieved for $n \approx 4.5$, the curve of $\tilde{\nu}_{\text{NMR}}^4(T)$ is shown for comparison in Fig. 2. We see that this curve is close to that of $\tilde{\varepsilon}_s(T)$ within the error of measurement. We note that $\tilde{H}_{ff}(T) \approx \tilde{m}^2(T)$.[9] A comparison of $\tilde{\varepsilon}_s(T)$ with $\tilde{H}_{ff}(T)$ shows that the relation $\tilde{\varepsilon}_s(T) \approx \tilde{H}_{ff}^2(T)$ is satisfactorily obeyed.

DISCUSSION

Let us first consider the field dependence of the magnetostriction in a style similar to the analysis in Ref. 13. We will then discuss the temperature dependence of the spontaneous magnetostriction.

Restricting discussion to anisotropic magnetoelastic interactions in the easy plane alone, we write the magnetoelastic energy with allowance for the hexagonal symmetry of the $CoCl_2$ crystal in the form[13]

$$E_{ME} = \sum_{\alpha\beta} \gamma_{\alpha\beta}(T)(n_{\alpha x}n_{\beta x} - n_{\alpha y}n_{\beta y})(U_{xx} - U_{yy})$$

$$+ \sum_{\alpha\beta} \lambda_{\alpha\beta}(T)(n_{\alpha x}n_{\beta y} + n_{\beta x}n_{\alpha y})U_{xy}$$

$$+ \sum_{\alpha\beta} \delta_{\alpha\beta}(T)(n_{\alpha x}^2 + n_{\alpha y}^2)(U_{xx} + U_{yy}), \tag{2}$$

where $\alpha, \beta = 1,2$ is the number of the sublattice ($\alpha \geq \beta$); γ, λ, and δ are temperature-dependent parameters of the magnetoelastic interactions, and $n_{\alpha x}$, $n_{\alpha y}$, and $n_{\beta x}$, $n_{\beta y}$ are the direction cosines of the magnetization vectors $\mathbf{M}_\alpha$ and $\mathbf{M}_\beta$. We will consider only two of the possible orientations of the field $\mathbf{H}_\perp$, with the x axis in the direction of $\mathbf{H}_\perp$ or perpendicular to it (the x and y axes lie in the easy plane). The first and second terms in Eq. (2) pertain to the anisotropic magnetoelastic interactions, which depend on the directions of the magnetic moments in the layers. The third term, which is anisotropic with respect to the hard axis, is isotropic within the layer. For $\alpha = \beta$ the parameters γ, λ, and δ specify the intralayer magnetoelasticity, while $\alpha \neq \beta$ refers to the interlayer magnetoelasticity.

The elastic energy for the strains in the plane is

$$E_{el} = \frac{1}{2} C_{11}(U_{xx}^2 + U_{yy}^2) + C_{12}U_{xx}U_{yy} + (C_{11} - C_{12})U_{xy}^2. \tag{3}$$

Minimizing the sum of the magnetoelastic and elastic energies, we determine the strain of the crystal as a function of the orientation of the sublattice magnetizations. We take into account the fact that in the single-domain state with $\mathbf{L} \perp \mathbf{H}_\perp$ the sublattice magnetizations are symmetric about the direction of the magnetic field $\mathbf{H}_\perp$. Therefore, if $\mathbf{H}_\perp$ is directed along the x or y axis, the second term in (2) will be equal to zero. We thus obtain

$$U_{xx} = -\frac{\sum_{\alpha\beta}\gamma_{\alpha\beta}(T)(n_{\alpha x}n_{\beta x} - n_{\alpha y}n_{\beta y})}{C_{11} - C_{12}}$$

$$- \frac{\sum_{\alpha\beta}\delta_{\alpha\beta}(T)(n_{\alpha x}n_{\beta x} + n_{\alpha y}n_{\beta y})}{C_{11} + C_{12}}, \tag{4}$$

$$U_{yy} = -U_{xx} - 2\frac{\sum_{\alpha\beta}\delta_{\alpha\beta}(T)(n_{\alpha x}n_{\beta x} + n_{\alpha y}n_{\beta y})}{C_{11} + C_{12}}.$$

In Eqs. (3) and (4) the dependence of the striction on the temperature is determined by the temperature dependence of $\gamma(T)$ and $\delta(T)$. We shall assume that the rotation of the vectors $\mathbf{M}_1$ and $\mathbf{M}_2$ toward the field $\mathbf{H}_\perp$ occurs without a change in their moduli; the orientation is defined in analogy with Ref. 16:

$$\cos\varphi(H_\perp, T) = \frac{H_\perp}{H_{ff}(T)}, \tag{5}$$

where $\varphi(H_\perp, T)$ is the angle between $\mathbf{H}_\perp$ and the sublattice magnetizations at temperature T. We write an expression for the strain U_{yy} when $\mathbf{H}_\perp$ is oriented along the y or x axis:

$$U_{yy}(H_\perp \| y, x) = A_0 \mp A_{12} + [A_\rho(T) \pm A_{11}(T)]$$

$$\times \left[1 - 2\left(\frac{H_\perp}{H_{ff}}\right)^2 \right], \tag{6}$$

where

$$A_0 = \frac{-2\delta_{11}}{C_{11} + C_{12}}, \quad A_\rho = \frac{\delta_{12}}{C_{11} + C_{12}},$$

$$A_{12} = \frac{\gamma_{12}}{C_{11} - C_{12}}, \quad A_{11}(T) = \frac{2\gamma_{11}(T)}{C_{11} - C_{12}}. \tag{7}$$

In expression (6) the upper sign corresponds to the orientation of $\mathbf{H}_\perp$ along y and the lower sign, along x. The terms appearing in A_{12} and A_{11} describe the anisotropic magnetostriction, which depends on the direction of $\mathbf{H}_\perp$. Its sign changes when the field direction is changed from the x to the y axis.

The contributions to the spontaneous magnetostriction from A_ρ and A_0 are isotropic. In measuring the magnetostriction of a sample containing these strain contributions, the strains are reckoned from the starting value of the strain at $H_\perp = 0$, i.e., these contributions to the strain are included in the initial size of the crystal at the measurement temperature. Therefore, for comparison of (6) with (1) it is necessary to ''shift'' the values of the strain in (6) by the amounts A_ρ and A_0. At the same time, the contribution from A_ρ is determined by the modulus of $\mathbf{L}$ and, hence, by the modulus of $\mathbf{H}_\perp$. Therefore, the field-dependent part of the magnetostriction will have a contribution containing A_ρ. Starting from the data of Ref. 13 on the magnetostriction in $CoCl_2$ in crossed magnetic fields, it was shown that the predominant terms in the field dependence of the magnetostriction of this crystal are those containing A_{11} and A_ρ. Thus, subtracting the isotropic contribution and neglecting the terms containing A_{12}, we can write the expression for the magnetostriction of $CoCl_2$ in the direction along the field $\mathbf{H}_\perp$ in the form

$$\varepsilon(H_\perp, T) = A_{11}(T) - 2[A_{11}(T) + A_\rho(T)]\left(\frac{H_\perp}{H_{ff}}\right)^2 \tag{8}$$

or

$$\varepsilon(H_\perp, T) = A_{11}(T)\left[1 - 2\left(1 + \frac{A_\rho(T)}{A_{11}(T)}\right)\left(\frac{H_\perp}{H_{ff}}\right)^2\right]. \tag{9}$$

For $H_\perp = 0$ we find from (9) that $\varepsilon(H_\perp = 0, T) = A_{11}(T)$. From a comparison of (1) with (9) one can conclude that $A_{11}(T)$ corresponds to the experimental spontaneous magnetostriction $\varepsilon_s(T)$. It can be inferred from Eq. (1) that for $CoCl_2$ the coefficient multiplying the square of the field in (9), containing the ratio $A_\rho(T)/A_{11}(T)$, is independent of temperature. This can be the case if the parameters A_ρ and A_{11} vary with temperature in the same way. We note that A_ρ depends on the intrasublattice contribution to the magnetoelasticity, while A_{11} depends on the intrasublattice contribution. The quantitative contributions to the magnetostriction from these terms are different. By comparing with experiment, we find that $A_{11} > 0$ and that the ratio $A_\rho/A_{11} = -0.2$; i.e., $A_\rho < 0$ and $|A_\rho| < A_{11}$.

In describing the temperature dependence of the spontaneous magnetostriction $\varepsilon_s(T)$ of the single-domain state, we take into account that it is due mainly to the intrasublattice

magnetoelasticity, as can be inferred from a comparison (made at $T = 4.2$ K in Ref. 13) of the magnetostriction in the direction of $\mathbf{H}_\perp$ and perpendicular to it. Here, unlike Eq. (2), we write the magnetoelastic energy as a functional of the direction cosines of the sublattice magnetizations and treat it as an expansion in the sublattice magnetizations, keeping terms up to fourth order:

$$E_{ME} = \sum_\alpha \gamma_{\alpha\alpha}^1 (U_{xx} - U_{yy})(M_{\alpha x}^2 - M_{\alpha y}^2)$$

$$+ \sum_\alpha \gamma_{\alpha\alpha}^{(2)} (U_{xx} - U_{yy})(M_{\alpha x}^4 - M_{\alpha y}^4)$$

$$+ \sum_\alpha \lambda_{\alpha\alpha}^{(1)} U_{xy} M_{\alpha x} M_{\alpha y}$$

$$+ \sum_\alpha \lambda_{\alpha\alpha}^{(2)} U_{xy} M_{\alpha x} M_{\alpha y}(M_{\alpha x}^2 + M_{\alpha y}^2), \tag{10}$$

where, unlike Eq. (2), $\gamma_{\alpha\alpha}^{(1)}$, $\gamma_{\alpha\alpha}^{(2)}$, $\lambda_{\alpha\alpha}^{(1)}$, and $\lambda_{\alpha\alpha}^{(2)}$ are temperature-independent parameters. In Eq. (10) only the anisotropic intraplane interactions are taken into account and are written in the form of a series including the second and fourth powers of the projections of the sublattice magnetizations, in accordance with the symmetry of the crystal. It follows from (10) that the parameters $\gamma_{\alpha\alpha}(T)$ and $\lambda_{\alpha\alpha}(T)$ in (2) can be written in terms of the parameters $\gamma_{\alpha\alpha}^{(1)}$, $\gamma_{\alpha\alpha}^{(2)}$, $\lambda_{\alpha\alpha}^{(1)}$, and $\lambda_{\alpha\alpha}^{(2)}$ used in Eq. (10):

$$\gamma_{\alpha\alpha}(T) = \gamma_{\alpha\alpha}^{(1)} M^2(T) + \gamma_{\alpha\alpha}^{(2)} M^4(T). \tag{11}$$

Analogous relations hold for $\lambda_{\alpha\alpha}$. Thus we obtain an expression for the temperature dependence of the spontaneous magnetostriction of $CoCl_2$, using the fourth and second powers of the sublattice magnetizations:

$$\varepsilon_s(T) = 2 \frac{\gamma_{11}^{(1)} M^2 + \gamma_{11}^{(2)} M^4}{C_{11} - C_{12}}. \tag{12}$$

Taking into account that the temperature dependence of the strain ε_s is close to that of the sublattice magnetizations to the fourth power (Fig. 2), we conclude that the predominant contribution to the magnetoelastic energy (10) is from the term containing the fourth power of the sublattice magnetizations.

In the phenomenological approach leading to expression (10) the question where the parameters $\gamma_{\alpha\alpha}^{(1)}$, $\gamma_{\alpha\alpha}^{(2)}$, $\lambda_{\alpha\alpha}^{(1)}$, and $\lambda_{\alpha\alpha}^{(2)}$ come from remains unanswered. In a conventional analysis of the magnetoelastic interactions the contributions to the magnetoelastic interactions containing the fourth power of the projections of the magnetization in (10) can be calculated under the assumption that the spins in the $CoCl_2$ crystal are coupled by interactions of fourth order in the spin.[9] Such interactions can in principle be present in the anisotropic part of the non-Heisenberg exchange interaction.

The phenomenological representation for the magnetostriction due to this type of interaction should have the form proposed in Ref. 17, which corresponds to Eq. (10). The predominance of the contribution to the magnetostriction from these interactions over those containing the second powers of the sublattice magnetizations is, general speaking, atypical, and it therefore demands additional analysis.

In closing we note that the induced magnetostriction in the $CoCl_2$ crystal upon the flipping of the sublattice spins is proportional to the square of the applied in-plane magnetic field throughout the temperature region in which the antiferromagnetic phase exists. This quadratic dependence in the single-domain region is in good agreement with the conjecture that the collapse of the sublattice magnetizations occurs through their rotation without a change in their magnetic moments. The temperature dependence of the spontaneous anisotropic magnetostriction of the $CoCl_2$ crystal can be explained physically by a predominant magnetoelasticity that is proportional to the fourth power of the sublattice magnetizations.

*E-mail: lozenko@iop.kiev.ua

[1] J. W. Leech and A. J. Manuel, Proc. Phys. Soc. B **59**, 210 (1956).
[2] J. Magarino, J. Tuchendler, A. R. Fert, and J. Gelard, Solid State Commun. **23**, 175 (1977).
[3] I. S. Jacobs, S. Roberts, and S. D. Silverstein, J. Appl. Phys. **39**, 816 (1968).
[4] S. A. Al'tshuler and B. M. Kozyrev, *Electron Paramagnetic Resonance* [in Russian], Nauka, Moscow (1972).
[5] K. R. A. Ziebeck, C. Escribe, J. P. Redoules, and J. Gelard, Solid State Commun. **23**, 857 (1977).
[6] M. E. Lines, Phys. Rev. **131**, 546 (1963).
[7] A. Yoshimori, Phys. Rev. **130**, 1312 (1963).
[8] I. S. Jacobs, S. Roberts, and P. S. Lawrence, J. Appl. Phys. **36**, 1197 (1965).
[9] A. F. Lozenko and S. M. Ryabchenko, Zh. Éksp. Teor. Fiz. **65**, 1085 (1973) [Sov. Phys. JETP **38**, 538 (1974)].
[10] F. V. Bragin and S. M. Ryabchenko, Fiz. Tverd. Tela (Leningrad) **15**, 1050 (1973) [Sov. Phys. Solid State **15**, 721 (1973)].
[11] H. Wilkinson, J. W. Cable, E. O. Wollan, and W. C. Koehler, Phys. Rev. **113**, 497 (1959).
[12] A. F. Lozenko, P. E. Parkhomchuk, S. M. Ryabchenko, and P. A. Trotsenko, Fiz. Nizk. Temp. **14**, 941 (1988) [Sov. J. Low Temp. Phys. **14**, 517 (1988)].
[13] V. M. Kalita, A. F. Lozenko, S. M. Ryabchenko, and P. A. Trotsenko, Ukr. Fiz. Zh. (Russ. Ed.) **43**, 1469 (1998).
[14] E. V. Gomonaj and V. M. Loktev, Fiz. Nizk. Temp. **25**, 699 (1999) [Low Temp. Phys. **25**, 520 (1999)].
[15] Z. A. Kazeï, M. V. Levanidov, and V. I. Sokolov, Prib. Tekh. Éksper. No. 2, 196 (1981).
[16] L. Néel, Izv. Akad. Nauk SSSR, Ser. Fiz. **21**, 890 (1957).
[17] E. A. Turov, *Physical Properties of Magnetically Ordered Crystals* [in Russian], Izd. Akad. Nauk SSSR, Moscow (1963).

Translated by Steve Torstveit

ELECTRONIC PROPERTIES OF METALS AND ALLOYS

Cyclotron resonance in organic metals

V. G. Peschansky* and J. C. Medina Pantoja

V. N. Karazin Kharkov National University, pl. Svobody 4, 61077 Kharkov, Ukraine
(Submitted February 3, 2000)
Fiz. Nizk. Temp. **26**, 678–680 (July 2000)

The velocity distribution of the charge carriers at the Fermi surface in layered organic conductors can be found from an experimental investigation of the cyclotron resonance in a magnetic field parallel to the layers. © *2000 American Institute of Physics.* [S1063-777X(00)00807-0]

The quasi-two-dimensional character of the electron energy spectrum of layered conductors of organic origin leads to a number of specific effects that are absent in ordinary metals or that exhibit extremely peculiar behavior (see, e.g., the reviews[1,2] and the references cited therein). A large fraction of organic layered conductors at sufficiently low temperatures T_c of the order of 10 K and below undergo a transition to a superconducting state, and in the normal (nonsuperconducting) state they have a metallic type of conduction with a sharply anisotropic conductivity. For this reason they are called organic metals, and at temperatures below T_c, organic superconductors.

Magnetoresistance measurements in high magnetic fields have been widely used to study the electron energy spectrum of layered organic conductors, and in recent years high-frequency effects have also been used.

The resonance interaction of charge carriers with an electromagnetic wave propagating perpendicular to the layers has been detected in certain tetrathiafulvalene (TTF) salts[3–5] in magnetic fields **H** that were sufficiently high that the gyration frequency of the conduction electrons $\Omega = eH/m^*c$ is larger than their collision frequency $1/\tau$ and comparable to the frequency ω of the electromagnetic wave. The cyclotron effective mass m^* of the charge carriers in a magnetic field parallel to the normal **n** to the layers in the conductor $(BEDT–TTF)_2KHg(SCN)_4$, is approximately three times as large as the mass m_0 of a free electron,[3,4] while in the compound $(BEDO–TTF)_2ReO_4(H_2O)$ it is almost the same as m_0.[5] As the angle θ between the vectors **H** and **n** increases, the cyclotron effective mass increases in inverse proportion to $\cos\theta$, which again confirms the validity of the proposed shape of the Fermi surface $\varepsilon(\mathbf{p}) = \varepsilon_F$ as a slightly corrugated cylinder.

The values found in Refs. 3–5 for the effective masses of the charge carriers are significantly different from the effective cyclotron masses determined from the temperature dependence of the amplitude of the Subnikov–de Haas oscillations of the magnetoresistance (in the charge-transfer complex $(BEDO–TTF)_2ReO_4(H_2O)$ the values of the cyclotron effective masses differs by a factor of 2.5–3). This circumstance has motivated us to analyze the cause of such a sharp disparity in the cyclotron effective masses, which casts doubt upon the applicability of one of the aforementioned

spectroscopic methods for studying the electron energy spectrum in organic conductors.

Cyclotron resonance in metals in a magnetic field parallel to the surface of the sample has proved to be a highly sensitive method of studying the extremal values of the cyclotron effective masses[6] and the extremal diameters of the Fermi surface.[7] The authors of Refs. 3–5 had a preference for studying the resonance absorption in the quasi-two-dimensional conductors mentioned above in the case when the Poynting vector and magnetic field are orthogonal to the surface of the sample. Under such conditions, because of the drift of charge carriers into the interior of the sample, a shift of the resonance frequencies occurs, and the error of determination of the cyclotron effective masses from the position of the resonance line is increased.

Let us consider the resonance absorption of the energy of electromagnetic waves propagating along the normal to the layers (the z axis) in a layered conductor with an arbitrary dispersion relation of the charge carriers:

$$\varepsilon(\mathbf{p}) = \sum_{n=0}^{\infty} \varepsilon_n(p_x, p_y)\cos\{anp_z/\hbar\};$$

$$\varepsilon_n(p_x, p_y) = \varepsilon_n(-p_x, -p_y). \tag{1}$$

The coefficients multiplying the cosines in Eq. (1), as a rule, fall off rapidly with increasing number n, and the maximum value of the function $\varepsilon_1(p_x, p_y)$ at the Fermi surface is $\eta\varepsilon_F \ll \varepsilon_F$, where η is the quasi-two-dimensionality parameter of the electron energy spectrum, so that the velocity of the charge carriers along the normal to the layers,

$$v_z = -\sum_{n=1}^{\infty} (an/\hbar)\varepsilon_n(p_x, p_y)\sin\{anp_z/\hbar\} \tag{2}$$

is much lower than the velocity along the layers. Here a is the distance between layers, and $\hbar$ is Planck's constant.

In a magnetic field $\mathbf{H} = (0, H\sin\theta, H\cos\theta)$ inclined to the surface of the sample $z_s = 0$, the charge carriers drift slowly into the interior of the conductor with a velocity $\bar{v}_z = \eta v_F\cos\theta$, where v_F is the characteristic Fermi velocity of the charge carriers along the layers. As θ increases, the drift of conductor electrons along the normal to the layers decreases, but for θ close to $\pi/2$ the orbits of the charge carri-

ers are highly elongated, and the condition $\Omega\tau\geqslant 1$ does not hold, so that the resonance curves become highly smeared.

For $\theta=\pi/2$ the charge carriers with energy ε_F move with an almost constant velocity v_x along open periodic orbits in momentum space (for momentum $p_H=\mathbf{p}\cdot\mathbf{H}/H$) with a comparatively short period:

$$T=\frac{c}{eH}\int_0^{2\pi h/a}\frac{dp_z}{v_x}.\tag{3}$$

In that case the motion of the charge carriers, which can drift only in the plane of the layers, completes many periods in the course of the mean free time τ, so that the displacement along the z axis is by a quantity only of the order of ηr_0, where $r_0=ch/eHa$, e is the electron charge, and c is the speed of light in vacuum. In this case the velocity distribution of the charge carriers in a plane orthogonal to the axis of the corrugated cylinder, i.e., the distribution of the velocities of the Fermi conduction electrons in the plane of the layers, can be found to a sufficient degree of accuracy from the cyclotron resonance condition $\omega T=2\pi$.

If $\eta\ll l/\delta$, where $l=v_F\tau$ and δ is the skin depth, in solving the electrodynamic problem one can use the approximation of a local coupling of the Fourier transform of the electrical current density and the alternating electric field.

In this approximation the roots of the dispersion relation

$$\det\left\{(k^2-\omega^2/c^2)\delta_{\alpha\beta}-\frac{4\pi i\omega}{c^2}\sigma_{\alpha\beta}(k)\right\}=0\tag{4}$$

determine to sufficient accuracy the damping length of the electromagnetic field and the surface impedance of the layered conductor.

The high-frequency conductivity tensor

$$\sigma_{\alpha\beta}(k)=\frac{2e^3H}{c(2\pi\hbar)^3}\int dp_H\int_0^T dt v_\alpha(t,p_H)$$

$$\times\int_{-\infty}^t dt' v_\beta(t',p_H)$$

$$\times\exp\{(1/\tau-i\omega)(t'-t)\}$$

$$\times\cos k\{z(t',p_H)-z(t,p_H)\}\tag{5}$$

in a magnetic field sufficiently strong that $kr_0\eta\ll 1$ takes the form

$$\sigma_{\alpha\beta}(k)=\frac{2e^2}{(2\pi\hbar)^3}\int dp_H\frac{2\pi m^* v_\alpha^{-n} v_\beta^n}{1/\tau+i(k\bar{v}_z+n\Omega-\omega)},\tag{6}$$

where

$$v_\alpha^n(p_H)=\frac{1}{T}\int_0^T dt v_\alpha(t,p_H)\exp\{-in\Omega t\},$$

and $T=2\pi/\Omega$ is the period of the motion of the conduction electrons along an orbit $\varepsilon=\varepsilon_F$, $p_H=\mathrm{const}$.

The roots $k=k_1+ik_2$ of the dispersion relation (4) are complex, so that along with a shift of the resonance frequency the drift of the charge carriers along the z axis also leads to additional broadening of the resonance line. As a result, instead of two cyclotron resonance lines, in magnetic fields satisfying the condition

$$H_n^\pm=(\omega\pm v_z^{\max}k_1)mc/en,\tag{7}$$

it is possible to observe only a "smeared" doublet on account of the broadening of the resonance lines due to the Doppler effect, so that one is able to determine the extremal values of the cyclotron effective masses of the conduction electrons m_{extr}^* from the position of the resonance lines at $\omega=n\Omega_{\mathrm{extr}}$ only with a relative error of the order of $\eta k_2 r_0\cos\theta$.

It is apparently this circumstance that is responsible for the significant disparity of the cyclotron effective masses of the charge carriers as determined from the study of the temperature dependence of the amplitude of the Shubnikov–de Haas oscillations and the cyclotron resonance in a magnetic field orthogonal to the layers.[3–5]

For $\theta=0$ and an isotropic energy spectrum in the $p_x p_y$ plane, the Fourier transforms of the velocity v_α^n are nonzero only for $n=\pm 1$, and resonance occurs only when the frequencies ω and Ω_{extr} coincide. If even one of these conditions is not met, i.e., if either the angle θ is nonzero or the velocities of the Fermi electrons are anisotropic in the plane of the layers, then the cyclotron resonance can occur at multiples of the frequency.

As the angle θ increases, the resonance lines narrow, and at $\theta=\pi/2$ the width of the cyclotron resonance lines is determined solely by the mean free time of the charge carriers taking part in the formation of the resonance. Here the relationship between the values of l and δ/η does not play an important role, since drift of the charge carriers into the interior of the sample does not occur in this case.

The period of the motion of the charge carriers along an open trajectory takes its minimum value at the central cross section of the Fermi surface, $p_H=0$, and under the condition

$$\omega T_{\min}=2\pi n,\quad n=1,2,3,...\tag{8}$$

the interaction of the charge carriers with the electromagnetic wave has a resonant character.

The growth of $T(p_H)$ with increasing p_H takes place on a self-intersecting orbit $p_H=p_c$, where the period T goes to infinity. In the case of a rather complex energy spectrum of the charge carriers along the path between $p_H=0$ and $p_H=p_c$, additional extremal values of $T(p_H)$ can arise, and, hence, additional resonance frequencies. However, the cyclotron resonance at frequencies satisfying the condition $\omega T(0)=2\pi n$ will always take place for any form of the electron energy spectrum.

Under conditions of the anomalous skin effect, when $\eta r_0\geqslant\delta$, the resonance condition (8) remains unchanged, and the cyclotron resonance at multiples of the frequency is most clearly manifested under the condition

$$\delta/\eta\ll r_0\ll l.\tag{9}$$

By studying the cyclotron resonance experimentally for different orientations of the magnetic field in the plane of the layers, one can determine the distribution of the average values of the carrier velocities $\bar{u}=2\pi r_0/T(0)$ in the xy plane, and ultimately find the velocity distribution over the entire Fermi surface with an accuracy up to the value of ηv_F.

*E-mail: vpeschansky@ilt.kharkov.ua

[1] V. G. Peschansky, Phys. Rep. **288**, 305 (1997).
[2] O. V. Kirichenko and V. G. Peschansky, Fiz. Nizk. Temp. **25**, 1119 (1999) [Low Temp. Phys. **25**, 837 (1999)].
[3] S. V. Demishev, N. E. Sluchanko, A. V. Semeno, and N. A. Samarin, JETP Lett. **61**, 313 (1995).
[4] S. V. Demishev, A. V. Semeno, N. E. Sluchanko, N. A. Samarin, I. B. Voskoboinikov, V. V. Glushkov, J. Singelton, S. J. Blundell, S. O. Hill, W. Hayer, M. V. Kartsovnik, A. E. Kovalev, M. Kurmoo, P. Day, and N. D. Kushch, Phys. Rev. B **53**, 12794 (1996).
[5] S. V. Demishev, A. V. Semeno, N. E. Sluchanko, N. A. Samarin, I. B. Voskoboǐnikov, M. V. Kartsovnik, A. E. Kovalev, and N. D. Kushch, Zh. Éksp. Teor. Fiz. **111**, 979 (1997) [JETP **84**, 540 (1997)].
[6] M. Ya. Azbel' and É. A. Kaner, Zh. Éksp. Teor. Fiz. **32**, 896 (1957) [Sov. Phys. JETP **5**, 730 (1957)].
[7] M. Ya. Azbel' and V. G. Peschanskiǐ, JETP Lett. **5**, 19 (1967).

Translated by Steve Torstveit

Point-contact-spectroscopy investigation of the Kondo size effect in CuCr and AuFe alloys

V. V. Fisun* and I. K. Yanson

B. Verkin Institute for Low Temperature Physics and Engineering, National Academy of Sciences of Ukraine 47, Lenin Ave., 61164, Kharkov, Ukraine

J. A. Mydosh and J. M. van Ruitenbeek

Kamerlingh Onnes Laboratorium, Leiden University, PO Box 9504, NL-2300 RA Leiden, The Netherlands

Size effects in Kondo scattering are studied on CuCr and AuFe alloys ($T_K = 2$ K and 0.2 K, respectively) by applying point-contact spectroscopy in break-junction type contacts. It is shown that as the contact diameter is decreased under the condition of ballistic electron transport, the size effect enhances the interaction of the conduction electrons with the Kondo impurity (as compared to the phonons) and increases the Kondo temperature in the contact region. In an external magnetic field the size effect decreases the negative magnetoresistance in CuCr and suppresses the Kondo peak splitting in AuFe. © *2000 American Institute of Physics.* [S1063-777X(00)00907-5]

INTRODUCTION

Point-contact (PC) spectroscopy measurements of Kondo alloys performed on pressed contacts[1] have revealed that the interaction between conduction electrons and magnetic impurities shows itself in the PC spectra as a peak at zero bias in the first derivative of the voltage–current ($V–I$) curve $dV/dI(V)$. The energy region of the Kondo peak manifestation is bounded from above by the energy of phonon features of the noble metals in which these impurities are dissolved and lies in the range between 0 and approximately 10 mV. The Kondo peak intensity is sensitive both to the chemical species of the magnetic impurity that defines the Kondo temperature and to its concentration (at. %) in a given alloy. For example, the PC spectra for CuFe (0.1 at. %) display a Kondo peak of high intensity with a pronounced smearing of the phonon characteristics, as opposed to the well-defined spectra of CuMn for the same concentration. A similar smearing of the phonon characteristics and an increase in the Kondo peak are observed with increasing impurity concentration in CuMn alloys as well.

The increase in the differential resistance in the vicinity of the Kondo peak follows approximately the logarithmic relation $dV/dI(V) \propto -\ln(V)$, also typical of the increase in the resistance of these alloys at low temperatures.

More recently, CuMn Kondo alloys with different magnetic impurity contents were studied using break-junction contacts.[2] It was found that a decrease in the point contact diameter resulted in an enhancement of the interaction between conduction electrons and Kondo impurities as compared to the electron–phonon interaction (EPI) and in a considerable increase of the apparent Kondo temperature in the point contact area. Moreover, the decrease in the contact diameter resulted in a disappearance of the Kondo peak splitting induced by an external magnetic field (see Fig. 7 in Ref. 2 (b)).

An explanation for the observed Kondo size effect was presented in a theoretical investigation of such systems[3] and may be induced by the fluctuation of a local electron density of states at the Fermi energy in a bridge-like point contact linking massive electrodes.

Size effects were also studied in measurements of the resistance of CuCr films as a function of their width at low temperatures, the film thickness remaining unchanged.[4] It was found that the Kondo resistance anomaly was suppressed in a film of width smaller then 10 μm. This length scale is consistent with an heuristic estimate of the radius of the spin–electron correlation. Note that the sign of the size effect observed is opposite to that in PC measurements.

Investigations into size dependences of the resistivity and thermopower[5] performed on mesoscopic AuFe films and wires demonstrate that for thickness smaller than 300 nm the Kondo contribution of $\Delta\rho$ and $\delta S(T)$ is also suppressed, i.e., the sign of the size effect is same as in the above-studied film. In addition, at high impurity concentrations spin-glass ordering destroys the size effect.

Resistive measurements of Kondo AuFe wires versus their widths were made in Ref. 6. The Kondo resistance was found to be independent of reduction in wire width down to a wire thickness less than 38 nm, much less than the Kondo correlation length $\xi_K = \hbar v_F / k_B T_K \approx 38 \ \mu$m.

EXPERIMENTAL

In this paper we present PC spectroscopy data on the Kondo size effect in CuCr (0.1 at. %) and AuFe (0.1 at. %) alloys, with Kondo temperatures of 2 and 0.2 K, respectively. Junctions that satisfy conditions for ballistic electron transport, where the junction diameter d is much smaller than the elastic and inelastic mean free paths l_e and l_i (ballistic regime), were formed between massive electrodes by the break-junction technique.[7] This makes it possible to study

the interaction of the conduction electrons in the contact area with phonons and magnetic impurities on the same constrictions of different diameters.

The Kondo alloys were prepared at the Kamerling Onnes laboratory. A massive sample was used to prepare a wire 0.2 mm thick. The use of a sample in the form of a small diameter wire permits notching by using a sharp knife at the site where we want it to break. This notch is produced at the middle of a 10-mm-long wire section and reduces its diameter severalfold. The sample with the notch was etched in a mixture of acids (1/3 acetic, 1/3 orthophosphoric, and 1/3 nitric acid for CuCr and aqua regia for AuFe) and annealed in high vacuum at $T = 600 °C$ for 2.5 hours followed by natural cooling down. The sample was fixed on a substrate of beryllium bronze coated with a kapton film, using Staycast epoxy. An important factor for PC resistance stability is that the glue droplets be placed as close as possible to the notch. The notch should be made at the middle of the substrate, which is 15 mm long in our measurements. The substrate with the glued sample is placed in a bending beam that permits the middle part of the substrate to be pressed from the side opposite to that carrying the sample, with the substrate edges remaining fixed. The bending is controlled from outside the cryostat. The substrate deflection results in a smooth extension of the sample at the site of the notch and hence in a decrease of its diameter to the required values. Four wires connect the sample with a measuring circuit. A temperature of 1.6 K is achieved in a liquid helium cryostat that contains a superconducting solenoid.

The first $dV/dI(V)$ and the second $d^2V/dI^2(V)$ derivatives of the current–voltage curves were measured by a standard modulation technique with the use of lock-in amplifiers. The Kondo peak was measured by using a bridge circuit to produce higher spectral resolution for lower modulation.

RESULTS

Typical spectra of the first $dV/dI(V)$ and the second $d^2V/dI^2(V)$ derivatives of the $V–I$ curves for CuCr (0.1 at. %) point contacts are shown in Fig. 1. The inset illustrates the Kondo peak in zero magnetic field on an expanded scale. This peak in the PC spectrum of copper is accounted for by conduction electron scattering off the Kondo impurities of Cr in the vicinity of the point contact and is characterized by an increase of the differential resistance by the logarithmic law $dV/dI(V) \propto -\ln(V)$ at voltage biases lower than for the phonons for Cu. The variations in the differential resistance due to the interaction between conduction electrons and the phonons, δR_{ph}, and the Kondo impurities, δR_K, are denoted by arrows. For the AuFe alloy, one can observe a similar phonon spectrum of Au, while there is a Kondo peak of lower intensity in a lower bias range than for the phonons (not shown). The lower intensity of the Kondo peak compared to that in CuCr is due to the fact that the Kondo temperature in AuFe is one order of magnitude lower than in CuCr.

It is known[8] that Kondo impurities such as Cr and Fe in copper form clusters at low concentrations, unlike the Mn impurity. Therefore, a portion of the samples (we measured more than 10 samples of CuCr alloy) exhibited a lower Kondo peak intensity for high diameters than those selected
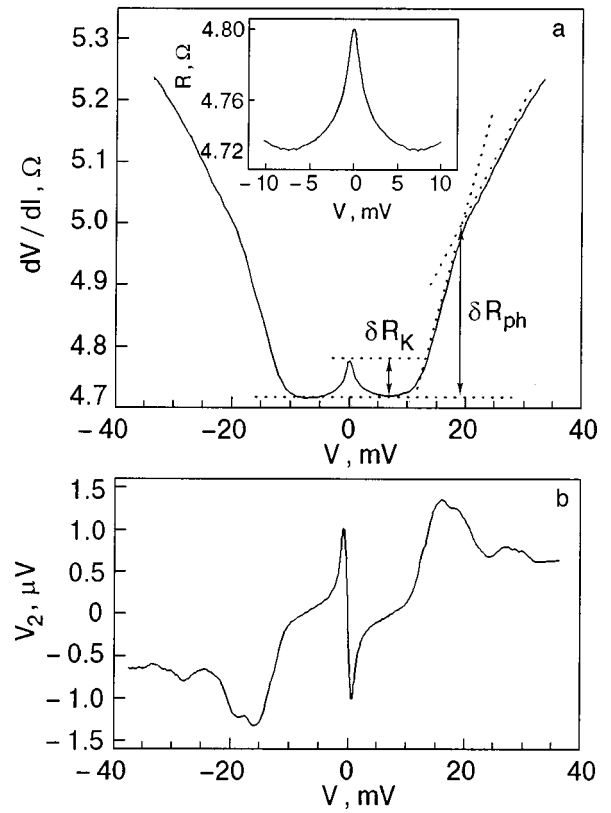

FIG. 1. Point contact spectrum for Kondo alloys of CuCr (0.1 at. %). The first $V–I$ derivative $R = dV/dI$, where the arrows indicate the contribution to the differential resistance due to the interaction of conduction electrons with phonons, δR_{ph}, and Kondo impurities, δR_K. Inset: the Kondo peak in zero magnetic field on an expanded scale (a). The second $V–I$ derivative (b). The rms modulation voltage V_1 equals 585 μV. The rms second harmonic signal V_2 is connected with the second derivative via the equation $(1/R)(dR/dV) = 2^{3/2}(V_2/V_1^2)$. $T = 1.6$ K, $H = 0$.

by us for detailed measurements. It should be emphasized that we studied all of the point contacts, even those whose lower peak intensities were indicative of clustering, and all of the samples display the size effect described below.

For pure metals, in the ballistic limit $dR/dV(V)$ is directly proportional to the electron-phonon interaction (EPI) function g_{PC} (Ref. 9)

$$\frac{1}{R}\frac{dR}{dV}(V) = \frac{8}{3}\frac{ed}{\hbar v_F} g_{PC}(eV). \tag{1}$$

The Sharvin resistance R_0 for zero bias is related to the Cu point contact diameter through the equation:[10]

$$d \approx \frac{30}{\sqrt{R[\Omega]}}[\text{nm}]. \tag{2}$$

This equation is valid for contacts in the shape of a clean orifice. For Au point contacts the diameter was estimated by this equation with a nominator of 28.

The essential parameter characterizing the PC spectrum is the maximum value of the EPI signal that determines the ballistic regime of electron transport through the point contact. The maximum value of the EPI signal for the point contacts was estimated by the relation which follows from (1) and (2):[9]
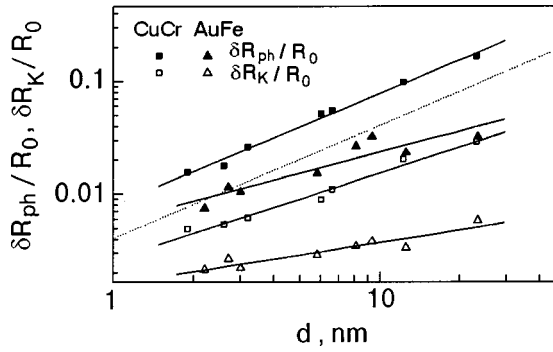
FIG. 2. Point-contact-diameter dependence of the relative variation of the differential resistance due to the conduction electron interaction with phonons and Kondo impurities for CuCr and AuFe. (The dashed line represents Eq. (3)). Note the difference of slopes between the linear fits to the phonon and Kondo-impurity interactions shown as straight lines.
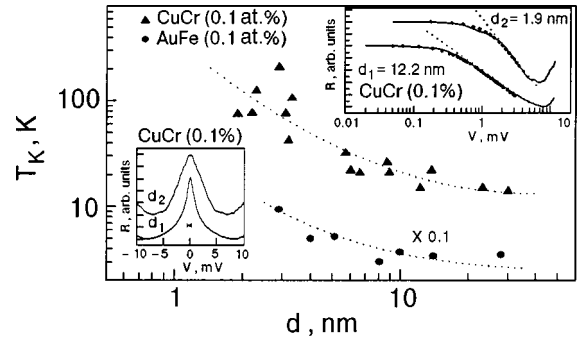

FIG. 3. Dependence of the Kondo temperature on the point contact diameter for CuCr and AuFe according to Eq. (4). Bottom inset: broadening of the Kondo peak (CuCr) with decreasing contact diameter; the spectral resolution is shown as a horizontal bar; top inset: the Kondo peak of the same alloy with a logarithmic voltage scale (d_1, d_2 are the diameters in both insets). For clarity, the points for the AuFe alloy are presented a decade below.

$$g_{PC}(eV) = \left(\frac{12.9}{\sqrt{R_0}} \right) \frac{dR}{dV},$$

where the resistances R_0 and R are expressed in ohms and the voltage V in millivolts.

The estimate $g_{PC}^{max} = 0.24$ for CuCr is in good agreement with the value for point contacts of pure copper in the clean orifice model. The value of maximum EPI intensity for the AuFe point contacts, $g_{PC}^{max} = 0.1$, is also consistent with that for pure Au.[9] Thus we are measuring point contacts with electron transport close to the ballistic regime.

Contact-size dependence of phonon and Kondo scatterings

A qualitative estimate of the electron–phonon interaction was made by determining the increase in the differential resistance from the minimum of the differential resistance for a given contact up to the resistance for a bias of about 20 mV at the intersection of the interpolation straight lines (δR_{ph}) (Fig. 1). The estimate was performed with the assumption that the PC spectra of pure Cu exhibit no zero-bias anomalies. The interaction with the Kondo impurities was estimated by the peak amplitude for zero bias (δR_K). The values of (δR_{ph}) and (δR_K) for the AuFe alloy were determined in a similar way.

The relative differential resistance $\delta R_{ph}/R_0$ and $\delta R_K/R_0$ versus the point contact diameter are shown in Fig. 2. R_0 is measured directly. The diameter is estimated from Eq. (2). The dashed line in the figure illustrates the diameter dependence of relative differential resistance associated with $\delta R_{ph}/R_0$ for the clean orifice model:[9]

$$\left(\frac{\delta R_{ph}}{R_0} \right)_{V=20mV} = \frac{8}{3} \frac{ed}{\hbar v_F} \int_0^{20mV} g_{PC}(\omega) d\omega$$

$$= 4.05 \times 10^{-3} d[nm]. \qquad (3)$$

The discrepancy between the experimental PC diameter dependence of the EPI and the model dependence is accounted for by the difference in PC area geometry. We propose that this discrepancy is due to the fact that the production of the point contact by the break-junction technique involves a contact elongation accompanying a diameter reduction. Hence, it is necessary to introduce a parameter L

that characterizes the PC length in Eq. (1), giving a linear interpolation between the theoretical limits for a clean orifice and a channel:[11]

$$\frac{1}{R} \frac{dR}{dV}(V) = \frac{8}{3} \frac{e(d + 3\pi L/4)}{\hbar v_F} g_{PC}(eV), \quad T \approx 0.$$

Here fluctuations of the local density of electron states at the Fermi energy in a channel-type point contact[3] result in an enhancement of electron scattering by Kondo impurities with decreasing PC diameter. Linear fitting of the experimental PC diameter dependence of the EPI in logarithmic coordinates gives a slope of 0.98 ± 0.04. For CuCr the experimental curve thus obtained lies slightly above the same dependence for the orifice-type PC. Linear fitting of the points determining the electron scattering by the Kondo impurities gives a slope of 0.77 ± 0.04. The difference in the slopes of the Kondo scattering and the EPI implies an enhancement of the electron scattering by the Kondo impurities with decreasing PC diameter. As to the AuFe alloy, the experimental points of the EPI do not lie above the theoretical dependence. We consider this to be due to the fact that the impurity concentration for this alloy is at the boundary of changing over to a spin glass lying between the diffusive and ballistic regimes. The slopes of the EPI and the Kondo interaction linear fittings for AuFe are 0.62 ± 0.10 and 0.37 ± 0.05, respectively, also indicating the enhanced size effect.

Energy dependence of Kondo scattering

The next parameter directly related to a size effect in the Kondo temperature is the energy broadening of the zero-bias peak. In Fig. 3 (the lower inset) the dependence of the Kondo peak differential resistance is shown for two diameters. It is clearly seen that a decrease in the PC diameter (the diameters for the curves d_1 and d_2 are 12.2 nm and 1.9 nm, respectively) causes the Kondo peak to become broader. We estimated the spectral broadening of the Kondo peak due to the experimental temperature and the modulation signal amplitude by the equation[12]

$$\delta(eV) \approx \sqrt{(3.53 k_B T)^2 + (1.73 e V_{1,0})^2},$$

where $V_{1,0}$ is the amplitude of the modulation voltage across the point contact at zero bias. The calculated value of the

spectral broadening, $\delta V \approx 0.86$ mV (indicated by the horizontal bar in the lower inset of Fig. 3), suggests that it does not result in significant instrumental broadening (though for the larger diameters the width of Kondo peak may suffer from experimental broadening). Note that the energy broadening of the Kondo peak is sensitive to the ballistic conditions of electron transport. The condition of ballistic electron transport $d \lesssim l_i, l_e$ depends on both the point contact preparation technology and contact area strain. The latter is due to multiple fracture and bringing the contact together repeatedly. The nature of the chemical element and concentration of magnetic impurities also have an effect.

Thus the peak broadening clearly observed with decreasing contact diameter is not related to the temperature and modulation smearing and is one more manifestation of a size effect. The upper inset in Fig. 3 illustrates the voltage characteristics of the same Kondo peaks on a semilogarithmic scale. It is evident that the energy broadening of the Kondo peak results in an increase in the slope of the logarithmic portion (the dashed line) which is in direct relation to the Kondo temperature. We believe now that the equations used in Ref. 2 to calculate the Kondo temperature give a poor method of estimating it correctly from the PC characteristics. Their application for contacts of large diameter gave a Kondo temperature value different from that in bulk materials. Moreover, the Kondo temperature increases by several orders of magnitude as the contact diameter is reduced. Here we use instead, following Refs. 13, the empirical relation between the Kondo impurity resistivity in bulk alloys as a function of temperature:[14]

$$\rho_m = A - B \ln[1 + (T/\theta)^2]; \qquad (4)$$

here $\ln(\theta/T_K) = -\pi[S(S+1)]^{1/2}$, where S is the impurity spin, which we take equal to 1/2 for both Cr and Fe.

To compare the temperature dependence of the resistance in a bulk sample with the dependence of the Kondo scattering upon the applied voltage in a point contact, we translate the energy scales using the relation $V[\text{mV}] = 0.31 T[\text{K}]$ (Ref. 15). The Kondo temperature is estimated from fitting of the experimental dependence of the normalized Kondo peak by this formula, Eq. (4) (Fig. 3, upper inset). The dependence of the Kondo temperature obtained in this way upon the point contact diameter is shown in the Fig. 3. It is seen that for both alloys the Kondo temperature is considerably higher when the contact diameter is smaller. For large diameter contacts the Kondo temperature saturates at a value exceeding the corresponding bulk value. This discrepancy may arise because the empirical formula cannot properly treat the character of the Kondo scattering in ballistic point contacts, while it is fairly adequate for resistive measurement in bulk. Besides, the AuFe (0.1%) alloy is in the spin-glass state at $T = 1.6$ K, which leads to an apparent increase of T_K determined by formula (4). Another reason for the different Kondo temperatures of a bulk sample and a larger-diameter point contact may be a deviation from a ballistic character of the electron transit through large diameters.

The enhanced intensity of the Kondo peak in the experiment may be attributed to the systematically increasing concentration of magnetic impurities in the point contact region,
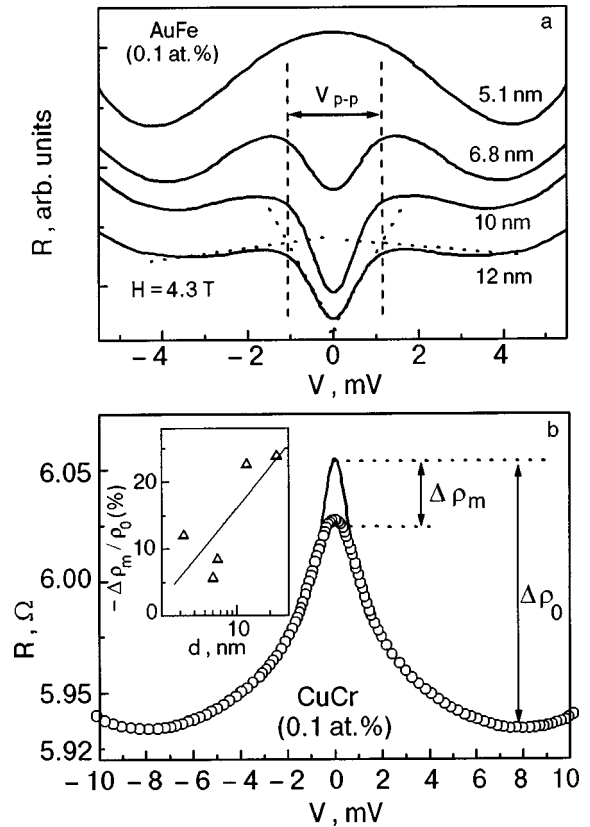

FIG. 4. Effect of an external magnetic field on the Kondo peak: An external field of 4.3 T splits the Kondo peak in AuFe alloys. The size effect results in suppression of splitting (curve with $d = 5.1$ nm) (a); the Kondo peak in zero field (line) and at 4.3 T (circles) for CuCr alloys (the arrow shows the magnetoresistance) (b). Inset: the negative magnetoresistance at a field of 4.3 T as a function of the point contact diameter.

for example, due to mechanical deformation causing displacement of the impurities. Indeed, the higher the Kondo impurity concentration, the higher is the peak.[1] We might then expect that this uncontrollable growth of the Kondo-impurity content would lead, at certain concentration and quite low temperatures, to the formation of a spin-glass state, i.e., the splitting of the peak in the frozen internal magnetic field. In reality, however, when the contact diameter is decreased, the peak splitting in external or internal magnetic fields (due to spin-glass ordering at high nominal concentrations) is always suppressed.

Size-effect of Kondo scattering in an external magnetic field

The dependence of the magnetoresistance upon the point contact diameter is the third parameter manifesting the Kondo size effect in point contacts. In an external magnetic field the negative magnetoresistance is caused by the Zeeman effect,[16] which restrains the spin degrees of freedom of the magnetic impurity and thus suppresses the Kondo effect. In our study the Kondo temperatures of the bulk CuCr and AuFe alloys are 2 K and 0.2 K, respectively. They are within the interval where our maximal external magnetic field of 4.3 T at $T = 1.6$ K is unable to split the Kondo peak in CuCr but it can do this in AuFe. The size dependences $dV/dI(V)$ of the AuFe Kondo peak split in the field 4.3 T at $T = 1.6$ K are shown in Fig. 4a. This splitting is clearly seen for large-diameter contacts (Fig. 4a, curves for $d = 12$ and 10 nm),

where it is not influenced by the size effect. When the point contact diameter is decreased (curves for $d=6.8$ and 5.1 nm), the splitting of the Kondo peak is suppressed, though the position V_{p-p} remains the same. The size effect enhances the interaction between the conduction electrons and the magnetic impurities. For small sizes it leads to the fact that the Zeeman energy $E=g\mu HS_z$ in a field 4.3 T is unable to fix the magnetic impurity spins with the field, i.e., to restrict their degree of freedom and to exclude them from the Kondo interaction.

For the CuCr alloy the Kondo temperature $T_K=2$ K and an external magnetic field 4.3 T is insufficient to split the peak. A similar result was obtained for CuFe in a magnetic field of 12 T at $T=0.5$ K.[14] The dependence $dV/dI(V)$ of the Kondo peak in zero field and 4.3 T are shown in Fig. 4b. The weaker intensity of the Kondo peak in the external magnetic field results from the negative magnetoresistance in these alloys due to the Zeeman energy (the magnetoresistance was taken as the differential resistance intensity of the Kondo peak at $V=0$). As follows from Fig. 3 of Ref. 17, the relative magnetoresistance $(-\Delta\rho_M/\rho_0)$ is directly proportional to the applied magnetic field and inversely proportional to temperature and to the Kondo temperature. In our experiments the negative magnetoresistance decreases due to a decrease in the point contact diameter, with the external magnetic field and the temperature fixed. Hence, the change in magnetoresistance results from the rise of the Kondo temperature when the point contact diameter becomes smaller. The variation of the relative magnetoresistance $(-\Delta\rho_M/\rho_0)$ as a function at the point contact diameter is shown in Fig. 4b (inset). It is seen that a decrease in the point contact diameter entails a considerable drop of the relative magnetoresistance. In our range of diameters the value of the drop coincides well with the increase in T_K in the same diameter range (Fig. 3, CuCr). The size effect thus enhances the interaction between the conduction electrons and the Kondo impurities and leads to a drop of the negative magnetoresistance.

CONCLUSIONS

In summary we can infer the following conclusions.

The point-contact-spectroscopic studies of the Kondo size effect on the alloys CuCr(0.1 at. %) and AuFe(0.1 at. %) using the break-junction technique permit us to investigate the interaction of the conduction electrons with phonons and the Kondo impurity on the same contact of variable diameter. These studies have shown that:

— the interaction of conduction electrons with the Kondo impurities increases, relative to the EPI, with decreasing point contact diameter, similar to our earlier results on CuMn[2] and CuFe[13] alloys;

— a decrease in the point contact diameter leads to a rise of the Kondo temperature, which results in energy broadening of the peak;

— in the external magnetic field, a decrease in the point contact diameter causes a considerable drop of the negative magnetoresistance in the CuCr(0.1 at. %) alloy and suppresses the Kondo peak splitting in AuFe(0.1 at. %);

— in the CuCr alloy, saturation of the Kondo temperature is observed for large diameters.

*E-mail: fisun@ilt.kharkov.ua

[1] A. A. Lysykh, I. K. Yanson, O. I. Shklyarevski, and Yu. G. Naidyuk, Solid State Commun. **35**, 987 (1980); A. G. M. Jansen, A. P. van Gelder, P. Wyder, and S. Straessler, J. Phys. F: Met. Phys. **11**, L15 (1981); Yu. G. Naidyuk, O. I. Shklyarevskii, and I. K. Yanson, Fiz. Nizk. Temp. **8**, 725 (1982) [Sov. J. Low Temp. Phys. **8**, 362 (1982)].

[2] I. K. Yanson, V. V. Fisum, R. Hesper, A. V. Khotkevich, J. M. Krans, J. A. Mydosh, and J. M. van Ruitenbeek, (a) Phys. Rev. Lett. **74**, 302 (1995), (b) Fiz. Nizk. Temp. **20**, 1062 (1984) [Low Temp. Phys. **20**, 836 (1994)].

[3] G. Zarand and L. Udvardi, Phys. Rev. B **54**, 7606 (1996).

[4] J. F. DiTusa, K. Lin, M. Park, M. S. Isaacson, and J. M. Parpia, Phys. Rev. Lett. **68**, 678 (1992).

[5] G. Chen and N. Giordano, Phys. Rev. Lett. **66**, 209 (1998); C. Strunk, M. Henny, and C. Schönenberger, Phys. Rev. Lett. **81**, 2982 (1998).

[6] V. Chandrasekhar, P. Santhaman, N. A. Penebe, R. A. Webb, H. Vloeberghs, C. Van Haesendonck, and Y. Bruynseraede, Phys. Rev. Lett. **72**, 2053 (1994).

[7] C. J. Muller, J. M. van Ruitenbeek, and L. J. de Jongh, Physica C **191**, 485 (1992).

[8] M. Hansen, *Constitution of Binary Alloys*, McGraw-Hill, New York (1958).

[9] A. V. Khotkevich and I. K. Yanson, *Atlas of Point Contact Spectra of Electron-Phonon Interactions in Metals*, Kluwer Academic Publ. (1995).

[10] Yu. V. Sharvin, Zh. Éksp. Teor. Fiz. **48**, 984 (1965) [Sov. Phys. JETP **21**, 655 (1965)].

[11] I. K. Yanson, V. V. Fisun, R. Hesper, J. M. Krans, J. A. Mydosh, N. van der Post, and J. M. van Ruitenbeek, Physica B **218**, 77 (1996).

[12] A. M. Duif, *Doctraalsriptie*, KUN Nijmegen, The Netherlands (1983).

[13] N. van der Post, F. Mettes, J. A. Mydosh, J. M. van Ruitenbeek, and I. K. Yanson, Fiz. Nizk. Temp. **22**, 313 (1996) [Low Temp. Phys. **22**, 245 (1996)]; Phys. Rev. B **53**, R476 (1996).

[14] M. D. Daybell, in *Magnetism*, G. Rado and H. Suhl (Eds.), Academic Press, New York (1973), Vol. 5, p. 121.

[15] B. I. Verkin, I. K. Yanson, I. O. Kulik, O. I. Shklyarevskii, A. A. Lysykh, and Yu. G. Naidyuk, Solid State Commun. **30**, 215 (1981).

[16] P. Monod and S. Schultz, Phys. Rev. **173**, 645 (1968).

[17] M. D. Daybell and W. A. Steyert, Phys. Rev. Lett. **20**, 195 (1968).

Break-junction experiments on the Kondo semiconductor CeNiSn: tunnelling versus direct conductance

Yu. G. Naidyuk*

B. Verkin Institute for Low Temperature Physics and Engineering, National Academy of Sciences of Ukraine, 47, Lenin Ave., 61164, Kharkov, Ukraine

K. Gloos

Institut für Festkörperphysik, Technische Universität Darmstadt, D-64289 Darmstadt, Germany; Max-Planck-Institut für chemische Physik fester Stoffe, D-01187 Dresden, Germany

T. Takabatake

Department of Quantum Matter, ADSM, Hiroshima University, Higashi-Hiroshima 739-8526, Japan
(Submitted February 28, 2000)

The rare-earth Kondo semiconductor CeNiSn is investigated by point-contact and tunneling spectroscopy using mechanically controllable break junctions. $I(V)$ characteristics and their derivatives are recorded for contacts from the metallic to the tunneling regime at temperatures between 0.1–8 K and in magnetic fields up to 8 T. It is found that CeNiSn behaves like a compound with typical metallic properties instead of exhibiting the expected semiconducting behavior. The main spectral feature is a pronounced zero-bias conductance minimum of about 10 meV width, which appears to be of magnetic nature. These break-junction experiments provide no clear-cut evidence for an energy (pseudo) gap in CeNiSn. © *2000 American Institute of Physics.* [S1063-777X(00)01007-0]

INTRODUCTION

Cerium intermetallic compounds show a large variety of extreme properties at low temperatures. The *f* electrons of the Ce ions can strongly hybridize with the conduction electrons, resulting in a number of different ground states. The heavy-fermion, the mixed-valent, and the Kondo-lattice state have attracted most of the interest. Among the Ce compounds, CeNiSn is usually classified as a Kondo semiconductor, mainly due to the enhanced electrical resistivity at low temperatures.[1]

As soon as high-quality samples became available, the low-temperature resistivity turned out to be metallic, unlike that of CeNiSn samples containing nonmagnetic impurities.[2] However, an anisotropic gap or V-shaped pseudogap in the electronic density of states is still used today to describe, e.g., the specific-heat measurements below 2 K.[3] Another example are the break-junction experiments by Ekino *et al.*[4] They observed $dI/dV(V)$ spectra with ~10 meV broad zero-bias minima. Assuming the junctions were in the tunneling regime, these anomalies were interpreted as being due to the gap in the electronic density of states. Later, break-junction experiments in high magnetic fields[5] revealed a suppression of the above zero-bias anomaly for fields along the *a* axis, unlike for fields along the *b* axis. This field-induced reduction of the gap structure was interpreted as crossover phenomenon from a pseudogap to a metallic heavy-fermion state.

Although the observation of a gaplike conductance minimum of the CeNiSn break junctions is an interesting fact, the tunneling regime in Refs. 4 and 5 was mainly postulated instead of experimentally verified. It is a severe drawback of the break-junction technique that one can not use a well-known superconductor like lead or aluminum as a counter-electrode to test the tunneling with a known superconducting quasiparticle density of states. The only way out of this dilemma seems to be to test the tunneling regime via the exponential variation of the contact resistance as the vacuum gap width between the two electrodes is varied or to find a conductance quantization in the metallic regime. Here we report our investigation of mechanically controllable break junctions of CeNiSn single crystals, both in the true vacuum-tunneling and in the metallic regime.

SPECTROSCOPY ON SMALL POINT CONTACTS

To investigate the interaction between conduction electrons and quasiparticles, point contact spectroscopy uses the nonlinear conductance of metallic point contacts, as reviewed, e.g., in Ref. 6. Energy-resolved spectroscopy is possible in the ballistic regime, when the electronic inelastic mean free path is much larger than the contact diameter. A voltage V applied to the contact accelerates the electrons to an excess energy eV.

In the opposite limit, when the inelastic mean free path is smaller than the contact diameter, energy is dissipated in the contact region due to relaxation processes. The excess energy is therefore much smaller than eV (see, e.g., the review).[7] Simultaneously, the temperature in the contact region T_{PC} is enhanced with respect to the bath temperature T_{bath}. In this thermal regime

$$T_{PC}^2 = T_{\text{bath}}^2 + \frac{V^2}{4L} \qquad (1)$$

with the Lorenz number L. A simple formula

$$R_{PC}(T) \simeq \frac{16\rho l}{3\pi d^2} + \frac{\rho(T)}{d} \qquad (2)$$

interpolates the contact resistance from the thermal to the ballistic regime.[6] Here ρ is the electrical resistivity, $\rho l = \hbar k_F / n e^2$, where n is the density of conduction electrons, e is the electron charge, and k_F is the Fermi wave number. The first term of Eq. (2) represents the ballistic resistance, dominating at small contact diameter d. The nonballistic second term depends on scattering processes of the material in the contact region. Therefore, in the thermal regime the nonlinear conductance of the junction is mainly due to the temperature dependence of $\rho(T)$. Since the latter is determined by the electron–quasi-particle interaction and peculiarities of the electronic structure, they can be resolved on point-contact spectra even in the thermal regime as anomalies of the contact conductance. But it is not possible to get more information than from $\rho(T)$ measurements. Additionally, in the thermal regime the energy scale set by eV is not directly related with the spectrum of the quasiparticles or other excitations, in contrast to the ballistic limit.

By reducing the cross-sectional contact area down to an atomic radius a, which corresponds to the Fermi wavelength for metals, on account of the quantum size effect the conductance of a 3D constriction assumes only well-defined values in multiples of $G_0 = 2e^2/h \simeq 77 \, \mu\Omega^{-1}$ (Refs. 8 and 9). Hence the maximal resistance[1)] of a contact of atomic dimension is of the order $R_{max} \simeq G_0^{-1} = 12.9 \, k\Omega$.

When the distance between the two electrodes is further increased, the direct metallic contact breaks, a vacuum gap opens, and tunneling across the vacuum barrier starts. It is often believed that the tunneling conductance directly images the density of states (DOS) of the electrodes. Actually, for a classical planar tunnel junction between normal metals the tunnel current depends on the DOS along the transverse direction only. This current, however, is strongly suppressed due to the exponential transmission coefficient of the barrier.[10] The influence of the DOS on the tunnel current can be seen preferentially in special tunneling geometries like a tip–plane setup, or when strong correlation effects break the single-electron representation.

EXPERIMENT

We prepared the CeNiSn samples (overall size approximately $1 \times 1 \times 5$ mm) by mechanically cutting a 0.5–0.7 mm deep notch to define the break position. The sample is affixed by electrically insulating glue onto a flexible bending beam. Twisted pairs of voltage and current leads were attached with silver epoxy on both sides of sample, which is then mounted onto the mixing chamber inside the vacuum can of the dilution refrigerator. With a micrometer screw the bending beam is bent at low temperatures, thereby breaking the sample at the notch. For further details of the experimental setup see Ref. 11.

The resistance of the break junction or its lateral contact size could be adjusted *in situ* both mechanically with the micrometer screw and with a piezo tube, which allows fine tuning of the contact resistance in the tunneling regime. The current–voltage characteristic and the differential resistance

were recorded in the standard four-terminal mode with current biasing at low contact resistances $R \lesssim 10 \, k\Omega$, while for contacts with $R \gtrsim 100 \, k\Omega$ a two-terminal mode was used, and the differential conductance was recorded with voltage biasing.

Three CeNiSn single crystals were investigated. Each had one long side in the a, b, and c directions of the orthorhombic crystal lattice, respectively. At room temperature, the contact resistance of the samples with the notch was between 0.1 and 1 Ω, instead of the expected few mΩ, estimated from the geometrical size. This difference points to microscopic cracks at the constriction. On cooling down, the resistance of some of the contacts further increased by an order of magnitude, probably due to different thermal expansion coefficients of the sample and the bending beam, producing additional cracks.

Note that the notch defines only the macroscopic position of the junction, while the microscopic contact is less well defined. After the sample was removed from the refrigerator, the surface of the junction was not mirrorlike or smooth, as expected for a single crystal, and the break was usually tilted with respect to the direction of the notch and thus to the crystal axis. Therefore the current flow through the contact deviates somewhat from the direction defined by the long side of the sample. A magnetic field up to 8 T could be applied perpendicular to the bending beam, i.e., perpendicular to the long side of the sample and to the current flow.

RESULTS

First one has to identify the regime of charge transport through the junctions, because this regime provides the basis for any further interpretation. To solve this problem we measured how the contact resistance depends on the piezo voltage, i.e., on the distance between the two broken pieces of the sample. Figure 1a clearly shows an exponential dependence of the current at constant bias voltage versus piezo voltage for contact resistances above 100 kΩ, as expected for true vacuum tunneling. For resistances below $G_0^{-1} = h/2e^2 \simeq 13 \, k\Omega$, the curves in Fig. 1b reveal a steplike change of conductance, which is characteristic for atomic-size metallic contacts. We therefore conclude that for contacts with resistance above 100 kΩ, the current is due to tunneling, while below 10 kΩ it is due to direct conductance of a metallic constriction. Note that this interpretation differs from that in Refs. 4 and 5.

Figure 2a shows the dV/dI spectra of several metallic contacts in the 20–5000 Ω range. In general, all the spectra look similar to each other. They have a pronounced peak at zero bias, and the differential resistance decreases logarithmically between 1 and 10 mV. According to Fig. 2b, the latter dependence can be fitted well by an empirical formula widely used to describe the temperature dependence of Kondo scattering if the temperature is replaced by the applied voltage. This seems to be a reasonable assumption for the thermal regime and follows from Eq. (1).

Figure 3 shows the temperature and field dependence of the dV/dI spectra of the sample in the b direction. In addition to the zero-bias peak, the curves have a background that gradually increases with V, resulting in a double-minimum structure. This kind of anomaly is very similar to that found
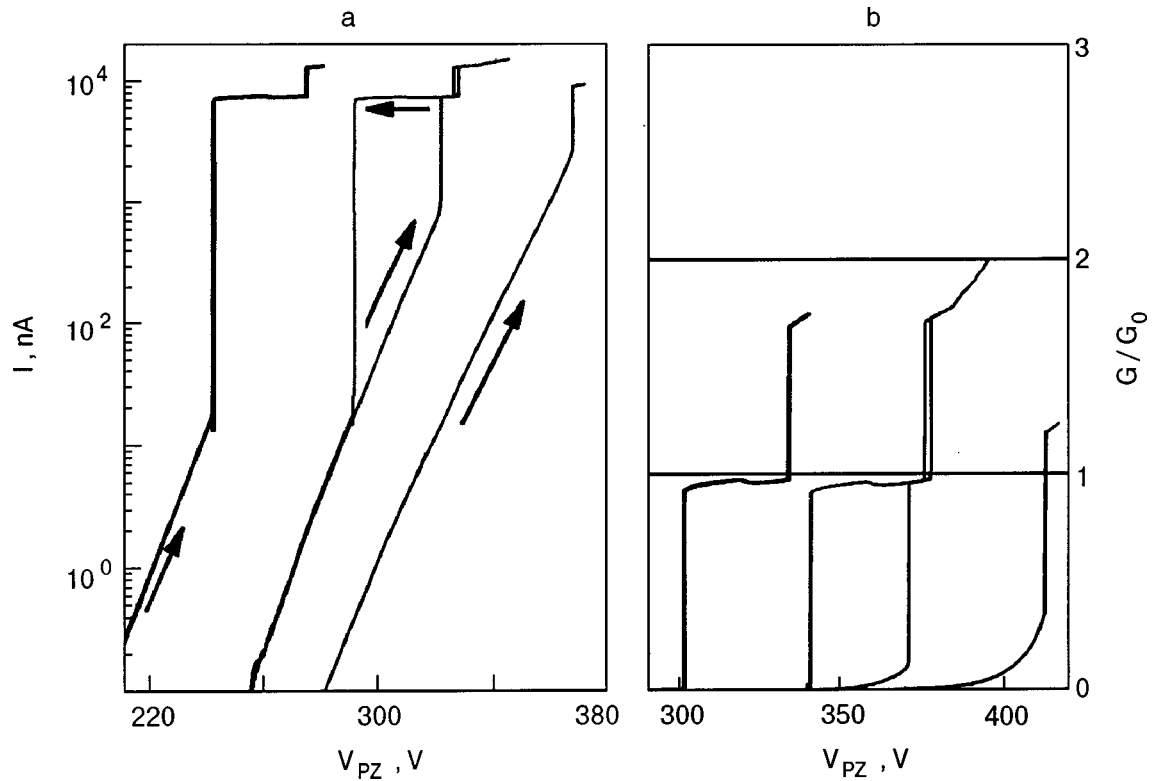
FIG. 1. Current I through a CeNiSn break junction in the c direction versus the piezo voltage V_{PZ} for several successive sweeps of the piezo voltage at T $=0.1$ K and at a constant bias voltage of 0.1 V (a). The data of Fig. 1a are in units of conductance normalized to the quantum conductance $G_0=2e^2/h$ $\simeq 77.5$ μS. The curves have been shifted along the V_{PZ} axis to fit into one diagram (b).

by Ekino *et al.*[4] and by Davydov *et al.*[5] if dV/dI is replaced by dI/dV. Note, however, that the $dV/dI(V)$ dependence looks like the temperature dependence of the zero-bias contact resistance $dV/dI(T,V=0)$; see the inset of Fig. 3a. Such

behavior characterizes the thermal regime, and not the ballistic one. A detailed discussion of the thermal regime and further literature can be found in Ref. 7. Since contacts with resistance below about 10 kΩ are not in the tunneling re-

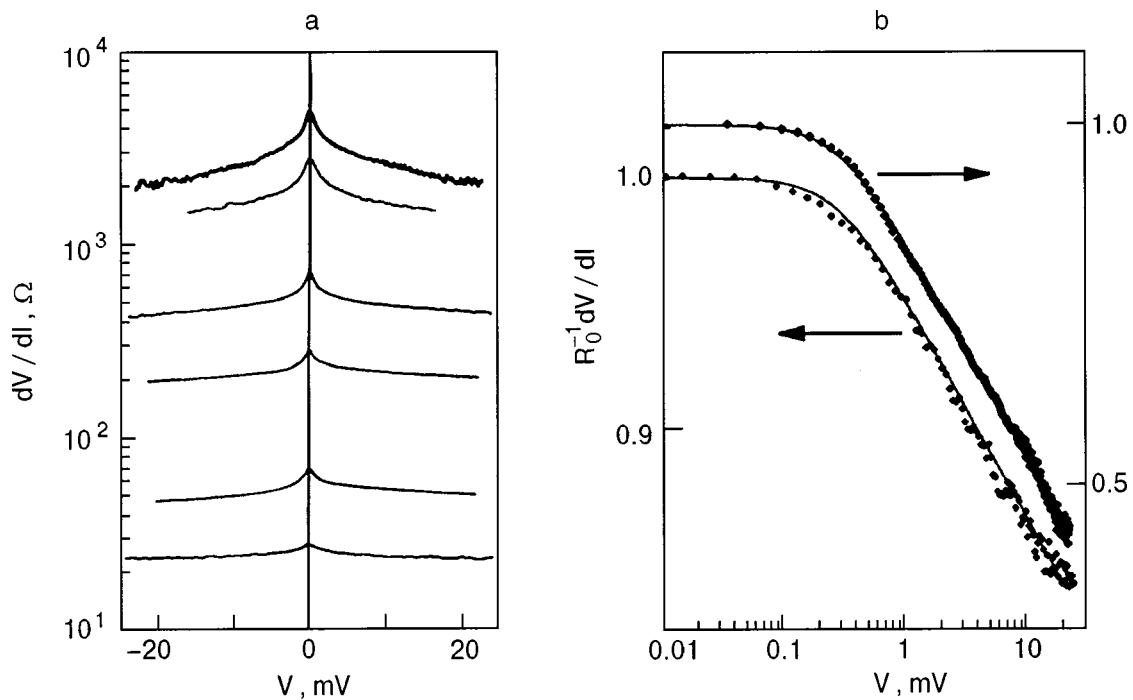FIG. 2. dV/dI versus V spectra of metallic CeNiSn break junctions in the a direction at $T=0.1$ K. Note the logarithmic abscissa (a). Normalized dV/dI versus V (symbols) for the two contacts in Fig. 2a with the lowest and highest resistance. The solid lines are fits to the Daybell formula[12] $R=1-A\log(1$ $+(V/V_0)^2)$ with $A=0.019(0.066), V_0=0.357(0.345)$ mV for the bottom (top) curve, respectively (b).
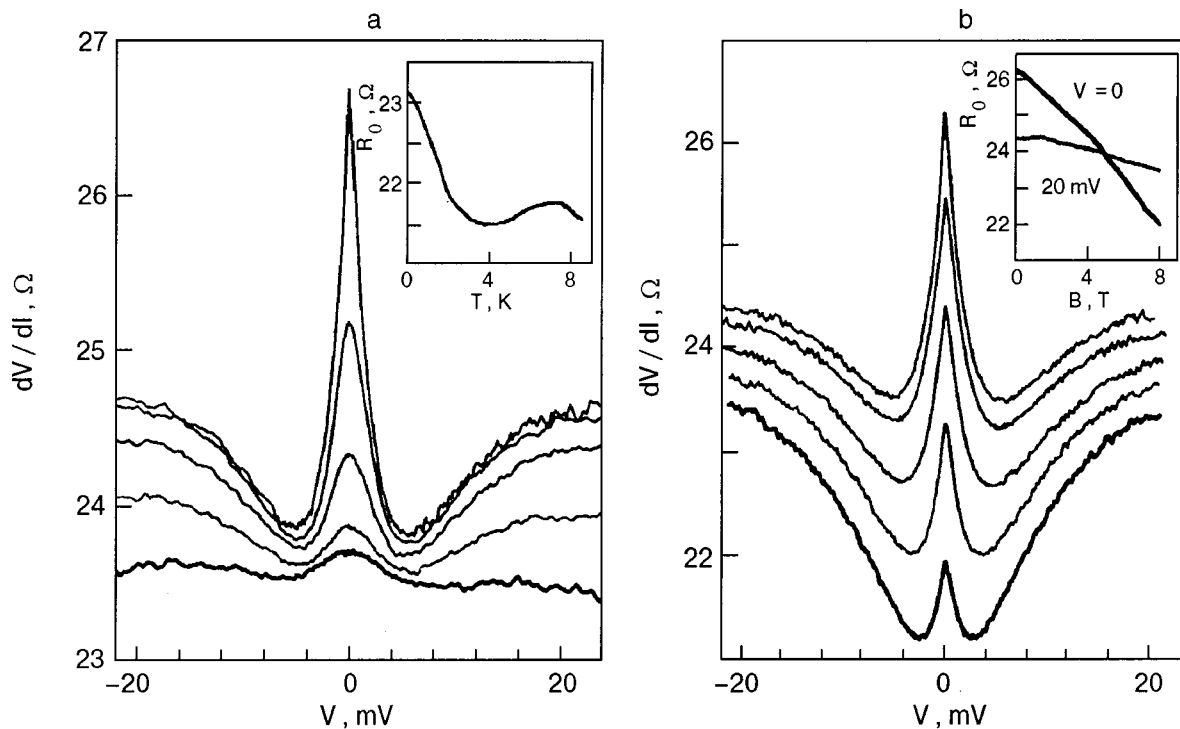
FIG. 3. Temperature dependence of dV/dI versus V for metallic CeNiSn break junctions in the b direction. The temperature is 0.1, 2, 4, 6, and 8 K (from top to bottom). The spectra are slightly offset against each other for clarity. The inset shows the temperature dependence of the contact resistance at zero bias for the same contact. The resistance is slightly lower because the junction changed somewhat after heating to 8 K (a). Magnetic field dependence of dV/dI versus V for the contact in Fig. 3a at $T=0.1$ K. The applied field is 0, 2, 4, 6, and 8 T (from top to bottom). The curves are again slightly offset against each other for clarity. The inset shows the contact magnetoresistance at zero bias and at $V=20$ mV, respectively (b).

gime, the zero-bias anomalies cannot be attributed directly to the density of states or to the energy gap, as proposed in Refs. 4 and 5. A natural explanation for the zero-bias peak in Fig. 3 with its logarithmic dependence could be Kondo scattering. The negative magnetoresistance shown in the inset of Fig. 3b also favors some magnetic or Kondo type of scattering.

For junctions in the tunneling regime, two cases have to be distinguished: i) Contacts with a large nonlinearity ($\sim$100%) in the dI/dV spectra also have a sharp zero-bias minimum, similar to the maximum in dV/dI of the metallic contacts (see Fig. 4a), and dI/dV increases nearly logarithmically in the 0.1–10 mV range. ii) Contacts with small nonlinearity ($\sim$10%) have a relatively broad zero-bias minimum. They are more asymmetric, and we found them also less reproducible. Applying a magnetic field slightly broadens the zero-bias minimum. Unfortunately, contacts of the first type were unstable when we started applying a magnetic field. We could therefore not check reliably how the field influences the spectra of the first type. The dI/dV spectra with small nonlinearity were measured on a slab prepared in the c direction. As we have said, the direction of current flow through the microscopic contact can deviate from the expected direction along the long side of the slab. For example, according to Fig. 1a, to increase the tunneling current by one order of magnitude one must increase the piezo voltage by about 15 V, while for the sample along the a direction only about 2 V is needed. This latter value ought to be expected in our setup for a change in the vacuum gap of about 0.1 nm. We conclude that for the sample in the c direction the changing vacuum gap between the two electrodes was probably

not oriented exactly perpendicular to the c axis.

DISCUSSION

For low-ohmic metallic contacts the dV/dI spectra look similar to the temperature dependence of the zero-bias contact resistance (Fig. 3a). Hence they reflect the behavior of the electrical resistivity in the contact region in the thermal limit, when the temperature inside the constriction increases with applied bias voltage according to Eq. (1). The increase of the contact resistance as the temperature is lowered very likely has the same origin as that observed earlier on the less perfect (that is, not very pure) CeNiSn samples.[2] We believe that in our experiments some intrinsic cracks with poor interface quality determine the microscopic properties of the junction. Alternatively, mechanical stress itself could distort the crystal lattice, producing imperfections. We found that the temperature dependence of the contact resistance of very low-ohmic CeNiSn contacts of about 70 mΩ for the slab in the c direction *before* applying a mechanical force showed a metalliclike decrease of the resistance down to 0.1 K. Hence, after the mechanical break the metal in the contact region may be distorted, or impurities like Ce ions may have been added to the interface, playing the role of scattering centers. The logarithmic Kondo-like dependence both for $dV/dI(V)$ and $dV/dI(T,V=0)$ favors a magnetic kind of scattering mechanism.

In the tunneling regime, the $dI/dV(V)$ spectra with a pronounced sharp minimum and logarithmic increase of conductance in Fig. 4a also look as if they are caused by magnetic scattering. For thin film metal–oxide–metal planar tun-
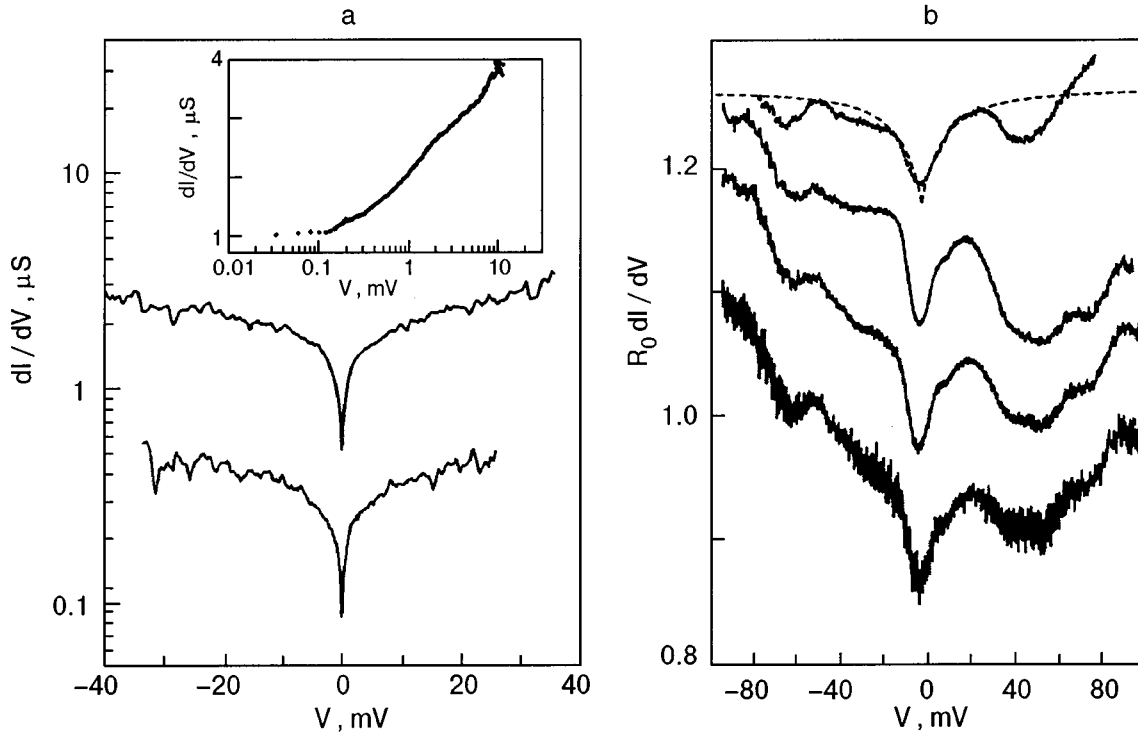
FIG. 4. dI/dV versus V for CeNiSn tunnel junctions in the *a* direction at $T=0.1$ K. The applied ac voltage was 0.1 mV. The inset shows one curve on a log plot (a). dI/dV versus V spectra normalized for zero conductance of CeNiSn tunnel junctions in the *c* direction at $T=0.1$ K. The zero-bias resistance is 1, 5, and 10 MΩ (from the second curve to the bottom curve). The curves are offset against each other for clarity. The applied ac voltage was 1 mV. The upper curve is a 1 MΩ contact in a magnetic field of 6 T together with a fit (dashed symmetric curve) to Coulomb blockade according to Eq. 3(b).

nel junctions, evaporating less than one monolayer of magnetic impurities can produce either a maximum or a minimum in the zero-bias conductance.[13] The size of this anomaly is of the order of 10%, and it depends on the sign of the exchange integral between the conduction electron spin and the magnetic impurity spin. A giant zero-bias resistance maximum similar to the conductance minimum in Fig. 4a, with logarithmic variation between a few mV and 100 mV, has been observed in Cr–oxide–Ag tunnel junctions.[10] This anomaly is possibly explained by Kondo scattering as well. However, the change in resistance is too large. Interestingly, a giant resistance peak was observed also for Al–oxide–Al tunnel junctions in which nonmagnetic Ni or Sn was evaporated onto the upper Al film.[14] This observation casts some doubt on the purely magnetic origin of the zero-bias anomalies, and so the nature of the giant zero-bias conductance minimum is a question still open to discussion.

Another explanation for a zero-bias conductance minimum of small point contacts could be Coulomb blockade. When the junction has a capacitance C, the tunneling electrons have to overcome the electrostatic charging energy $E_C=e^2/2C$. At large voltages, C equals the intrinsic capacitance C_0 of the junction.[11] But at small voltages, C is enhanced due to the lead capacitance $Kc\hbar/e|V|$. Here K is the capacitance per length of the setup and c is the speed of light. Consequently, the conductance of an otherwise ohmic junction shows a more or less pronounced zero-bias dip like[11]

$$R\frac{dI}{dV}=1-\frac{e^2Kc\hbar}{2(e|V|C_0+Kc\hbar)^2} \tag{3}$$

due to Coulomb blockade. In our setup the relative size of such a Coulomb anomaly is about 5%.[11] Its width depends

on the intrinsic static capacitance of the specific junction. Coulomb blockade could explain at least part of the zero-bias minima of the $dI/dV(V)$ spectra in Fig. 4b, while curves in Fig. 4a have a several times larger anomaly of the conductance, which cannot be explained only by Coulomb blockade.

One could also suppose that in the latter case some free isolated metallic (magnetic) clusters are formed accidentally during the breaking of the junction. These clusters could have rather small capacitances, increasing the effect of Coulomb blockade, while simultaneously depending on the magnetic field.

Let us come back to the $dI/dV(V)$ spectra in Fig. 4b, with small nonlinearities and broad zero-bias maxima. If we assume that this structure reflects the gap in the electronic density of states, then the width of the gap is determined by the position of maximum, corresponding to $2\Delta\simeq20$mV. This is two times larger than that found in Ref. 4, where the value of the gap is also too large when compared to the characteristic temperature of about 10 K.

CONCLUSION

We have studied CeNiSn using mechanically controllable break junctions from the metallic to the vacuum tunneling regime. We observed quantization of the conductance with a value near the conductance quantum G_0 at the transition from metallic contact to vacuum tunneling. This observation characterizes CeNiSn as a good metal even for temperatures well below 1 K. The pronounced zero-bias anomalies observed both in the metallic and in the vacuum-tunneling regime seem to be mainly due to scattering of elec-

trons on the disordered magnetic Ce ions or other imperfections at the interface between the electrodes, which could also be produced by mechanical stress. This hinders the use of break junction tunneling experiments for unequivocally identifying the proposed energy (pseudo) gap in the electronic density of states of CeNiSn.

[*]E-mail: naidyuk@ilt.kharkov.ua

[1)]Interestingly, the Sharvin formula for an orifice of atomic radius yields the same value $R_{atom} = 16\rho l/(3\pi d^2) \simeq 4/(ak_F)^2 h/(2e^2) = 4/(ak_F)^2 G_0^{-1}$, where $(ak_F)^2 \simeq 4$ for ordinary metals.[9]

[1] T. Takabatake, F. Teshima, H. Fujii, S. Nishigori, T. Suzuki, T. Fujita, Y. Yamaguchi, J. Sakurai, and D. Jaccard, Phys. Rev. B **41**, 9607 (1990).

[2] T. Takabatake, Y. Echizen, T. Yoshino, K. Kobayashi, G. Nakamoto, H. Fujii, and M. Sera, Phys. Rev. B **59**, 13878 (1999).

[3] K. Izawa, T. Suzuki, T. Fujita, T. Takabatake, G. Nakamoto, H. Fujii, and K. Maezawa, Phys. Rev. B **59**, 2599 (1999).

[4] T. Ekino, T. Takabatake, H. Tanaka, and H. Fujii, Phys. Rev. Lett. **75**, 4262 (1995).

[5] D. N. Davydov, S. Kambe, A. G. M. Jansen, P. Wyder, N. Wilson, G. Lapertot, and J. Flouquet, Phys. Rev. B **55**, 7299 (1997).

[6] A. Duif, A. G. M. Jansen, and P. Wyder, J. Phys.: Condens. Matter **1**, 3157 (1989).

[7] Yu. G. Naidyuk and I. K. Yanson, J. Phys.: Condens. Matter **10**, 8905 (1998).

[8] A. M. Zagoskin and I. O. Kulik, Fiz. Nizk. Temp. **16**, 911 (1990) [Sov. J. Low Temp. Phys. **16**, 533 (1990)].

[9] J. A. Torres, J. I. Pascual, and J. J. Saenz, Phys. Rev. B **49**, 16581 (1994).

[10] E. L. Wolf, *Principles of Electron Tunneling Spectroscopy*, Oxford University Press, New York (1985).

[11] K. Gloos and F. Anders, J. Low Temp. Phys. **116**, 21 (1999).

[12] M. D. Daybell, in *Magnetism*, G. T. Rado and H. Suhl (Eds.), Academic Press, New York **5**, 121 (1973).

[13] J. R. Cooper and A. F. G. Wyatt, J. Phys. F: Met. Phys. **3**, L120 (1973).

[14] M. A. El-Semary, Y. Kaahwa, and J. S. Rogers, Solid State Commun. **12**, 593 (1973).

The influence of single magnetic impurities on the conductance of quantum microconstrictions

A. Namiranian and Yu. A. Kolesnichenko

Institute for Advanced Studies in Basic Sciences, 45195-159, Gava Zang, Zanjan, Iran

Yu. A. Kolesnichenko*

Institute for Advanced Studies in Basic Sciences, 45195-159, Gava Zang, Zanjan, Iran;
B. Verkin Institute for Low Temperature Physics and Engineering, National Academy of Sciences
of Ukraine, 47 Lenin Ave., 61164 Kharkov, Ukraine

Yu. A. Kolesnichenko and A. N. Omelyanchouk

B. Verkin Institute for Low Temperature Physics and Engineering, National Academy of Sciences
of Ukraine, 47 Lenin Ave., 61164 Kharkov, Ukraine

The nonlinear ballistic conductance of three-dimensional quantum microconstrictions containing magnetic impurities is investigated. The nonlinear part of the conductance, which is due to the interaction of electrons with magnetic impurities, is obtained. The analytical results are analyzed numerically. It is shown that the intensity of the Kondo anomaly in the conductance as a function of the applied voltage depends on the diameter of the constriction and the positions of the impurities. © *2000 American Institute of Physics.* [S1063-777X(00)01107-5]

The impurity–electron interaction in Kondo systems can be effectively studied by using point contacts (PCs). In the first measurements of the differential PC resistance $R(V)$ in metals with magnetic impurities the zero-bias Kondo anomaly was observed.[1–3] These experiments were explained by quasiclassical theory of Kondo effect in PCs.[4] It was shown that in the second-order Born approximation the magnetic impurity contribution to the PC resistance includes the logarithmic dependence $R(V) \sim \ln(V)$ for $eV \gg T_K$ and saturation for $eV \ll T_K$ (T_K is the Kondo temperature, V is the voltage applied to the PC). In accordance with the theory,[4] the nonlinear correction to the ballistic PC resistance is proportional to the contact diameter. But in the experiments[1–3] the size dependence of the PC current was not investigated due to the limited range of contact diameters accessible.

The development of the technique of mechanically controllable break junctions (MCBJ) has made it possible to create stable PCs with diameters adjustable over a broad range, down to a single atom.[5,6] In the MCBJ experiments[7,8] the authors studied the resistance of ultrasmall contacts with magnetic impurities as a function of the PC diameter d. In contrast to the prediction of the quasiclassical theory,[4] Yanson et al.[7,8] observed that the Kondo scattering contribution to the contact resistance is nearly independent of the contact diameter d for small d. This behavior was explained by the authors[7,8] as being due to an increase of the Kondo impurity scattering cross section with decreasing contact size.

It has been shown in theoretical works[9] that in very small contacts the discreteness of impurity positions must be taken into account, and the experiments[7,8] may be explained by the ''classical'' mesoscopic effect of the dependence of the point contact conductance on the spatial distribution of impurities. This effect is essential in ''short'' contacts, and in the quasiclassical approximation it disappears with increasing contact length. Zarand and Udvardi[10] considered a contact in the form of a long channel and suggested that the Kondo temperature T_K is changed due to the strong fluctuations of the local density of states generated by the reflections of conduction electrons at the surface of the contact. As a result of that, the effective cross section of electrons has a maximum if the position of the impurity inside the contact corresponds to the maximum in the local electron density of states. But the mesoscopic effect of the spatial distribution of impurities in quantum contacts was not analyzed in that paper.[10]

In ultrasmall contacts the quantum phenomena known as the quantum size effect occur. The effect of the $2e^2/h$ conductance quantization has been observed in experiments on contacts in the two-dimensional electron gas[11,12] and in ultrasmall three-dimensional constrictions, which are created by using scanning tunneling microscopy[13,14] and mechanically controllable break junctions.[15] Defects produce backscattering of electrons and thus break the quantization of the conductance. On the other hand, the impurities situated inside the quantum microconstriction produce a nonlinear dependence of the conductance on the applied voltage.[16] This dependence is the result of the interference of electron waves reflected by these defects.[17,18]

In this paper we present a theoretical solution of this problem for the conductance of a quantum microconstriction in the form of a long ballistic channel containing single magnetic impurities. We study the first- and second-order corrections to the conductance of the ballistic microconstriction in the Born approximation. The effect of impurity positions is taken into account. Within the framework of the long-channel model the quantum formula for the conductance G is

obtained. By using the model of a cylindrical microconstriction, the nonlinear conductance as a function of voltage V and the width of constriction d is analyzed numerically for different positions of a single impurity.

Let us consider a quantum microconstriction in the form of a long and perfectly clean channel with smooth boundaries and a diameter d comparable to the Fermi wavelength $\lambda_F = h/\sqrt{2m\varepsilon_F}$, where ε_F is the Fermi energy. We assume that this channel is smoothly (over the Fermi length scale) connected with bulk metal "banks." As was shown in Refs. 19 and 20, in such a constriction an accurate quantization can be obtained in the zeroth approximation in the adiabatic parameter $|\nabla d| \ll 1$. The corrections to the tunneling and reflection coefficients of electrons due to deviation from the adiabatic constriction are exponentially small, except near the points where the modes are switched on and off.[21]

When a voltage V is applied to the constriction, a net current I starts to flow. In the limit $V \to 0$, the ballistic conductance of the quantum microconstriction is given by the formula

$$G = \frac{dI}{dV} = G_0 \sum_\beta f_F(\varepsilon_\beta), \tag{1}$$

where f_F is the Fermi function, ε_β is the minimal energy of the transverse electron mode, and β is the full set of transverse discrete quantum numbers. The ballistic quantum PC displays specific nonlinear properties, such as the conductance jumps e^2/h. For the two-dimensional PC these effects were considered in Refs. 22 and 23. The aim of this study is to analyze the zero-bias Kondo minimum in the PC conductance. We assume that the bias eV is much smaller than not only the Fermi energy ε_F but also the distances between the energies ε_β of the quantum modes. In this case the influence of the applied bias on the transmission is negligibly small.

Impurities and defects scatter the electrons, decreasing the transmission probability. In accordance with the standard procedure,[24,25] the decrease of the electrical current ΔI due to the electron–impurity interaction is connected with the rate of dissipation of the energy E by the relation:

$$V\Delta I = \frac{dE}{dt} = \frac{d\langle H_1 \rangle}{dt}. \tag{2}$$

The Hamiltonian H of the electrons contains the following terms:

$$H = H_0 + H_1 + H_{\text{int}}, \tag{3}$$

where

$$H_0 = \sum_{k,\sigma} \varepsilon_k c_{k\sigma}^+ c_{k\sigma} \tag{4}$$

is the Hamiltonian of free electrons, and

$$H_1 = \frac{eV}{2} \sum_{k,\sigma} \text{sign}(v_z) c_{k\sigma}^+ c_{k\sigma} \tag{5}$$

describes the interaction of electrons with the electric field. The Hamiltonian of the interaction of electrons with magnetic impurities H_{int} can be written as

$$H_{\text{int}} = \sum_{j,k,k'} J_{j,k,k'} [S_z (c_{k'\uparrow}^+ c_{k\uparrow} - c_{k'\downarrow}^+ c_{k\downarrow}) \\ \times S^- c_{k'\uparrow}^+ c_{k\downarrow} + S^+ c_{k'\downarrow}^+ c_{k\uparrow}]. \tag{6}$$

Here the operator $c_{k\sigma}^+$ ($c_{k\sigma}$) creates (annihilates) a conduction electron with spin σ, wave function φ_k, and energy ε_k; $\mathbf{S}$ denotes the spin of the impurity; v_z is the electron velocity along the channel; $\mathbf{J}_{j,k,k'}$ is the matrix element of the exchange interaction of an electron with an impurity at the point $\mathbf{r}_j$; $k\sigma$ is the full set of quantum numbers; and,

$$\mathbf{J}_{j,k,k'} = \int d\mathbf{r} J(\mathbf{r}, \mathbf{r}_j) \varphi_k(\mathbf{r}) \varphi_{k'}^*(\mathbf{r}). \tag{7}$$

The electron wave functions and eigenvalues in the long channel in the adiabatic approximation are

$$\varphi_k(\mathbf{r}) = \psi_\beta(\mathbf{R}) \exp\left(\frac{i}{\hbar} p_z z \right); \tag{8}$$

$$\varepsilon_k = \varepsilon_\beta + \frac{p_z^2}{2m_e}, \tag{9}$$

where $k = (\beta, p_z)$, p_z is the momentum of an electron along the contact axis; m_e is the electron mass; $\mathbf{r} = (\mathbf{R}, z)$, with $\mathbf{R}$ the coordinate in the plane perpendicular to the z axis.

Differentiating $\langle H_1 \rangle$ with respect to the time t, we obtain an equation for the change ΔI of the current as a result of the interaction of electrons with magnetic impurities:

$$V\Delta I = \frac{1}{i\hbar} \langle [H_1(t), H_{\text{int}}(t)] \rangle, \tag{10}$$

where

$$\langle \dots \rangle = \text{Tr}(\rho(t) \dots). \tag{11}$$

All operators are in the interaction representation. The density matrix $\rho(t)$ satisfies the equation

$$i\hbar \frac{\partial \rho}{\partial t} = [H_{\text{int}}(t), \rho(t)], \tag{12}$$

which can be solved using perturbation theory:

$$\rho(t) = \rho_0 + \frac{1}{i\hbar} \int_{-\infty}^{t} dt' [H_{\text{int}}(t'), \rho_0] \frac{1}{(i\hbar)^2} \\ \times \int_{-\infty}^{t} dt' \int_{-\infty}^{t'} dt'' [H_{\text{int}}(t'), [H_{\text{int}}(t''), \rho_0]] \dots . \tag{13}$$

By means of Eq. (13) the change in the electric current due to magnetic impurities can be determined as

$$\Delta I = I_1 + I_2 + \dots = -\frac{1}{\hbar^2 V} \\ \times \int_{-\infty}^{t} dt' \, \text{Tr}(\rho_0 [[H_1, H_{\text{int}}(t), H_{\text{int}}(t')]]) \\ - \frac{1}{i\hbar^3 V} \int_{-\infty}^{t'} dt'' \int_{-\infty}^{t} dt' \, \text{Tr}(\rho_0 [[[H_1, H_{\text{int}}(t)], H_{\text{int}}(t')], \\ \times H_{\text{int}}(t'')]) + \dots . \tag{14}$$

After simple but cumbersome calculations, we find the first-and second-order corrections to the PC current

$$I_1 = -\frac{\pi e}{\hbar} s(s+1) \sum_{n,m} \sum_{i,j} (\text{sign } v_{zk} - \text{sign } v_{zn})$$

$$\times (f_m - f_n) \delta(\varepsilon_n - \varepsilon_m) J_{j,n,m} J_{i,m,n}. \tag{15}$$

$$I_2 = \frac{\pi e}{\hbar} s(s+1) \sum_{n,m,k} \sum_{i,j,l} (\text{sign } v_{zk} - \text{sign } v_{zn})$$

$$\times \left[\delta(\varepsilon_n - \varepsilon_k) \text{Pr} \frac{1}{\varepsilon_m - \varepsilon_k} + \delta(\varepsilon_m - \varepsilon_k) \text{Pr} \frac{1}{\varepsilon_n - \varepsilon_k} \right]$$

$$\times [\mathbf{J}_{j,n,k} \mathbf{J}_{i,m,n} \mathbf{J}_{l,k,m} + \mathbf{J}_{j,k,n} \mathbf{J}_{i,n,m} \mathbf{J}_{l,m,k}]$$

$$\times (f_m - f_k)(1 - 2 f_n), \tag{16}$$

where $f_n = f_F[\varepsilon_n + (eV/2)\text{sign } v_z]$. The first addition I_1 to the PC current describes a small spin-dependent correction (of order $(J/\varepsilon_F)^2$) to the change of the current due to the usual scattering. The second addition I_2 is also small too, but contains the Kondo logarithmic dependence on the voltage, and it is the most important for the analysis of the nonlinear conductance of constrictions containing magnetic impurities.

The expressions (15) and (16) can be further simplified in the case of a δ-function potential of the impurities,

$$J(\mathbf{r}) = \frac{J}{n_e} \delta(\mathbf{r}), \tag{17}$$

where n_e is the electron density. In this case the addition I_2 to the ballistic current has the form:

$$I_2 = \frac{2\pi e^2}{\hbar} \left(\frac{J}{n_e}\right)^3 s(s+1) \sum_{n,m,k} \sum_{i,j,l} (\text{sign } v_{zk} - \text{sign } v_{zn})$$

$$\times \left[\delta(\varepsilon_n - \varepsilon_k) \text{Pr} \frac{1}{\varepsilon_m - \varepsilon_k} + \delta(\varepsilon_m - \varepsilon_k) \text{Pr} \frac{1}{\varepsilon_n - \varepsilon_k} \right]$$

$$\times (f_m - f_k)(1 - 2 f_n)$$

$$\times \text{Re}[\varphi_k^*(\mathbf{r}_j) \varphi_n^*(\mathbf{r}_i) \varphi_m^*(\mathbf{r}_l) \varphi_k(\mathbf{r}_l) \varphi_m(\mathbf{r}_i) \varphi_n(\mathbf{r}_j)]. \tag{18}$$

It follows from Eqs. (16) and (18) that the current I_2 depends on the positions of the impurities. Two effects influence the value of I_2: the effect of quantum interference of scattered electron waves, which depends on the distances between impurities, and effect of the electron density of states at the points where the impurities are situated. The nonlinear part of the conductance can be easy obtained after differentiation of Eq. (18) with respect to the voltage: $G_2 = dI_2/dV$. In the case of a single impurity and at zero temperature $T=0$, this equation can be integrated analytically over the momentum p_z, and the conductance G_2 takes the form
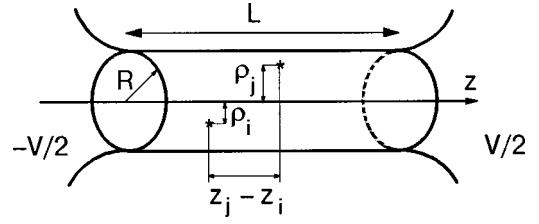

FIG. 1. Schematic representation of a ballistic microconstriction in the form of a long channel, adiabatically connected to large metallic reservoirs. Magnetic impurities inside the constriction are shown.

$$G_2 = -\frac{\pi e^2 m_e^3}{\hbar^4} \left(\frac{J}{n_e}\right)^3 s(s$$

$$+1) \sum_{\alpha,\beta,\gamma} \sum_{\kappa=\pm} |\psi_\alpha(\mathbf{R})|^2 |\psi_\beta(\mathbf{R})|^2 |\psi_\gamma(\mathbf{R})|^2$$

$$\times [p_\alpha^{(\kappa)} p_\beta^{(\kappa)} p_\gamma^{(\kappa)}]^{-1} \left[\ln \left| \frac{p_\gamma^{(\kappa)} - p_\gamma^{(-\kappa)}}{p_\gamma^{(\kappa)} + p_\gamma^{(-\kappa)}} \left(\frac{p_\alpha^{(\kappa)}}{p_\gamma^{(\kappa)}}\right) \right| \right.$$

$$+ (1 - \delta_{\alpha\beta}) \ln \left| \frac{p_\alpha^{(\kappa)} p_\beta^{(-\kappa)} - p_\alpha^{(-\kappa)} p_\beta^{(\kappa)}}{p_\alpha^{(\kappa)} p_\beta^{(-\kappa)} + p_\alpha^{(-\kappa)} p_\beta^{(\kappa)}} \right|$$

$$\left. + \delta_{\alpha\beta} \ln \left| \frac{(p_\alpha^{(\kappa)})^2 - (p_\beta^{(-\kappa)})^2}{(p_\alpha^{(-\kappa)})^2} \right| \right], \tag{19}$$

where

$$p_\alpha^{(\pm)} = \left[2 m_e \left(\varepsilon_F \pm \frac{eV}{2} - \varepsilon_\alpha \right) \right]^{1/2}, \tag{20}$$

and the transverse parts of the wave function $\Psi_\alpha(\mathbf{R})$ and the electron energy ε_α are given by Eqs. (8) and (9).

Carrying out the numerical calculations, we use the free electron model of a point contact consisting of two infinite half spaces connected by a long ballistic cylinder of a radius R and length L (Fig. 1). In the limit $L \to \infty$ the electron wave functions $\Psi_\alpha(\mathbf{R})$ and eigenstates ε_α can be written as

$$\psi_\alpha(\mathbf{R}) = \frac{1}{\sqrt{\pi} R J_{m+1}(\gamma_{mn})} J_m(\gamma_{mn}\rho/R) \exp(im\varphi);$$

$$\varepsilon_\alpha = \frac{\hbar^2}{2 m_e R^2} \gamma_{mn}^2, \tag{21}$$

where we have used cylindrical coordinates $\mathbf{r} = (\rho, \varphi, z)$ with the z axis along the channel axis. Here γ_{mn} is the nth zero of the Bessel function J_m. Because of the degeneracy of the electron energy with respect to azimuthal quantum number m (as a result of the symmetry of the model), quantum modes with $\pm m$ give the same contribution to the conductance. In this model the ballistic conductance (1) has not only steps G_0, but also steps $2G_0$ (Refs. 20 and 26).

In Fig. 2 the dependence of the nonlinear conductance on the applied bias is shown for different positions of a single magnetic impurity inside the channel. The results obtained confirm that the nonlinear effect is strongly dependent on the position of the impurity. If the impurity is situated near the surface of the constriction, $\mathbf{r} = \mathbf{R}$, where the square modulus of the electron wave function is small, its influence on the conductivity is negligible. This conclusion is con-
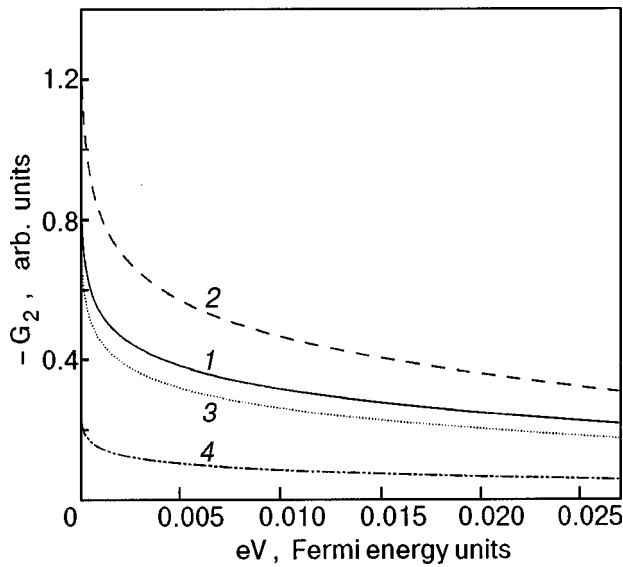
FIG. 2. The voltage dependence of the nonlinear part of the conductance G_2 (19) for different distances of the impurity from the contact axis ($2\pi R = 5.2\lambda_F$; $T=0$; $1-2\pi\rho=1.5\lambda_F$; $2-2\pi\rho=2.5\lambda_F$; $3-2\pi\rho=3.0\lambda_F$; $4-2\pi\rho=3.5\lambda_F$).
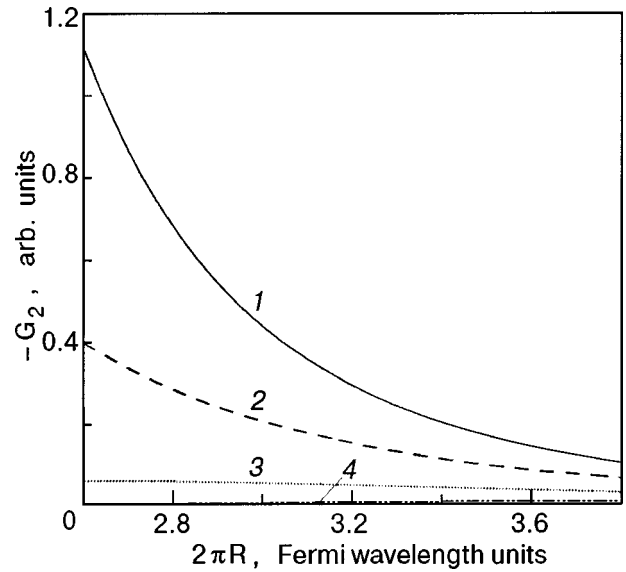

FIG. 4. The dependence of G_2 (19) on the radius of the constriction for a single-mode channel and different positions of the impurity ($V=0.02\varepsilon_F$; $T=0$; $1—2\pi\rho=0.5\lambda_F$; $2—2\pi\rho=1.0\lambda_F$; $3—2\pi\rho=1.5\lambda_F$; $4—2\pi\rho=2.0\lambda_F$).

firmed by the calculations of the dependence G_2 on the position of the impurity for different numbers of quantum modes (Fig. 3). The results indicate that the mesoscopic effect of the impurity position is more essential for ultrasmall contacts, which contain only a few conducting modes, and G_2 has a maximum. Similar results are obtained for the dependence of G_2 on the radius R of the constriction (Figs. 4 and 5). In the single-mode constriction (Fig. 4) the conductance G_2 displays a much stronger dependence on R than in the contact with five conducting modes (Fig. 5).

Thus we have shown that in long quantum microconstrictions the spatial distribution of magnetic impurities influences the nonlinear dependence of the conductance on the

applied voltage. This mesoscopic effect is due to the strong dependence the electron scattering amplitude on the positions of the impurities. As a result of the reflection from the boundaries of the constriction, the electron wave functions corresponding to bounded electron motion in the direction transverse to the contact axis are standing waves. If the impurity is situated near a point at which the electron wave function is equal to zero (near the surface of the constriction or, for quantum modes with numbers $n>1$, at some points inside), its scattering of electrons is small. The fact is that the amplitude of the Kondo minimum of the conductance of a quantum contact displays the mesoscopic effect of a dependence on the positions of single impurities. This effect is
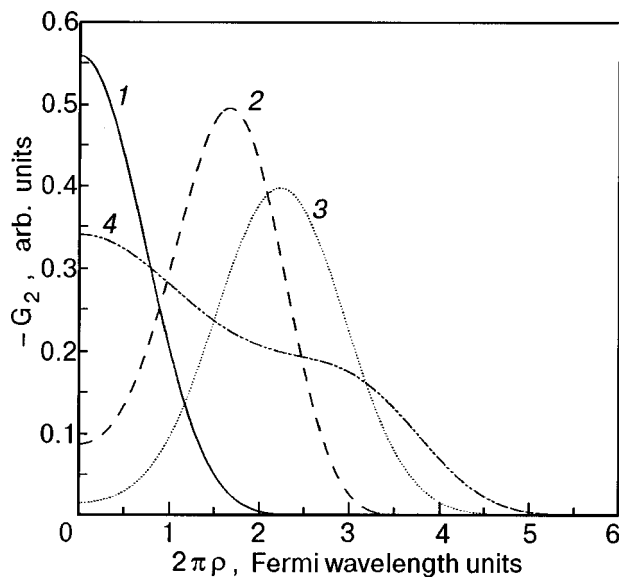
FIG. 3. The dependence of G_2 (19) on the position of the impurity for different numbers of quantum modes in the constriction $V=0.02\varepsilon_F$; $T=0$; 1—one mode ($2\pi R=3\lambda_F$); 2—three modes ($2\pi R=4\lambda_F$); 3—five modes ($2\pi R=5.3\lambda_F$); 4—six modes ($2\pi R=6\lambda_F$).
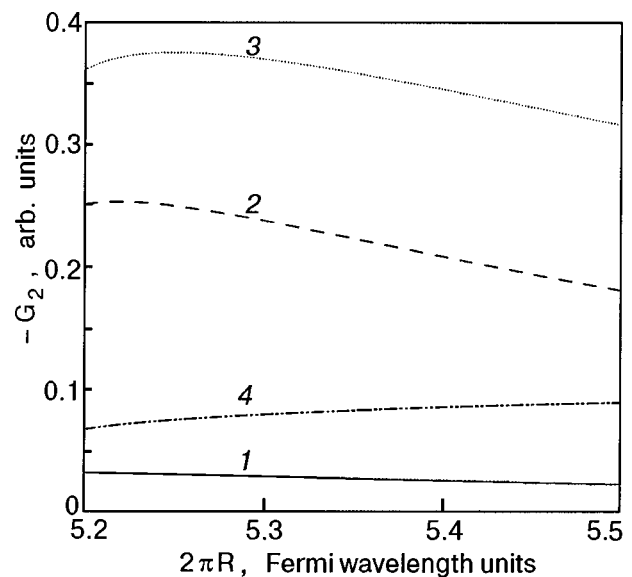
FIG. 5. The dependence of G_2 on the radius for a microconstriction with five quantum modes and different positions of the impurity ($V=0.02\varepsilon_F$; $T=0$; $1—2\pi\rho=0.5\lambda_F$; $2—2\pi\rho=1.5\lambda_F$; $3—2\pi\rho=2.5\lambda_F$; $4—2\pi\rho=4.5\lambda_F$).

most important in the case when only a few quantum modes are responsible for the conductivity of the constriction.

We acknowledge fruitful discussions with M. R. H. Khajehpour, V. G. Peschansky, and I. K. Yanson.

*E-mail: kolesnichenko@ilt.kharkov.ua

[1] A. A. Lysykh, I. K. Yanson, O. I. Shklyarevskii, and Yu. G. Naidyuk, Solid State Commun. **35**, 987 (1980).

[2] A. G. M. Jancen, A. P. van Gelder, P. Wyder, and S. Strassler, J. Phys. F: Metal Phys. **11**, L15 (1981).

[3] Yu. G. Naidyuk, O. I. Shklyarevskii, and I. K. Yanson, Fiz. Nizk. Temp. **8**, 725 (1982) [Sov. J. Low Temp. Phys. **8**, 362 (1982)].

[4] A. N. Omelyanchouk and I. G. Tuluzov, Fiz. Nizk. Temp. **6**, 1286 (1980); **11**, 388 (1985) [Sov. J. Low Temp. Phys. **11**, 211 (1985)].

[5] C. J. Muller, J. M. van Ruitenbeek, and L. J. de Jong, Physica C **191**, 482 (1992).

[6] J. M. Krans, C. J. Muller, I. K. Yanson, Th. C. M. Govaert, R. Hesper, and J. M. van Ruitenbeek, Phys. Rev. B **48**, 14721 (1993).

[7] I. K. Yanson, V. V. Fisun, R. Hesper, A. V. Khotkevich, J. M. Krans, J. A. Mydosh, and J. M. van Ruitenbeek, Phys. Rev. Lett. **74**, 302 (1995).

[8] I. K. Yanson, V. V. Fisun, A. V. Khotkevich, R. Hesper, J. M. Krans, J. A. Mydosh, and J. M. van Ruitenbeek, Fiz. Nizk. Temp. **20**, 1062 (1994) [Low Temp. Phys. **20**, 836 (1994)].

[9] Yu. A. Kolesnichenko, A. N. Omelyanchouk, and I. G. Tuluzov, Fiz. Nizk. Temp. **21**, 851 (1995) [Low Temp. Phys. **21**, 655 (1995)]; Physica B **218**, 73 (1996).

[10] G. Zarand and L. Udvardi, Phys. Rev. B **54**, 7606 (1996).

[11] B. J. van Wees, H. van Houten, C. W. J. Beenakker, J. G. Williamson, L. P. Kouwenhoven, D. van der Marel, and C. T. Foxon, Phys. Rev. Lett. **60**, 848 (1988).

[12] D. A. Wharam, M. Pepper, H. Ahmed, J. E. F. Frost, D. G. Hasko, D. C. Peacock, D. A. Ritchie, and G. A. C. Jones, J. Phys.: Solid State Phys. **21**, L209 (1988).

[13] J. I. Pascual, J. Mendez, J. Gomez-Herrero, A. M. Baro, N. Garsia, and Vu Thien Binh, Phys. Rev. Lett. **71**, 1852 (1993).

[14] N. Agrait, J. G. Rodrigo, and S. Viera, Phys. Rev. B **47**, 12345 (1993).

[15] C. J. Muller, J. M. van Ruitenbeek, and L. J. de Jongh, Phys. Rev. Lett. **69**, 140 (1992).

[16] A. Namiranian, Yu. A. Kolesnichenko, and A. N. Omelyanchouk, Phys. Rev. B **61 No**, 23 (2000).

[17] C. Untidt, G. Rubo Bollinger, S. Vieira, and N. Agrait, in *Quantum and Mesoscopic Phenomena and Mesoscopic Devices in Microelectronics*, Bilkent University, Ankara, Turkey (1999), p. 78.

[18] B. Ludoph, M. H. Devoret, D. Esteve, C. Urbina, and J. M. van Ruitenbeek, Phys. Rev. Lett. **82**, 1530 (1999).

[19] L. I. Glazman, G. B. Lesovik, D. E. Khmel'nitskii, and R. I. Shekhter, JETP Lett. **48**, 238 (1988).

[20] E. N. Bogachek, A. M. Zagoskin, and I. O. Kulik, Fiz. Nizk. Temp. **16**, 1404 (1990) [Sov. J. Low Temp. Phys. **16**, 796 (1990)].

[21] A. Yacoby and Y. Imry, Phys. Rev. B **41**, 5341 (1990).

[22] L. I. Glazman and A. V. Khaetskii, JETP Lett. **48**, 591 (1988).

[23] A. M. Zagoskin, JETP Lett. **52**, 435 (1990).

[24] I. O. Kulik and I. K. Yanson, Fiz. Nizk. Temp. **4**, 283 (1978) [Sov. J. Low Temp. Phys. **4**, 596 (1978)].

[25] I. O. Kulik, A. N. Omelyanchouk, and I. G. Tuluzov, Fiz. Nizk. Temp. **14**, 149 (1988) [Sov. J. Low Temp. Phys. **14**, 82 (1988)].

[26] J. A. Torres, J. A. Pascual, and J. J. Saenz, Phys. Rev. B **49**, 16581 (1994).

The quantum conductance of ballistic microconstrictions in metals with an open Fermi surface

A. Namiranian and Yu. A. Kolesnichenko

Institute for Advanced Studies in Basic Sciences, 45195-159, Gava Zang, Zanjan, Iran

Yu. A. Kolesnichenko*

Institute for Advanced Studies in Basic Sciences, 45195-159, Gava Zang, Zanjan, Iran;
B. Verkin Institute for Low Temperature Physics and Engineering, National Academy of Sciences
of Ukraine, 47 Lenin Ave., 61164 Kharkov, Ukraine

It is shown that the conductance G of a quantum microconstriction in a metal with an open Fermi surface undergoes jumps e^2/h of the opposite sign as a function of the contact diameter. The negative jumps are a result of the limitation of the energy of the electron motion along the direction in which the Fermi surface is open. The point contact spectrum dG/dV of such a constriction has additional peaks at the bias eV where the maximum energy ε_{max} of the quantum subband is equal to the energies $\varepsilon_F \pm eV/2$ (ε_F is the Fermi energy). © *2000 American Institute of Physics.* [S1063-777X(00)01207-X]

The quantum size effect in conductors was predicted theoretically by I. Lifshits and A. Kosevich in 1955[1] and was found experimentally in thin films of metals and semiconductors (see, for example, Ref. 2). In those studies, quasiclassical oscillations of the thermodynamic and kinetic properties were investigated, because of the limited range of the sample thicknesses d which were then accessible (as usual $d \gg \lambda_F$, where λ_F is the Fermi wavelength). Advances in the modern technology of nanofabrication make it possible to realize the ultraquantum limit of the size effect in the conducting properties by using small ballistic contacts of a size comparable to the Fermi wavelength. The current I through such a microconstriction is governed by the currents of one-dimensional quantum subbands, each of which contribute to the conductance $G = dI/dV$ a value $G_0 = 2e^2/h$ (V is the voltage applied to the contact). As a result, the conductance G displays a step-like structure versus contact size. For ''large'' contacts ($d \gg \lambda_F$) this structure turns into quasiclassical oscillations. The conductance quantization effect was first observed in a model system in the two-dimensional (2D) electron gas formed at a GaAs–Al$_x$Ga$_{1-x}$As heterojunction.[3,4] The development of methods of scanning tunneling microscopy and mechanically controllable break junctions enables one to investigate the conductivity of ultrasmall (down to atomic size) contacts in real metals.[5–8] By using these methods the quantum steps of the conductance were observed in three-dimensional (3D) point contacts. In the simple metals (Na, Cu, Au) the conductance steps are rather similar to the conductance of 2D contacts.[8–10] But for metals with a more complicated electronic structure, such as Al and Pt, the size dependence of the conductance has a more irregular behavior as compared to simple metals.[9] In Al and Pt the first few conductance plateaus have positive slope. It signifies that the conductance decreases when the contact size increases. In some cases weakly expressed negative steps of the conductance have been observed.[9] One of the

reasons for the negative slope may be the resonances due to electron reflection at the ends of the constriction.[11]

The theory of electron transport in mesoscopic microconstrictions (see, e.g., Ref. 12) explains the conductance quantization as being the result of the existence of discrete transverse electron states (modes). With increasing contact diameter new modes open up, and the conductance increases in a sequence of steps of height G_0.[13] At finite voltages, as a result of the splitting of the Fermi surface in the constriction by the applied bias eV,[14,15] a steplike structure of the nonlinear conductance occurs, at integer multiples of $G_0/2$, as a function of the constriction width.[16] The new period of the quantum steps is caused by the difference of the maximum energy of electrons with different directions of the electron velocity $v_\parallel$ along the contact axis. With increasing contact width a new quantum mode opens up nonsimultaneously for electrons with the energy $\varepsilon_F + eV/2$ and the energy $\varepsilon_F - eV/2$. Each time, when a quantum mode opens up for one of the two directions of the vector $v_\parallel \lessgtr 0$, the conductance increases by $G_0/2$. If the bias eV is larger than the distances between the energy levels of quantum modes, it is possible to change the number of open modes by changing the voltage V. In this case the conductance jumps in a sequence of steps of height $G_0/2$, as a function of the voltage V. This effect can be used for spectroscopy of energy levels in quantum constrictions.[17] The conductance quantization in 3D point contacts of a metal with a spherical Fermi surface was considered in the theoretical papers.[18,19] It was found that for sufficiently long constrictions the conductance has a steplike dependence on the contact diameter. For the symmetric model of the contact, because the degeneracy of the electron energy with respect to one of discrete quantum numbers, the conductance has not only steps G_0, but also steps $2G_0$.[18,19]

In a majority of real metals the Fermi surface is a complicated periodic surface, which continuously passes through the whole inverse lattices (open Fermi surface). The energy

$\varepsilon_{\parallel}$ of the electron motion in the direction in which the Fermi surface is open is limited ($0 \leqslant \varepsilon_{\parallel} \leqslant \varepsilon_1$), and its maximum value ε_1 may be considerably smaller than the Fermi energy ε_F. That leads to phenomena such as, for example, the linear magnetoresistance of polycrystals[20] (Kapitsa effect[21]) or the oscillation of the resistance of single crystals as a function of the direction of the strong magnetic field,[22] which are absent in conductors with a closed Fermi surface. The limitation of the electron velocity in some direction is most important in the ''organic layered metals,'' the Fermi surface of which is a slightly ''warped'' cylinder.[23]

In this paper we analyze the conductance of a 3D quantum microconstriction in a metal with an open Fermi surface. It is shown that the conductance G may display not only steps G_0 but also negative steps $-G_0$, as a result of the finite width of quantum conducting subbands $\Delta \varepsilon = \varepsilon_{\max} - \varepsilon_{\min}$. The point contact spectrum (dG/dV) contains two series of maxima. One of them corresponds to the voltages $eV = \pm 2(\varepsilon_F - \varepsilon_{\min})$, as in 2D microconstrictions and 3D point contacts in metals with an isotropic Fermi surface.[17] The second series of maxima satisfies the condition $eV = \pm 2(\varepsilon_F - \varepsilon_{\max})$.

If the contact axis coincides with the axis of the open Fermi surface, for the participation of the nth quantum mode in the electrical current, not only must the minimum energy of the transverse mode $\varepsilon_{\min}(\mathbf{n})$ be smaller than $\varepsilon_F \pm eV/2$, but it is necessary that also $\varepsilon_{\max}(\mathbf{n}) \geqslant \varepsilon_F \pm eV/2$, where $\mathbf{n} = (n_1, n_2)$ is the set of two transverse discrete quantum numbers, $\varepsilon_{\min}(\mathbf{n})$ and $\varepsilon_{\max}(\mathbf{n})$ are the minimum and maximum energies of the quantum subband, which is characterized by the set $\mathbf{n}$. As a result, with increasing contact diameter d, starting from the energy $\varepsilon_{\max}(\mathbf{n}, d) = \varepsilon_F \pm eV/2$, the nth mode does not contribute to the conductivity.

We consider a model of the microconstriction in the form of a long ballistic channel of length L and diameter $d \ll L$, which is smoothly (adiabatically[24]) connected with bulk metallic reservoirs. In the long ($L \gg d$) ballistic channel the ''duplicated'' electron distribution function $f(\varepsilon)$ has the form[14,15]

$$f(\varepsilon) = f_F\left(\varepsilon + \frac{eV}{2} \operatorname{sign} v_z\right), \tag{1}$$

where $f_F(\varepsilon)$ is the equilibrium Fermi distribution. The distribution function $f(\varepsilon)$ (1) is valid if the bias is small $eV \ll \sqrt{\varepsilon_F \delta \varepsilon}$ (where $\delta \varepsilon$ is the characteristic distance between quantum levels of the transverse motion). With this inequality, which we suppose is fulfilled, the distribution (1) satisfies the condition of electrical neutrality, and the electric field inside the channel is negligible.

The total current flowing through the contact can be described by a Landauer-type formula,[25] which at finite voltages is given by

$$I = \frac{2e}{h} \sum_n \int_{\varepsilon_{\min}}^{\varepsilon_{\max}} d\varepsilon \left[f_F\left(\varepsilon - \frac{eV}{2}\right) - f_F\left(\varepsilon + \frac{eV}{2}\right) \right]. \tag{2}$$

Expression (2) has a clear physical meaning: The bias eV applied to the contact splits the Fermi surface of the electrons injected into the channel into two parts ($v_{\parallel} > 0$ and $v_{\parallel} < 0$) with maximum energies differing by eV. The net current inside the contact is determined by the contributions of
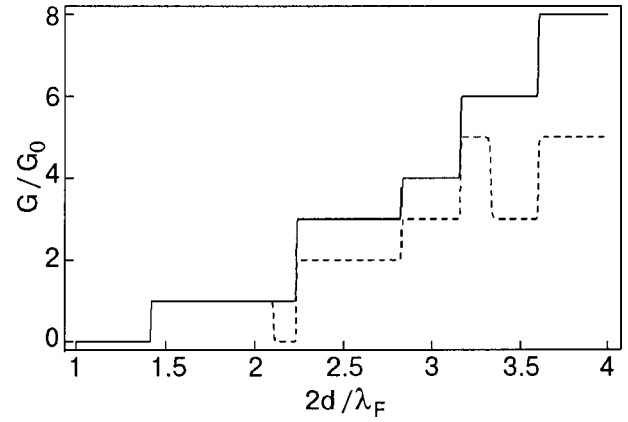

FIG. 1. Quantum steps of the conductance in the limit $V \to 0$. The solid line is for $\varepsilon_1 = 0.9 \varepsilon_F$, the dashed line for $\varepsilon_1 = 0.55 \varepsilon_F$; $T = 0.001 \varepsilon_F$.

these two electron streams moving in opposite directions, with energies differing by the bias energy eV.

After the integration in Eq. (2) over the energy ε we obtain the following equation for the ballistic conductance:

$$G = \frac{dI}{dV} = \frac{1}{2} G_0 \sum_{\mathbf{n}} \left[f_F\left(\varepsilon_{\min} + \frac{eV}{2}\right) + f_F\left(\varepsilon_{\min} - \frac{eV}{2}\right) \right.$$
$$\left. - f_F\left(\varepsilon_{\max} + \frac{eV}{2}\right) - f_F\left(\varepsilon_{\max} - \frac{eV}{2}\right) \right]. \tag{3}$$

At $V \to 0$ formula (3) describes the G_0 steps of the conductance as a function of the contact size:

$$G = G_0 \sum_{\mathbf{n}} \left[f_F(\varepsilon_{\min}) - f_F(\varepsilon_{\max}) \right]. \tag{4}$$

Let us consider a ''model metal'' with the Fermi surface

$$\varepsilon(\mathbf{p}) = \varepsilon_0(\mathbf{p}_{\perp}) + \varepsilon_1(\mathbf{p}_{\perp}) \cos\left(\frac{p_{\parallel} a}{\hbar}\right); \quad \varepsilon_1 < \varepsilon_0, \tag{5}$$

where a is the separation between the atoms. The ''warped'' cylinder $\varepsilon(\mathbf{p})$ is an infinite surface in the direction $p_{\parallel}$ and in this direction passes through all cells of the reciprocal space. If the contact axis is parallel to the $p_{\parallel}$ axis, the transverse part ε_0 of the total energy is quantized $\varepsilon_0 = \varepsilon_0(\mathbf{n})$. But unlike the case of a spherical Fermi surface, the widths of quasi-one-dimensional subbands have the finite value $\varepsilon_1(\mathbf{n})$. So, if the energy $\varepsilon_{\max}(\mathbf{n}) = \varepsilon_0(\mathbf{n}) + \varepsilon_1(\mathbf{n})$ is smaller than the Fermi energy ε_F, the subband below the Fermi level is completely filled and does not participate in the current. That results in negative steps $-G_0$ under the condition $\varepsilon_{\max}(\mathbf{n}) = \varepsilon_F$. Figure 1 illustrates the conductance of a channel of square cross section as a function of the size d. For simplicity we used a model of the Fermi surface in which $\varepsilon_0 = \mathbf{p}_{\perp}^2/2m$ and $\varepsilon_1 = \text{const}$.

By changing the voltage eV we can change the number of open quantum modes for different directions of the electron velocity.[17] In a metal with a closed Fermi surface, if the bias is larger than the distances between energy levels, then as the voltage is increased, the number of quantum modes below the energy level $\varepsilon_F + eV/2$ increases (and each time the conductance increases by $G_0/2$), while the number of modes below the level $\varepsilon_F - eV/2$ decreases, and that leads to jumps $-G_0/2$. The peaks on the point-contact spectrum
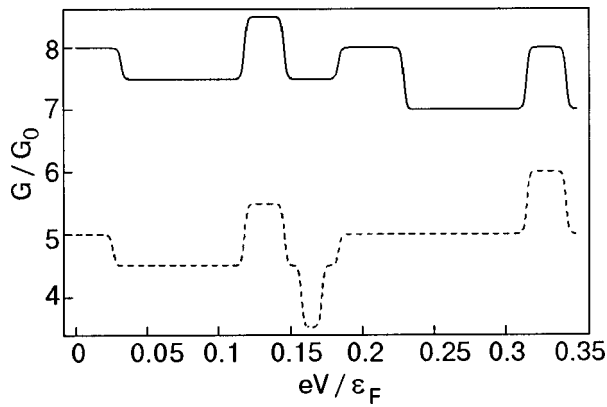
FIG. 2. The dependence of the conductance on the applied voltage. The solid line is for $\varepsilon_1 = 0.9\varepsilon_F$, the dashed line for $\varepsilon_1 = 0.5\varepsilon_F$; $T = 0.001\varepsilon_F$; $d = 1.95\lambda_F$.

dG/dV are determined by the minimum energies of the transverse electron modes $\varepsilon_{\min}$.[17] In the case of an open Fermi surface, increasing the bias leads not only to this but also to the opposite process: at some voltages the maximum energies $\varepsilon_{\max}$ of the subbands go through the energy levels $\varepsilon_F \pm eV/2$, changing the conductance by values $\pm G_0/2$. As a result, the point-contact spectrum has two series of sharp peaks at energies $\varepsilon_F \pm eV/2 = \varepsilon_{\min}(\mathbf{n})$ and $\varepsilon_F \pm eV/2 = \varepsilon_{\max}(\mathbf{n})$. Measuring the distances between these peaks makes it possible to find not only the (minimal) energy of quantum modes in the constriction but also the width of the quantum subbands and its dependence on the number of the mode. In Figs. 2 and 3 the voltage dependence of the quantized conductance and the point contact spectrum of the same constriction are shown.

In the quasiclassical case, we can use the Poisson formula for the summation over discrete quantum numbers in Eq. (3). Using the method developed by Lifshits and Kosevich,[1] we can write the conductance at zero temperature in the form

$$G = G_{\mathrm{Sh}} + G_0 \frac{2}{\pi} \sum_{\mathbf{k},i} \sum_{\alpha=1}^{2} (-1)^\alpha \left[|\mathbf{k}|^{1/2} |\nabla \varepsilon(\mathbf{n}_{i,\alpha})| \right.$$

$$\times |K_{i,\alpha}|^{1/2} \left(\mathbf{k}\frac{\partial \mathbf{n}_{i,\alpha}}{\partial \varepsilon} \right) \Big]^{-1} \sin\left(2\pi \mathbf{k}\mathbf{n}_{i,\alpha} \pm \frac{\pi}{4} \right)$$

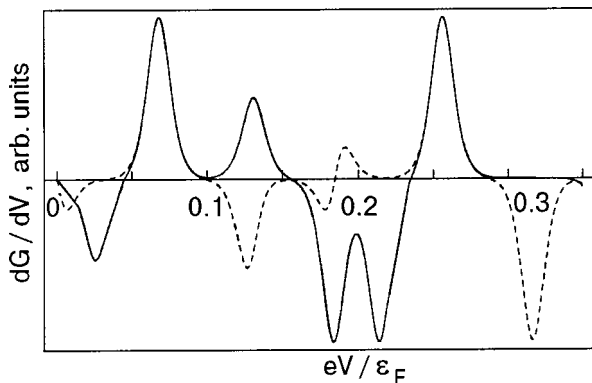$$\times \cos \pi \mathbf{k}\frac{\partial \mathbf{n}_{i,\alpha}}{\partial \varepsilon} eV. \qquad (6)$$

FIG. 3. The point contact spectrum of the microconstriction. The solid line is for $\varepsilon_1 = 0.9\varepsilon_F$, the dashed line for $\varepsilon_1 = 0.5\varepsilon_F$; $T = 0.005\varepsilon_F$; $d = 1.95\lambda_F$.

Here G_{Sh} is the Sharvin conductance;[14] the vector $\mathbf{k}$ is the aggregate of two positive integers k_1 and k_2; $\mathbf{n}_{i,1}$ are the coordinates of the points on the curve $\varepsilon_{\max}(\mathbf{n}) = \varepsilon_F$, and $\mathbf{n}_{i,2}$ are the coordinates of the points on the curve $\varepsilon_{\min}(\mathbf{n}) = \varepsilon_F$, at which the normal to these curves is parallel to the vector $\mathbf{k}$; $K_{i,\alpha}$ is the curvature of the curve $\varepsilon(\mathbf{n}) = \varepsilon_F$ at the points $n_{i,\alpha}$. The sign in front of the phase $\pi/4$ is minus if at the point $\mathbf{n}_{i,\alpha}$ the convexity of the curve is directed in the direction of vector $\mathbf{k}$. In the opposite case, the sign in front of $\pi/4$ is plus. In Eq. (6) the summation is over $\mathbf{k} \neq 0$ and all points $\mathbf{n}_{i,\alpha}$ in the first quadrant. Hence, in the quasiclassical region the conductance oscillates as a function of the constriction diameter and the applied bias, and also depends on the maximum energy of electron motion along the constriction.

Thus the conductance of three-dimensional point contacts between metals with an open Fermi surface may display positive and negative steps $2e^2/h$ as a function of the contact diameter. The negative steps can be observed in the experimental geometry in which the contact axis is parallel to the direction in which the Fermi surface is open. The decreasing of the conductance is a result of the complete occupation of quantum subbands below the Fermi level. The negative steps of the quantum conductance in Al and Pt, which have an open Fermi surface, could be a result of this effect. Of course, the electronic structure of Al and Pt is very complicated, and the electrical properties of these metals cannot be described by the simple model (5). The effect of the open part of the Fermi surface may be masked by the influence on the conductivity of other parts, and instead of negative jumps a negative slope of the conductance plateaus was observed in the experiments of Ref. 9. Recently research on of the nonlinear quantum conductance has begun.[26,27] The ultrasmall size of a point contact makes it possible to produce biases up to 1 V,[26] which opens up the possibility of point-contact spectroscopy of quantum energy modes in three-dimensional contacts. An experimental investigation of point-contact spectra for different directions of the contact axis with respect to the crystallographic orientation of the sample to be studied could enable observation of the effects discussed theoretically in this paper, manifested in the voltage dependence of the conductance of quantum microconstrictions.

We acknowledge fruitful discussions with M. R. H. Khajehpour, A. N. Omelyanchouk, V. G. Peschansky, and I. K. Yanson.

[1] I. M. Lifshits and A. M. Kosevich, Izv. AN SSSR Ser. Fiz. **19**, 395 (1955).
[2] For review see, Yu. F. Komnik, *Physics of Metallic Films* [in Russian], Atomizdat, Moscow (1979).
[3] B. J. van Wees, H. van Houten, C. W. J. Beenakker, J. G. Williamson, L. P. Kouwenhoven, D. van der Marel, and C. T. Foxon, Phys. Rev. Lett. **60**, 848 (1988).
[4] D. A. Wharam, M. Pepper, H. Ahmed, J. E. F. Frost, D. G. Hasko, D. C. Peacock, D. A. Ritchie, and G. A. C. Jones, J. Phys. C: Solid State Phys. **21**, L209 (1988).
[5] J. I. Pascual, J. Mendez, J. Gomez-Herrero, A. M. Baro, N. Garsia, and Vu Thien Binh, Phys. Rev. Lett. **71**, 1852 (1993).
[6] N. Agrait, J. G. Rodrigo, and S. Viera, Phys. Rev. B **47**, 12345 (1993).
[7] C. J. Muller, J. M. van Ruitenbeek, and L. J. de Jongh, Phys. Rev. Lett. **69**, 140 (1992).

[8] J. M. Krans, C. J. Muller, I. K. Yanson, Th. C. M. Govaert, R. Hesper, and J. M. van Ruitenbeek, Phys. Rev. B **48**, 14721 (1993).

[9] J. M. Krans, C. J. Muller, and J. M. van Ruitenbeek, Physica B **194−196**, 1033 (1994).

[10] J. M. Krans, J. M. van Ruitenbeek, V. V. Fisun, I. K. Yanson, and L. J. de Jongh, Nature (London) **375**, 767 (1995).

[11] J. A. Torres and J. J. Saenz, Physica B **218**, 234 (1996).

[12] Y. Imry, *Introduction to Mesoscopic Physics,* Oxford, New York (1997).

[13] A. Szafer and A. D. Stone, Phys. Rev. Lett. **62**, 300 (1989).

[14] I. O. Kulik, A. N. Omelyanchouk, and R. I. Shekhter, Fiz. Nizk. Temp. **7**, 1543 (1977) [Sov. J. Low Temp. Phys. **7**, 740 (1977)].

[15] I. O. Kulik and I. K. Yanson, Fiz. Nizk. Temp. **4**, 1267 (1978) [Sov. J. Low Temp. Phys. **4**, 596 (1978)].

[16] L. I. Glazman and A. V. Khaetskii, JETP Lett. **48**, 591 (1988).

[17] A. M. Zagoskin, JETP Lett. **52**, 435 (1990).

[18] E. N. Bogachek, A. M. Zagoskin, and I. O. Kulik, Fiz. Nikh. Temp. **16**, 1404 (1990) [Sov. J. Low Temp. Phys. **16**, 796 (1990)].

[19] J. A. Torres, J. A. Pascual, and J. J. Saenz, Phys. Rev. B **49**, 16581 (1994).

[20] I. M. Lifshits and V. G. Peschansky, Sov. Phys. JETP **8**, 875 (1958).

[21] P. L. Kapitsa, Proc. Roy. Soc. A **129**, 358 (1928).

[22] V. G. Peschansky, J. A. Roldan Lopes, and Toji Gnado Jao, J. Phys. (France) **1**, 1469 (1991).

[23] O. V. Kirichenko, Yu. A. Kolesnichenko, and V. G. Peschansky, ''Electron phenomena in layered conductors,'' Physics Reviews, I. M. Khalatnikov (Ed.), 18, Part 4 (1996).

[24] L. I. Glazman, G. B. Lesovik, D. E. Khmel'nitskii, and R. I. Shekhter, JETP Lett. **48**, 238 (1988).

[25] R. Landauer, IBM J. Res. Dev. **1**, 233 (1957); Philos. Mag. **21**, 863 (1970).

[26] C. Untidt, G. Rubo Bollinger, S. Vieira, and N. Agrait, in *Quantum and Mesoscopic Phenomena and Mesoscopic Devices in Microelectronics, Bilkent University*, Ankara, Turkey (1999), p. 78.

[27] B. Ludoph, M. H. Devoret, D. Esteve, C. Urbina, and J. M. van Ruitenbeek, Phys. Rev. Lett. **82**, 1530 (1999).

LOW-TEMPERATURE PHYSICS OF PLASTICITY AND STRENGTH

Viscous dislocation drag in KBr crystals at temperatures of 77–300 K

V. P. Matsokin* and G. A. Petchenko

V. N. Karazin Kharkov National University, pl. Svobody 4, 61077 Kharkov, Ukraine
(Submitted December 30, 1999; revised March 13, 2000)
Fiz. Nizk. Temp. **26**, 705–710 (July 2000)

The resonance dislocation absorption of ultrasound in KBr crystals in the frequency region 7.5–217.5 MHz is investigated in the temperature interval 77–300 K. The temperature dependences of the shear modulus G, Debye temperature Θ, dislocation damping coefficient B, and the mean effective length L of a dislocation segment are determined in this temperature interval. The experimentally obtained $B(T)$ curve is compared with the Al'shits–Indenbom theory of dynamic dislocation drag. © *2000 American Institute of Physics.* [S1063-777X(00)01307-4]

1. INTRODUCTION

This paper is a continuation of Refs. 1 and 2, which were devoted to a study of the dynamic characteristics of crystals and, in particular, of the frequency coefficient of the effective viscosity B. The problem of the dynamic mobility of dislocations had been developed quite intensively prior to the studies of Refs. 1 and 2. It had been established that the mobility of dislocations in crystals is governed by mechanisms of different natures—thermal-fluctuation and dynamic. The effect of the latter is most fully manifested in the high-velocity motion, when a dislocation, having a large kinetic energy, overcomes short-range barriers without thermal fluctuations. Under these conditions the force and the dislocation velocity v are related by $F = Bv$ (where F is the force acting on a unit length of dislocation), and its motion can be treated as translation in a viscous medium. In the above-barrier motion of a dislocation energy is dissipated as a result of its interaction with various elementary excitations of the crystal—phonons, electrons, other dislocations, etc. The effect on the dislocation from the forces arising in these interactions is expressed by the coefficient B. Phonon drag on dislocations had been studied both experimentally and theoretically on more than one occasion prior to the studies of Refs. 1 and 2 (a summary of the results is presented in the reveiw[3]). An attempt was made to describe the results in the framework of the Leibfried[4] or Mason[5] theories. However, because of the unusually large discrepancy among the experimental results and their disagreement with the theories,[4,5] for a long time the value of the dynamic viscosity for most of the crystals studied could not be established even in order of magnitude. Its temperature dependence also remained unclear. These difficulties were overcome only after the publication of the Al'shits–Indenbom quantum theory of dynamic dislocation drag.[3] With the help of that theory it became possible to describe a considerable fraction of the experimental material, to refine the conclusions of the theories of Refs. 4 and 5, and to discover new channels of energy dissipation from dislocations, but it was not possible to put this theory to a comprehensive test. The studies of Ref. 6 showed that the method of shock loading, which had been used in the over-

whelming majority of the measurements of the drag coefficient B, was being used in a manner that was methodologically incorrect and was therefore in need of substantial modification. This circumstance stimulated some new studies in which the use of modern experimental technologies made it possible to obtain more reliable data on the temperature dependence of $B(T)$ for the alkali halide crystals LiF,[7,8] NaCl,[8,9] and CsI[8,10] and also Cu[11] and Sb.[12] The results confirmed the correctness of the theoretical conclusions[3] that near the Debye temperature the dislocation damping is is due to a combination of two phonon mechanisms: the phonon wind, and the relaxation of ''slow'' phonons. Nevertheless, this agreement between theory and experiment did not finish the development of this topic—it just marked the beginning of the real possibility of accumulating some new experimental data on the dynamic dislocation drag for crystals with different lattices over a wide range of temperatures, so that it became possible to check not only the aforementioned channels of energy dissipation from a moving dislocation but also some new channels involving Raman scattering, the flutter effect, etc.

Judging from the available data[7–10] on the temperature dependence of $B(T)$, it is advisable to continue this research on other ionic crystals, KBr in particular. This will make it possible to ascertain the general trends in the variation of the phonon dislocation drag in materials of the same structural type and to establish the relative roles of the mechanisms governing these processes, and also to compare the numerical estimates of B with the available data obtained by other experimental methods.[13,14] In addition, because of their low Debye temperature Θ, KBr crystals are promising for studying the drag exerted on dislocations on account of the thermoelastic potentials, which, owing to its quadratic temperature dependence, can be appreciable at high temperatures.[3]

With the goal of identifying the phonon mechanisms governing the dynamic mobility of dislocations in KBr crystals, in this study we have attempted to investigate the temperature dependence of the coefficient of viscosity B by a traveling-wave pulsed method in the megahertz range.
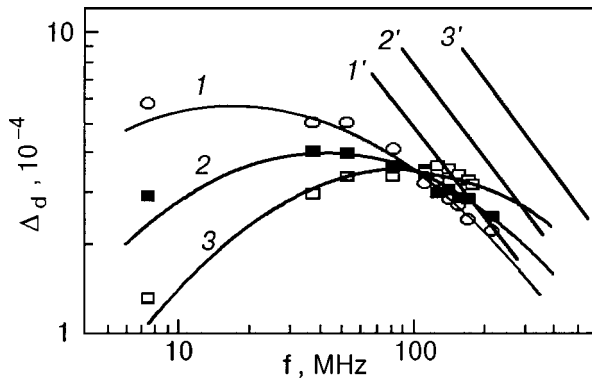
FIG. 1. Frequency dependence of the dislocation damping rate at various temperatures T, K: 300 (*1*), 200 (*2*), 77 (*3*). The solid curves are the theoretical results[15] and their high-frequency asymptotes.

FIG. 2. Temperature dependence of the mean effective length L of a dislocation segment, the maximum damping rate Δ_m, the resonance frequency f_m, and the dislocation damping constant B.

2. EXPERIMENTAL PROCEDURE

For this study we used an original multifunctional apparatus[7] that permits making precision measurements of the damping and the velocities of elastic waves in an automatic mode over a wide range of frequency and temperature, with simultaneous recording of the load curve for different strain rates. The acoustical characteristics were measured in a pulsed scheme with the use of waves of different modes, polarizations, frequencies, and amplitudes. The ultrasound velocity was measured by a pulsed interference method, and its damping by the superimposed exponential method.

This apparatus made it possible to obtain most of the characteristics needed for calculating the damping constant B. The frequency spectra of the acoustical loss were studied in the frequency range 7.5–217.5 MHz and in the temperature interval 77–300 K for longitudinal waves with the use of a quartz piezotransducer with a fundamental frequency of 7.5 MHz. The measurements were made on single-crystal samples of KBr having a purity of 10^{-4} wt.% and dimensions of $18 \times 18 \times 30$ mm, cleaved from the same crystal along cleavage planes and finely ground and polished on the working surface. To remove traces of the mechanical treatment they were annealed in a regime similar to that described in Ref. 9. The working surfaces of the prepared samples were parallel to within about ± 1 μm/cm. Fresh dislocations were introduced into the crystal by compressing it in the $\langle 100 \rangle$ direction until a residual deformation of 0.23% appeared. The ultrasound was passed through the sample in the same direction. The densities of dislocations in the initial (annealed, undeformed) and deformed samples were determined by selective etching and found to be 5.5×10^{8} m^{-2} and 2×10^{9} m^{-2}, respectively. The dislocation contribution Δ_d to the measured ultrasound absorption was determined as the difference of the values obtained for the same sample in the deformed and initial states.

3. EXPERIMENTAL RESULTS AND DISCUSSION

The results on the frequency dependence of the dislocation damping rate Δ_d measured at temperatures of 77, 200, and 300 K on KBr samples with a residual deformation of 0.23% are presented in Fig. 1. The curves for other temperatures in the interval 77–300 K have a similar form and are therefore not shown. It can be seen that the experimentally
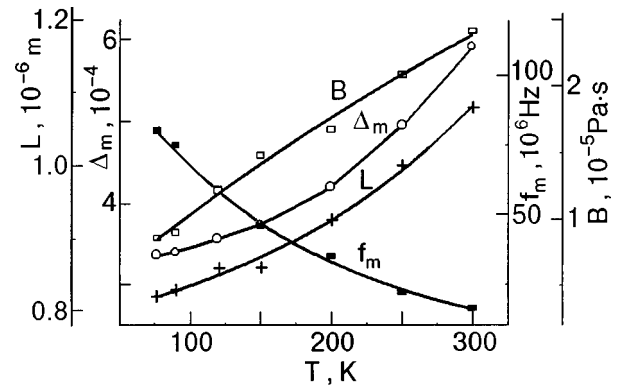
obtained dependence $\Delta_d(f)$ agrees with the normalized frequency profile[15] calculated for the case of an exponential length distribution of dislocation segments. A comparison of the theoretical curve with the experimental curve plotted in the coordinates $\log \Delta_d(\log f)$ was done by numerical methods. Using the results of Ref. 16, the theoretical curve was "tied in" using the points lying on the initial branch and in the resonance region. As we see from Fig. 1, as the temperature is lowered the level of acoustic loss in the sample is lowered, and the frequency spectrum is shifted to higher frequencies. This shift of the height and frequency of the resonance peak is shown by the curves Δ_m and f_m in Fig. 2. The position of the maximum and of the descending branch of the resonance curve, according to Ref. 17, are described by the equations

$$\Delta_m = 2.3 \, \Omega M \Lambda L^2, \tag{1}$$

$$f_m = \frac{0.084 \pi C}{2BL^2}, \tag{2}$$

$$\Delta_\infty = \frac{4\Omega G b^4 \Lambda}{\pi^2 B f}, \tag{3}$$

where Δ_m and f_m are the maximum damping rate and the peak frequency, Δ_∞ is the damping rate for frequencies $f \gg f_m$, Λ is the density of dislocations, L is the mean effective length of a dislocation segment, $M = 8Gb^2/(\pi^3 C)$, C is the effective stress of a bent dislocation, G is the shear modulus in the active slip system, Ω is an orientational factor, ν is Poisson's ratio, and b is the modulus of the Burgers vector. Equation (3), by virtue of of the insensitivity of the limiting absorption to the length distribution of the dislocation loops, can be used to calculate the parameter B if one first determines Δ_∞ from the high-frequency asymptote and Λ by the etch pit method. We note that analogous estimates of B can also be obtained from the resonance parameters Δ_m, f_m, and Λ appearing in formulas (1) and (2). Since the error of determination of the elastic constants due to differences in the samples can be more than 10% (Ref. 18), in the present paper the necessary quantities for finding the viscosity coefficient B were measured on the same sample. To ascertain the temperature dependence of the elastic properties of KBr crystals, we measured the propagation velocity V_l of longitudinal sound waves in the $\langle 100 \rangle$ and $\langle 110 \rangle$ di-
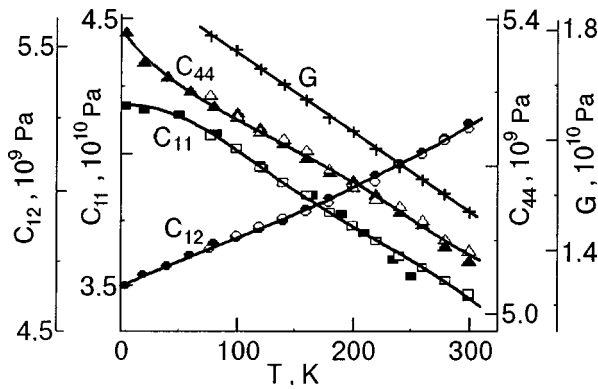
FIG. 3. Temperature dependence of the elastic constants of potassium bromide: C_{12}, C_{11}, C_{44}, G_{110} ($\square$, $\triangle$, $+$, $\bigcirc$—data of the present study; $\blacksquare$—Ref. 21, $\bullet$, $\blacktriangle$—Ref. 20).
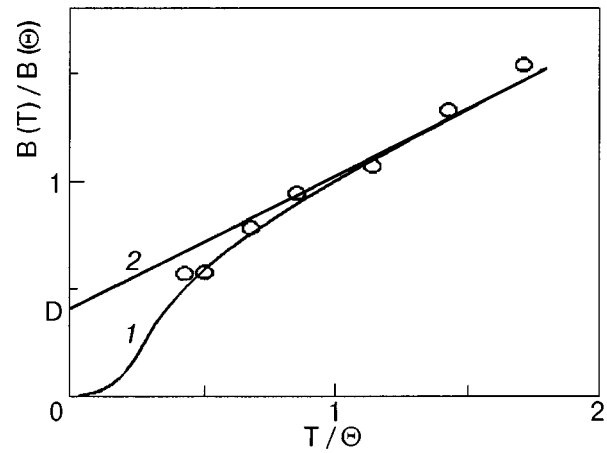

FIG. 4. Comparison of the temperature dependence of $B(T)$ according to formula (5) (curve *1*) with the experimental points for the KBr crystal; curve *2* is the high-temperature asymptote; D is a parameter of the theory[3] and is used in (5).

rections and the velocity V_s for transverse sound waves along the $\langle 100 \rangle$ direction in the initial samples. Then, using the velocity data and the formulas[19]

$$\rho^2(V_{l\langle 100 \rangle}) = C_{11}, \quad \rho^2(V_{s\langle 100 \rangle}) = C_{44},$$

$$\rho^2(V_{l\langle 100 \rangle}) = 0.5(C_{11} + C_{12} + 2C_{44}),$$

we calculated the elastic constants C_{ik}. The results of a comparison of the temperature dependence of C_{ik} with the published data[20,21] are shown in Fig. 3. In these calculations the temperature dependence of the density ρ of the crystals, their working length l, the modulus of the Burgers vector b, and the lattice parameter a were estimated using the formulas given in Refs. 22 and 23. As can be seen from Fig. 3, the results of the present study differ somewhat from the data of Refs. 20 and 21, on account of the differences in the samples. Using the values obtained for C_{ik} we determined the temperature dependence of the orientation factor Ω and shear modulus G (see Fig. 3) for the active slip system $\langle 110 \rangle \{110\}$. The value of Ω varied almost linearly from 0.42 to 0.44 as the temperature was decreased from 300 to 77 K. Such a character of the temperature dependence on decreasing temperature was also observed for the Poisson's ratio ν evaluated from the velocity measurements: it increased from 0.41 to 0.42. Following Ref. 20, from the results for C_{ik} we determined the Debye temperature Θ at 0 K:

$$\Theta^3 = \frac{81N}{4\pi(18+\sqrt{3})}\left(\frac{h}{k}\right)^3\left(\frac{C_{44}}{\rho}\right)^{3/2} f(s,q), \tag{4}$$

where $f(s,q)$ is the elastic anisotropy function, $s = (C_{11}^0 - C_{44}^0)/(C_{12}^0 + C_{44}^0)$, $q = (C_{12}^0 - C_{44}^0)/C_{44}^0$, ρ and C_{ik}^0 are the density and elastic constants of the crystal at $T = 0$ K, k is Boltzmann's constant, h is Planck's constant, $N = 8/a^3$ is the number of lattice sites per unit volume, and a is the lattice constant. For calculating C_{ik}^0 the temperature dependences of C_{11}, C_{12}, and C_{44} were processed on a computer, which yielded the following expressions:

$$C_{11} = (4.17725 + 5.01378 \times 10^{-4}T - 3.35786 \times 10^{-5}T^2$$

$$+ 1.3672 \times 10^{-7}T^3 - 1.89921 \times 10^{-10}T^4)10^{10}\,\text{Pa},$$

$$C_{12} = (4.65914 + 0.00186T - 1.96226 \times 10^{-6}T^2$$

$$+ 6.80952 \times 10^{-9}T^3) \times 10^9\,\text{Pa},$$

$$C_{44} = (5.38125 - 0.00182T + 9.92802 \times 10^{-6}T^2$$

$$- 4.04611 \times 10^{-8}T^3 + 5.50959 \times 10^{-11}T^4)$$

$$\times 10^9\,\text{Pa}.$$

On the basis of the values obtained for the elastic constants C_{ik}^0 and the function $f(s,q)$, we determined the Debye temperature $\Theta = 174.5$ K using the tables of Ref. 20. This value of the Debye temperature is in good agreement with the data of calorimetric measurements and, to a lesser degree, with other results obtained by acoustical methods.[20] Analysis showed that the difference is apparently due to the fact that the change in the lattice constant a with temperature was neglected in Ref. 20, to a slight difference in the slope of the $C_{ik}(T)$ curve, and to the errors associated with finding the values of C_{ik}^0 by a linear extrapolation of the elastic constants from 77 to 0 K.

Using the experimental data on the elastic, acoustical, and dislocation characteristics, we determined the functional form of $B(T)$ and $L(T)$, which are plotted in Fig. 2. One can see that decreasing the temperature from 300 to 77 K leads to a decrease in the dislocation damping and to a shortening of the length of a dislocation segment.

Figure 4 shows the results of a comparison of the measured temperature dependence of $B(T)$ with the theory of Ref. 3, using the Debye temperature Θ calculated according to formula (4).

The theoretical curve was calculated in accordance with Ref. 3 using a formula describing the contribution to the dislocation drag from two phonon mechanisms—the phonon wind, and slow-phonon relaxation:

$$\frac{B(T)}{B(\Theta)} = \frac{f_1(T/\Theta)}{f_1(1)}(1 - Df_2(1)) + D\frac{\Theta}{T}f_2(T/\Theta), \tag{5}$$

where D is a dimensionless parameter determined from experiment by extrapolating to 0 K the high-temperature asymptote of $B(T)/B(\Theta)$ as a function of T/Θ. The values of

the other functions entering Eq. (5) were taken from Ref. 3. We see from Fig. 4 that the theoretical curve gives a good description of the experimental data for $D=0.4$. On the basis of the existing agreement of the temperature dependence of the experimental and theoretical curves, we can conclude that the viscous dislocation drag in KBr crystals is due to a superposition of two mechanisms: the phonon wind and slow-phonon relaxation. This conclusion as to the predominant role of these two phonon mechanisms to the dislocation drag at temperatures close to Θ turns out to be general for both KBr and other crystals.[7–12] However, upon a more detailed analysis of the dislocation drag effects in alkali halide crystals, one can also discern a number of substantial differences. For example, it has been found, in particular, that the value of B at room temperature is smaller by a factor of approximately 1.9 in KBr than in LiF, according to the refined data on the latter crystal,[7] which has a high Debye temperature Θ. An even greater difference is found between the temperature dependence of the dynamic viscosity $B(T)$ in the two crystals.

The slope S of the high-temperature asymptote of $B(T)$ (Fig. 4), which determines the value of the parameter D in relation (5), was found to be approximately 2.5 times larger for KBr than for LiF.[7] These estimates indicate that in KBr crystals the predominant role in the dislocation drag at the temperatures studied is played by processes involving the scattering of phonons rather than their relaxation, as in the case of LiF.[7]

A substantial difference in the values of B is also observed in a comparison of the results of room-temperature measurements in the present study and in Refs. 13 and 14. The value we found, $B=2.4\times10^{-5}$ Pa·s, differs by roughly an order of magnitude from the corresponding values found in those papers: 2.4×10^{-4} Pa·s,[13] and 1.7×10^{-4} Pa·s.[14] The large difference of the results in Ref. 13 may be due to the methodological inaccuracies in the shock loading method of determining the parameter B, which were brought to light in Ref. 6. The overestimate of B obtained by the low-frequency ultrasonic method[14] is apparently due to neglect of the relaxation component of the total dislocation damping, which, according to Ref. 11, can represent a significant contribution.

It remains unclear why the effective length L of a dislocation segment decreases as the temperature is lowered, an effect observed here and elsewhere,[7,9,12] and it is not yet possible to give a rigorous quantitative estimate of the temperature dependence of L. We can, however, suggest some possible factors which we believe might be responsible for the temperature dependence of $L(T)$ (a quantitative analysis of this dependence will require further theoretical and experimental studies).

In the crystal that has been subjected to deformation a dislocation depinned from impurity atoms will execute forced oscillations of a certain amplitude in the field of an ultrasonic wave. The force of interaction F_i between a dislocation and an impurity atom ($F_i=\partial W_i/\partial r$, where $W_i \sim Gb^4/r$ is the binding energy of the dislocation to the impurity atom at a distance between them of r) is insufficient to pin the dislocation. Pinning is also prevented by thermal fluctuations at room temperature; these decrease with decreasing temperature. As the temperature is lowered from 300 to 77 K, the increase in the shear modulus G (Fig. 3) causes an increase in the interaction energy W_i of a dislocation with impurity atoms (even when the temperature dependence of the modulus of the Burgers vector b is taken into account), and because of this the potential obstacles (impurity atoms) can become real pinning points. This leads to changes in the parameters of the length distribution function of the loops, in particular, in the mean value of the length of a dislocation segment and its effective length. This effect is analogous to the introduction of an additional impurity content into the crystal.

The change in $L(T)$ is manifested in a shift of the resonance peak in height and in frequency (Fig. 1). Because of the increase in the shear modulus as the temperature is lowered, the force of linear tension in the dislocations increases ($\sim Gb^2$). At a specified level of external stress (in the amplitude-independent region) there is a decrease in the curvature of the dislocation segment and hence in the area swept out by it in its oscillatory motion. This results in a decrease in the damping rate Δ_d as the temperature is lowered. When the temperature is raised from 77 to 300 K all of the processes take place in the opposite direction.

CONCLUSION

1. We have established the temperature dependence of the dislocation drag coefficient $B(T)$ from the results on the frequency dependence of the dislocation damping rate and ultrasound velocity in KBr crystals by an acoustical echo method in the megahertz frequency range (7.5–217.5 MHz) in the temperature interval (77–300 K).

2. From an analysis of the result for B in the framework of the Al'shits–Indenbom theory of phonon dislocation drag,[3] we have concluded that the dislocation drag is limited to a superposition of the phonon wind and slow-phonon relaxation mechanisms.

3. From measurements of the ultrasound velocity we have determined the temperature dependences of the elastic constants and used them to find the Debye temperature Θ at 0 K, obtaining a value that agrees with the calorimetric measurements.

4. Using the temperature dependences of the resonance frequency, maximum damping rate, shear modulus, and damping coefficient B, we have established the temperature dependence of the mean effective length L of a dislocation segment. We have given a qualitative explanation for why the value of L decreases with decreasing temperature.

*E-mail: matsokin@dcph.kharkov.ua

[1] A. M. Petchenko and V. I. Startsev, Fiz. Tverd. Tela (Leningrad) **16**, 3655 (1974) [Sov. Phys. Solid State **16**, 2373 (1974)].

[2] V. M. Andronov, A. M. Petchenko, and V. I. Startsev, Akust. Zh. **21**, 502 (1975) [Sov. Phys. Acoust. **21**, 314 (1975)].

[3] V. I. Al'shits and V. L. Indenbom, Usp. Fiz. Nauk **115**, 3 (1975) [Sov. Phys. Usp. **18**, 1 (1975)].

[4] G. Leibfried, Z. Phys. **127**, 344 (1950).

[5] W. P. Mason, J. Appl. Phys. **35**, 2779 (1964).

[6] Yu. F. Boĭko, S. V. Lubenets, and L. S. Fomenko, Izv. Vyssh. Uchebn. Zaved., Radiofiz. **7**, 129 (1978).

[7] A. M. Petchenko, Kristallografiya **37**, 458 (1992) [Sov. Phys. Crystallogr. **37**, 237 (1992)].

[8] V. I. Alshits, E. V. Darinskaya, and A. A. Urusovskaya, Phys. Status Solidi A **91**, 533 (1985).

[9] A. M. Petchenko, V. I. Mozgovoĭ, and A. A. Urusovskaya, Fiz. Tverd. Tela (Leningrad) **30**, 2992 (1988) [Sov. Phys. Solid State **30**, 1724 (1988)].

[10] A. M. Petchenko, D. L. Stroilova, and A. A. Urusovskaya, Fiz. Tverd. Tela (Leningrad) **30**, 3456 (1988) [Sov. Phys. Solid State **30**, 1983 (1988)].

[11] N. P. Kobelev, Ya. M. Soĭfer, and V. I. Al'shits, Fiz. Tverd. Tela (Leningrad) **21**, 1172 (1979) [Sov. Phys. Solid State **21**, 680 (1979)].

[12] P. P. Pal-Val and V. Ya. Platkov, Phys. Status Solidi A **38**, 383 (1976).

[13] V. B. Pariĭskiĭ and A. I. Tret'yak, Fiz. Tverd. Tela (Leningrad) **9**, 2457 (1967) [Sov. Phys. Solid State **9**, 1933 (1967)].

[14] V. Ya. Platkov, V. P. Efimenko, and V. I. Startsev, Fiz. Tverd. Tela (Leningrad) **9**, 2799 (1967) [Sov. Phys. Solid State **9**, 2200 (1967)].

[15] O. S. Oen, D. K. Holmes, and M. T. Robinson, US AEC Report NORNL-3017, 3 (1960).

[16] V. Naundorf and K. Lücke, in *Mechanisms of Internal Friction in Solids* [Russian translation], Nauka, Moscow (1976).

[17] A. Granato and K. Lücke, J. Appl. Phys. **27**, 583 (1956).

[18] S. Hart, J. Appl. Phys. **1**, 1277 (1968).

[19] R. Truell, Ch. Elbaum, and B. B. Chick, *Ultrasonic Methods in Solid State Physics*, Academic Press, New York (1969); Mir, Moscow (1972).

[20] A. A. Botaki, A. A. Vorob'ev, and V. A. Ul'yanov, *Radiation Physics of Ionic Crystals* [in Russian], Atomizdat, Moscow (1980).

[21] J. K. Galt, Phys. Rev. **73**, 1460 (1948).

[22] V. E. Ivanov, L. G. Merkulov, and V. A. Shchukin, Ul'trazvukovaya Tekhnika **2**, 3 (1965).

[23] K. K. Srivastava and N. D. Merchant, J. Phys. Chem. Solids **34**, 2069 (1973).

Translated by Steve Torstveit

Statistical analysis of the low-temperature α peak of the internal friction in iron single crystals

V. D. Natsik, P. P. Pal-Val,* L. N. Pal-Val, and Yu. A. Semerenko

B. Verkin Institute for Low Temperature Physics and Engineering, National Academy of Sciences of Ukraine, pr. Lenina 47, 61164 Kharkov, Ukraine

The effect of changes in the ultrasonic frequency or in the dislocation structure of the samples on the parameters of the low-temperature α peak of the internal friction and the Young's modulus defect corresponding to it is investigated experimentally in single crystals of pure iron. A statistical interpretation of the temperature dependence and structural sensitivity of the characteristics of the dynamic relaxation in the neighborhood of the α peak is proposed, based on the assumption of a random scatter of the values of the activation energy of the elementary relaxators. Empirical estimates are obtained for the attempt period and for the mean value and variance of the activation energy of the relaxation process responsible for the α peak of the internal friction in iron. © *2000 American Institute of Physics.* [S1063-777X(00)01407-9]

1. INTRODUCTION

It has been shown in previously published studies[1–6] that a preliminary plastic deformation of single crystals of high-purity iron gives rise to a low-temperature peak of the acoustic absorption, having properties typical of the α peaks in bcc metals. At vibrational frequencies of the order of 10^5 Hz this peak is observed in a region of temperatures of the order of 50 K. The temperature dependence of the elastic modulus corresponding to the investigated vibrational mode of the sample exhibits a characteristic ''step'' in the same temperature region. Those papers also mentioned certain features in the behavior of the shape and parameters of this absorption peak and of the ''step'' of the modulus defect, which indicated that this peak is sensitive to the details of the defect structure of the samples and which could not be explained completely in the framework of the existing theory. In particular, they mentioned a broadening of the peaks, a smearing of the ''step,'' and an upward shift of the temperature of the peak and of the inflection point of the ''step'' after plastic deformation, and the restoration of these parameters after a prolonged annealing.

It should be noted that a low-temperature absorption peak has also been observed in a study of the internal friction of pure iron by low-frequency methods: at vibrational frequencies of the order of 1 Hz such a peak is detected in the temperature interval 28–35 K.[7–9] In Ref. 4 it was conjectured that the peaks observed in Refs. 1–3 and 7–9 have a common physical nature—the resonance interaction of elastic vibrations with the thermally activated nucleation of kink pairs on non-screw dislocations. If it is assumed that the temperature dependence of the relaxation time $\tau(T)$ for this process is described by the standard Arrhenius relation,

$$\tau(T) = \tau_0 \exp(U/kT), \tag{1}$$

then the results of Refs. 1–4 and 7–9 lead to the following empirical estimates for the activation energy and attempt period: $U \approx 0.071$ eV, $\tau_0 \approx 2 \times 10^{-13}$ s.

However, the correctness of this interpretation and the quantitative values of the parameters of the relaxation process are open to question, since the different studies not only used different methods of investigating the internal friction but also samples with different and uncontrolled defect structure.

An internal friction peak with analogous properties has been detected in niobium: at frequencies of the order of 10^5 Hz this peak is localized near 200 K.[10] Unlike the case of iron, in niobium the α peak is observed even in undeformed samples, and a preliminary plastic deformation leads only to a change in its height, width, and position on the temperature axis. Detailed experimental and theoretical studies of the α peak in niobium have shown[10] that the effect of plastic deformation on the shape and parameters of this peak can be explained by assuming a statistical character of the parameters of the elementary relaxators responsible for this peak, and that plastic deformation affects the variance of the activation energies and the volume density of the relaxators.

In the present study this theory is developed further. As a supplement to the results of Ref. 10, where we analyzed the influence of the statistical distribution of the activation energy of the relaxators on the peak of the relaxational absorption of elastic vibrations, here we also describe the statistical smearing of the elastic-modulus defect corresponding to the relaxation resonance. The conclusions of the theory are used to analyze the temperature dependence of the decrement and modulus defect of samples of plastically deformed iron. Additional experiments are carried out to investigate the properties of the α peak recorded in Refs. 1–6, and refined values of the parameters of the elementary relaxators responsible for this peak are obtained.

2. EXPERIMENTAL PROCEDURE

A single crystal of high-purity iron grown by the strain-anneal method[11] was chosen as the object of study. High purity of the sample was achieved by a sevenfold zone re-

fining of the the initial commercial metal (from the firm of Johnson and Matthew, U.K.) and a prolonged (~ 7 days) annealing of the resulting single crystal in an atmosphere of dried hydrogen with a hot zirconium absorber.[12] The final concentration of interstitial impurities (C, N, etc.) was less than 1×10^{-4} at. %. The initial density of growth dislocations was $\sim 10^5 - 10^6$ cm^{-2}.

The sample had the shape of a cylindrical rod, with a diameter of 4 mm and a length of 27 mm. Acoustical measurements were made by the method of a two-component composite oscillator.[13,14] Longitudinal standing waves were excited in the sample, with a frequency of around 88 and 352 kHz (the corresponding angular frequencies of the vibrations were $\omega_1 \approx 5.5 \times 10^5$ s^{-1} and $\omega_2 \approx 22.1 \times 10^5$ s^{-1}). The amplitude of the ultrasonic deformation in our experiments had a value $\varepsilon_0 \sim 10^{-7}$, which corresponded to amplitude-independent acoustical relaxation.

To establish the relation of the acoustical properties of the investigated material with dislocation processes, fresh dislocations were introduced into the sample at room temperature by means of a plastic deformation by the four-point bending method without detaching the samples from the piezoelectric transducer. The measure of plastic deformation used was the residual strain of the outer ''fiber'' or outside-line, which had a value $\varepsilon_{pl} \approx 3\%$.

The orientation of the sample was determined from outside-line Laue diffraction patterns. The longitudinal axis of the sample coincided with the vector of the longitudinal sound wave and the axis of loading during the plastic deformation and had a direction close to $\langle 731 \rangle$, coplanar with the directions $\langle 111 \rangle$ and $\langle 101 \rangle$ and making an angle of $\sim 45°$ with them. The chosen orientation of the sample ensured that in deformation by bending there is single slip in the $(\bar{1}01)$ plane, with a maximum resolved stress in the direction of the Burgers vector $[111]$.[15]

In the temperature region $6\,K < T < 150\,K$ we measured the temperature dependence of the decrement δ of the sample and the resonant frequency of the composite oscillator, from which we calculated the dynamic elastic Young's modulus E.[14]

The first measurements on undeformed and preliminarily deformed samples of the orientation indicated above were made in 1988. Subsequently the deformed samples were held at room temperature for 11 years, and low-temperature acoustical experiments were again performed on them. This procedure made it possible to establish how the α peak of dislocation acoustic relaxation is affected by the changes occurring in deformed samples during prolonged low-temperature annealing.

The measurements were made on both the undeformed and deformed samples in the absence of magnetic field. It has been shown[6] that placing a sample in a saturating magnetic field does not affect the position or shape of the peak in question, while it increases the background acoustical absorption considerably.

3. RESULTS OF THE MEASUREMENTS

Figure 1 shows the temperature dependence of the decrement $\delta(T)$ measured at a frequency of $\omega_1/2\pi = 88$ kHz in an undeformed sample, in a sample that has been subjected
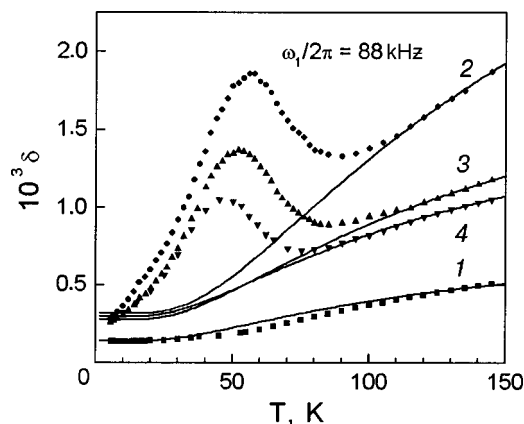

FIG. 1. Temperature dependence of the decrement of vibrations of a single-crystal sample of high-purity iron: *1*—undeformed sample; *2*—the sample deformed at room temperature to a residual plastic deformation $\varepsilon_{pl} \approx 3\%$, the measurements being made immediately after the deformation; *3*—the same sample 3 days after deformation; *4*—the deformed sample 11 years after deformation. The solid curves are the background absorption described by formula (14) with the parameters given in Table I.

to plastic deformation, and in the latter sample after low-temperature annealing (at room temperature) for a short and a long time. The preliminary deformation increases the decrement significantly over the entire temperature interval and gives rise to the so-called α peak of acoustical relaxation on the $\delta(T)$ curve at $T \sim 54$ K. The height of the peak, as was shown in Ref. 1–6, increases with increasing ε_{pl}, and its position on the temperature axis in general depends on the structural state of the samples. Precise values of the peak temperatures $T_p(\omega_1)$ for various types of structural states of the sample are presented in Table I.

Increasing the vibrational frequency while maintaining the same structural state of the sample shifts the peak to higher temperatures. Figure 2 illustrates the influence of the vibrational frequency on the temperature dependence of the decrement of a sample that had been plastically deformed and then held at room temperature for a long time prior to the measurements (structural state *4* in Fig. 1 and Table I). It is seen that increasing the frequency of the ultrasound by a factor of 4 causes the peak temperature to increase from $T_p(\omega_1) = 44.4$ K to $T_p(\omega_2) = 50.7$ K.

Figure 3 shows the temperature dependence of the dynamic Young's modulus $E(T)$ measured at a frequency of $\omega_1/2\pi = 88$ kHz on undeformed and deformed samples. The plastic deformation leads to a significant decrease in the Young's modulus and gives rise to a ''step'' on the $E(T)$ curve, centered at the temperature T_p of the α peak. Low-temperature annealing (a hold at room temperature) will partially restore the properties altered in the deformation: the decrement decreases and Young's modulus increases. The temperature of the absorption peak and the inflection point of the modulus ''step'' are shifted to lower temperatures (Figs. 1 and 3).

4. INFLUENCE OF THE STATISTICAL DISTRIBUTION OF THE ACTIVATION ENERGY OF THE RELAXATORS ON THE TEMPERATURE DEPENDENCE OF THE ACOUSTICAL ABSORPTION AND MODULUS DEFECT

The evolution of the temperature dependence of the decrement of vibrations and the dynamic elastic modulus as a

TABLE I. Dependence of the acoustical relaxation parameters in iron on the structural state of the sample, and the empirical values of the parameters of the theory.

Parameter of the peak or "step"	Structural state of the samples			
	1	2	3	4
$T_P(\omega_2)$, K	–	–	–	50.7
$T_P(\omega_1)$, K	–	54.3	49.5	44.4
$A_1 \times 10^4$	1.4	3.2	3.0	2.8
$A_2 \times 10^3$	0.8	4.2	2.1	1.7
U_{BG}, eV	0.01	0.01	0.01	0.01
E_0, GPa	186.2	184.0	184.4	185.3
$B \times 10^7$ K^{-2}	6.91	9.19	8.33	7.87
$(C_r \Delta_0) \times 10^3$	–	4.72	2.71	1.80
d	–	7.55	6.10	5.80
D, eV	–	0.0177	0.0143	0.0136
U_0, eV	–	0.037	0.037	0.037
τ_0, s	–	2.5×10^{-11}	2.5×10^{-11}	2.5×10^{-11}

result of plastic deformation and subsequent low-temperature annealing is apparently due to the introduction of fresh dislocations into the sample. Fresh dislocations, on the one hand, are relaxators: kink pairs are nucleated on them in a fluctuational manner. The resonance of acoustical vibrations with this process gives rise to the relaxation peak. On the other hand, the random distribution of dislocations leads to a statistical distribution of local values of the internal stress fields and of the parameters of the kinks in the bulk of the sample. In the annealing process a partial relaxation of the dislocation structure and of the long-range internal stress fields due to dislocations occurs. As was shown in Ref. 10, the different influences causing structural changes in a sample can alter the parameters of the statistical distribution of the activation energies U of the relaxation process that gives rise to the peak in the acoustical absorption. An increase in the variance of the activation energy will increase the asymmetry and broaden the peak and will also cause the location of the peak to shift to higher temperatures. Clearly, a decrease in the variance (as occurs during annealing of the sample) will give a result of the opposite sign.

The corresponding changes should also occur in the temperature dependence of the modulus defect, but no statistical analysis of the modulus defect was done in Ref. 10. Let us take the approach of Ref. 10 to analyze the temperature de-
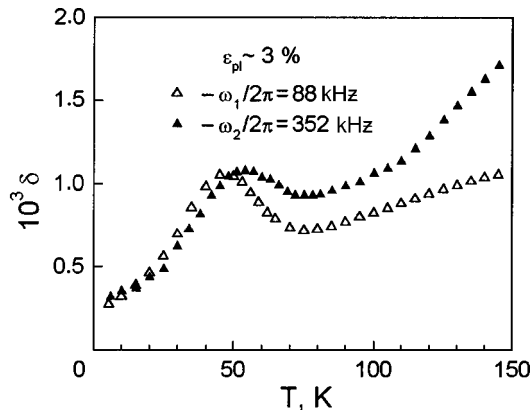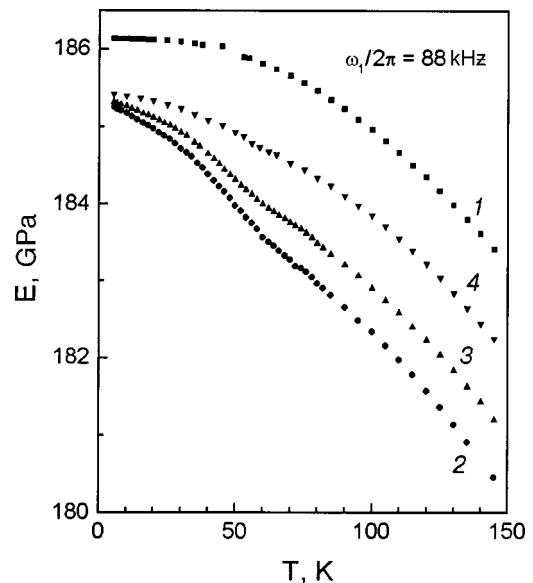
pendence of the modulus defect in the presence of a statistical distribution of the activation energy U of the relaxation process.

Consider the changes brought about in the elastic and dissipative properties of a crystal by a thermally activated relaxation process for which the temperature dependence of the relaxation time $\tau(T)$ is described by the exponential expression (1). In a rather perfect crystal such a process can be assigned three parameters whose values are determined, to a first approximation, by the geometric and energy parameters of the defect-free crystal: the activation energy U_0, the attempt period τ_0, and the characteristic elementary contribution of an individual relaxator to the decrement of vibrations, Δ_0. If C_r stands for the relative volume concentration of these relaxators which interact with the vibrational mode under consideration, the expressions for the temperature dependence of their total contribution in the linear response ap-

FIG. 2. Shift of the ultrasonic absorption peak upon a change in the vibrational frequency in the sample with structural state *4* in Fig. 1 and Table I.

FIG. 3. Temperature dependence of the dynamic Young's modulus of a single-crystal sample of high-purity iron: *1*—undeformed sample; *2*—the sample deformed at room temperature to a residual plastic deformation $\varepsilon_{pl} \approx 3\%$, the measurements being made immediately after the deformation; *3*—the same sample 3 days after deformation; *4*—the deformed sample 11 years after deformation.

proximation have the form of a Debye peak for the decrement of vibrations $\delta(T,\omega)$ and of a ''step'' for the modulus defect $\Delta M(T,\omega)/M_0$:

$$\delta(T,\omega)=2\,\delta_p\frac{\omega\tau(u_0)}{1+\omega^2\tau^2(u_0)};$$

$$\frac{\Delta M(T,\omega)}{M_0}=\frac{2\,\delta_p}{\pi}\frac{1}{1+\omega^2\tau^2(u_0)};\tag{2}$$

$$\delta_p=C_r\Delta_0,\quad u_0=U_0/kT,\quad \tau(u)=\tau_0 e^u.\tag{3}$$

The peak temperature $T_p^{(0)}$ and the inflection point on the ''step'' are given by

$$\omega\tau(u_0)=1,\quad T_p^{(0)}=\frac{U_0}{k\ln(\omega\tau_0)}.\tag{4}$$

The heights of the peak, δ_p, and of the ''step,'' $2\delta_p/\pi$, are proportional to both the contribution Δ_0 of an individual relaxator and the relaxator concentration C_r.

If the crystal contains a complex system of local structural inhomogeneities and long-range internal stress fields due to a random distribution of various defects, the parameters of an elementary relaxor acquire random increments in different regions of the crystal, and they should instead be treated as random quantities with their corresponding distribution functions. The decrement of vibrations and modulus defect of the macroscopic sample are thereby converted to certain complicated functions $\bar{\delta}(T,\omega)$ and $\Delta\bar{M}(T,\omega)/M_0$, obtained by statistical averaging of expressions (2).[16]

As was shown in Ref. 10, if it is assumed that the effects on the structure of the crystal are weak (the variance D^2 of the activation energy is small, $D\ll U_0$), in the low-temperature region ($kT\ll U_0$) one can to a first approximation perform the statistical averaging using only the distribution of the activation energy and to exponential accuracy neglecting the variance of the parameters Δ_0 and τ_0. Thus, in view of the comments made above, we shall consider the single random parameter of the problem to be the activation energy U of an elementary relaxator. As the statistical characteristic of this quantity we introduce the probability density of values of U in the form of a function $P(U)$ defined on the interval $(0,\infty)$ and satisfying the normalization condition

$$\int_0^\infty P(U)dU=1.\tag{5}$$

In the presence of a statistical distribution $P(U)$ of values of the activation energy, the functions $\bar{\delta}(T,\omega)$ and $\Delta\bar{M}(T,\omega)/M_0$ are defined by the expressions

$$\bar{\delta}(T,\omega)=2\Delta_0 C_r\int_0^\infty dU\,P(U)\frac{\omega\tau_0\exp(U/kT)}{1+\omega^2\tau_0^2\exp(2U/kT)},\tag{6}$$

$$\frac{\Delta\bar{M}(T,\omega)}{M_0}=\frac{2\Delta_0 C_r}{\pi}\int_0^\infty dU\,P(U)\frac{1}{1+\omega^2\tau_0^2\exp(2U/kT)}.\tag{7}$$

As the simplest example of a distribution $P(U)$ that will permit a satisfactory description of the influence of random internal stresses on the low-temperature relaxation resonances, a quasi-Gaussian function was proposed in Ref. 10:

$$P(U)=\frac{1}{\sqrt{2\pi}D}\left(\frac{U}{U_0}\right)\exp\left[-\frac{(U-U_0)^2}{2D^2}\right],$$

$$D\ll U_0.\tag{8}$$

As $D\to 0$ the distribution (8) goes over to a Dirac delta function, $P(U)=\delta(U-U_0)$, so that the functions $\bar{\delta}(T,\omega)$ and $\Delta\bar{M}(T,\omega)/M_0$ go over to functions (2) at small values of the variance. Increasing the parameter D causes broadening of the distribution (8) and shifts its maximum to higher energies. This leads to a broadening of the peak and ''step'' on the temperature curves of the averaged decrement $\bar{\delta}(T,\omega)$ and modulus defect $\Delta\bar{M}(T,\omega)/M_0$ and also an upward shift of the peak temperature T_p. The asymmetry of distribution (8) about U_0 on account of the factor of U in the pre-exponential factor leads to additional asymmetry of the temperature dependence of $\bar{\delta}(T,\omega)$ and $\Delta\bar{M}(T,\omega)/M_0$ about T_p.

The integrals (6) and (7) with the distribution function (8) can be evaluated by numerical integration methods. To put the integral into a form convenient for numerical integration, we change to a new integration variable x and a new set of parameters of the problem, according to the relations

$$\ln x=\frac{U}{kT},\quad \theta=\frac{T}{T_P^{(0)}},\quad \Omega=\frac{1}{\omega\tau_0},$$

$$U_0 kT_p^{(0)}\ln\Omega,\quad d=\frac{\sqrt{2}D}{kT_p^{(0)}}=\frac{\sqrt{2}D}{U_0}\ln\Omega.\tag{9}$$

Here we have introduced a dimensionless temperature θ, a dimensionless inverse frequency Ω, and a dimensionless characteristic variance d. When these substitutions are made, formulas (6) and (7) take the form

$$\bar{\delta}=C_r\Delta_0 F_1(\theta,\Omega,d),$$

$$F_1=\frac{2\Omega\theta^2}{\sqrt{\pi}d\ln\Omega}\int_1^\infty dx\,\frac{\ln x}{x^2+\Omega^2}\exp\left[-\left(\frac{\theta\ln x-\ln\Omega}{d}\right)^2\right],\tag{10}$$

$$\frac{\Delta\bar{M}(T,\omega)}{M_0}=\frac{C_r\Delta_0}{\pi}F_2(\theta,\Omega,d),$$

$$F_2=\frac{2\Omega^2\theta^2}{\sqrt{\pi}d\ln\Omega}\times\int_1^\infty\frac{dx}{x}\frac{\ln x}{x^2+\Omega^2}$$

$$\times\exp\left[-\left(\frac{\theta\ln x-\ln\Omega}{d}\right)^2\right].\tag{11}$$

In real situations $\ln\Omega=-\ln(\omega\tau_0)\geq 10$, and therefore our initial assumption that $D\ll U_0$ is consistent with taking $d>1$ (zero variance corresponds to the limit $d\to 0$, and a relatively large variance to $d\geq 1$).

The nature of the influence of the statistical distribution of the activation energy of the relaxators on the temperature dependence of the absorption and modulus defect in the neighborhood of the relaxation resonance is illustrated in Fig. 4. At small values of d the temperature dependence of the function $F_1(\theta,\Omega,d)$ has a maximum, while the function $F_2(\theta,\Omega,d)$ has an inflection point at $\theta\cong 1$, and these func-
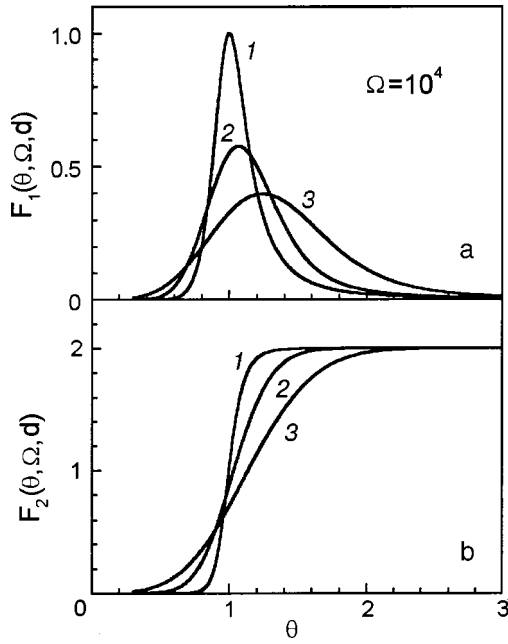
FIG. 4. Transformation of the temperature dependence of the absorption peak (a) and of the elastic modulus defect (b) in the region of the relaxation resonance as the variance of the activation energy of the relaxator is increased. The curves show the results of a numerical integration in formulas (10) and (11) at a fixed value of the frequency parameter $\Omega = 10^4$ and values of the variance parameter $d = 0$ (*1*), 2.5 (*2*), and 5 (*3*).

tions practically coincide with the Debye peak and the classical ''step'' (curves *1* in Fig. 4). Increasing the parameter d causes the peak and ''step'' to shift to higher temperatures, broaden, and increase their asymmetry (curves *2* and *3* in Fig. 4).

It should be kept in mind that the various influences affecting the statistical characteristics of the relaxators in a crystal can also change the relaxator concentration C_r. Because of this, the behavior of the heights of the absorption peak and the ''step'' of the modulus defect can have additional features not present in Fig. 4. In particular, there can be an increase (decrease) of max $\bar{\delta}$ and max $\Delta \bar{M}/M_0$ together with a shift of T_p to higher (lower) temperatures in those cases when the change in C_r is more significant than the change in max F_1 and max F_2. This means that in interpreting the experimental data, the parameter $C_r \Delta_0$ must be treated as one of the phenomenological parameters of the theory, subject to experimental determination.

5. ANALYSIS OF THE EXPERIMENTAL RESULTS

The experimentally observed shift of the absorption peak upon a relatively small change in the vibrational frequency (Fig. 2) makes it possible to employ the standard formulas of dynamic relaxation theory[16] and to obtain estimates of the parameters of the relaxation process—the attempt period τ_0 and the effective value U_{eff} of the activation energy:

$$\tau_0^{-1} = \omega \exp\left[T_p \left(\frac{\partial T_p}{\partial \ln \omega} \right)^{-1} \right]$$

$$\cong \omega_1 \exp \frac{T_p(\omega_2)\ln(\omega_2/\omega_1)}{T_p(\omega_2) - T_p(\omega_1)}, \tag{12}$$

$$U_{\text{eff}} = kT_p^2 \left(\frac{\partial T_p}{\partial \ln \omega} \right)^{-1} \cong \frac{kT_p(\omega_1)T_p(\omega_2)\ln(\omega_2/\omega_1)}{T_p(\omega_2) - T_p(\omega_1)}. \tag{13}$$

Using the values of $T_p(\omega)$ given in Table I for the sample with structural state *4*, we obtain $\tau_0 \approx 2.5 \times 10^{-11}$ s, $U_{\text{eff}} \approx 0.043$ eV.

Since we are neglecting the statistical distribution (or scatter) of the attempt period, the value obtained for τ_0 can be regarded as the final estimate for one of the main parameters of the relaxation process under study. But if the crystal contains random structural inhomogeneities, then the parameter U_{eff} given by formula (13) will only indirectly reflect the value of the second of the leading parameters of the relaxators, U_0. The value of U_{eff}, generally speaking, depends on the value of U_0 and on the variance D^2 of the activation energy.[10] Obtaining empirical estimates for U_0 and D will require an additional, deeper and less simplified, analysis of the experimental data.

To perform a statistical analysis of the experimental data it will be necessary first to subtract off correctly the background absorption for all the peaks in Fig. 1 and to separate out from the temperature dependence of the Young's modulus in Fig. 3 the background temperature dependence unrelated to the relaxation process under investigation.

5.1. Background of temperature dependence of the decrement of vibrations

In view of the high sensitivity of the background absorption to the temperature and structural state, one can assume that it is partly due to nonconservative viscous motion of dislocations,[17,18] with an activation energy of the process U_{BG}, which is different from the activation energy of the process responsible for the α peak:

$$\delta_{BG} = A_1 + A_2 \exp\left(-\frac{U_{BG}}{kT} \right). \tag{14}$$

The coefficients A_1 and A_2 and the parameter U_{BG} are adjustable parameters whose values change upon changes in the defect structure of the sample; in particular, the coefficient A_1 can be substantially altered by changes in the magnetic structure of the samples.[6] Graphs of the function (14) for undeformed and deformed samples with the values of the parameters A_1, A_2, and U_{BG} given in Table I are shown by the solid curves in Fig. 1. Thus we are talking about checking whether the experimentally obtained temperature dependence $\delta^{(e)}(T)$ (Fig. 1) can be described by the relation

$$\delta^{(e)} = A_1 + A_2 \exp\left(-\frac{U_{BG}}{kT} \right) + C_r \Delta_0 F_1(\theta, d, \Omega) \tag{15}$$

for a suitable choice of the constants appearing in it.

5.2. Background temperature dependence of the Young's modulus

To perform a statistical analysis of the temperature dependence of the Young's modulus $E(T)$ it is necessary first to separate out that part of the temperature dependence which is due to the relaxation process under study.

It is well known that the total strain of a real crystal under mechanical loading is the sum of an elastic component

and an inelastic component. The main difference between them is that the elastic strain occurs instantaneously, while the inelastic has a certain time dependence determined by the relaxation processes. In connection with the presence of a relaxation component it is customary to distinguish two limiting values of the elastic modulus: the unrelaxed modulus M_U, which determines the reaction of the crystal to a load in the absence of the inelastic contribution, and the relaxed modulus M_R, which is measured after a lapse of time much greater than the characteristic relaxation times for all the relaxation processes that are important in the temperature interval under consideration. If the crystal is subjected to periodic loading with an angular frequency ω, then its mechanical properties will be determined by the dynamic elastic modulus $M(\omega,T)$, the value of which depends on both the vibrational frequency and the temperature. Here $M_R < M(\omega,T) < M_U$, and there exists a certain modulus defect $M_U - M(\omega,T)$.

In our case the contribution to the modulus defect from the relaxation process under study is described by formula (11) with $M_0 = M(\omega,0)$. In addition, there is a certain contribution to the modulus defect from the nonresonance interaction of the sound with dislocations of various slip systems, with the magnetic structure of the sample, and with thermal phonons and conduction electrons.[18–21] To establish the most important mechanisms determining the modulus defect in the temperature interval under study one requires data on the frequency dependence of the modulus over a rather wide range of vibrational frequencies. Such data are lacking for the single-crystal iron investigated here. However, the temperature dependence of the Young's modulus $E^{(e)}(T)$ measured in experiments at a fixed vibrational frequency for the undeformed sample (i.e., in the absence of dislocation resonance) has a rather simple and smooth form (curve *1* in Fig. 3). Thus we propose to describe the temperature dependence $E^{(e)}(T)$ measured for an iron sample in different structural states by a single analytical approximation:

$$E^{(e)}(T) = E_0 \left[1 - BT^2 - \frac{C_r \Delta_0}{\pi} F_2(\theta, \Omega, d) \right]. \qquad (16)$$

The quantities E_0 and B appearing in this expression will be treated as adjustable parameters subject to experimental determination; in general their values should depend on the vibrational frequency and on the structural state of the sample (including the magnetic structure[6]).

Empirical values of E_0 are easily determined by extrapolating the curves shown in Fig. 3 to the value $T = 0$ K (see Table I). The last term in (16) describes the statistically averaged contribution to the modulus defect of the relaxation resonance under study and must be matched with the last term in expression (15) for the vibrational decrement.

5.3. Relaxation resonance

The form of the temperature dependence of the decrement after the background absorption is subtracted off is shown in Fig. 5a.

To obtain the parameters U_0 and D and to be convinced of the quantitative agreement of the experimental data and formula (15), one can do a numerical analysis on a computer. Judging from the crude estimates for U_{eff} and τ_0 obtained at
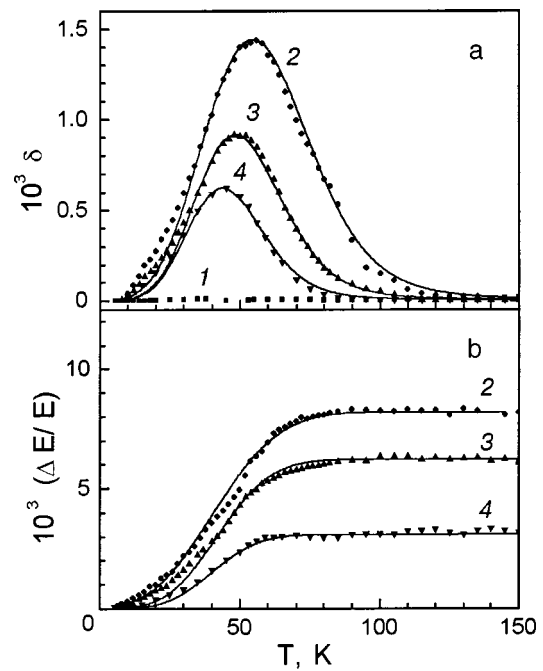

FIG. 5. Comparison of the experimental data on the temperature dependence of the decrement of vibrations (a) and the dislocation part of the dynamic Young's modulus defect (b) for different structural states of the sample (see Figs. 1 and 3) with the theoretical dependences (15) and (16) plotted for the set of parameters U_0, D, and $C_r\Delta_0$ chosen by numerical analysis and presented in Table I.

the beginning of this Section, we can choose values of the parameters U_0, D, and $C_r\Delta_0$ that will permit lining up the experimental points for $\delta(T)$ with the graphs of the function (15) to a high degree of accuracy. The possible of doing this is illustrated by the solid curves in Fig. 5a, and the corresponding best-fit values of the parameters of the theory are given in the bottom rows of Table I. The values of U_0, D, and $C_r\Delta_0$ were chosen so as to come as close as possible to the experimental points of the theoretical graphs in the central region.

The possible of using formula (16) to describe the experimentally measured temperature dependence of the Young's modulus of iron is illustrated in Fig. 5b. The solid curves show the theoretical temperature dependence of that part of the modulus defect which is due to the relaxation process under study: these are graphs of the function (11) constructed for the values of the parameters U_0, D, and $C_r\Delta_0$ found from analysis of the absorption peak (see Table I). The graphs are compared with the experimental points obtained after subtraction from the experimentally measured values of the Young's modulus $E^{(e)}(T)$ a background $E_0(1 - BT^2)$, with the numerical values of E_0 and B given in Table I.

Thus, after correctly subtracting the nonresonance background from the experimentally measured values of the vibrational decrement $\delta^{(e)}(T)$ and Young's modulus $E^{(e)}(T)$, the main features in these quantities due to the relaxation process under study are described satisfactorily by the theory of a statistically "smeared" relaxation resonance with a distribution function of the activation energy in the quasi-Gaussian form (8). The statistical scatter of the values of the activation energy for the relaxation process giving rise

to the α peak in iron turns out to be very large ($d \gg 1$). Therefore, the refined value of the activation energy for this process obtained as a result of a statistical analysis, $U_0 = 3.7 \times 10^{-2}$ eV, differs considerably from the estimate $U_{\text{eff}} = 4.3 \times 10^{-2}$ eV obtained by the conventional method using formula (13).

Our statistically refined values for the parameters of the relaxation processes giving rise to the α peak of the internal friction in iron ($\tau_0 = 2.4 \times 10^{-11}$ s and $U_0 = 3.7 \times 10^{-2}$ eV) differ very strongly from the values $\tau_0 = 2 \times 10^{-13}$ s and $U = 7.1 \times 10^{-2}$ eV obtained in Ref. 4 from a comparison of this peak with the peak of the low-frequency internal friction in the temperature region around 30 K.[7–9] This circumstance does not support the view that these peaks have a common physical nature. However, a final answer to this question can be given only after it becomes possible to perform a statistical analysis of the second peak. Unfortunately, the set of experimental data obtained in Refs. 7–9 is not complete enough to permit such an analysis.

6. CONCLUSIONS

The main goal of this study was the further development of the method proposed in Ref. 10 for the statistical description of the acoustical relaxation in crystals with random structural inhomogeneities. We have assumed that the elastic vibrations excite a thermally activated relaxation process in the crystal, with an activation energy that is a random quantity with a quasi-Gaussian distribution function. In Ref. 10 an analysis was made of these features present in the temperature dependence of the decrement of vibrations on account of the statistical ''smearing'' of the relaxation resonance. In the present paper we have analyzed the influence of the statistical distribution of the activation energy on the temperature dependence of the contribution of the relaxation process to the elastic modulus defect.

In this paper, as in Ref. 10, the results of the statistical theory of the relaxation resonance have been used to interpret experimental data obtained in the study of a concrete physical object. In this connection a series of experiments was done to study the properties of the low-temperature α peak of the internal friction measured on plastically deformed samples of high-purity iron.[1–6] Measurements were made of the shift of the peak temperature upon a change in the vibrational frequency and as a result of the rearrangement of the defect structure of an iron sample. The changes in the shape of the corresponding ''step'' on the temperature de-

pendence of the Young's modulus defect was also studied. It was shown that the experimental behavior of the acoustical relaxation in iron in the region of the α peak finds a satisfactory interpretation in terms of the statistical theory of the relaxation resonance.

As a result of a statistical analysis we obtained empirical estimates for the attempt period and for the mean value and variance of the activation energy of the relaxation process responsible for the α peak of the internal friction in iron.

*E-mail: palval@ilt.kharkov.ua

[1] M. Kakegawa and K. Sakamoto, Jpn. J. Appl. Phys. **9**, 1057 (1970); K. Takita and K. Sakamoto, Scr. Metall. **4**, 403 (1970).

[2] P. P. Pal-Val and S. Kadečkova, Phys. Status Solidi A **94**, K29 (1986).

[3] P. P. Pal-Val, V. D. Natsik, and S. Kadečkova, Phys. Status Solidi A **105**, K37 (1986).

[4] P. P. Pal-Val, V. D. Natsik, and S. Kadečkova, Philos. Mag. A **56**, 407 (1987).

[5] P. P. Pal-Val, Fiz. Nizk. Temp. **23**, 1250 (1997) [Low Temp. Phys. **23**, 938 (1997)].

[6] P. P. Pal-Val, Fiz. Nizk. Temp. **25**, 83 (1999) [Low Temp. Phys. **25**, 63 (1999)].

[7] V. Hivert, P. Groh, P. Moser, and W. Frank, Phys. Status Solidi A **42**, 511 (1977).

[8] I. G. Ritchie, J. F. Dufresne, and P. Moser, Phys. Status Solidi A **50**, 617 (1978).

[9] J. San Juan, G. Fantozzi, C. Esnouf, F. Vanoni, and A. Bernalte, J. Phys. (France) **44**, C9-685 (1983).

[10] V. D. Natsik, P. P. Pal-Val, L. N. Pal-Val, and Yu. A. Semerenko, Fiz. Nizk. Temp. **25**, 748 (1999) [Low Temp. Phys. **25**, 558 (1999)].

[11] K. Z. Saleeb and S. Kadečkova, Kristall und Technik **9**, 1265 (1974).

[12] T. Hejnal, S. Kadečkova, V. Novak, and B. Šestak, Czech. J. Phys. B **27**, 1263 (1977).

[13] P. P. Pal'-Val' and H. J. Kaufmann, Fiz. Nizk. Temp. **9**, 325 (1983) [Sov. J. Low Temp. Phys. **9**, 163 (1983)].

[14] V. D. Natsik, P. P. Pal'-Val', and S. N. Smirnov, Akust. Zh. **44**, 640 (1998) [Acoustical Phys. (Moscow) **44**, 553 (1998)].

[15] B. Šestak and J. Blahovec, Phys. Status Solidi **40**, 595 (1970).

[16] A. S. Nowick and B. S. Berry, *Anelastic Relaxation in Crystalline Solids*, Academic Press, New York (1972); Atomizdat, Moscow (1975).

[17] G. Schoeck, E. Bisogni, and J. Shyne, Acta Metall. **12**, 1466 (1964).

[18] V. S. Postnikov, *Internal Friction in Metals* [in Russian], Metallurgiya, Moscow (1974).

[19] G. Leibfried, ''Gittertheorie der mechanischen und thermischen Eigenschaften der Kristalle,'' in *Handbuch der Physik*, edited by S. Flügge, Vol. 7, Part 1, Springer-Verlag, Berlin (1955).

[20] G. A. Alers, in *Physical Acoustics*, edited by W. P. Mason, Vol. IV, Part A, Academic Press, New York (1960); Mir, Moscow (1969).

[21] T. Bernstein, Phys. Rev. **132**, 50 (1963)

Translated by Steve Torstveit

Features of the microstructure and low-temperature yield stress of quenched Al–Li alloys

I. S. Braude, T. V. Grigorova, N. V. Isaev,* V. V. Pustovalov, and V. S. Fomenko

B. Verkin Institute for Low Temperature Physics and Engineering, National Academy of Sciences of Ukraine, pr. Lenina 47, 61164 Kharkov, Ukraine

The features of the microstructure of quenched Al–Li alloys with lithium concentration below the solubility limit (3.8 at. %) and above the solubility limit (7.0 and 10.4 at. %) are studied by the x-ray diffractometry. In addition to the standard structural reflections, the diffraction patterns of all the alloys show diffuse halos that fall off in intensity as the lithium concentration is increased. As a result of an analysis of the intensity of the diffuse scattering of x rays it is established that the observed halos are due to short-range order of the layered type in regions with a characteristic radius of 1.5 nm. The decrease in the intensity of the diffuse halo on the diffraction pattern of the alloy Al–10.4 at. %Li and the appearance of new structural reflections are explained by the precipitation of disperse particles of the δ' phase. It is shown that these particles have a substantial influence on the mechanism of plastic deformation in these alloys in the temperature region 40–170 K. © *2000 American Institute of Physics.* [S1063-777X(00)01507-3]

INTRODUCTION

It is known that the temperature dependence of the yield stress of the majority of fcc solid solutions at moderately low temperatures is governed by the thermally activated motion of dislocations through impurity barriers. The empirical parameters of this motion in the binary alloys Al–Li subjected to homogenizing annealing and quenching were discussed recently in Refs. 1 and 2. The analysis in those papers of the experimental dependence of the flow stress on the impurity concentration, temperature, and strain rate of the samples showed that the values of some of the parameters of the thermally activated plasticity were in disagreement with the theoretical ideas about the motion of dislocations through point obstacles. The reason for this lies in the features of the phase state of the alloy: at lithium concentrations above 4–5 at. % the annealing and quenching process gives rise to the nucleation of the lithium-rich ordered δ' phase (Al$_3$Li).[3] In the earliest stages of the decomposition one also observes the formation of clusters or regions with short-range order.[4] A study of these defects is of interest from the standpoint of understanding the mechanisms of low-temperature plasticity of aluminum–lithium alloys, since they can serve as additional obstacles to the thermally activated motion of dislocations.

In the present study we have carried out an x-ray structural analysis of quenched aluminum–lithium alloys, and the results are compared with the temperature and concentration dependences of the yield stress of these alloys in the temperature range 40–170 K, where the plastic deformation is of a pronounced thermally activated character.

EXPERIMENTAL PROCEDURE

We investigated Al–Li binary alloys with equilibrium (3.8 at. %) and nonequilibrium (7.0 and 10.4 at. %) lithium concentrations. All of the samples were subjected to a homogenizing anneal in an argon atmosphere at a temperature of 823 K for 5 h and then quenched in ice water. In terms of their composition and heat treatment, the polycrystalline samples corresponded to those used in a study of low-temperature plastic deformation in Refs. 1 and 2.

The x-ray powder-pattern method was used to study powders obtained by crushing the initial samples. The powders were placed in a quartz container mounted in a holder. To estimate the distortions of the crystal lattice due to the crushing of the samples, we analyzed the profiles of the diffraction estimating the value of the microdeformation and the size of the coherent scattering region. An estimate by an approximation method showed that the microdeformation and coherent scattering region in pure Al have values of 0.09% and 70 nm, while in the alloy Al–7 at. %Li they are 0.16% and 77 nm. The close values of these parameters indicates that the technology used to obtain the powders did not introduce substantial distortions to the crystal lattice.

The x-ray diffraction patterns were taken on a DRON-2.0 diffractometer in Cu-K_α radiation (with a Ni filter) at room temperature in a $\theta - 2\theta$ scheme with the use of the following collimating slits: in front of the sample—a slit 2 mm wide and a Soller slit; behind the sample—a collimator, a Soller slit, and a slit 1 mm wide; in front of the counter—a slit 0.5 mm high. The intensity of the scattering was measured point-by-point, by counting the number of pulses in 40 s at intervals of $\Delta(2\theta) = 0.01°$ across the angular range $10° < 2\theta < 140°$. From the position of the maximum, which is determined in this way to an accuracy of 10^{-2} deg, we studied the intensity distribution of the diffuse scattering and calculated the value of the lattice parameter of the crystal by a least-squares averaging of the data from nine reflections.
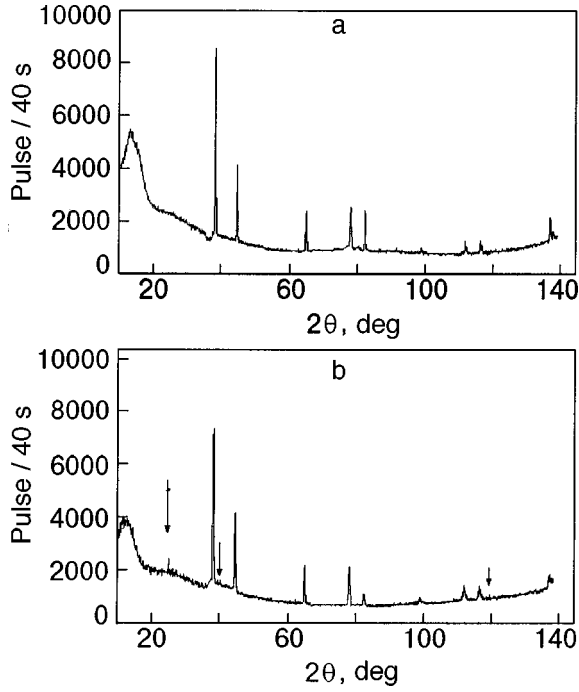
FIG. 1. Dependence of the x-ray scattering intensity I on the scattering angle (2θ) in the angle interval 10–140° for the alloys Al–3.8 at. %Li (a) and Al–10.4 at. %Li (b).

EXPERIMENTAL RESULTS AND DISCUSSION

The general view of the diffraction patterns of the Al–Li alloys is shown in Fig. 1. It is seen that the diffraction patterns consist of structural diffraction peaks and diffuse halos. As the Li concentration is increased from 3.8 to 10.4 at. %, the maximum intensity of the diffuse halos decreases by approximately 30%. The diffuse maxima are not observed on the diffraction patterns of pure Al. The structural diffraction reflections for all of the alloys studied are narrow lines with a redistributed intensity, their position depending weakly on the concentration of the doping element. The diffraction patterns of the supersaturated alloys showed additional reflections (Fig. 1b).

1. Microstructure of the alloys

One of the main characteristics of the fine structure of an alloy is the short-range order parameter α. For its precise determination one usually uses data on the intensity of the diffuse scattering of x rays by single crystals. In the case of polycrystalline samples with a metastable short-range order the required calculations simplify substantially in the case of cubic symmetry, for which α depends only on the moduli of the radius vectors ρ_m of the sites of the average lattice and does not depend on their direction. For this reason, in calculating the short-range order parameters $\alpha(\rho_m)$ we shall take into account the values of the intensity of the diffuse scattering in the interval of angles 10–40° and use the expression for two-component alloys,[5]

$$I_D(\mathbf{k}) = N c_A c_B (f_A - f_B)^2 \sum_m \alpha_{\text{eff}}(\rho_m) e^{i\mathbf{k}\cdot\rho_m}, \quad (1)$$

where N is the number of atoms, c_A, c_B and f_A, f_B are the concentrations of the alloy components and their atomic
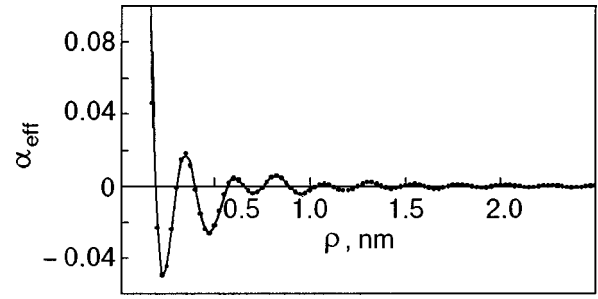

FIG. 2. Dependence of the effective short-range order parameter α_{eff} on the distance ρ for the alloy Al–10.4 at. %Li.

scattering factors, respectively, ρ_m are the radius vectors of the sites of the average lattice, $\mathbf{k} = 2\pi\mathbf{S}$, $|\mathbf{S}| = 2 \sin\theta/\lambda$, 2θ is the angle between the incident and scattered rays, $\alpha_{\text{eff}}(\rho_m)$ is the effective short-range order parameter. We write H in the form $H(\mathbf{k}) = I_D(\mathbf{k})/N[c_A c_B (f_A - f_B)^2]$ and, using the least-squares method, require that the sum of the squares of the deviations of the calculated $H(\mathbf{k})$ from the experimentally determined value be minimum:

$$\left| \sum_s H(k_s) - \sum_s \sum_i c_i \alpha_{\text{eff}}^{(i)} \cos \mathbf{k}_s \cdot \rho_m \right|^2 = \min, \quad (2)$$

where the c_i are the coordination numbers.

The number of equations in (2) is equal to the number of coordination spheres taken into account. Since the measurements were made on polycrystalline samples, after averaging over all $\mathbf{k}$ and taking the inverse Fourier transform of the sum, we obtain the expression

$$\alpha_{\text{eff}}(\rho) = \int_0^\infty \frac{I_D(s)\sin(2\pi\rho s)4\pi s^2 d\,s(2\pi\rho s)^{-1}}{N c_A c_B (f_A - f_B)^2}. \quad (3)$$

Because $\alpha_{\text{eff}}(0) = 1$, for calculating $\alpha_{\text{eff}}(\rho)$ it is sufficient to take into account the relative changes in intensity:

$$\alpha_{\text{eff}}(\rho) = \frac{1}{2\pi\rho} \frac{\int I_D(s)\sin(2\pi\rho s)s\,d\,s}{\int I_D(s)s^2 d\,s}. \quad (4)$$

The integration of expression (2) was done by a special computer program between the limits $5° < 2\theta < 38°$. The error in the evaluation of the integral due to the cutting off of the range of integration is not more than 10%.

For all the alloys the calculated dependence of α_{eff} on ρ has the form shown in Fig. 2. Within the limits of the first coordination sphere ($\rho < 0.3$ nm) the values $\alpha_{\text{eff}} > 0$ are characteristic for short-range order of the layered type (negative short-range order[5]) and agree with the data obtained in Ref. 4 for single crystals of Al–11.4 at. %Li. With increasing ρ the parameter α_{eff} is periodically alternating in sign and becomes equal to zero at $\rho > 1.5$ nm. This dependence of $\alpha_{\text{eff}}(\rho)$ is typical for a correlated position of atoms of one type. An estimate showed that for the alloys investigated in this work the characteristic size of the ordered regions is not larger than 1.5 nm.

Using the data on $\alpha_{\text{eff}}(\rho)$, let us attempt to determine the partial order parameters in these alloys. For this we make a number of simplifying assumptions:
1) $\alpha_{\text{eff}}(\rho) = \alpha_{AB}(\rho)$;
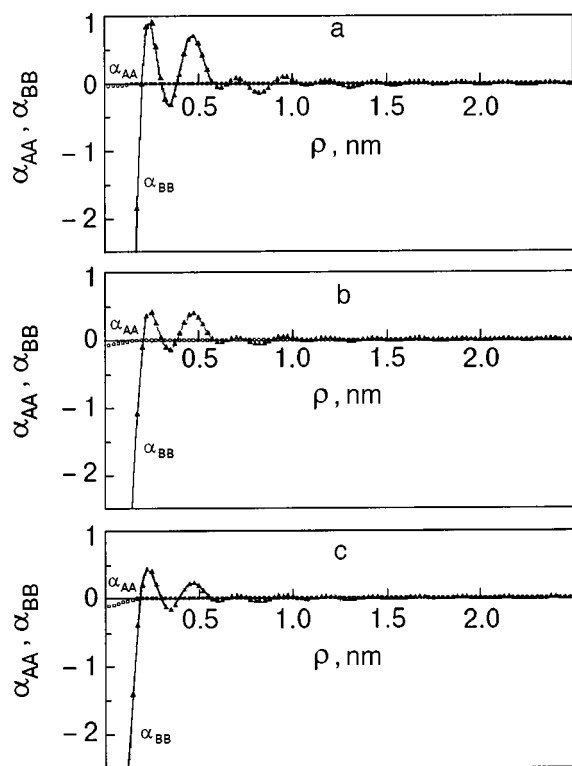2) the parameters $\alpha_{AB}(\rho) = \alpha_{BA}(\rho)$;

FIG. 3. The partial short-range order parameters for the arrangement of same-type atoms, α_{AA} and α_{BB}, versus ρ for the alloys Al–3.8 at. %Li (a), Al–7 at. %Li (b), and Al–10.4 at. %Li (c).

FIG. 4. The partial short-range order parameters α_{AA}, α_{BB}, and α_{AB} as functions of the distance ρ in the alloy Al–3.8 at. %Li; i is the number of the coordination sphere.

3) the probability n_{pj} that an atom of type p is adjacent to an atom of type j is proportional to the concentration of atoms of type j. Then α_{pj} is unrelated to the concentrations of the elements, and $\alpha_{AB}(\rho)$ depends linearly on the amount of the introduced impurity c_j. That this assumption is realistic is confirmed by the known experimental data on the short-range order parameter in the binary alloys Al–Zn, Ti–Mo, Pt–Co, and Fe–Al.[5] In the framework of the simplifying assumptions, the parameters of the pair correlations in the position of the same-type atoms α_{AA} and α_{BB} can be obtained from the relations

$$\alpha_{AA} = -\frac{c_B}{c_A}\alpha_{AB}, \quad \alpha_{BB} = -\frac{c_A}{c_B}\alpha_{BA}. \quad (5)$$

The results of the corresponding calculations for the three alloys investigated here are shown in Fig. 3. The correlated position of the same-type atoms, which is included in the fluctuation of their average concentration and is due to the short-range order, is characterized by the amplitudes of the parameters α_{AA} and α_{BB}. Such correlation is inherent in a greater degree for lithium (α_{BB}) and in a lesser degree for aluminum (α_{AA}). Thus the first coordination sphere is enriched with lithium atoms in comparison with their average concentration in the alloy. After that one observes an alternation of depleted and enriched coordination spheres. The correlations in the position of the same-type atoms, on the contrary, are such that within the first coordination sphere there is a deficit of atoms of the other type than the central atom in comparison with their average concentration in the alloy (see Fig. 2). Figure 4 shows the dependence of the partial order parameters α_{AA}, α_{BB}, and α_{AB} in the alloy
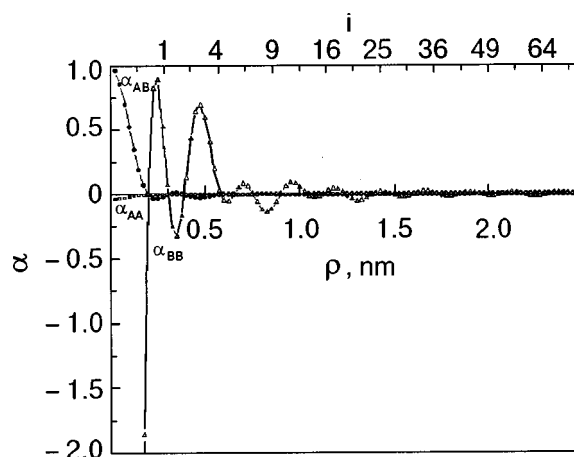
Al–3.8 at. %Li for the case when the central atom is Al. In the first coordination sphere the Li atoms are surrounded by Al atoms ($\alpha_{AB} > 0$), while a rearrangement occurs in the second coordination sphere: the Li atoms collect into ordered regions. As ρ increases, there is a successive alternation of coordination spheres enriched and depleted in lithium atoms. In contrast, an ordered arrangement of aluminum atoms in the alloy is not observed.

Our analysis of the x-ray diffuse scattering intensity has shown that the structures of all the alloys studied have regions of short-range order enriched or depleted in lithium atoms. An estimate of their average radius (1.5 nm) agrees with the average size of the clusters (1.8 nm) in Al–11.4 at. %Li single crystals[4] and with the radius of the nuclei of the new δ' phase (1.3 nm), which have a crystal lattice of the type $L1_2$ and are formed in the very early stages of decomposition in the alloy Al–7.0 at. %Li.[3] As the concentration of the doping element increases (above the solubility limit) the number of ordered regions decreases, as is indicated by the falloff of the intensity of the diffuse halo (see Fig. 1). Here new reflections appear on the diffraction pattern: their intensity is weak, but their position corresponds to the position of the reflections of the δ' phase recorded in Ref. 7.

The maximum intensity of the diffuse halo in Al–3.8 at. %Li indicates a high concentration of ordered regions below the solubility limit of the doping element. This may be due to the high mobility of lithium in aluminum, to the different electronic structure of the atoms,[5,6] and to the prolonged irradiation of the sample during the x-ray measurements. At the same time, the diffraction pattern. The diffraction pattern of this alloy does not contain any additional new-phase reflections (see Fig. 1a).

2. Lattice parameter of the crystal

It is known that lithium only distorts the crystal lattice of aluminum slightly, but the published data on the sign of the distortions are contradictory. For example, in one of the first papers[6] devoted to this question it was shown that the aluminum lattice is slightly compressed upon the dissolution of lithium, on account of the different ionic radii and valences of the atoms, and the dependence $a(c)$ is close to linear in
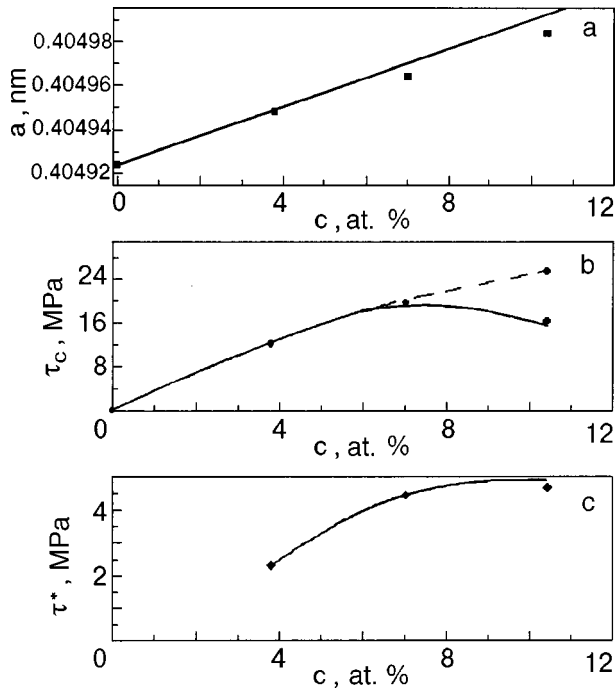
FIG. 5. Concentration dependence of the lattice parameter a of the crystal (a), of the critical stress τ_c for activationless motion of a dislocation (the dashed curve corresponds to expression (9)) (b), and of the effective stress τ^* at $T = 77$ K (c).

TABLE I. Parameters of the thermally activated motion of dislocations in Al–Li alloys.

c, at. %	c^*, at. %	τ_i, MPa	τ_c, MPa	H_0, eV	f
3.8	3.8	4.8	12.7	0.24	–
7.0	5.9	7.3	19.9	0.26	0.06
10.4	8.5	10.5	15.4	0.40	0.13

The estimates of f given in Table I are in good agreement with the data obtained in Ref. 3 for quenched alloys subjected to a similar heat treatment, which indirectly confirms the validity of the assumptions made.

3. Influence of microstructure on the thermally activated motion of dislocations

In Refs. 1 and 2 it was noted that not all of the regularities of the plastic deformation of quenched Al–Li alloys in the temperature range 40–170 K agree with the concepts of thermally activated motion of dislocations through barriers formed by impurity atoms. According to those concepts, the strain rate $\dot{\varepsilon}$, the applied stress τ, and the temperature T are related by the Arrhenius equation as

$$\dot{\varepsilon} = \dot{\varepsilon}_0 \exp[-H(\tau^*/kT)], \qquad (7)$$

where $\dot{\varepsilon}_0$ is a temperature-independent pre-exponential factor, $\tau^* = \tau - \tau_i$ is the effective stress, τ_i is the characteristic value of the internal stress, H is the effective activation energy (enthalpy), and k is Boltzmann's constant. The experimentally observed temperature dependence of the yield stress and the other parameters of the plasticity in the indicated temperature interval are best described by Eq. (7) with an $H(\tau^*)$ of the form

$$H(\tau^*) = H_0 [1 - (\tau^*/\tau_c)^{2/3}]^{3/2}, \qquad (8)$$

where τ_c is the critical stress for activationless (forced) depinning of the dislocations from the impurity barriers, and H_0 is the characteristic energy parameter of the interaction of a dislocation with a barrier, which in the case of barriers of a single type is independent of their concentration. For fcc solid solutions of substitution this parameter has a value of 0.1–0.2 eV, as a rule.

The empirical values of some of the parameters of the thermally activated motion of dislocations for Al–Li alloys deformed directly after quenching from 823 K in ice water are presented in Table I and Fig. 5b,c.

It is seen that some of the values obtained are inconsistent with the concepts described above. For example, under the condition that all three alloys represent an "ideal" solid solution, in which the effective barriers for dislocations are impurity atoms, the value of the characteristic energy parameter H_0 of the interaction of a dislocation with such barriers should not depend on their concentration c, and the critical stress τ_c, as follows from expressions (7) and (8), should vary by a power law:

$$\tau_c \sim c^n, \qquad (9)$$

where $n = 0.5$–0.7. The curve of $\tau_c(c)$ presented in Fig. 5b is inconsistent with the theoretical relation (9). In addition,

---

the interval 3.5–5.0 at. %Li. In Ref. 7, on the contrary, a linear growth of $a(c)$ was observed in the interval 3.8–13 at. %Li. The anomalously weak expansion of the lattice was explained by an appreciable ionization of the lithium atoms: both neutral atoms and positive ions of lithium are substituted in the aluminum lattice. As a result, some of the cells undergo expansion and other compression, and the averaged parameter a determined by the x-ray method depends only weakly on the composition of the solid solution. The complex microstructure of the quenched alloys was not taken into account in those studies.

In connection with the contradictory data on the dependence $a(c)$, in the present study we investigated the dependence of the lattice parameter of the alloys on the initial lithium concentration; the result is shown in Fig. 5a. Doping with lithium leads to a weak expansion of the lattice, $(1/a)\Delta a/\Delta c = 1.5 \times 10^{-3}$, and the dependence $a(c)$ itself deviates from linear.

The aforementioned features of the microstructure of the quenched alloys suggest that the observed nonlinearity of $a(c)$ is due to the diffusion of lithium from the matrix into particles of the δ' phase. Since Al–3.8 at. %Li is an equilibrium alloy, one can estimate the true lithium concentration c^* in the matrices of the two supersaturated alloys, which will be lower than the initial concentration (see Table I and Fig. 5a). For an estimate of the volume fraction of second-phase inclusions we use the relation

$$f = \frac{c - c^*}{c_\rho - c^*}, \qquad (6)$$

where $c_p = 0.23$ corresponds to the lithium concentration in a particle of the second phase (see Ref. 8).

the value of H_0 in the alloy Al–10.4 at. %Li reaches values that are atypical for fcc solid solutions of substitution (see Table I).

The reasons for the observed contradictions lie in the structural features of the quenched state. For mobile dislocations the regions with short-range order, or clusters, and the nuclei of the δ' phase can act as additional barriers which affect the rate of plastic deformation at low temperatures. The number of such barriers per unit length of dislocation will be less than the number of single atoms, which leads to a decrease in τ_c, since c in expression (9) has the meaning of the concentration of any effective thermal-activation barriers. At the same time, the corresponding value of H_0 will be larger than for a single lithium atom.

It follows from Fig. 5a,b that the correction to the true lithium concentration in an atomically dispersed phase [on the assumption of a linear dependence of the lattice parameter $a(c)$] does not ensure that the power law (9) will be obeyed for all the alloys studied. In addition, the slight size mismatch of the aluminum and lithium atoms (weak lattice distortion) does not account for the large value of the parameter H_0 given for Al–10.4 at. %Li in Table I.

On the other hand, the data on the intensity of the diffuse halos (see Fig. 1) and the change in the short-range order parameters (Fig. 4) are evidence that the number of ordered clusters per unit volume decreases with doping. However, this is not reflected in the value of the empirical parameters of the thermally activated plasticity obtained for the equilibrium alloy Al–3.8 at. %Li, which has a high concentration of such clusters.

Thus the most effective thermal-activation barriers are the disperse nuclei of the second phase, the volume fraction of which increases in the concentrated alloy. It is known that the mechanism for the cutting apart of a paired dislocation of a δ' particle, which has an ordered lattice ($L1_2$) is controlled by specific barriers that arise within a particle as a result of the transverse slip of screw dislocation segments.[8] At temperatures above 50 K this mechanism also has a pronounced thermally activated character. As was shown in Ref. 9, when the temperature is raised from 50 to 100 K the growth of the effective stress, due to the cutting apart of the particles, can compensate the decrease in the effective stress due to friction in the matrix. This accounts for the fact that, unlike the nonmonotonic behavior of $\tau_c(c)$ at $T=0$, the experimentally observed dependence of $\tau^*(c)$ at $T=77$ K (see Fig. 5c) is monotonic, i.e., it corresponds to the theoretical expression (9).

CONCLUSION

1. The diffraction patterns of the three investigated Al–Li alloys contain diffuse halos with great intensity in addition to the diffraction peaks. Analysis of the intensities of the diffuse halos showed that they are due to regions with short-range order of the layered type, with radii of 1.5 nm or less. The falloff of the intensity of the diffuse halo as the lithium concentration is increased is accompanied by the appearance of new structural reflections, corresponding to inclusions of the δ' phase.

2. Doping of aluminum with lithium and the observed phase transformations cause a slight expansion of the crystal lattice of the alloy.

3. Inclusions of the δ' phase should be regarded as effective barriers for the thermal-fluctuational motion of dislocations at temperatures in the range 40–170 K.

[*]E-mail: isaev@ilt.kharkov.ua

----

[1] V. S. Fomenko, N. V. Isaev, and V. V. Pustovalov, Fiz. Nizk. Temp. **19**, 429 (1993) [Low Temp. Phys. **19**, 301 (1993)].
[2] N. V. Isaev, V. V. Pustovalov, V. S. Fomenko, and S. É. Shumilin, Fiz. Nizk. Temp. **20**, 832 (1994) [Low Temp. Phys. **20**, 653 (1994)].
[3] V. Mahadev, K. Mahlingam, G. L. Liedliedl, and T. H. Sanders, Jr., Acta Metall. Mater. **42**, 1039 (1994).
[4] V. I. Iveronova and A. A. Katsnel'son, in *Short-Range Order in Solid Solutions* [in Russian], Nauka, Moscow (1977).
[5] H. J. Axon and W. Hume-Rothery, Proc. Roy. Soc. A **193**, 1 (1948).
[6] M. I. Zamotorin, in *Proceedings of the Leningrad Polytechnical Institute*, No. 180 (1955).
[7] J. Perez-Landazabal, M. L. No, G. Madariaga, and J. San Juan, in *Proceedings of the IV International Aluminum-Lithium Conference*, Garmisch-Pantenkirchen, Germany (1991), p. 149.
[8] S. Takeuchi and E. Kuramoto, Acta Metall. **21**, 415 (1973).
[9] N. V. Isaev, V. V. Pustovalov, V. S. Fomenko, and S. É. Shumilin, Fiz. Nizk. Temp. **22**, 99 (1996) [Low Temp. Phys. **22**, 74 (1996)].

Translated by Steve Torstveit

SHORT NOTES

Low-temperature pyroelectricity in thermodynamically nonequilibrium media

V. K. Novik* and N. D. Gavrilova

Physics Department, M. V. Lomonosov Moscow State University, Vorob'evy Gory, 119899 Moscow, Russia
(Submitted January 20, 2000; revised March 6, 2000)
Fiz. Nizk. Temp. **26**, 728–732 (July 2000)

The temperature dependence of the pyroelectric coefficient $\gamma^{\sigma}(T)$ of pyroelectrics in thermodynamic equilibrium at $T \rightarrow 0$ varies in accordance with Nernst's theorem by the law $\gamma^{\sigma}(T) \propto T^{n \geqslant 3}$, which means a sharp drop in $\gamma^{\sigma}(T)$ for $T < 1.5\,\mathrm{K}$ and precludes the efficient use of pyroelectrics in technical applications. It is shown experimentally that this fundamental limitation does not apply to thermodynamically nonequilibrium polar media, for which $\gamma^{\sigma}(T) \cong \mathrm{const}$ for $T < 1.5\,\mathrm{K}$. © *2000 American Institute of Physics.* [S1063-777X(00)01607-8]

INTRODUCTION

Low-temperature ($T < 4$ K) pyroelectricity is of current interest in connection with a number of promising applications, deriving, in particular, from the possibility of amplifying weak signals. The unique properties of low-temperature IR sources[1] and α-particle detectors[2] have been plainly demonstrated even for universal (unspecialized for low temperatures) pyroelectric materials. According to the theoretical predictions,[3] lowering the working temperatures to $T < 2$ K will permit an improvement in the characteristics of these transducers by at least an order of magnitude. Moreover, the development of materials for this temperature region runs up against some fundamental obstacles—the third law of thermodynamics, in accordance with which the transducing properties of a thermodynamically equilibrium polar medium fall off sharply as $T \rightarrow 0$.

Experiments have confirmed these relationships. There is some hope of surmounting this barrier by using materials with a temperature-dependent dipole charge,[4] but even for them the existing theory[5] predicts a falloff of the transducing properties, albeit a slower one. In this paper we present the results of experiments which open up a way of overcoming this fundamental barrier through the use of thermodynamically nonequilibrium polar media.

THEORY

It has been shown repeatedly that the thermodynamic relations for the pyroelectric effect imply that the pyroelectric coefficient $\gamma^{\sigma}(T)$ measured at a constant stress can be written as a sum of two components:

$$\gamma^{\sigma}(T) = \gamma^{\varepsilon}(T) + \gamma^{s}(T), \tag{1}$$

where $\gamma^{\varepsilon}(T)$ is the primary pyroelectric coefficient, which can be measured at a constant size and shape of the crystal, i.e., in the absence of temperature-induced deformation, $\varepsilon = \mathrm{const} = 0$, and $\gamma^{s}(T)$ is the secondary pyroelectric coefficient,

$$\gamma^{s}(T) = d_{ijk}^{T,E}(T) c_{jklm}^{T,E}(T) \alpha_{lm}^{\alpha,E}(T).$$

Here $d_{ijk}^{T,E}$, $c_{jklm}^{T,E}$, and $\alpha_{lm}^{\sigma,E}$ are the piezoelectric coefficients, the elastic stiffness constants, and the coefficient of thermal expansion, respectively, and the sum is over all repeated indices; i is the direction parallel to the spontaneous polarization, and E is the electric field.

It is customary to assume that general phenomenological theories can be developed only for the component $\gamma^{\varepsilon}(T)$, since the second term $\gamma^{s}(T)$, which especially for lower symmetries, contains a significant number of temperature-dependent components, reflects the individual properties of the crystals.

The conditions of thermodynamic stability (integrity) of the crystal[6] and the third law of thermodynamics[7] impose restrictions on the type of dependence $\gamma^{\varepsilon}(T)$ as $T \rightarrow 0$ for $T \leqslant 0.1 \Theta_D$ (Θ_D is the Debye temperature).

According to Ref. 6, the following condition should hold:

$$|\gamma^{\varepsilon}(T)| < \beta T \tag{2}$$

where β is a constant coefficient. At the same time, Ref. 7 gives a dependence of the form

$$|\gamma^{\varepsilon}(T)| \propto T^n \quad \text{with} \quad n \geqslant 3. \tag{3}$$

It following that for thermodynamically *equilibrium* polar media at $T \rightarrow 0$ the temperature dependence of the primary pyroelectric coefficient must be of cubic or higher power.

For thermodynamically *nonequilibrium* polar media the following condition can hold:[8]

$$\gamma^{\sigma}(T) = \mathrm{const}. \tag{4}$$

All of the experimentally confirmed theories of low-temperature pyroelectricity as a phenomenon wherein the total (consisting of several components) dipole moment per unit volume (the spontaneous polarization $P_s^{\varepsilon}(T)$ at a constant volume and shape) changes with temperature are based on the assumption that the change with temperature of the dipole moment of any component comes about solely as a result of spatial displacements of the charges forming these dipoles, with no change in the charges themselves, which remain constant for any change in temperature. Since the

first experimental evidence that the values of the charges also change with temperature for $T \geq 300$ K has appeared,[4] it is appropriate to call attention to the theoretical paper of Ohmura *et al.*,[5] who considered the contribution to the pyroelectricity from dipoles with a temperature-dependent charge.

The known experimental facts indicate that only two general fundamental mechanisms are involved in the low-temperature displacements of the charged structural units: anharmonicity of the acoustical and optical oscillations of the lattice, and displacements of the charged structural units in asymmetric potential wells.

The particular mechanisms of low-temperature structural and magnetic phase transitions manifested in pyroelectricity have practically escaped study, there is no generally accepted theory for them, and they will not be discussed here.

Anharmonicity

The temperature dependence of the pyroelectric coefficient due to collective anharmonicity of the acoustical vibrations has the form[9–12]

$$\gamma^{\varepsilon}(T) = AD(\Theta_D/T), \qquad (5a)$$

and that due to anharmonicity of the individual polar optical modes has the form[9,10,12–14]

$$\gamma^{\varepsilon}(T) = \sum B_i E(\Theta_{E_i}/T), \qquad (5b)$$

where $\gamma^{\varepsilon}(T)$ is the primary pyroelectric coefficient, A and B_i are constant coefficients, $D(\Theta_D/T)$ and $E(\Theta_{E_i}/T)$ are the Debye and Einstein functions for the specific heat at constant volume; Θ_D and Θ_{E_i} are the corresponding characteristic temperatures, and T is the absolute temperature.

It has repeatedly been shown experimentally that the temperature dependence $\gamma^{\sigma}(T)$ is described by expression (5a) for linear pyroelectrics and by (5b) for all types of ferroelectrics.

Displacement of charged structural units in asymmetric potential wells

At low and ultralow temperatures the thermal and electrical properties of polar crystals clearly reflect the presence of features of the potential relief with characteristic values $\delta \sim 1$ meV for the energy gap (the difference in the depths of adjacent wells). In particular, the presence of two or more wells in the potential field of the elements of the lattice structure with such a difference in depths should lead to displacements of their average spatial distribution as the temperature is lowered, owing to an ordering of the localization of these elements in the potential wells.

To describe the manifestations of this mechanism we used the Ising model in the mean field approximation,[15] which, after the simplification $\delta(T) = \delta(T=0 \text{ K}) = \text{const}$, which is justified at low temperatures, allows us to express the temperature dependence $\gamma^{\varepsilon}(T)$ in the form

$$\gamma^{\varepsilon}(T) = K\left(\frac{\delta/2k_B T}{\cosh(\delta/2k_B T)}\right)^2, \qquad (6)$$
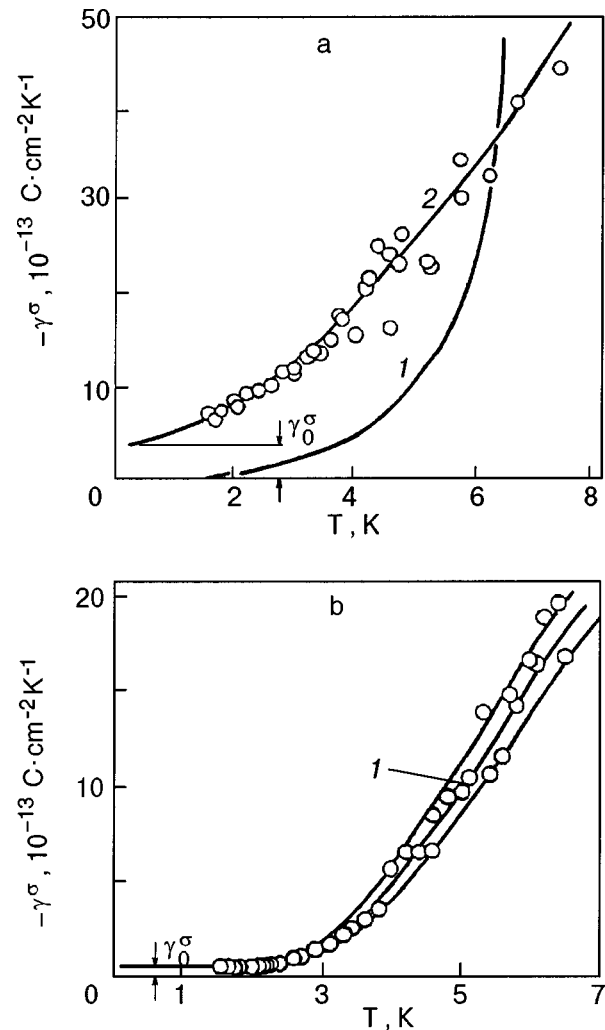

FIG. 1. Constant component in the temperature dependence of $\gamma^{\sigma}(T)$ for ferroelectrics containing a nonequilibrium phase. Single crystals of the TGS group: perfect TGS single crystals (*1*), γ-irradiated single crystals of the ATGS type, dose 35 Mrad (*2*), approximated by the dependence $\gamma^{\sigma}(T) = (3.6 + 1.43T^{1.709} + \dots) \times 10^{-13} \text{ C} \cdot \text{cm}^{-2}\text{K}^{-1}$ (a); PZT-40 ceramic ferroelectric; curve *1*—midline of the corridor encompassing all of the experimental points, approximated by a dependence $\gamma^{\sigma}(T) = [0.5 + E(24 \text{ K}) + \dots] \times 10^{-13} \text{ C} \cdot \text{cm}^{-2}\text{K}^{-1}$ (b).

where K is a constant coefficient, and k_B is Boltzmann's constant.

Expressions (5) and (6) correspond to the thermodynamic Equation (3) and, as is obvious from the type of functions that appear, will give a sharp drop in the values of the pyroelectric coefficient for $T \to 0$.

The results of experimental studies of the temperature dependence $\gamma^{\sigma}(T)$ of perfect and real (containing defects) linear pyroelectrics [Li$_2$SO$_4 \cdot$H$_2$O (Ref. 16)] and ferroelectrics [triglycine sulfate, LiTaO$_3$, and LiNbO$_3$ (Ref. 17) and potassium dihydrogen phosphate (Ref. 18)] are described precisely by expressions (5) and (6), and for $T \to 0$ (curve *1* in Fig. 1a), vanishingly small values have been obtained for the pyroelectric coefficient: $\gamma^{\sigma}(T < 2 \text{ K}) \leq 10^{-14}$ C $\times$ cm^{-2}K^{-1}, in complete agreement with Nernst's rule for the temperature derivatives.

The only possible way of overcoming this fundamental limitation is to create a thermodynamically nonequilibrium polar medium.

The artificial formation of a medium with $\gamma^\sigma(T) \neq 0$ for $T \to 0$ is stimulating interest on two fronts: purely academic interest, i.e., from the standpoint of understanding and describing the properties of such a medium, and interest in relation to applied materials science.

At the present time, two possible ways of realizing nonequilibrium states have been found: nonequilibrium with respect to localization of the charged elements of the lattice that still maintain mobility at $T \ll 4$ K (these could only be protons), and nonequilibrium with respect to charges injected from outside, i.e., an electrically induced state (electret). The density of these charges can be very large (an order of magnitude greater than the spontaneous polarization), and a tiny thermal expansion in this case will give an acceptable value of the pyroelectric coefficient.

Experiments done for both types of nonequilibrium systems demonstrate that it is possible in principle to obtain $\gamma^\sigma(T) \neq 0$ as $T \to 0$, or, more precisely, $\gamma^\sigma(T) \cong \text{const}$ as $T \to 0$.

Figure 1a shows $\gamma^\sigma(T)$ for a single crystal of triglycine sulfate doped with L, α-alanine and phosphorus (ATGS) obtained by irradiation with γ rays in a total dose of 35 Mrad. The constant component of the preliminary coefficient obtained by fitting the experimental data, $\gamma_0^\sigma(T) = 3.6 \times 10^{-13}$ C·cm^{-2}K^{-1} at $T \to 0$ is explained by a temperature-induced ordering of protons delocalized by irradiation in the many double- or multiple-minimum potential wells, with an energy gap $\delta(x,y,z) = (0-1)$ meV.

Figure 1b shows $\gamma^\sigma(T)$ for a PZT ceramic ferroelectric (PZT-40), with the most complex composition of the samples available to the authors. Approximating the experimental data in the temperature interval 1.5–6 K (Fig. 1b) gives

$$\gamma^\sigma(T) = [0.5 + E(24\,\text{K}) + \ldots] \cdot 10^{-13}[\text{C·cm}^{-2}\,\text{K}^{-1}].$$

The presence of a constant component and Einstein terms in this approximation can be interpreted as indicating a contribution to $\gamma^\sigma(T)$ of only the ideal electret phase (charged grain boundaries) and ideal ferroelectric phase (ceramic grains) without the inclusion of the reaction of an intermediate defect phase. It is natural to associate the constant component to the first term in the $\gamma^s(T)$ and the Einstein term with the second.

A materials science figure of merit for the working medium of a pyroelectric transducer is the ratio of the pyroelectric coefficient to the specific heat, $\gamma^\sigma(T)/C_p(T)$.

By studying the temperature dependence of $C_p(T)$ for polar dielectrics containing defects as $T \to 0$, it will be possible to establish the mechanism by which defects interact with the lattice. If these mechanisms create a dependence $C_p(T) \sim T$ (Ref. 19) and the condition $\gamma^\sigma(T) \approx \text{const}$ holds, then for $T \to 0$ the ratio $\gamma^\sigma(T)/C_p(T)$ will increase, i.e., the transducing properties of the pyroelectric will be improved.

It follows that for creating pyroelectric materials efficient in the region $T \leqslant 1.5$ K it is necessary to investigate media in which an appreciable fraction of the volume or the entire volume belongs to the nonequilibrium structural phase.

The following materials of this type have been investigated to varying degrees at helium temperatures:

— single crystals of the TGS group irradiated by γ rays to a does above 15 Mrad;[20]

— polarized polymer films;[21]

— conventional ferroelectric ceramics[1] and polar glassy ceramics;[22]

— quenched polarized ferroelectric glasses.[23]

The search for qualitatively new pyroelectric materials with a temperature-dependent change of the dipole elements of the structure at $T \leqslant 4$ K would also be of fundamental interest.

CONCLUSION

We have presented some fundamental causes that limit the efficient use of conventional pyroelectric materials at $T < 1.5$ K.

For thermodynamically nonequilibrium polar media, to which the Nernst theorem does not apply, these causes are fundamentally eliminated. Demonstration experiments have shown that such media can be used with good effect. The basic types of thermodynamically nonequilibrium polar dielectrics that have promising low-temperature pyroelectric properties are listed.

*E-mail: novikmp@orc.ru

[1] F. Bordoni, P. Carelli, I. Modena, and G. L. Romani, Infrared Phys. **19**, 653 (1979).

[2] T. E. Pfafman, M. Le Gros, E. Silver, J. Beerman, N. Madden, F. Goulding, and D. Landis, J. Low Temp. Phys. **93**, 721 (1993).

[3] V. K. Novik, N. D. Gavrilova, and B. N. Fel'dman, *Pyroelectric Transducers* [in Russian], Sov. Radio, Moscow (1979).

[4] V. Fonseca, P. Simon, and F. Gervias, *Abstracts of the 9th European Meeting on Ferroelectricity*, Prague, August 1999, MO-P**89**, 115.

[5] Y. Ohmura, P. J. Grout, and N. H. March, J. Phys. Chem. Solids **42**, 323 (1981).

[6] P. J. Grout, N. H. March, and T. L. Thorp, J. Phys. **8**, 2167 (1975).

[7] R. Radebaugh, Phys. Rev. Lett. **40**, 572 (1978).

[8] P. J. Grout, N. H. March, and Y. Ohmura, Appl. Phys. Lett. **32**, 453 (1978).

[9] S. Boguslawski, Phys. Z. **15**, 805 (1914).

[10] M. Born, *Atomtheorie des Festen Zustandes (Dynamik der Kristallgitter)*, Teubner, Leipzig–Berlin (1923).

[11] B. Szigetti, Phys. Rev. Lett. **35**, 1532 (1975).

[12] N. D. Gavrilova, E. G. Maksimov, V. K. Novik, and S. N. Drozhdin, Ferroelectrics **100**, 223 (1989).

[13] S. Boguslawski, Phys. Z. **15**, 569 (1914).

[14] M. E. Lines and A. M. Glass, Phys. Rev. Lett. **39**, 1362 (1977).

[15] V. Yu. Galitskiĭ, Fiz. Tverd. Tela (Leningrad) **23**, 815 (1981) [Sov. Phys. Solid State **23**, 463 (1981)].

[16] A. B. Esengaliev, V. K. Novik, V. N. Novikov, and N. D. Gavrilova, Fiz. Nizk. Temp. **18**, 395 (1992) [Sov. J. Low Temp. Phys. **18**, 268 (1992)].

[17] V. N. Novikov, V. K. Novik, A. B. Esengaliev, and N. D. Gavrilova, Ferroelectrics **118**, 59 (1991).

[18] A. B. Esengaliev, V. K. Novik, V. N. Novikov, N. D. Gavrilova, N. P. Zaĭtseva, A. M. Lotonov, and S. V. Bogatyreva, Fiz. Nizk. Temp. **18**, 1022 (1992) [Sov. J. Low Temp. Phys. **18**, 718 (1992)].

[19] I. Henning and E. Hegenbarth, Ferroelectrics **25**, 319 (1988).

[20] A. B. Esengaliev, V. K. Novik, V. N. Novikov, N. D. Gavrilova, and C. N. Drozhdin, Fiz. Nizk. Temp. **18**, 386 (1992) [Sov. J. Low Temp. Phys. **18**, 262 (1992)].

[21] R. W. Newsone and E. Y. Andrei, Phys. Rev. B **55**, 7264 (1997).

[22] W. Xie, Z. Ding, and P. Zhang, J. Am. Ceram. Soc. **79**, 3336 (1996).

[23] A. M. Glass, M. E. Lines, K. Nassau, and J. W. Shiever, Appl. Phys. Lett. **31**, 249 (1977)

Translated by Steve Torstveit

Nuclear spin echo with allowance for the dynamic frequency shift

T. L. Buishvili, L. L. Chotorlishvili, and M. G. Tsanava

*Tbilisi State University, ul. Chavchavadze 3, 380028 Tbilisi, Georgia**
(Submitted February 1, 2000)
Fiz. Nizk. Temp. **26**, 733–734 (July 2000)

The two-pulse nuclear spin echo is studied with allowance for the dynamic frequency shift due to the Suhl–Nakamura interaction. The time dependence of the echo signal amplitude is obtained for small angles of deviation of the magnetization. © *2000 American Institute of Physics.* [S1063-777X(00)01707-2]

Various pulsed methods have been successfully employed to study the dynamics of nuclear spin motion in magnetic crystals;[1] one, in particular, is the spin echo method, in which a nuclear spin system with inhomogeneous broadening of the magnetic resonance (MR) line is excited by one or several radio-frequency (rf) pulses and the response of the nuclear spin system to this stimulus is observed in the form of echo signals. As was shown in Refs. 2 and 3, in spin systems with a dipole–dipole interaction a strong alternating field will substantially alter the relaxation processes that occur due to the spin–spin interaction. Therefore, an analysis based on the application of the Bloch equations, in which the change in the relaxation processes (at pulse durations of the order of the spin–spin interaction times) is not taken into account, is inconsistent. In Ref. 4 a quantum-statistical theory of the nuclear echo in spin systems with the Suhl–Nakamura (SM) interaction was constructed, and results of a more general validity than in Ref. 5 were obtained. However, in Ref. 4 the dynamic frequency shift was neglected so that the authors could obtain an analytical expression for the intensity of the echo signal. On the other hand, in Ref. 5 the dynamic frequency shift due to the SN interaction was studied, and it was shown that as a result of the change in the interaction between spins the value of the dynamic frequency shift depends not only on the average value of the z component of the nuclear spin but also on the ratio between the detuning and amplitude of the strong alternating field. In this paper we tie up the loose ends. For this purpose we employ the model proposed in Refs. 7 and 8 for the frequency mechanism of echo formation. Under the assumptions of zero detuning of the applied pulses (the pulses are at the NMR frequency) and small angles of deviation of the nuclear magnetization after the first and second pulses, $\alpha, \beta < \pi$, the intensity of the echo signal is given by an expression of the form

$$m_\perp(t) = \left[m_0 \alpha \sum_{k=2}^{\infty} (-i)^k J_k[\lambda(t-\tau_{12})] \right.$$

$$\times \int_{-\infty}^{+\infty} g(\Delta\omega) e^{-i\Delta\omega(t-k\tau_{12})} d\Delta\omega + m_0\beta$$

$$\times \sum_{k=1}^{\infty} (-i)^k J_k[\lambda(t-\tau_{12})]$$

$$\times \int_{-\infty}^{\infty} g(\Delta\omega) e^{-i\Delta\omega[t-(k+1)\tau_{12}]} d\Delta\omega \right]$$

$$\times \exp\left(-\frac{t-2\tau_{12}}{T_2} \right). \tag{1}$$

where $J_k[\lambda(t-\tau_{12})]$ is the Bessel function, $g(\Delta\omega)$ is the NMR line shape function, which is Lorentzian,

$$g(\Delta\omega) = \frac{1}{\pi} \frac{(1/T_2^*)^2}{(\Delta\omega - \Delta\omega_0)^2 + (1/T_2^*)^2},$$

$1/T_2^*$ is a quantity characterizing the NMR linewidth, $\Delta\omega_0 = \omega_0 - \omega$ is the detuning between the center of the NMR line and the external alternating field, λ is the dynamic frequency shift, calculated in Ref. 6, and τ_{12} is the interval between pulses. The exponent in (1) contains the damping of the echo signal (T_2 is the transverse relaxation time) for standard values of the quantities appearing in (1):

$$\omega_n \approx 500 \text{ Mhz}, \quad \omega \sim 100 \text{ MHz}, \quad \tau_{12} \sim 10^{-6} \text{ s},$$

$$1/T_2^* \sim 10^7 \text{ s}^{-1}, \quad T_2 \sim 10^{-5} \text{ s}, \quad \lambda = 50 \text{ MHz}.$$

Using numerical methods, we obtained a plot of the time dependence of the echo signal amplitude (Fig. 1). We believe that this result may be useful in experimental research on magnetically ordered crystals, and on the dynamic frequency
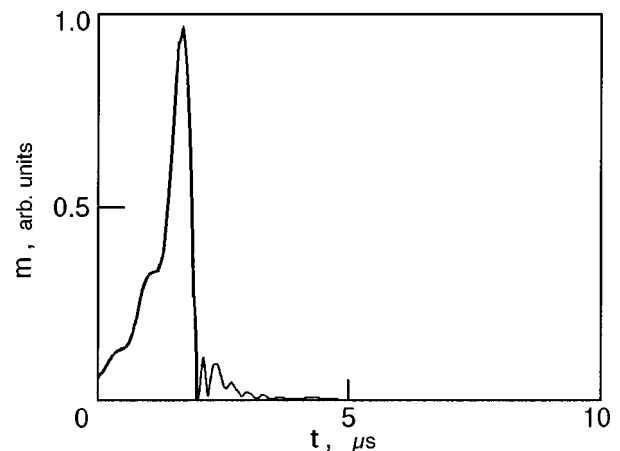

FIG. 1. Time dependence of the echo signal amplitude.

shift as a parameter affecting the shape of the echo signal and carrying information about the change in the value of the interaction between nuclear spins.

*E-mail: kjandieri@altavista.com

[1] Yu. M. Bun'kov and B. S. Dumesh, in *Problems of Magnetic Resonance* [in Russian], Nauka, Moscow (1978).
[2] A. G. Redfied, Phys. Rev. **98**, 787 (1955).

[3] C. P. Slichter, *Principles of Magnetic Resonance*, 3rd ed., Springer-Verlag, Berlin (1990); Mir, Moscow (1981).
[4] L. L. Buishvili, E. B. Volzhan, and K. O. Khutsishvili, Fiz. Tverd. Tela (Leningrad) **24**, 3184 (1982) [Sov. Phys. Solid State **24**, 1808 (1982)].
[5] V. P. Chekmarev, M. I. Kurkin, and S. I. Goloshchapov, Zh. Éksp. Teor. Fiz. **76**, 1675 (1979) [Sov. Phys. JETP **49**, 851 (1979)].
[6] L. L. Buishvili, T. G. Vardosanidze, and A. I. Ugulava, Zh. Éksp. Teor. Fiz. **70**, 1921 (1976) [Sov. Phys. JETP **43**, 1000 (1976)].
[7] W. Gold, Phys. Lett. A **29**, 347 (1969).
[8] P. M. Richards, Phys. Rev. B **4**, 2216 (1971)

Translated by Steve Torstveit

ERRATA

Erratum: Influence of intrinsic point defects on the electrophysical properties of NbSe₃ [Low Temp. Phys. 26, 130–133 (February 2000)]

A. A. Mamaluĭ, T. N. Shelest, and Kh. B. Chashka

Kharkov State Polytechnical University, ul. Frunze 21, 310002 Frunze, Ukraine
Fiz. Nizk. Temp. **26**, 735 (July 2000)

[S1063-777X(00)01807-7]

In the caption to Fig. 2 the curve labels (*1*) and (*2*) should be ignored, and the data indicated by (+) refers to 323 K instead of 327 K, as printed.